

**Deformable registration using shape statistics with  
applications in sinus surgery**

by

Ayushi Sinha

A dissertation submitted to The Johns Hopkins University in conformity with the  
requirements for the degree of Doctor of Philosophy.

Baltimore, Maryland

May, 2018

© Ayushi Sinha 2018

All rights reserved

# Abstract

Evaluating anatomical variations in structures like the nasal passage and sinuses is challenging because their complexity can often make it difficult to differentiate normal and abnormal anatomy. By statistically modeling these variations and estimating individual patient anatomy using these models, quantitative estimates of similarity or dissimilarity between the patient and the sample population can be made. In order to do this, a spatial alignment, or registration, between patient anatomy and the statistical model must first be computed.

In this dissertation, a *deformable most likely point paradigm* is introduced that incorporates statistical variations into probabilistic feature-based registration algorithms. This paradigm is a variant of the most likely point paradigm, which incorporates feature uncertainty into the registration process. The deformable registration algorithms optimize the probability of feature alignment as well as the probability of model deformation allowing statistical models of anatomy to estimate, for instance, structures seen in endoscopic video without the need for patient specific computed tomography (CT) scans. The probabilistic framework also enables the algorithms to

## ABSTRACT

assess the quality of registrations produced, allowing users to know when an alignment can be trusted. This dissertation covers three algorithms built within this paradigm and evaluated in simulation and in-vivo experiments.

# Thesis Committee

## Primary Reader

Russell H. Taylor (Primary Advisor)  
John C. Malone Professor  
Department of Computer Science  
The Johns Hopkins University

## Secondary Readers

Gregory D. Hager (Co-Advisor)  
Mandell Bellmore Professor  
Department of Computer Science  
The Johns Hopkins University

Masaru Ishii  
Associate Professor  
Department of Otolaryngology - Head and Neck Surgery  
Johns Hopkins Medical Institutions

Austin Reiter  
Assistant Research Professor  
Department of Computer Science  
The Johns Hopkins University

# Dedication

To my parents,

*Pushpa and Ranjit Kumar Sinha,*

for placing their trust in my decisions

and giving me the motivation to achieve my goals.

# Acknowledgments

For everyone who lead me to and through this journey, I am extremely grateful.

First and foremost, I would like to express my sincerest thanks to my thesis committee. Thank you to my advisor, Dr. Russell Taylor, for guiding me along the path that lead to this dissertation. Without your invaluable advice and faith in me, this dissertation would not have been possible. Thank you for your unrelenting support. Thank you to my co-advisor, Dr. Greg Hager, for bringing me onto the project that lead to my dissertation work. Your indispensable feedback was essential to my progress. Thank you, Dr. Masaru Ishii, for your patience and advice. Your guidance was critical to my understanding of clinical perspectives. Thank you, Dr. Austin Reiter, for helping me step outside my comfort zone and deliberate broader applications and solutions.

I am grateful to everyone else who has mentored me during my graduate career. Thank you, Dr. Misha Kazhdan, for your guidance during my initial years at the Johns Hopkins University and for helping me learn to think critically. Thank you, Dr. Jerry Prince, for you insightful comments. Thank you, Dr. Yoshito Otake and

## ACKNOWLEDGMENTS

Dr. Yoshinobu Sato, for your guidance and the incredible opportunity to work in Japan. Thank you, also, to Dr. Randal Burns, Dr. Yanif Ahmad and Dr. Ben Langmead for your advice through different projects, and also to all the professors whose incredible courses helped me learn so much through the years. I hold deep gratitude for the counsel I received during my undergraduate studies at Providence College. Thank you, Dr. Liam Donohoe, for encouraging me to pursue research. Thank you, Dr. Richard Connelly, for creating courses for me to prepare me for graduate school. Thank you, Prof. Frank Ford, for your invaluable advice. Thank you, everyone at Providence College for believing in me.

I would like to thank all my current and former colleagues at the Johns Hopkins University, in the Department of Computer Science, the Laboratory for Computational Sensing and Robotics (LCSR), and the Malone Center for Engineering in Healthcare (MCEH). Thank you, Dr. Seth Billings, for being ever so willing to help me through the work that went into this dissertation. Your elegant software framework was a joy to work with. Thank you, Rob Grupp, for showing me the ropes when I was first introduced to medical image data. Thank you, Anton Deguet, for your patience in answering my countless queries about servers and data storage, and Dr. Simon Leonard, for your immeasurable help with everything endoscopic data related. Thank you, Dr. Ming Chuang, for your invaluable advice during my first few years. Thank you to everyone who has enriched my graduate experience in one way or another - Dr. Narges Ahmidi, Jonathan Jones, Molly O'Brien, Razieh Nabi,

## ACKNOWLEDGMENTS

Rob DiPietro, Dr. Anand Malpani, Princy Parsana, Mike Peven, Disa Mhembere, Da Zheng, Katie Henry, Nikita Ivkin, Javad Fotouhi, Sing Chun Lee, Mathias Umberath, Xingtong Liu, Preetham Chalasani, Kate Fischl, Alycen Wiacek, Huda Khayrallah, Michelle Graham, Dr. Will Gray Roncal, and anyone that I have inevitably missed. Thank you for your friendship, advice and stimulating conversations about pretty much any topic under the sun.

I am also extremely thankful for the wonderful staff in the Department of Computer Science, LCSR and MCEH. Thank you, Zack Burwell, for your patience in answering my countless questions. Thank you, Debbie DeFord, for your lovely conversations. Thank you, Tonette McClamy and Javonnia Thomas, for your help with finances. Thank you, Nina Jackson-Goode and Tracy Marshall, for your hard work and lovely conversations. Thank you, also, to Shani McPherson, Laura Graham, Alison Morrow, Cathy Thornton and everyone who helped make my journey through graduate school so smooth. I am also grateful to the IT support staff, Steve Rifkin and Steve DeBlasio, for your patience in helping me not break things. I am also thankful to the Department of Computer Science for supporting me during my initial years in graduate school, as well as to the National Institutes of Health and Intuitive Surgical, Inc. for funding my research.

I would also like to thank the friends I have made outside my work. Your friendship has made my time in Baltimore and this journey an incredible one. Thank you, Dr. Shoumyo Majumdar, Nitya Majumdar, Deena Jamal, Natt Athamanolap, Mar-



## ACKNOWLEDGMENTS

tin Vilarino, Sandra Hwang, Megan Hodgdon, Marie Ferguson, Sid Gupta, Aymeric Matthieu Dominique Blanc, Megan Ritchie, James Corcoran, Yuchuan Miao, Martina Leistner, and many more, for the many beautiful memories from around the globe that I will forever cherish. Thank you, also, to Francesca Genova, Laura Tresca and Yi Cao. Your continued support and friendship is irreplaceable. Finally, a very special thank you to my boyfriend, Luke Osborn. Your wonderful friendship and continued support made this journey so much easier. Thank you for standing by me, often with food, during the most demanding periods of my graduate career.

Last but not least, I would like to give my sincerest thanks to my family for inspiring and supporting me throughout my life. Thank you to my parents, Pushpa and Ranjit Kumar Sinha, for trusting my judgment and supporting my choices. I would not be here without your love and encouragement. I am also thankful to my sister, Toshi Sinha, for her love and support.

I owe my deepest gratitude to each and every one of you.

# Contents

<b>Abstract</b>	<b>ii</b>
<b>Acknowledgments</b>	<b>vi</b>
<b>List of Tables</b>	<b>xviii</b>
<b>List of Figures</b>	<b>xix</b>
<b>List of Algorithms</b>	<b>xxxii</b>
<b>1 Introduction</b>	<b>1</b>
1.1 Clinical background . . . . .	2
1.2 Technical background . . . . .	10
1.3 Thesis Statement . . . . .	18
1.4 Thesis outline . . . . .	18
1.5 Contributions . . . . .	22
1.6 Published Work . . . . .	25

## CONTENTS

<b>2</b>	<b>Segmentation and statistical modeling of CT data</b>	<b>27</b>
2.1	Automatic segmentation . . . . .	29
2.2	Statistical shape modeling . . . . .	36
2.3	Simultaneous segmentation and correspondence improvement . . . . .	41
2.4	Experimental results and discussion . . . . .	44
2.4.1	GVF experiment . . . . .	44
2.4.2	Constrained GVF experiment . . . . .	46
2.5	Concluding Remarks . . . . .	50
2.6	Contributions . . . . .	52
2.7	Published Work . . . . .	52
<b>3</b>	<b>The deformable most-likely-point paradigm</b>	<b>53</b>
3.1	Probabilistic model . . . . .	58
3.1.1	Probabilistic model for shape deformation . . . . .	59
3.1.2	Probabilistic model for deformable registration . . . . .	61
3.2	Correspondence phase . . . . .	64
3.3	Registration phase . . . . .	66
3.4	Concluding remarks . . . . .	68
3.5	Contributions . . . . .	69
3.6	Published work . . . . .	70
<b>4</b>	<b>Deformable iterative most likely point (D-IMLP) algorithm</b>	<b>71</b>

## CONTENTS

4.1	Probabilistic model . . . . .	72
4.2	Algorithm overview . . . . .	75
4.3	Correspondence phase . . . . .	84
4.4	Registration phase . . . . .	86
4.5	Experimental results and discussion . . . . .	91
4.5.1	Sample size experiment . . . . .	93
4.5.1.1	Experiment 1: Isotropic position noise . . . . .	94
4.5.1.2	Experiment 2: Anisotropic position noise . . . . .	95
4.5.2	Regularization term experiment . . . . .	98
4.5.3	Noise model experiment . . . . .	102
4.5.3.1	Experiment 1: Varying isotropic position noise . . . . .	102
4.5.3.2	Experiment 2: Varying anisotropic position noise . . . . .	104
4.5.3.3	Experiment 3: Noise parameter sweep . . . . .	104
4.5.4	Outlier experiment . . . . .	107
4.5.5	Scale experiment . . . . .	110
4.5.6	Leave-one-out experiment . . . . .	112
4.5.6.1	Experiment 1: Middle turbinates . . . . .	113
4.5.6.2	Experiment 2: Right nasal airway . . . . .	116
4.5.6.3	Experiment 3: Right nasal airway with outliers . . . . .	119
4.5.7	Partial data experiment . . . . .	120
4.5.7.1	Experiment 1: Pelvis . . . . .	122

## CONTENTS

4.5.7.2	Experiment 2: Right nasal airway . . . . .	122
4.5.8	Failure detection experiment . . . . .	124
4.5.8.1	Experiment 1: Known noise . . . . .	127
4.5.8.2	Experiment 2: Unknown noise . . . . .	127
4.5.9	Non-medical data experiment . . . . .	131
4.5.9.1	Experiment 1: Human expression . . . . .	131
4.5.9.2	Experiment 2: Human pose . . . . .	132
4.6	Concluding remarks . . . . .	134
4.7	Contributions . . . . .	137
4.8	Published work . . . . .	138
<b>5</b>	<b>Deformable iterative most likely oriented point (D-IMLOP) algo-</b>	
	<b>rithm</b>	<b>139</b>
5.1	Probabilistic model . . . . .	141
5.2	Algorithm overview . . . . .	144
5.3	Correspondence phase . . . . .	152
5.4	Registration phase . . . . .	153
5.5	Experimental results and discussion . . . . .	158
5.5.1	Sample size experiment . . . . .	159
5.5.1.1	Experiment 1: Isotropic position noise . . . . .	159
5.5.1.2	Experiment 2: Anisotropic position noise . . . . .	159
5.5.2	Regularization term experiment . . . . .	164

## CONTENTS

5.5.3	Noise model experiment . . . . .	165
5.5.3.1	Experiment 1: Varying isotropic position noise . . .	165
5.5.3.2	Experiment 2: Varying anisotropic position noise . .	167
5.5.3.3	Experiment 3: Varying orientation noise . . . . .	167
5.5.3.4	Experiment 4: Noise parameter sweep . . . . .	172
5.5.4	Outlier experiment . . . . .	174
5.5.5	Scale experiment . . . . .	177
5.5.6	Leave-one-out experiment . . . . .	177
5.5.6.1	Experiment 1: Middle turbinates . . . . .	179
5.5.6.2	Experiment 2: Right nasal airway . . . . .	179
5.5.6.3	Experiment 3: Right nasal airway with outliers . . .	184
5.5.7	Partial data experiment . . . . .	184
5.5.7.1	Experiment 1: Pelvis . . . . .	184
5.5.7.2	Experiment 2: Right nasal airway . . . . .	187
5.5.8	Failure detection experiment . . . . .	190
5.5.8.1	Experiment 1: Known noise . . . . .	190
5.5.8.2	Experiment 2: Unknown noise . . . . .	193
5.5.9	Non-medical data experiment . . . . .	196
5.5.9.1	Experiment 1: Human expression . . . . .	196
5.5.9.2	Experiment 2: Human pose . . . . .	196
5.6	Concluding remarks . . . . .	198

## CONTENTS

5.7	Contributions . . . . .	201
5.8	Published work . . . . .	201
<b>6</b>	<b>Generalized deformable iterative most likely oriented point (GD- IMLOP) algorithm</b>	<b>203</b>
6.1	Probabilistic model . . . . .	204
6.2	Algorithm overview . . . . .	209
6.3	Correspondence phase . . . . .	216
6.4	Registration phase . . . . .	217
6.5	Experimental results and discussion . . . . .	222
6.5.1	Sample size experiment . . . . .	223
6.5.1.1	Experiment 1: Isotropic position noise . . . . .	223
6.5.1.2	Experiment 2: Anisotropic position noise . . . . .	226
6.5.2	Regularization term experiment . . . . .	229
6.5.3	Noise model experiment . . . . .	230
6.5.3.1	Experiment 1: Varying isotropic position noise . . . . .	230
6.5.3.2	Experiment 2: Varying anisotropic position noise . . . . .	230
6.5.3.3	Experiment 3: Varying orientation noise . . . . .	233
6.5.3.4	Experiment 4: Noise parameter sweep . . . . .	233
6.5.4	Outlier experiment . . . . .	237
6.5.5	Scale experiment . . . . .	238
6.5.6	Leave-one-out experiment . . . . .	241

## CONTENTS

6.5.6.1	Experiment 1: Middle turbinates . . . . .	241
6.5.6.2	Experiment 2: Right nasal airway . . . . .	241
6.5.6.3	Experiment 3: Right nasal airway with outliers . . . . .	244
6.5.7	Partial data experiment . . . . .	248
6.5.7.1	Experiment 1: Pelvis . . . . .	248
6.5.7.2	Experiment 2: Right nasal airway . . . . .	249
6.5.8	Failure detection experiment . . . . .	253
6.5.8.1	Experiment 1: Known noise . . . . .	253
6.5.8.2	Experiment 2: Unknown noise . . . . .	256
6.5.9	Non-medical data experiment . . . . .	262
6.5.9.1	Experiment 1: Human expression . . . . .	262
6.5.9.2	Experiment 2: Human pose . . . . .	262
6.6	Concluding remarks . . . . .	267
6.7	Contributions . . . . .	268
6.8	Published work . . . . .	268
<b>7</b>	<b>Deformable video-CT registration</b>	<b>270</b>
7.1	Deformable registration . . . . .	273
7.1.1	The deformable most-likely-point paradigm . . . . .	274
7.1.2	Dense reconstruction from video . . . . .	275
7.2	Experimental results and discussion . . . . .	277
7.2.1	Reconstruction from single frame . . . . .	278



## CONTENTS

7.2.2	Reconstruction from multiple frames . . . . .	281
7.3	Concluding remarks . . . . .	285
7.4	Contributions . . . . .	287
7.5	Published Work . . . . .	287
<b>8</b>	<b>Clinical applications of statistical shape models of sinuses and sur- rounding structures</b>	<b>289</b>
8.1	Experimental results and discussion . . . . .	292
8.1.1	Variation in population . . . . .	293
8.1.2	Nasal cycle . . . . .	309
8.1.3	Shape inference . . . . .	310
8.1.3.1	Internal nasal valve . . . . .	316
8.1.3.2	External nasal valve . . . . .	318
8.2	Concluding Remarks . . . . .	321
8.3	Contributions . . . . .	322
8.4	Published Work . . . . .	322
<b>9</b>	<b>Conclusions</b>	<b>324</b>
9.1	Future work . . . . .	327
	<b>Bibliography</b>	<b>331</b>
	<b>Vita</b>	<b>360</b>

# List of Tables

1.1	Summary of the deformable registration algorithms presented in this dissertation. . . . .	19
2.1	Segmentation errors computed using the Hausdorff distance metric: GVF and constrained GVF (C-GVF) both produce comparable improvement over deformable registration (DR). C-GVF has the added advantage of maintaining correspondences (Figure 2.11). . . . .	47
4.1	Different $\chi^2_{\text{thresh}}$ values based on different values of $p$ for 3 DOF. . . . .	83
4.2	Sample size experiment: percent successful registration runs, i.e., runs producing TREs less than 1 mm and, in parentheses, percent successful runs correctly detected as successful using residual errors. . . . .	98
5.1	Sample size experiment: percent successful registration runs, i.e., runs producing TREs less than 1 mm and, in parentheses, percent successful runs correctly detected as successful using residual errors. . . . .	164
6.1	Sample size experiment: percent successful registration runs, i.e., runs producing TREs less than 1 mm and, in parentheses, percent successful runs correctly detected as successful using residual errors. . . . .	226
7.1	Registration results using single frame reconstruction from in-vivo data.	279
7.2	Residual errors produced by registrations on clinical data. . . . .	283
8.1	Percent errors in cross-sectional area estimation of the internal nasal valve. . . . .	318
8.2	Percent errors in cross-sectional area estimation of the external nasal valve. . . . .	321

# List of Figures

1.1	Anatomy of the nasal cavity. Licensed under the Creative Commons Attribution 3.0 Unported license . . . . .	3
1.2	Anatomy of the sinuses. Licensed under the Creative Commons Attribution - Share Alike 3.0 Unported license . . . . .	5
2.1	Template creation pipeline: all input images are deformably registered to one target image, which is then deformed by the mean of the deformation fields resulting from the registrations. The colors in the deformation fields represent the direction of the deformation vectors, whereas the intensity of the colors indicates the magnitude of the vectors. Deforming the target image by the mean deformation field takes the target image towards the mean of the input images. This process is iterated with the output image as the new target image. Individual variation from the initial target image decreases with every iteration, and the resulting output moves closer to the mean of the input set of images. . . . .	31
2.2	Sampling scheme (blue dots represent sampled vertices, blue lines indicate adjacency; dotted lines imply that connected points should not be attracted to each other; translucent lines cut through the shape): Random sampling (top) causes inconsistent internal and external directions. The middle sphere shows a vertex (circled) with external energy pointing inwards into the sphere, and the right sphere shows one (circled) with internal energy pointing outwards. The spiral sampling scheme maintains internal and external direction consistency. . .	35
2.3	Segmentation improvement illustrated in 2D: from left to right, vertices in the snake spline (orange) move towards the edge in the image. Since corner points must not be drawn inward toward each other, corner points are not allowed to move. However, these points are updated during other iterations when they are not corner points. After several iterations all vertices converge to the closest edge. . . . .	35

## LIST OF FIGURES

2.4	Given correspondences between shapes in a dataset, PCA can be used to understand the mean and variance in the dataset. <sup>1</sup> . . . . .	39
2.5	Correspondence improvement algorithm presented by Seshamani et al. <sup>2</sup> using the middle turbinate as an example shape. . . . .	40
2.6	2D example illustrating the constrained GVF algorithm: Initial shape (gray curve) is evolved to new updated shape (black curve), which is then estimated using an SSM (dashed curve). Vertices (black dots) on the updated shape are moved along the surface toward corresponding vertices on the estimated shape to obtain new vertex positions (yellow dots) that preserve correspondence between the update shape and SSM. . . . .	42
2.7	Simultaneous segmentation and correspondence improvement using the middle turbinate as an example shape. The middle (green) section performs the constrained segmentation improvement which is followed by the correspondence improvement method presented by Seshamani et al. <sup>2</sup> . . . . .	43
2.8	Left: contours of hand-segmented (blue) and deformably registered (red) left and right maxillary sinuses. Right: contours after GVF (green) overlap almost perfectly with the hand-segmented contours. . . . .	45
2.9	Top: errors from deformable registration visualized on the right maxillary sinus mesh with lighting (left) to show structure and without lighting (right) to focus on errors without distractions from specularities or shadows. Bottom: errors after GVF, visualized similarly as above. . . . .	45
2.10	Left: Initial segmentation (red) of the maxillary sinus using deformable registration does not capture details such as sharp corners, therefore introducing errors when compared with hand-segmented gold standard (blue). Right: Constrained GVF is able to capture these details (green). . . . .	48
2.11	Residual surface errors from leave-one-out analysis: since the shapes produced by constrained GVF (C-GVF) contain more detail than those produced by deformable registration (DR) (Figure 2.10), it is hard to estimate shapes with few modes. However, with more than roughly 30 modes, shape estimation errors for segmentations improved using C-GVF show improvement (green) over the original shapes obtained using DR (red). On the other hand, segmentations improved using traditional GVF (purple) do not maintain correspondence between shapes, as reflected in the deteriorating mean residual errors. . . . .	49
2.12	Meshes obtained using GVF (left) can contain skinny triangles near corners causing pinching artifacts and flipped triangles, whereas meshes obtained using constrained GVF (right) avoid these problems producing more stable meshes. . . . .	51

## LIST OF FIGURES

4.1	Registration metrics: TSE (top) measures the Hausdorff distance between the ground truth shape (green) and the shape estimated by our algorithm in shape space (blue), not taking the final transformation computed by the algorithm into consideration. TRE (bottom) measures the Hausdorff distance between the ground truth shape (green) and the estimated shape (blue) transformed to sample point space, therefore also adding the transformation computed by our algorithms into the error metric. . . . .	92
4.2	Sample size experiment: translation (left) and rotation (right) errors produced using, from top to bottom, 1000, 1500 and 2000 data points sampled from the pelvis model in Exp. 1 (Sec. 4.5.1.1) . . . . .	96
4.3	Sample size experiment: increasing TSE (top) and TRE (bottom) with increasing number of sample points in Exp. 1 (Sec. 4.5.1.1). Note that errors are increasing with increasing modes because for this experiment the number of modes used to estimate the shapes equals the number of modes used to simulate a new shape from which points were sampled.	97
4.4	Sample size experiment: translation (left) and rotation (right) errors produced using, from top to bottom, 1000, 1500 and 2000 data points sampled from the pelvis model in Exp. 2 (Sec. 4.5.1.2) . . . . .	99
4.5	Sample size experiment: residual errors compared against TRE using 2000 sample points in Exp. 1 (left) and Exp. 2 (right). The two measures exhibit correlation in both experiments 1 and 2 with correlation coefficients of 0.95 and 0.88, respectively. . . . .	100
4.6	Regularization term experiment: registrations produced by D-IMLP in the presence of small noise were unaffected by the absence of the regularization term. . . . .	101
4.7	Noise model experiment: a general trend of increasing TRE as the uncertainty in the sample points increases. Note that errors are increasing with increasing modes because for this experiment the number of modes used to estimate the shapes equals the number of modes used to simulate a new shape from which points were sampled. . . . .	103
4.8	Noise model experiment: residual errors compared against TRE using 500 sample points with $2 \times 2 \times 2 \text{ mm}^3$ SD positional noise and $2^\circ$ SD angular noise in Exp. 1 of the noise model experiment (Sec. 4.5.3.1). The two measures exhibit correlation with correlation coefficient of 0.86.	103
4.9	Noise model experiment: a general trend of increasing TRE as the uncertainty in the sample points increases. Note that errors are increasing with increasing modes because for this experiment the number of modes used to estimate the shapes equals the number of modes used to simulate a new shape from which points were sampled. . . . .	105

## LIST OF FIGURES

4.10	Noise model experiment: residual errors compared against TRE using 500 sample points with $2 \times 2 \times 3 \text{ mm}^3$ SD positional noise and $2^\circ$ SD angular noise in Exp. 2 of the noise model experiment (Sec. 4.5.3.2). The two measures exhibit correlation with correlation coefficient of 0.87.	105
4.11	Noise model experiment: parameter sweep results show that D-IMLP is unaffected by changing angular noise assumptions since orientations are not taken into account by D-IMLP. Therefore, only the last plot ( $20^\circ$ ) is visible since the plots overlap almost perfectly. Errors are also stable (top) or gradually decreasing (bottom) under changing position noise assumptions, although increasing anisotropy tends to increase TRE (bottom).	106
4.12	Outlier experiment: mean TRE with different number of outliers using D-IMLP. Note that errors are increasing with increasing modes because for this experiment the number of modes used to estimate the shapes equals the number of modes used to simulate the deformed shape from which points were sampled.	108
4.13	Residual errors compared against TRE using the right nasal cavity meshes in the outlier experiment with 0% outliers. The two measures exhibit correlation with a correlation coefficient of 0.88.	108
4.14	Residual errors compared against TRE using the right nasal cavity meshes in the outlier experiment with 10% (top) and 20% (bottom) outliers. The two measures exhibit high correlation when the sample points contain 10% outliers with a correlation coefficient of 0.81, and weak correlation with the sample points contain 20% outliers with a correlation coefficient of 0.59.	109
4.15	Scale experiment: additional scale optimization increases TRE as compared to when scale optimization is not required.	111
4.16	Scale experiment: errors in scale estimation using D-IMLP with increasing number of modes remain stable.	111
4.17	Leave-one-out experiment: TSE (top) and TRE (bottom) produced by D-IMLP compared against that produced by CPD and SSM using the middle turbinate meshes in the leave-one-out experiment.	114
4.18	Leave-one-out experiment: runtime comparison between CPD and D-IMLP.	115
4.19	Leave-one-out experiment: TSE (top) and TRE (bottom) produced by D-IMLP compared against that produced by the SSM estimate using the right nasal cavity meshes in the leave-one-out experiment.	117
4.20	Leave-one-out experiment: residual errors compared against TRE using the middle turbinate meshes in the leave-one-out experiment. The two measures exhibit correlation with correlation coefficients of 0.91.	118

## LIST OF FIGURES

4.21	Leave-one-out experiment: residual errors compared against TRE using the right nasal cavity meshes in the leave-one-out experiment. The two measures exhibit correlation with correlation coefficients of 0.95. . . . .	118
4.22	Leave-one-out experiment: TRE produced by D-IMLP with 0%, 10% and 20% outliers in the data points sampled from the right nasal cavity meshes in the leave-one-out experiment. . . . .	119
4.23	Partial data experiment: An example of data generated for the partial data experiment: (top) points are sampled only from the ilium and ischium on the pelvis mesh, and (bottom) points are sampled from the front section of the right nostril which include parts of the septum and middle and inferior turbinates. . . . .	121
4.24	Partial data experiment: TSE (top) and TRE (bottom) produced by D-IMLP compared against that produced by the SSM estimate using the pelvis meshes. . . . .	123
4.25	Partial data experiment: TSE (top) and TRE (bottom) produced by D-IMLP compared against that produced by the SSM estimate using the right nasal airway meshes. . . . .	125
4.26	Partial data experiment: residual errors compared against TRE using the pelvis (top) and right nasal airway (bottom) meshes. The two measures exhibit weak correlation in both experiments 1 and 2 with correlation coefficients of 0.52 and 0.56, respectively. . . . .	126
4.27	Failure detection experiment: Confusion matrix (top) and correlation between $E_p$ and TRE (bottom) with a correlation coefficient of 0.90 when the noise in the data is known. . . . .	128
4.28	Failure detection experiment: Confusion matrix (top) and weak correlation between $E_p$ and TRE (bottom) with a correlation coefficient of 0.46 when the noise in the data is unknown. . . . .	130
4.29	Leave- $n$ -out experiment: TSE (top) and TRE (bottom) produced by D-IMLP. . . . .	133
4.30	Leave- $n$ -out experiment: TSE (top) and TRE (bottom) produced by D-IMLP. . . . .	135
4.31	Leave- $n$ -out experiment: residual errors compared against TRE show that the two measures exhibit high correlation using the facial expression data with a correlation coefficient of 0.81 (top), and no correlation using the human pose data with a correlation coefficient of 0.03 (bottom). . . . .	136
5.1	Sample size experiment: translation (left) and rotation (right) errors produced using, from top to bottom, 1000, 1500 and 2000 data points sampled from the pelvis model in Exp. 1 (Sec. 5.5.1.1) . . . . .	160
5.2	Sample size experiment: increasing TSE (top) and TRE (bottom) with increasing number of sample points in Exp. 1. . . . .	161

## LIST OF FIGURES

5.3	Sample size experiment: translation (left) and rotation (right) errors produced using, from top to bottom, 1000, 1500 and 2000 data points sampled from the pelvis model in Exp. 2 (Sec. 5.5.1.2) . . . . .	162
5.4	Sample size experiment: residual errors compared against TRE using 2000 sample points in Exp. 1 (left) and Exp. 2 (right). The two measures exhibit correlation in both experiments 1 and 2 with correlation coefficients of 0.96 and 0.94, respectively. . . . .	163
5.5	Regularization term experiment: registrations produced by D-IMLOP without the regularization term showed deterioration with increasing shape parameters. . . . .	165
5.6	Noise model experiment: a general trend of increasing TRE as the uncertainty in the sample points increases. Note that errors are increasing with increasing modes because for this experiment the number of modes used to estimate the shapes equals the number of modes used to simulate a new shape from which points were sampled. . . . .	166
5.7	Noise model experiment: residual errors compared against TRE using 500 sample points with $2 \times 2 \times 2 \text{ mm}^3$ SD positional noise and $2^\circ$ SD angular noise in Exp. 1 of the noise model experiment (Sec. 5.5.3.1). The two measures exhibit correlation with correlation coefficient of 0.87. . . . .	166
5.8	Noise model experiment: a general trend of increasing TRE as the uncertainty in the sample points increases. Note that errors are increasing with increasing modes because for this experiment the number of modes used to estimate the shapes equals the number of modes used to simulate a new shape from which points were sampled. . . . .	168
5.9	Noise model experiment: residual errors compared against TRE using 500 sample points with $2 \times 2 \times 3 \text{ mm}^3$ SD positional noise and $2^\circ$ SD angular noise in Exp. 2 of the noise model experiment (Sec. 5.5.3.2). The two measures exhibit correlation with correlation coefficient of 0.88. . . . .	168
5.10	Noise model experiment: mean TREs produced by D-IMLP (top) and D-IMLOP (bottom) in Exp. 3 show that small changes in orientation noise do not have large influence on registration result. Note that the errors are increasing with increasing modes only because for this experiment the number of modes used to estimate the shapes equals the number of modes used to simulate a new shape from which points were sampled. . . . .	169
5.11	Noise model experiment: residual errors compared against TRE using 500 sample points with $1 \times 1 \times 1 \text{ mm}^3$ SD positional noise, $4^\circ$ SD angular noise (top), and $1 \times 1 \times 2 \text{ mm}^3$ SD positional noise, $8^\circ$ SD angular noise (bottom) in Exp. 3 of the noise model experiment. The two measures exhibit correlation for both isotropic and anisotropic position noise with correlation coefficient of 0.91 and 0.92, respectively. . . . .	170



## LIST OF FIGURES

5.12	Noise model experiment: residual errors compared against TRE using 500 sample points with $1 \times 1 \times 1 \text{ mm}^3$ SD positional noise, $4^\circ$ SD angular noise (top), and $1 \times 1 \times 2 \text{ mm}^3$ SD positional noise, $8^\circ$ SD angular noise (bottom) in Exp. 3 of the noise model experiment. The two measures exhibit correlation for both isotropic and anisotropic position noise with correlation coefficient of 0.72 and 0.78, respectively. . . . .	171
5.13	Noise model experiment: parameter sweep results show that D-IMLOP produces lower errors when the noise assumptions are optimistic, and errors increase as noise assumptions become more pessimistic. . . . .	173
5.14	Outlier experiment: mean TRE with different number of outliers using D-IMLOP. Note that errors are increasing with increasing modes because for this experiment the number of modes used to estimate the shapes equals the number of modes used to simulate the deformed shape from which points were sampled. . . . .	175
5.15	Outlier experiment: residual errors compared against TRE using the right nasal cavity meshes with 0% outliers. The two measures exhibit correlation with a correlation coefficient of 0.93. . . . .	175
5.16	Outlier experiment: residual errors compared against TRE using the right nasal cavity meshes with 10% (top) and 20% (bottom) outliers. The two measures exhibit high correlation in both experiments with correlation coefficients of 0.95 and 0.92, respectively. . . . .	176
5.17	Scale experiment: additional scale optimization increases TRE as compared to when scale optimization is not required. . . . .	178
5.18	Scale experiment: errors in scale estimation using D-IMLOP with increasing number of modes remain stable, and are lower than those produced using D-IMLP. . . . .	178
5.19	Leave-one-out experiment: TSE (top) and TRE (bottom) produced by D-IMLOP compared against that produced by CPD and SSM using the middle turbinate meshes in the leave-one-out experiment. . . . .	180
5.20	Leave-one-out experiment: runtime comparison between CPD, D-IMLP and D-IMLOP. . . . .	181
5.21	Leave-one-out experiment: TSE (top) and TRE (bottom) produced by D-IMLOP compared against that produced by the SSM estimate using the right nasal cavity meshes in the leave-one-out experiment. . . . .	182
5.22	Leave-one-out experiment: residual errors compared against TRE using the middle turbinate meshes in the leave-one-out experiment. The two measures exhibit correlation with correlation coefficients of 0.65. . . . .	183
5.23	Leave-one-out experiment: residual errors compared against TRE using the right nasal cavity meshes in the leave-one-out experiment. The two measures exhibit correlation with correlation coefficients of 0.75. . . . .	183

## LIST OF FIGURES

5.24	Leave-one-out experiment: TRE produced by D-IMLOP with 0%, 10% and 20% outliers in the data points sampled from the right nasal cavity meshes in the leave-one-out experiment. . . . .	185
5.25	Partial data experiment: TSE (top) and TRE (bottom) produced by D-IMLOP compared against that produced by the SSM estimate using the pelvis meshes. . . . .	186
5.26	Partial data experiment: TSE (top) and TRE (bottom) produced by D-IMLOP compared against that produced by the SSM estimate using the right nasal airway meshes. . . . .	188
5.27	Partial data experiment: residual errors compared against TRE using the pelvis (top) and right nasal airway (bottom) meshes. The two measures exhibit weak correlation with correlation coefficients of 0.49 in both experiments. . . . .	189
5.28	Failure detection experiment: confusion matrix using $E_p$ alone (top) and both $E_p$ and $E_o$ (bottom). . . . .	191
5.29	Failure detection experiment: both $E_p$ (top) and $E_o$ (bottom) are correlated with the TRE with correlation coefficients of 0.73 and 0.62, respectively, when the noise in the data is known. . . . .	192
5.30	Failure detection experiment: confusion matrix using $E_p$ alone (top) and both $E_p$ and $E_o$ (bottom). . . . .	194
5.31	Failure detection experiment: although $E_p$ is weakly correlated with the TRE (top) with a correlation coefficient of 0.58, $E_o$ does not show correlation with the TRE (bottom) when the noise in the data is unknown. . . . .	195
5.32	Leave- $n$ -out experiment: TSE (top) and TRE (bottom) produced by D-IMLOP. . . . .	197
5.33	Leave- $n$ -out experiment: TSE (top) and TRE (bottom) produced by D-IMLOP. . . . .	199
5.34	Leave- $n$ -out experiment: residual errors compared against TRE show that the two measures exhibit high correlation using the facial expression data with a correlation coefficient of 0.81 (top), and weak correlation using the human pose data with a correlation coefficient of 0.51 (bottom). . . . .	200
6.1	Sample size experiment: translation (left) and rotation (right) errors produced using, from top to bottom, 1000, 1500 and 2000 data points sampled from the pelvis model in Exp. 1 (Sec. 6.5.1.1) . . . . .	224
6.2	Sample size experiment: increasing TSE (top) and TRE (bottom) with increasing number of sample points in Exp. 1. . . . .	225
6.3	Sample size experiment: translation (left) and rotation (right) errors produced using, from top to bottom, 1000, 1500 and 2000 data points sampled from the pelvis model in Exp. 2 (Sec. 6.5.1.2) . . . . .	227

## LIST OF FIGURES

6.4	Residual errors compared against TRE using 2000 sample points in Exp. 1 (left) and Exp. 2 (right) of the sample size experiment. The two measures exhibit correlation in both experiments 1 and 2 with correlation coefficients of 0.94 and 0.91, respectively. . . . .	228
6.5	Regularization term experiment: registrations produced by GD-IMLOP without the regularization term showed larger errors than with the term.	229
6.6	Noise model experiment: a slight increase in TRE as the uncertainty in the sample points increases. Note that errors are increasing with increasing modes because for this experiment the number of modes used to estimate the shapes equals the number of modes used to simulate a new shape from which points were sampled. . . . .	231
6.7	Sample size experiment: residual errors compared against TRE using 500 sample points with $2 \times 2 \times 2 \text{ mm}^3$ SD positional noise and $2^\circ$ SD ( $e = 0.5$ ) angular noise in Exp. 1 of the noise model experiment (Sec. 6.5.3.1). The two measures exhibit correlation with correlation coefficient of 0.83. . . . .	231
6.8	Noise model experiment: a slight increase in TRE as the uncertainty in the sample points increases. Note that errors are increasing with increasing modes because for this experiment the number of modes used to estimate the shapes equals the number of modes used to simulate a new shape from which points were sampled. . . . .	232
6.9	Noise model experiment: residual errors compared against TRE using 500 sample points with $2 \times 2 \times 3 \text{ mm}^3$ SD positional noise and $2^\circ$ SD ( $e = 0.5$ ) angular noise in Exp. 2 of the noise model experiment (Sec. 6.5.3.2). The two measures exhibit correlation with correlation coefficient of 0.85. . . . .	232
6.10	Noise model experiment: mean TRE produced by GD-IMLOP in Exp. 3. Note that the errors are increasing with increasing modes only because for this experiment the number of modes used to estimate the shapes equals the number of modes used to simulate a new shape from which points were sampled. . . . .	234
6.11	Noise model experiment: residual errors compared against TRE using 500 sample points with $1 \times 1 \times 1 \text{ mm}^3$ SD positional noise, $4^\circ$ SD ( $e = 0.5$ ) angular noise (top), and $1 \times 1 \times 2 \text{ mm}^3$ SD positional noise, $8^\circ$ SD ( $e = 0.5$ ) angular noise (bottom) in Exp. 3 of the noise model experiment. The two measures exhibit correlation for both isotropic and anisotropic position noise with correlation coefficient of 0.81 and 0.83, respectively. . . . .	235
6.12	Noise model experiment: parameter sweep results show that GD-IMLOP produces lower errors as the noise assumptions become more pessimistic	236

## LIST OF FIGURES

6.13	Outlier experiment: mean TRE with different number of outliers using GD-IMLOP. Note that errors are increasing with increasing modes because for this experiment the number of modes used to estimate the shapes equals the number of modes used to simulate the deformed shape from which points were sampled. . . . .	239
6.14	Scale experiment: additional scale optimization increases TRE as compared to when scale optimization is not required. . . . .	240
6.15	Scale experiment: errors in scale estimation using GD-IMLOP are similar to those using D-IMLOP and remain stable with increasing number of modes. These errors are lower than those produced using D-IMLP. . . . .	240
6.16	Leave-one-out experiment: TSE (top) and TRE (bottom) produced by GD-IMLOP compared against that produced by CPD and SSM using the middle turbinate meshes in the leave-one-out experiment. . . . .	242
6.17	Leave-one-out experiment: runtime comparison between CPD, D-IMLP, D-IMLOP and GD-IMLOP. . . . .	243
6.18	Leave-one-out experiment: errors produced by CPD compared against TSE using the middle turbinate meshes in the leave-one-out experiment. The two measures do not exhibit correlation and, therefore, errors produced by CPD cannot be used to assign success or failure to the registration. . . . .	243
6.19	Leave-one-out experiment: TSE (top) and TRE (bottom) produced by GD-IMLOP compared against that produced by the SSM estimate using the right nasal cavity meshes. . . . .	245
6.20	Leave-one-out experiment: TSE (top) and TRE (bottom) produced by GD-IMLOP with $e = 0$ (dotted green curve) compared against that produced by D-IMLOP using the right nasal cavity meshes. . . . .	246
6.21	Leave-one-out experiment: residual errors compared against TRE using the middle turbinate meshes in the leave-one-out experiment. The two measures exhibit correlation with correlation coefficients of 0.61. . . . .	247
6.22	Leave-one-out experiment: residual errors compared against TRE using the right nasal cavity meshes in the leave-one-out experiment. The two measures exhibit correlation with correlation coefficients of 0.85. . . . .	247
6.23	Leave-one-out experiment: TRE produced by D-IMLOP with 0%, 10% and 20% outliers in the data points sampled from the right nasal cavity meshes in the leave-one-out experiment. . . . .	248
6.24	Partial data experiment: TSE (top) and TRE (bottom) produced by GD-IMLOP compared against that produced by the SSM estimate using the pelvis meshes. . . . .	250
6.25	Partial data experiment: TSE (top) and TRE (bottom) produced by D-IMLOP compared against that produced by the SSM estimate using the right nasal airway meshes. . . . .	251

## LIST OF FIGURES

6.26	Partial data experiment: residual errors compared against TRE using the pelvis (top) and right nasal airway (bottom) meshes. The two measures exhibit correlation in both experiments 1 and 2 with correlation coefficients of 0.56 and 0.64, respectively. . . . .	252
6.27	Failure detection experiment: Confusion matrix using $E_p$ alone (top) and both $E_p$ and $E_o$ (bottom). . . . .	254
6.28	Failure detection experiment: Both $E_p$ and $E_o$ are correlated with the TRE (bottom) with correlation coefficients of 0.92 and 0.96, respectively, when the noise in the data is known. . . . .	255
6.29	Failure detection experiment: Confusion matrix using $E_p$ alone (top) and both $E_p$ and $E_o$ (bottom) at $p = 0.95$ . . . . .	257
6.30	Failure detection experiment: Confusion matrix using $E_p$ alone (top) and both $E_p$ and $E_o$ (bottom) at $p = 0.9975$ . . . . .	258
6.31	Failure detection experiment: both $E_p$ (top) and $E_o$ (bottom) are weakly correlated with the TRE with correlation coefficients of 0.56 and 0.58, respectively, when the noise in the data is unknown. . . . .	259
6.32	Failure detection experiment: mean TRE and standard deviation increase as $E_o$ increases (top), and average error at each vertex computed over all left-out trials using 50 modes (bottom). . . . .	261
6.33	Non-medical data experiment: this particular target shape (right) has a large amount of detail which is necessary to convey the emotion in this face. 1000 sample points are too few to capture this detail resulting in an inaccurate reconstruction (left). However, with 2000 sample points, we are able to estimate this expression better (middle) since more sample points are better able to capture the detail in the target. . . . .	263
6.34	Leave- $n$ -out experiment: TSE (top) and TRE (bottom) produced by GD-IMLOP. . . . .	264
6.35	Leave- $n$ -out experiment: TSE (top) and TRE (bottom) produced by GD-IMLOP. . . . .	265
6.36	Leave- $n$ -out experiment: residual errors compared against TRE show that the two measures exhibit high correlation using the facial expression data with a correlation coefficient of 0.78 (top), and no correlation using the human pose data with a correlation coefficient of 0.18 (bottom). . . . .	266

## LIST OF FIGURES

7.1	Using RcnStr01 (top), registration results using D-IMLP (left) and D-IMLOP (middle) show failed registrations, while that using GD-IMLOP (right) shows good alignment (along with some outliers). RcnStr02 (bottom) yields better results, with all three algorithms producing good alignments. However, we can see that the number of outliers or bad matches (red points matched to the outside of the nose) goes down as we go from D-IMLP (left) to D-IMLOP (middle) to GD-IMLOP (right). . . . .	280
7.2	A dense point cloud obtained from a single frame of endoscopic video using the method of Liu et al. <sup>3</sup> . . . . .	281
7.3	$E_p$ (top) and $E_o$ (bottom) for all registration computed using GD-IMLOP, plotted for each sequence. Within each sequence, from left to right, the plot points indicate scores achieved using 0 to 50 modes at increments of 10. Crossed out plot points indicate rejected registrations.	284
7.4	Top: One of the frames from the video sequence used to extract the dense structure. Bottom: Visualization of the final registration and reconstruction for Seq01 using 50 modes with dense structure points depicted in white. . . . .	286
8.1	Front view of the right maxillary sinus: (L-R) Modes 1 to 5 with variance ranging from $-3$ (top) to $3$ (bottom) SDs. . . . .	295
8.2	Right view of the right maxillary sinus: (L-R) Modes 1 to 5 with variance ranging from $-3$ (top) to $3$ (bottom) SDs. . . . .	296
8.3	Front view of the left maxillary sinus: (L-R) Modes 1 to 5 with variance ranging from $-3$ (top) to $3$ (bottom) SDs. . . . .	297
8.4	Left view of the left maxillary sinus: (L-R) Modes 1 to 5 with variance ranging from $-3$ (top) to $3$ (bottom) SDs. . . . .	298
8.5	Front view of the inferior turbinates: (L-R) Modes 1 to 5 with variance ranging from $-3$ (top) to $3$ (bottom) SDs. . . . .	300
8.6	Right view of the inferior turbinates: (L-R) Modes 1 to 5 with variance ranging from $-3$ (top) to $3$ (bottom) SDs. . . . .	301
8.7	Front view of the middle turbinates: (L-R) Modes 1 to 5 with variance ranging from $-3$ (top) to $3$ (bottom) SDs. . . . .	302
8.8	Right view of the middle turbinates: (L-R) Modes 1 to 5 with variance ranging from $-3$ (top) to $3$ (bottom) SDs. . . . .	303
8.9	Front view of the right nasal airway: (L-R) Modes 1 to 5 with variance ranging from $-3$ (top) to $3$ (bottom) SDs. . . . .	305
8.10	Right view of the right nasal airway: (L-R) Modes 1 to 5 with variance ranging from $-3$ (top) to $3$ (bottom) SDs. . . . .	306
8.11	Front view of the left nasal airway: (L-R) Modes 1 to 5 with variance ranging from $-3$ (top) to $3$ (bottom) SDs. . . . .	307

## LIST OF FIGURES

8.12	Left view of the left nasal airway: (L-R) Modes 1 to 5 with variance ranging from $-3$ (top) to $3$ (bottom) SDs. . . . .	308
8.13	Top: Population variation in the skull model. The middle shape is the mean shape, the left shape shows mean shape with $-1\sigma$ , where $\sigma$ is the standard deviation, and the right shape is the mean shape with $+1\sigma$ . Bottom: The left image shows the pre-op patient skull, and the right image shows the post-op patient skull. The two images show no, or negligible, difference, where minute difference can sometimes be observed due to errors in registration. However, we can see that the population variation is not reflected in the two patient images. . . . .	311
8.14	Top: Population variation in the inferior turbinate (IT) model. The middle shape is the mean shape, the left shape shows mean shape with $-1\sigma$ , and the right shape is the mean shape with $+1\sigma$ . Bottom: The left image shows the pre-op patient IT, and the right image shows the post-op patient IT. The two images show significant differences, allowing us to conclude that the population variation is reflected in the patient images. . . . .	312
8.15	Intersection (top) between a plane and a mesh, shown here at the external nasal valve, produces contours which enable the computation of the cross-sectional area within the contours (bottom). . . . .	314
8.16	Top: Mean relative error and standard deviation in cross-sectional area estimation of the internal nasal valve. Bottom: Median relative error along with the 25th and 75th percentile errors (box) and min and max errors (bars) excluding outliers, which are marked with $+$ signs. . . . .	317
8.17	Top: Mean relative error and standard deviation in cross-sectional area estimation of the external nasal valve. Bottom: Median relative error along with the 25th and 75th percentile errors (box) and min and max errors (bars) excluding outliers, which are marked with $+$ signs. . . . .	320

# List of Algorithms

2.1	Clockwise order vertices in one-ring neighborhood . . . . .	33
2.2	Sample vertices . . . . .	34
2.3	Build SSM . . . . .	39
2.4	Correspondence improvement . . . . .	40
2.5	Simultaneous segmentation and correspondence improvement . . . . .	43
4.1	Deformable Iterative Most Likely Point (D-IMLP) . . . . .	76
4.1	D-IMLP ( <i>continued...</i> ) . . . . .	77
5.1	Deformable Iterative Most Likely Oriented Point (D-IMLOP) . . . . .	145
5.1	D-IMLOP ( <i>continued...</i> ) . . . . .	146
6.1	Generalized Deformable Iterative Most Likely Oriented Point (GD-IMLOP)	210
6.1	GD-IMLOP ( <i>continued...</i> ) . . . . .	211



# Chapter 1

## Introduction

Understanding the range normal anatomy is a key step towards identifying abnormalities, associating deviations from normal to disease, and determining the best course of treatment to improve quality of life. For some parts of anatomy, understanding this normal range can be difficult. The nasal cavity and the paranasal sinuses belong to this class of complex anatomical structures where accurately locating deviation from normal and identifying the exact cause of discomfort in patients can be challenging. Therefore, although anatomical variations are understood be associated with an increased likelihood of nasal diseases such rhinosinusitis,<sup>4</sup> a large percentage of population continues to suffer from these diseases. In the following section, the anatomical structure of the nasal cavity and sinuses will be described and the clinical condition known as rhinosinusitis will be explained, including how it affects the population and the challenges it presents to modern medicine. This will be followed

## CHAPTER 1. INTRODUCTION

by a review of the technical methods that have been introduced in the past in order to address the problems involved in various surgical treatments, especially those that can be applied to the treatment of rhinosinusitis, and where these methods fall short. The following chapters will present new methods that facilitate a better understanding of the sinonasal anatomy, as well as methods that can exploit this improved understanding to enhance endoscopic navigation during minimally invasive surgeries that are performed to treat sinonasal diseases.

### 1.1 Clinical background

The term *rhinosinusitis* describes the general co-occurrence and coexistence of the conditions rhinitis, which affects the nasal cavity, and sinusitis, which affects the paranasal sinuses.<sup>4</sup> The nasal cavity extends from the nostrils to the nasopharynx (Fig. 1.1) in the antero-posterior direction, and is divided into left and right by the nasal septum. Both sides have a roof, a floor, a medial wall or nasal septum, and a lateral wall.<sup>5</sup> Each nasal passage, or meatus, lying between these boundaries contains three nasal conchae, or turbinates. The inferior turbinate is one of several bones that make up the uneven and complicated lateral wall, while the middle and superior turbinates are projections of the ethmoid bone.<sup>5</sup> The turbinates are covered by a thick and highly vascular mucous membrane, or mucosa, that warms and humidifies incoming air as it travels through the nasal cavity.<sup>5</sup> The turbinates undergo periodic

CHAPTER 1. INTRODUCTION

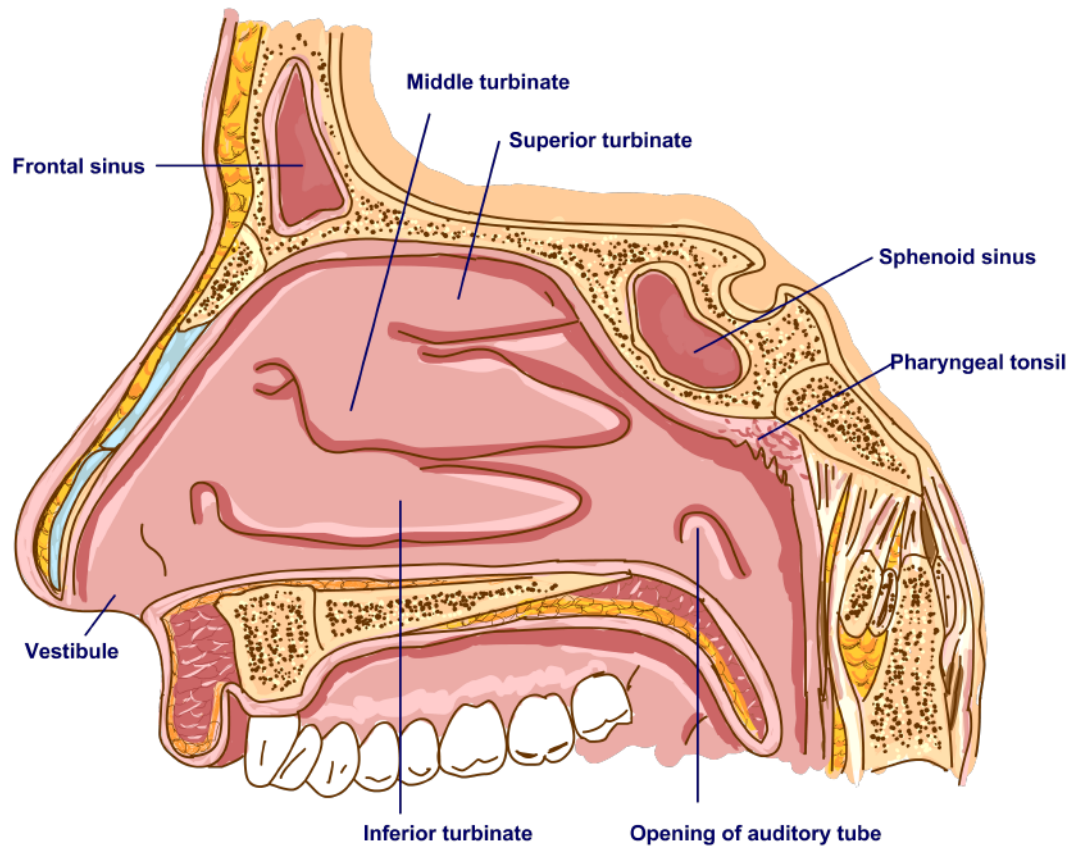


**Figure 1.1:** Anatomy of the nasal cavity. Licensed under the Creative Commons Attribution 3.0 Unported license ([https://commons.wikimedia.org/wiki/File:714\\_Bone\\_of\\_Nasal\\_Cavity.jpg](https://commons.wikimedia.org/wiki/File:714_Bone_of_Nasal_Cavity.jpg))

## CHAPTER 1. INTRODUCTION

alternating contraction and expansion, known as the nasal cycle.<sup>6</sup> The decongested side of the nasal cavity facilitates humidification of incoming air, and alternating is thought to shift the workload back and forth.<sup>6</sup>

The nasal cavity presents openings, or ostia, for the four paranasal sinuses which are cavities within the maxilla and the frontal, ethmoid, and sphenoid bones.<sup>5</sup> Accordingly, they are named the maxillary, frontal, ethmoid, and sphenoid sinuses, respectively (Fig. 1.2). Not all of these sinuses are fully developed at birth. The process of pneumatization, or cavities forming within bones, occurs over several years. The maxillary and ethmoid sinuses are present at birth, but continue to grow until the age of 15-16 years.<sup>7,8</sup> The maxillary sinus turns into the largest of the sinuses, while the ethmoid sinus ends up being comprised of numerous small cells that make up the ethmoidal labyrinth.<sup>5</sup> The frontal sinuses are not distinguishable from the anterior ethmoid cells at birth, but begin growing around the fourth year and continue to grow until adult size is attained at around 19 years.<sup>7,8</sup> Similarly, the sphenoid sinuses are extremely small at birth, but experience a growth spurt around 6-10 years of age, and complete their growth by 15 years.<sup>7,8</sup>

Rhinosinusitis is defined in slightly different ways depending on several factors. The main difference depends on the purpose of diagnosis. Diagnoses made in a clinical setting require a clearly defined protocol to accurately describe patient population (phenotypes) in order to provide standard treatment to patients with similar symptoms, as well as to maintain consistency in clinical studies relating to diagnosis and

## CHAPTER 1. INTRODUCTION

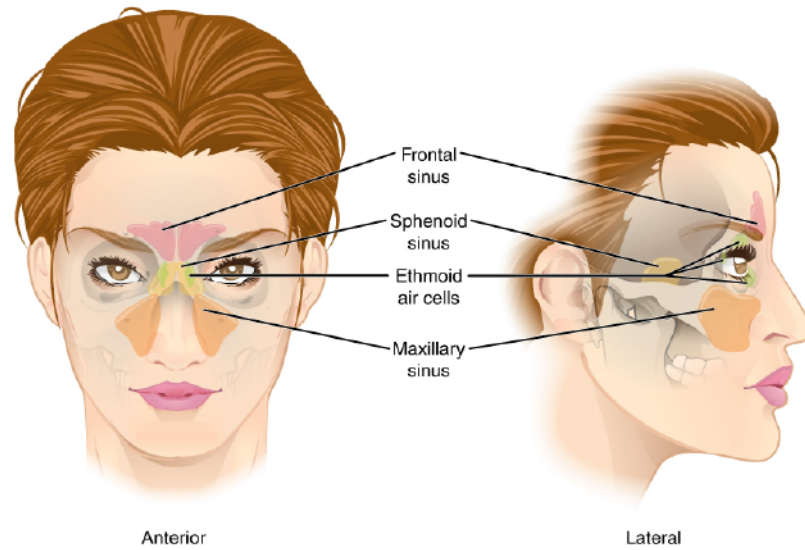


**Figure 1.2:** Anatomy of the sinuses. Licensed under the Creative Commons Attribution - Share Alike 3.0 Unported license ([https://commons.wikimedia.org/wiki/File:724\\_Paranasal\\_Sinuses.jpg](https://commons.wikimedia.org/wiki/File:724_Paranasal_Sinuses.jpg))

treatment.<sup>4</sup> Therefore, rhinosinusitis in adults is clinically defined as the inflammation of the nose and paranasal sinuses characterized by two or more symptoms:<sup>4</sup>

- One of the symptoms should be either nasal obstruction/congestion or nasal discharge in the form of anterior or posterior nasal drip often accompanied by
  - facial pain or pressure, and/or
  - reduction or loss of smell.<sup>4</sup>
- The other symptom should be endoscopic signs of
  - nasal polyps, and/or
  - mucopurulent discharge primarily from the middle meatus, and/or
  - oedema/mucosal obstruction primarily in the middle meatus,

## CHAPTER 1. INTRODUCTION

and/or mucosal changes within the osteomeatal complex and/or sinuses observed in computed tomography (CT) scans.<sup>4</sup>

The definition of rhinosinusitis in children varies only slightly. In pediatric care, one of the accompanying symptoms is cough, instead of reduction or loss of smell.<sup>4</sup> The duration of the condition dictates whether the condition should be termed acute or chronic. If the symptoms described above are completely resolved within 12 weeks, then the condition is termed acute.<sup>4</sup> If the symptoms persist beyond 12 without complete resolution, then the condition is termed chronic.<sup>4</sup>

The epidemiological definition of rhinosinusitis imposes fewer restrictions in order to facilitate the study of larger populations.<sup>4</sup> Therefore, the epidemiological definition of *acute rhinosinusitis* (ARS) in adults is simply the sudden onset of two or more symptoms, one of which should be either nasal blockage/obstruction/congestion or nasal discharge, as described above, often accompanied by facial pain or pressure, and/or reduction or loss of smell lasting fewer than 12 weeks.<sup>4</sup> In children, this definition is further simplified to the sudden onset of two or more of the following symptoms lasting fewer than 12 weeks:

- nasal blockage/obstruction/congestion, and/or
- discolored nasal discharge, and/or
- cough during the night or day.<sup>4</sup>

The presence or absence of symptoms need only be validated over the telephone or

## CHAPTER 1. INTRODUCTION

in an interview.<sup>4</sup> The epidemiological definition of *chronic rhinosinusitis* (CRS) in adults is similar to that of ARS, with symptoms lasting 12 weeks or more, and in children, the reduction or loss of smell is replaced by the presence of cough, as in the clinical definition.<sup>4</sup> For research purposes, ARS is diagnosed according to the epidemiological definition, with bacteriological and/or radiological tests advised but not required.<sup>4</sup> However, for the more serious CRS, the diagnosis is made as per the clinical definition.

Studies show that ARS affects about 6-15% of the population in the United States,<sup>9,10</sup> while CRS affects about 2-4%.<sup>11-13</sup> Rhinosinusitis can be caused by both viruses and bacteria. The epithelial cells of the airway serve as the first line of defense against the infectious agents.<sup>4</sup> These release mucous to trap the microorganisms, which are then mechanically removed from the body by ciliated cells.<sup>14</sup> Further, the ecosystem in the nasal cavity is determined by specific parameters like temperature, pH, etc., and only microorganisms that require a similar ecosystem are able to survive.<sup>14</sup> The microorganisms that are able to breach these barriers disrupt the epithelial cells and decrease the number of ciliated cells<sup>15</sup> obstructing the sinus ostia in the nasal cavity.<sup>16</sup> The change in pressure caused by mucus retention in the sinuses due to this obstruction changes the ecosystem in the nasal cavity, worsens congestion, and further impedes the removal of the microorganisms.<sup>15-19</sup> These changes form an ideal environment for the growth of infectious microorganisms.<sup>20</sup> This creates a vicious cycle of inflammation and blockage leading to obstructed nasal passage and

## CHAPTER 1. INTRODUCTION

difficulty in breathing for the affected population.

In most cases, such infections are resolved without antibiotic treatment.<sup>21-23</sup> Although antibiotic treatment has been shown to not be useful in treating mild and uncomplicated ARS and is not recommended by clinical guidelines, rhinosinusitis is the fifth most common diagnosis for which antibiotics are prescribed.<sup>21-24</sup> Long-term antibacterial treatment can lead to the emergence of resistant bacterial strains. Other treatments that are employed include oral antihistamines, nasal decongestants, nasal irrigation, etc. When these other treatments are unable to relieve symptoms, surgical treatments are employed to alleviate symptoms. These could include widening of the sinus ostia in order to improve drainage from the sinuses, turbinate reduction to reduce nasal obstruction, septoplasty in cases of severely deviated septum, etc. Most such surgical treatments today are performed minimally invasively via endoscopic sinus surgery (ESS). ESS involves accessing the nasal cavity through the nostrils and visualizing the anatomy using an endoscope. In order to enhance the limited field of view of endoscopes, patients are generally required to obtain a preoperative CT scan since it has high contrast between bone, soft tissue, and air making it easy to differentiate between the sinonasal cavity and the surrounding bone and mucosa. The purpose of the CT scan is to inform the surgeon about the area surrounding the site of surgery in order to prevent accidental damage to critical structures that surround the sinonasal cavity. The accuracy of the methods performing the alignment between endoscopic video and preoperative CT scan can have an effect on the outcome of the



## CHAPTER 1. INTRODUCTION

treatment. Studies have shown that overconfidence in technology can have detrimental effects on surgical outcomes.<sup>25</sup> Therefore, high accuracy in such systems and an awareness of when this is not attained is critical.

Studies have also shown that although both medical and surgical treatments improve symptoms of rhinosinusitis, significant difference is not seen between the medical and surgical groups.<sup>26</sup> It must be noted, however, that many of these studies do not include results from medical treatment for those who proceeded to ESS having failed medical treatment. Surgeries that increased the patency of the nasal cavity showed that increased patency was maintained after several months, although this did not improve subjective outcomes.<sup>27,28</sup> Patients undergoing septoplasty only showed improved quality of life (QoL) when septal deviation was accompanied with moderate or severe nasal symptoms, whereas those with mild nasal symptoms did not.<sup>29</sup> QoL was even showed to degrade in those mild nasal symptoms, especially among older patients.<sup>29</sup> Although in some cases it may be clear that septoplasty will improve QoL, there is a fine line between cases where surgical intervention will or will not improve QoL.<sup>29</sup> Most studies that have evaluated nasal patency among normal population only presented approximations.<sup>30-32</sup> This may contribute to the difficulty in finding correlation between patency and improved nasal obstruction among patients. Improving these measurements to gain a better understanding of normal anatomy has the potential not only to better inform when surgical treatment is necessary, but also to improve patient outcome

## 1.2 Technical background

As mentioned earlier, in order to make up for the limited field of view of endoscopes, most endoscopic sinus surgeries are accompanied by a preoperative CT scan in order to better inform the surgeon of critical structures in the area surrounding the surgical site. The view in the CT scan corresponding to the view seen by the surgeon in endoscopic video is computed through a process known as *registration*, which finds the spatial *transformation* between data in two different coordinate frames that maps them into a common coordinate frame. In addition to guidance or navigation during endoscopy, registration is has several other applications in modern medical practice, such as fusion of images for diagnosis, postoperative evaluation, or time-varying change detection.<sup>33</sup> These images may be of different modalities like magnetic resonance (MR) or ultrasound (US) scans. Registration also has several applications in other fields like robotics and computer vision. Image registration methods can be divided into two broad classes based on the type of information used to compute the alignment: intensity-based registration and feature-based registration.<sup>34</sup> Intensity-based registration methods compare information defined on the pixels of the images being registered, like intensity or gradients.<sup>34</sup> Feature-based registration methods compare geometric information extracted from images, like point clouds, contours, curves, or triangular mesh models, that describe positions of salient landmarks.<sup>34</sup>

Information from the images are compared using some similarity metric that allows corresponding pixels or features to be matched correctly. Metrics used in intensity-

## CHAPTER 1. INTRODUCTION

based registration methods include sum of square differences (SSD), sum of absolute differences (SAD), correlation coefficient (CC), normalized correlation coefficient (NCC), mutual information (MI), etc. Some of these metrics, like SSD and SAD, are suitable for comparing images belonging to the same modality, while CC and NCC are suitable when the intensities of the images being registered are linearly related. MI is useful for comparing images from different modalities, when the two images intensities have considerable differences between them without a simple relation to map one to the other.<sup>34</sup> Feature-based registration methods use metrics that compare geometric distances between shape descriptors like points,<sup>35</sup> surface normals,<sup>36</sup> surface curvature,<sup>37</sup> color,<sup>38</sup> etc. Based on the metric used, different optimization schemes can be used to compute the alignment between images. These include gradient-based methods like gradient descent, Levenberg-Marquardt, quasi-Newton methods, etc., and gradient-free methods like random search methods, genetic algorithms, etc.<sup>39</sup> The remainder of this section will discuss feature-based methods since the focus of this dissertation is on feature-based deformable registration techniques.

These optimization methods are used to solve for different types of transformations that are required to align data into a common coordinate frame. Transformations can be broadly classified as *rigid* and *non-rigid* (or *deformable*). Rigid registration methods produce rigid-body transformations like global *rotations* and *translations* to reposition the transformed data while maintaining the relative distance between points in each dataset.<sup>40</sup> In medical applications, such methods are useful when reg-

## CHAPTER 1. INTRODUCTION

istration is computed between the same object at different times or using different imaging modalities with the knowledge that the object has not undergone any structural changes. One of the most popular registration algorithms is a feature-based rigid registration algorithm called the iterative closest point (ICP) algorithm<sup>35</sup> which finds an alignment between a fixed set of points or shape (*model shape*) and a moving set of points (*data points*). ICP is an iterative algorithm that iterates between two phases: a *correspondence phase* and a *registration phase*. During the correspondence phase, the closest point on the model shape is found for each data point by minimizing Euclidean distances, whereas during the registration phase, a spatial transformation is computed to align the corresponding points.<sup>35</sup> Prior to ICP, a specialized registration method for registering 3D images of the human head was introduced which found correspondences by finding intersections with the model shape of rays extending from the centroid of the data points through the data points being matched, and computed a registration in a derivative-free manner.<sup>41</sup> Champleboux et al. presented a more general registration method that was able to quickly compute closest point to surface distances by representing the model shape using a hierarchical distance map, known as an octree-spline, and directly minimize the sum of square distances using a nonlinear least-squares optimization.<sup>42</sup>

After the introduction of ICP, several variants were introduced to compensate for the disadvantages of standard ICP. For instance, a robust ICP variant was introduced to handle outliers and occlusion in the correspondence phase by incorporating

## CHAPTER 1. INTRODUCTION

robust statistics and adaptive thresholding.<sup>43</sup> In order to perform outlier rejection in the registration phase, weighted point pairs were used by Maurer et al.,<sup>44</sup> which also enabled normalization for non-uniformly point densities. In order to eliminate ambiguities stemming from matching only point features using Euclidean distances, several methods have augmented the match metric using additional features like surface normals<sup>45</sup> and curvature.<sup>37</sup> Surface normals are critical in disambiguating point sets facing different directions. Alternate metric-based distance functions have also been introduced to take into account both translation and rotation errors produced by sensors in 2D<sup>46</sup> and 3D<sup>47</sup> scan-matching problems. Several methods have been introduced that perform a soft matching between each data point and each model point with varying weight or probability assigned to each match.<sup>48-50</sup> More recently, a series of algorithms based on the most-likely-point paradigm (IMLP, IMLOP, and G-IMLOP) were presented that compute registrations by incorporating noise models associated with the model shape and data features into both the correspondence and registration phases making them more robust.<sup>51-53</sup> Several of these methods have been employed for the application of image guided navigation during endoscopic surgery. Other methods that use optical or EM tracking have also been used. However, changes that might occur in patient anatomy between preoperative image acquisition and the time of surgery due to breathing and other natural functions as well as due to the insertion of surgical instruments make rigid registration methods inadequate for accurate surgical navigation.

## CHAPTER 1. INTRODUCTION

Non-rigid registration methods, on the other hand, deform the data in some way in addition to repositioning them. The simplest deformable registration methods compute a global *scale* in addition to rotation and translation producing a *similarity* transformation,<sup>54–56</sup> or a general linear mapping producing an *affine* transformation. Several extensions of ICP that additionally compute scale have been presented.<sup>54,55,57</sup> More complex deformable registration methods compute local transformations like displacement or deformation fields.<sup>40</sup> These local transformation parameters could be defined at each pixel in a 2D image, each voxel in a 3D image or each point in a point cloud or triangular mesh. Since the number of parameters to solve for is much larger than the amount of available information, the problem of finding the best displacement field is ill-posed. Therefore, in order to compensate for the ill-posedness of the problem, most deformable registration methods incorporate a regularization term or smoothness constraint within the registration cost function that is optimized. For instance, deformations smoothed using thin-plate splines have been used to compute deformable registrations.<sup>58</sup> A deformable extension of EM-ICP which uses Gaussian mixture models (GMMs) optimized within an expectation maximization (EM) framework<sup>49</sup> enforced coherency between backward and forward deformations to produce a symmetric and consistent registration framework.<sup>59</sup> Coherent point drift (CPD) is another EM-based method which computes a closed form M-step solution for rigid registration and uses Gaussian radial basis functions for deformable registration computation.<sup>50</sup> However, CPD only deforms the part of the model shape that data points

## CHAPTER 1. INTRODUCTION

are matched to, which might not be ideal for surgical navigation where only a limited portion of anatomy is visible at a time and, therefore, data points extracted from these regions might cause sudden and unrealistic deformations in the model shape. Further, noise in the data can result in deformations not anatomically plausible. Several variations of CPD have also been explored. One method treats both the model shape and data points as kernel densities formed from Gaussian kernel functions centered at each point and computes registration by maximizing a kernel correlation (KC) metric between the two densities.<sup>60</sup> Another forms GMMs from both the model shape and data points and minimizes L2 distance between the GMMs to compute registration.<sup>61</sup> Although CPD and its variants can achieve high accuracy, the exhaustive point pairings make these methods less efficient than methods that perform single-point matching. The deformable registration methods described in this dissertation are extensions of the most-likely-point algorithms which compute single-point matching. More thorough details of these most-likely-point algorithms will be explained in the chapters corresponding to the deformable registration methods. These deformable algorithms inherit the advantage of the most-likely-point algorithms in that their formulation seamlessly incorporates measurement noise associated with both the model shape and data points into the correspondence and registration phases making it robust to noise in the data. This is critical since data extracted from real world applications generally contains some amount of noise. Further, the deformations computed are based in statistics learned from variations seen in anatomy. Therefore, regardless of

## CHAPTER 1. INTRODUCTION

the amount of noise in the data, deformations computed using these methods should be anatomically plausible.

Up to this point, it has been assumed that features can be extracted from medical images. However, this is often a difficult task. For endoscopic navigation, features must be extracted from both preoperative CT scans and intraoperative video frames. Several techniques have been introduced to automatically extract these features. In many types of images, features can be extracted by segmenting or partitioning the image into nonoverlapping constituent regions that are characterized by homogeneity in some characteristic like intensity or texture.<sup>62</sup> Segmentation can be obtained simply by thresholding image intensities.<sup>63</sup> However, such methods are sensitive to noise and intensity inhomogeneities. Region growing is another segmentation technique based on intensity information. This technique requires an initial seed point and segments all pixels connected to the seed under some criteria, for instance, all pixels with similar intensities.<sup>64</sup> This method is also sensitive to noise and can result in segmentations with holes or disconnected components, and requires user interaction in the selection of the seed point. Clustering based methods alleviate the problem of user interaction by iteratively alternating between segmenting the image and characterizing the properties of each cluster.<sup>62</sup> Clustering methods like K-means iteratively compute the mean intensity in each cluster and classify each pixel in the cluster with the closest mean.<sup>65</sup> Such methods, again, suffer from sensitivity to noise, and may not directly incorporate spatial features resulting in misclassifications.<sup>62</sup> Other methods



## CHAPTER 1. INTRODUCTION

use deformable models to delineate object boundaries by placing a closed curve inside the object of interest, and allowing the curve to evolve using cues like image gradients.<sup>66,67</sup> However, again, this requires user interaction in placing the initial curve within the object of interest. Atlas-guided approaches require the existence of an atlas with segmentations. Given this requirement, any target image requiring segmentation simply needs to be aligned with the atlas using a one-to-one transformation.<sup>39</sup> Due to anatomical variability, the transformation must be deformable.<sup>68-71</sup> Ideally, in order to avoid unnatural deformations in anatomical structures, the deformation should be a differentiable one-to-one function with a differentiable inverse. Once aligned, the segmentations from the atlas can simply be deformed to the target image. Further, triangular meshes can be extracted from the pre-segmented atlas, and these can also be deformed to the target image. One important advantage of this method is that all segmented meshes produced are in correspondence with each other. These correspondences can be exploited to build statistical shape models (SSMs) using standard methods like principal component analysis (PCA).<sup>1</sup> These SSMs explain the variance in the data, and are also able to estimate any shape that is in correspondence with those used to build the SSM.

These segmentation methods are able to extract 3D shapes from volume data like CT scans. However, these methods are not sufficient to extract 3D structure from video due to the motion between frames. In order to extract 3D features from a sequence of video frames, a structure from motion (SfM) framework was developed

## CHAPTER 1. INTRODUCTION

that used features extracted from each frame to triangulate to 3D points.<sup>72</sup> Several improvements to this initial method using improved feature extraction methods like SIFT or SURF that provide rich features have been made.<sup>54</sup> Further, methods to jointly produce optimal structure and relative camera motion using bundle adjustment have also been presented.<sup>73</sup> However, due to the paucity of texture in endoscopic images, these methods are only able to produce sparse 3D structures. Newer methods based on machine learning techniques are able to produce dense 3D structures from single video frames<sup>3,74</sup> and provide reconstructions that can be used to compute reliable registrations to features extracted from preoperative images.

### 1.3 Thesis Statement

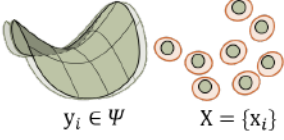
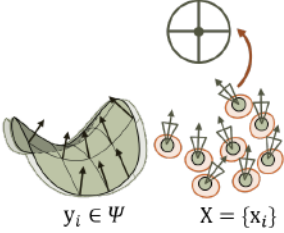
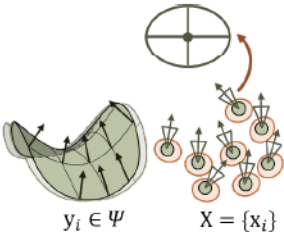
Deformable feature-based registration algorithms that incorporate statistical shape models (SSMs) demonstrate accurate registration to features not seen before by the SSM as well as accurate reconstruction of the shape described by these features.

### 1.4 Thesis outline

This dissertation presents a method to build improved SSMs, and a family of feature-based deformable registration methods belonging to the *deformable most-likely-point paradigm* that use these SSMs to estimate shapes that are *not* in correspondence with the SSM (Table 1.1). For instance, given dense features extracted

CHAPTER 1. INTRODUCTION

**Table 1.1:** Summary of the deformable registration algorithms presented in this dissertation.

	Algorithm	Feature type	Noise model
	D-IMLP	3D positions	anisotropic
	D-IMLOP	3D positions, 3D orientations	anisotropic for position features, isotropic for orientation features
	GD-IMLOP	3D positions, 3D orientations	anisotropic for position and orientation fea- tures

from video sequences containing a structure, the registration algorithms developed within the deformable most-likely-point paradigm enable an SSM containing the same structure to estimate the shape represented by the video features despite a lack of correspondence between the two. This property can be harnessed during endoscopic examinations to estimate patient anatomy and make quantitative measurements without the need for patient specific CT scans.

Chapter 2 outlines established methods for automatic segmentation<sup>75</sup> and statis-

## CHAPTER 1. INTRODUCTION

tical modeling<sup>1</sup> of anatomical structures. It also covers established methods to improve segmentation<sup>66,67</sup> and correspondences<sup>2</sup> between shapes in an effort to improve SSMs. However, previous methods<sup>2,66,67</sup> treat segmentation and correspondence improvement as separate tasks resulting in segmentation improvement methods that allow correspondences to deteriorate and correspondence improvement methods that assume perfect segmentation. In this chapter, a simultaneous segmentation and correspondence improvement method is introduced.<sup>76</sup> This new method simultaneously improves segmentation by moving the vertices in a mesh closer to edges in the corresponding CT image and improves correspondences between shapes using SSMs to constrain the motion of vertices along the surface of the improved mesh.

Chapter 3 introduces the *deformable most-likely-point paradigm*<sup>77</sup> which describes how SSMs can be used in combination with probabilistic rigid registration algorithms to include statistically informed deformations in the registration computation. The algorithms developed in Chapters 4–6 follow the algorithm design process described in this chapter. This paradigm was first introduced by Billings,<sup>78</sup> and was improved and implemented during the course of this dissertation work. Chapter 4 presents the deformable iterative most likely point (D-IMLP) algorithm,<sup>77</sup> which registers sample points with positional components characterized by anisotropic uncertainty to a mean shape and, simultaneously, deforms the mean shape according to the corresponding SSM to fit the sample points. Chapter 5 presents the deformable iterative most likely oriented point (D-IMLOP) algorithm,<sup>77</sup> which registers sample

## CHAPTER 1. INTRODUCTION

points with positional components characterized by anisotropic uncertainty and orientation components characterized by isotropic uncertainty to a mean shape. The mean shape, again, deforms according to the corresponding SSM to fit the sample points. The additional orientation components allow the algorithm to disambiguate points samples from surfaces facing different directions. Finally, Chapter 6 presents the generalized deformable iterative most likely oriented point (GD-IMLOP) algorithm,<sup>77</sup> which registers sample points with positional and orientation components characterized anisotropic uncertainty to a mean shape and, again, deforms the mean shape according to the corresponding SSM to fit the sample points. Mechanisms for autonomously assessing the outcome of a registration in order to assign confidence to the result is also presented for each of the three algorithms.<sup>79</sup> All three algorithms are thoroughly evaluated on several different datasets.

Chapter 7 evaluates the efficacy of these algorithms in a clinical setting using in-vivo data.<sup>77,79</sup> Dense point clouds are extracted from single frames of sinonasal endoscopy video data<sup>3,74</sup> and deformably registered to SSMs built from population data. Further, confidence is assigned to each registration based on the autonomous assessment mechanism designed for each deformable registration algorithm. Chapter 8 presents several other applications of SSMs and registration algorithms using SSMs in clinical use, for instance, understanding the types and extents of variability present in different anatomical structures,<sup>75</sup> showing that population data is able to compensate for individual variation such as that resulting from the nasal cycle,<sup>75</sup>

and estimating measurements of cross sectional areas of the nasal cavity at different landmarks to quantitatively evaluate the patency of a patient’s nasal passage. Chapter 9 discusses the conclusions of this dissertation as well as future directions such as ways to improve and extend methods discussed in this dissertation and different applications that could benefit from this work.

### 1.5 Contributions

This dissertation presents several contributions with the most notable contribution being the development of the *deformable most-likely-point paradigm* which incorporates SSMs into a probabilistic registration framework. This paradigm enables statistically informed model deformation during feature-based registration computation. This dissertation also presents methods to build improved SSMs as well as clinical applications of SSMs and registration algorithms built within the deformable most-likely-point paradigm. A detailed outline of the contribution of this dissertation is presented below:

1. An novel method for simultaneous improvement of segmentation and correspondences among a set of shapes in order to build better SSMs (Chapter 2)<sup>76</sup>
2. An implementation of the *deformable most-likely-point paradigm*, a general probabilistic paradigm for incorporating deformable shape transformations within a probabilistic registration framework that was first introduced conceptually by

## CHAPTER 1. INTRODUCTION

Billings.<sup>78</sup> This framework, an extension to the software architecture developed by Billings,<sup>78</sup> enables the development of deformable registration algorithms for registering sample points to a deformable model shape that is characterized by an SSM, where the shape deformations computed by the registration are driven by the modes of the SSM (Chapter 3)<sup>77,78</sup>

3. A user friendly command line interface to perform registrations with different datasets using several algorithms including but not limited to ICP, directional ICP, the deformable registration algorithms presented in this dissertation, and their corresponding rigid counterparts.
4. The improvement, implementation and evaluation of the deformable iterative most likely point (D-IMLP) algorithm (Chapter 4)<sup>77</sup>
  - (a) a probabilistic algorithm that computes deformable registration between an SSM and point features with unconstrained or anisotropic noise
  - (b) an efficient implementation of PD-tree update to accommodate a deforming model shape
  - (c) a gradient-based solution to the optimization problem which is computed using an off-the-shelf nonlinear box-constrained BFGS quasi-Newton optimizer<sup>80</sup>
  - (d) a mechanism for autonomously evaluating a registration in order to assign confidence to the resulting alignment

## CHAPTER 1. INTRODUCTION

5. The development, implementation and evaluation of the deformable iterative most likely oriented point (D-IMLOP) algorithm (Chapter 5)<sup>77</sup>
  - (a) a probabilistic algorithm that computes deformable registration between an SSM and features with position and orientation components, where unconstrained noise is associated with the position features and constrained or isotropic noise is associated with orientation features
  - (b) an efficient implementation of PD-tree update to accommodate a deforming model shape
  - (c) a gradient-based solution to the optimization problem which is computed using an off-the-shelf nonlinear box-constrained BFGS quasi-Newton optimizer<sup>80</sup>
  - (d) a mechanism for autonomously evaluating a registration in order to assign confidence to the resulting alignment
  
6. The development, implementation and evaluation of the generalized deformable iterative most likely oriented point (GD-IMLOP) algorithm (Chapter 6)<sup>77</sup>
  - (a) a probabilistic algorithm that computes deformable registration between an SSM and features with position and orientation components, where unconstrained noise is associated with both position and orientation features
  - (b) an efficient implementation of PD-tree update to accommodate a deforming model shape



## CHAPTER 1. INTRODUCTION

- (c) a gradient-based solution to the optimization problem which is computed using an off-the-shelf nonlinear box-constrained BFGS quasi-Newton optimizer<sup>80</sup>
  - (d) a mechanism for autonomously evaluating a registration in order to assign confidence to the resulting alignment<sup>79</sup>
7. An evaluation of the algorithms presented in Chapters 4–6 in a clinical setting through deformable registration between SSMs and dense reconstructions from in-vivo endoscopic video frames along with confidence estimates for each registration (Chapter 7)<sup>77,79</sup>
8. A set of clinical applications (Chapter 8) including
- (a) evaluation of anatomical variation in the maxillary sinuses, inferior and middle turbinates, right and left nasal cavities in a normal population<sup>75</sup>
  - (b) demonstration of the nasal cycle in one patient with preoperative and postoperative CT scans<sup>75</sup>
  - (c) automatic and exact measurement of the cross-sectional area at the internal and external nasal valves

## 1.6 Published Work

Material from this dissertation appears in the following publications:

1. A. Sinha, S. Leonard, A. Reiter, M. Ishii, R. H. Taylor, G. D. Hager, “Automatic

## CHAPTER 1. INTRODUCTION

- segmentation and statistical shape modeling of the paranasal sinuses to estimate natural variations,” Proc. SPIE 9784, Medical Imaging 2016: Image Processing, 97840D (2016)
2. S. D. Billings, A. Sinha, A. Reiter, S. Leonard, M. Ishii, G. D. Hager, R. H. Taylor, “Anatomically Constrained Video-CT Registration via the V-IMLOP Algorithm,” In: Ourselin S., Joskowicz L., Sabuncu M., Unal G., Wells W. (eds) Medical Image Computing and Computer-Assisted Intervention – MICCAI 2016. MICCAI 2016. Lecture Notes in Computer Science, vol 9902. Springer, Cham (2016)
  3. A. Sinha, A. Reiter, S. Leonard, M. Ishii, G. D. Hager, R. H. Taylor, “Simultaneous segmentation and correspondence improvement using statistical modes,” Proc. SPIE 10133, Medical Imaging 2017: Image Processing, 101331B (2017)
  4. A. Sinha, S. D. Billings, A. Reiter, X. Liu, M. Ishii, G. D. Hager, R. H. Taylor, “The deformable most-likely-point paradigm,” *submitted to Medical Image Analysis* (2018)
  5. A. Sinha, X. Liu, A. Reiter, M. Ishii, G. D. Hager, R. H. Taylor, “Endoscopic navigation in the absence of CT imaging,” *submitted to MICCAI* (2018)
  6. X. Liu, A. Sinha, M. Ishii, G. D. Hager, R. H. Taylor, A. Reiter, “Depth Map Estimation from Endoscopic Video using Deep Network,” *submitted to MICCAI* (2018)

## Chapter 2

# Segmentation and statistical modeling of CT data

Computed tomography (CT) scans are 3D volumes containing grayscale intensity values at each voxel. These intensity values indicate the Hounsfield units (HU) which comprise a quantitative scale used to describe radiointensity. Since different materials exhibit different amounts of x-ray attenuation, they are associated with different HU. Different tissue types have different material makeup, and therefore HU can be used to differentiate them. CT scans allow for clear distinction between air, soft tissue, and bone. This makes it relatively easy to automatically segment the airway and sinuses. Although bones are generally also easy to segment in CT scans due to high contrast, the bones surrounding the sinuses tend to be extremely thin making segmentation more difficult.

## CHAPTER 2. SEGMENTATION AND STATISTICAL MODELING

Automatic segmentation of CT scans and other medical images has become increasingly more important as the use of non-invasive medical imaging techniques became more prevalent in the medical community making manual labeling too time consuming and impractical. Several different methods have been explored that attempt to accurately segment CT scans.<sup>81</sup> Many early methods presented semi-automatic ways to segment CT scans or images, for instance, region growing methods that require manual seed placement,<sup>82</sup> intensity thresholding, or error correction.<sup>83</sup> More complex automated ways of assigning labels to each voxel have also been presented. Automated region growing techniques have been explored, like adaptive region growing.<sup>84</sup> Other evolution based methods include gradient vector flow snakes,<sup>66</sup> which require an initial curve or segmentation that can be evolved using gradients in the image to converge to the boundaries of objects being segmented. Clustering and majority voting based multi-atlas segmentation methods have also been explored. Several of these methods require a rigid registration to transform given images into the coordinate frame of images with predefined landmarks or segmentations. However, rigid image registration may not be sufficient due to the variability in different anatomical structures between individuals.

Deformable registration techniques have been explored to produce deformation or displacement fields that indicate how each voxel in one image should be displaced in order to best match the target image. Different applications have different constraint requirements for the deformable model, for instance, topology preservation or

diffeomorphism, but almost all methods have a smoothing or regularization term.<sup>85</sup> Both topology preserving and diffeomorphic deformable transformations fulfill the desirable property of the transformation being invertible. This property has been exploited by several segmentation techniques that deformably register an image,  $\mathbf{I}$ , to some standard template with presegmented labels, which can then be transformed back to  $\mathbf{I}$  using the inverse deformation field.

## 2.1 Automatic segmentation

The automatic segmentation method described here assembles different tools presented in the past into one pipeline that enables accurate automatic segmentation of particular structures or regions of interest (ROIs). This method relies on the existence of a *template* CT image with labels for relevant structures or ROIs. The template CT image is built using one target CT image, and  $n_{\text{CT}}$  other CT images of the same dimensions and resolution as the target image. These  $n_{\text{CT}}$  images are deformably registered to the target image using a diffeomorphic deformable registration algorithm, like the ANTs registration software,<sup>86</sup> resulting in deformation fields that can transform each of the  $n_{\text{CT}}$  CT images to the target image. Since the deformations computed are invertible, the target image can also be transformed to each of the  $n_{\text{CT}}$  CT image coordinate frames. The mean of these deformation fields can be computed and used to deform the target image, moving the target image towards the space of

## CHAPTER 2. SEGMENTATION AND STATISTICAL MODELING

the mean of  $n_{\text{CT}}$  CT images.<sup>87</sup> The transformed target image then becomes the new target image, and the process can be repeated. Each iteration further reduces the individual variation of the initial target image, and moves the target image closer to the population mean. The resulting image is a highly symmetric CT image, and will be referred to as the template CT image in the following discussion (Fig 2.1).

Relevant anatomical structures and ROIs can be semi-automatically segmented in the template CT image under the supervision of and with consultation from an otolaryngologist. The semi-automatic segmentation involves selecting seed points in regions that need to be segmented and performing 3D region growing to segment the regions. The final segmentations are manually cleaned up to eliminate errors in segmentation. This semi-automatic segmentation of the template is a one-time task for each segmented structure or ROI. It is important to create these segmentations in a template CT image that represents the mean of a population rather than in a CT image of an individual in order to reduce bias from individual variation. Triangular surface meshes are extracted from these segmentations using marching cubes.<sup>88</sup> Once a labeled template CT image is established, any CT image that covers the same anatomical extent as the template can be deformably registered to the template. If the deformable registration is successful, the resulting deformation field can be used to deform the template meshes to the CT image. This method is not only able to automatically segment CT scans, but also ensures that for each segmented structure, meshes segmented from different CT scans in this manner are in correspondence with

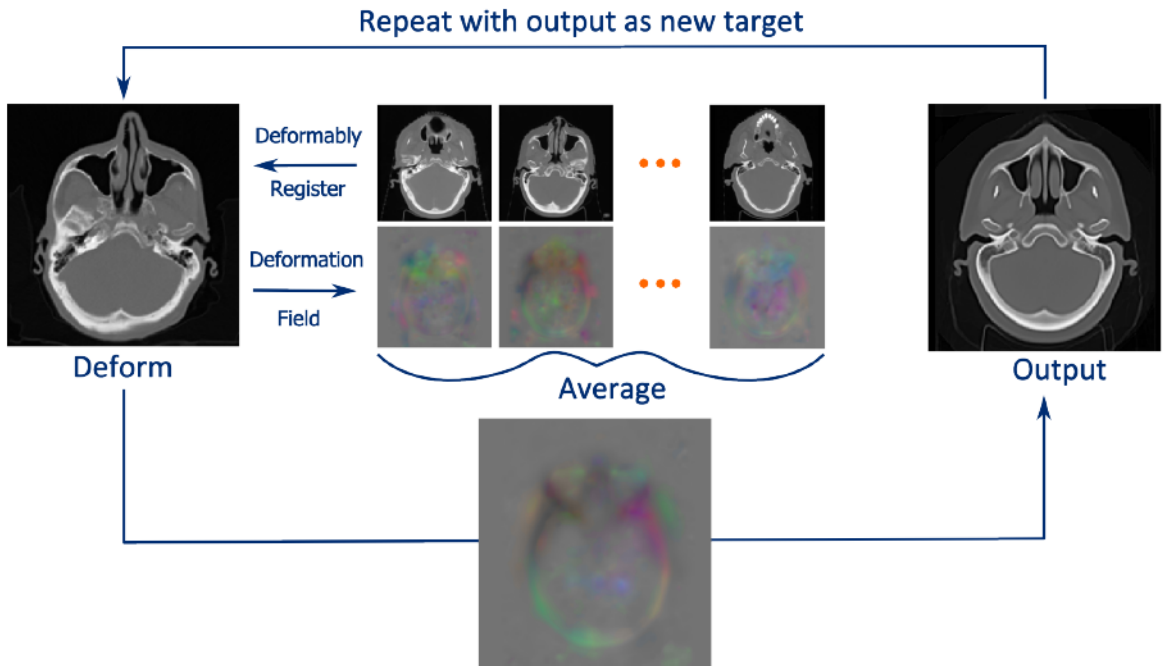


**Figure 2.1:** Template creation pipeline: all input images are deformably registered to one target image, which is then deformed by the mean of the deformation fields resulting from the registrations. The colors in the deformation fields represent the direction of the deformation vectors, whereas the intensity of the colors indicates the magnitude of the vectors. Deforming the target image by the mean deformation field takes the target image towards the mean of the input images. This process is iterated with the output image as the new target image. Individual variation from the initial target image decreases with every iteration, and the resulting output moves closer to the mean of the input set of images.

each other.

Since deformable registration may contain some errors, a segmented mesh obtained using deformable registration may also contain errors. In order to reduce errors in this initial segmentation, gradient based energies, like gradient vector flow (GVF), in the corresponding CT image can be used to pull vertices in the mesh towards edges in the CT image.<sup>66</sup> The vertices in the mesh are treated as control points on a 3D snake spline, which is evolved using GVF.<sup>67</sup> In 2D, vertices on a curve can be sequentially ordered to define control points on a snake spline. However, it is not trivial to sequentially order vertices in 3D. Adjacency matrices that store per vertex neighborhood information are often used, but these can have large memory requirements. Simple blob-like structures have been approximated with high accuracy using parametrized ellipsoids, which can then be evolved.<sup>89</sup> However, structures in the sinuses are often too complex to be approximated using parametrized ellipsoids.

Instead, a simple and efficient sampling technique is introduced to select vertices that can serve as control points on a 3D snake spline. Points are sampled in a spiral around each vertex (Fig. 2.2), as explained in Algorithms 2.1 and 2.2, so that points on this curve can be stored in a sequential order into a vector. These ordered vertices, serving as control points on a snake spline defined by the spiral curve, can be evolved using simple vector-matrix operations. The number of points to be sampled at each iteration, which defines the length of the curve, can be user specified. These curves have consistent internal and external directions making it easy to define internal and



## CHAPTER 2. SEGMENTATION AND STATISTICAL MODELING

external energies<sup>67</sup> which are required for the evolution of the spline using gradients in the image (Fig. 2.2). The only points of concern with this sampling technique are the source and end points on the curve. Due to the closed-loop snake spline formulation, these two points are attracted to each other despite being spatially distant from each other. This is resolved by updating all points except the source and end points at each iteration. These points are updated in other sampling iterations when they are not source or end points (Fig. 2.3). GVF guides these control points toward edges in the corresponding CT image producing highly accurate segmentations<sup>67</sup> (Table 2.1). Fine details that are not captured by deformable registration can be captured using GVF (Fig. 2.8), resulting in lower segmentation errors (Fig. 2.9).

---

**Algorithm 2.1:** Clockwise order vertices in one-ring neighborhood

---

**Input** : Model shape:  $\Psi$

**Output:** List of ordered neighbors for all vertices:  $\mathbf{O}$

```
1 for each vertex  $i$  in  $\Psi$  do
2   Find faces incident on vertex  $i$ , ordered clockwise:90
    $f \leftarrow \text{find\_faces}(i)$ 
4   for  $j \leftarrow 0$  to  $f.size()$  do
5      $\mathbf{O}_{ij} \leftarrow$  vertex at far end of half-edge90 incident on vertex  $i$ 
   end
end
```

---

---

**Algorithm 2.2:** Sample vertices

---

**Input** : Model shape:  $\Psi$   
List of ordered neighbors for all vertices:  $\mathbf{O}$   
Number of vertices to sample:  $n_{\text{samples}}$   
Source vertex for spiral sampling:  $i$

**Output:** Vector of sampled vertices:  $\mathbf{S}$

- 1 Initialize  $k \leftarrow 0, x \leftarrow 0$
- 2 Initialize  $\mathbf{S.resize}() \leftarrow n_{\text{samples}}$
- 3 Initialize  $\mathbf{S}_0 \leftarrow i$
- for**  $j \leftarrow 1$  **to**  $n_{\text{samples}}$  **do**
- 5 | Visit all neighboring vertices around current source vertex,  $i$ :
- if**  $k < \mathbf{O}_i.size()$  **then**
- 7 |     **if** *current neighbor  $k$  is unvisited* **then**
- 8 |         Add unvisited vertex in one-ring neighborhood of  $i$  to list of  
sampled vertices:
- $\mathbf{S}_j \leftarrow \mathbf{O}_{ik}$
- 10 |     Mark  $\mathbf{O}_{ik}$  as visited
- 11 |     Increment  $k$ :
- $k \leftarrow k + 1$
- 13 | Once all neighbors of current source vertex have been visited,  
update current source vertex:
- else**
- 16 |      $k \leftarrow 0$
- 17 |      $x \leftarrow x + 1$
- 18 |      $i \leftarrow \mathbf{S}_x$
- end**
- end**

---

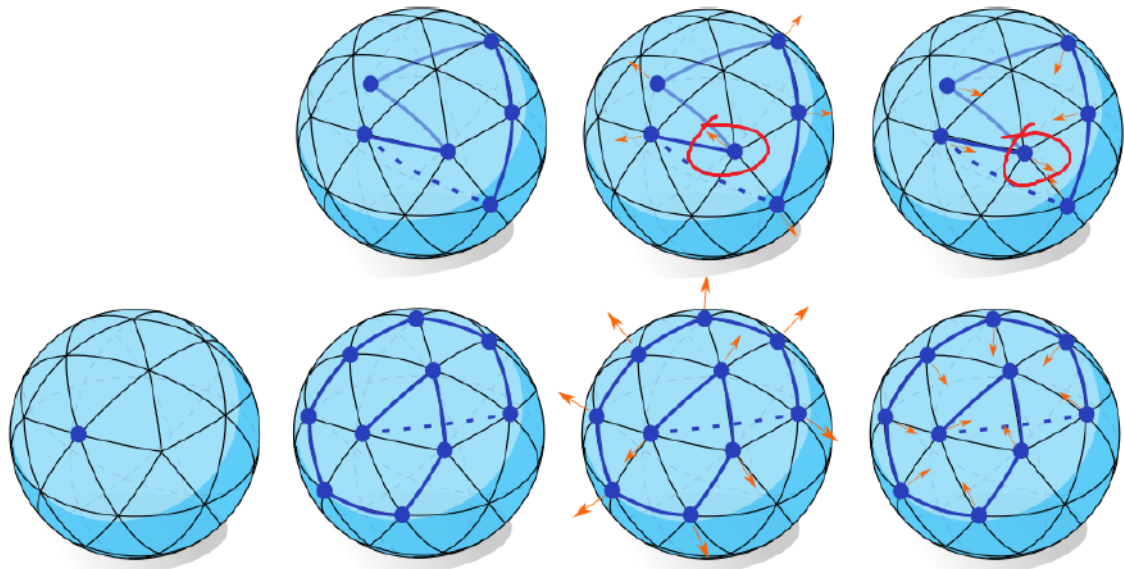


**Figure 2.2:** Sampling scheme (blue dots represent sampled vertices, blue lines indicate adjacency; dotted lines imply that connected points should not be attracted to each other; translucent lines cut through the shape): Random sampling (top) causes inconsistent internal and external directions. The middle sphere shows a vertex (circled) with external energy pointing inwards into the sphere, and the right sphere shows one (circled) with internal energy pointing outwards. The spiral sampling scheme maintains internal and external direction consistency.

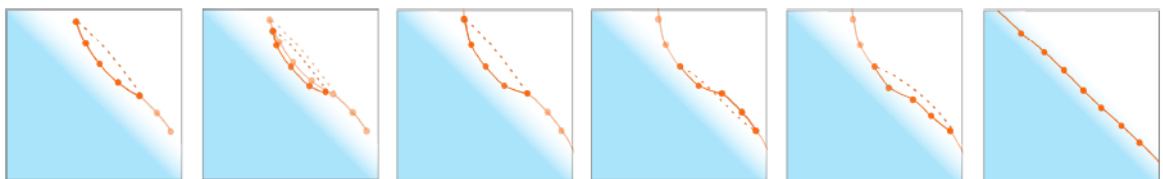


**Figure 2.3:** Segmentation improvement illustrated in 2D: from left to right, vertices in the snake spline (orange) move towards the edge in the image. Since corner points must not be drawn inward toward each other, corner points are not allowed to move. However, these points are updated during other iterations when they are not corner points. After several iterations all vertices converge to the closest edge.

## 2.2 Statistical shape modeling

The segmentation pipeline described in Sec. 2.1 not only produces high quality segmentations, but also ensures that the meshes representing these segmentations are in correspondence. Segmenting images of several healthy individuals using this method enables the statistical analysis of each segmented structure in this population. One standard way of performing statistical analysis on these shapes is by using principal component analysis (PCA).<sup>1</sup> In order to compute shape statistics, the meshes are first aligned and centered, and the vertices in each mesh arranged into a column vector called the *shape vector*,

$$\mathbf{V} = \begin{bmatrix} \mathbf{v}_1 \\ \mathbf{v}_2 \\ \vdots \\ \mathbf{v}_{n_v} \end{bmatrix} ,$$

where  $n_v$  is the number of vertices in the mesh. Since the shapes are homologous, that is, in correspondence with each other, the mean shape,  $\bar{\mathbf{V}}$ , can be computed by simply averaging the shape vectors,

$$\bar{\mathbf{V}} = \frac{1}{n_s} \sum_{i=1}^{n_s} \mathbf{V}_i ,$$

## CHAPTER 2. SEGMENTATION AND STATISTICAL MODELING

where  $\mathbf{V}_i$  is the shape vector for the  $i$ th mesh, and  $n_s$  is the number of meshes.

Similarly, the shape covariance matrix can be computed as

$$\Sigma = \frac{1}{n_s} \sum_{i=1}^{n_s} (\mathbf{V}_i - \bar{\mathbf{V}})(\mathbf{V}_i - \bar{\mathbf{V}})^{\mathbf{T}} \quad .$$

Eigen decomposition of this matrix,  $\Sigma$ , results in the modes and mode weights of shape variation:

$$\Sigma = [\mathbf{m}_1 \dots \mathbf{m}_{n_s}] \begin{bmatrix} \lambda_1 & & \\ & \ddots & \\ & & \lambda_{n_s} \end{bmatrix} [\mathbf{m}_1 \dots \mathbf{m}_{n_s}]^{\mathbf{T}} \quad ,$$

where  $\mathbf{m}_i$  are the orthonormal set of eigenvectors that represent the modes of variation, and  $\lambda_i$  are the eigenvalues, or mode weights, that represent the amount of variation along the direction of each mode (Fig. 2.4, Alg. 2.3). These SSMs are able to show how different structures vary across the sample population. For some structures, SSMs can also reflect natural variations that occur periodically in all individuals. These observations are discussed in more detail in Chapter 8.

Using the mean shape and the modes of variation, any homologous shape,  $\mathbf{V}^*$ , can be estimated as

$$\tilde{\mathbf{V}}^* = \bar{\mathbf{V}} + \sum_{i=1}^{n_m} b_i \mathbf{m}_i \quad , \quad (2.1)$$

where  $n_m < n_s$  is a user selected number of modes, and  $b_i$  are the mode weights or

shape parameters, which can be computed as

$$b_i = \mathbf{m}_i^T(\mathbf{V}^* - \bar{\mathbf{V}}) \quad . \quad (2.2)$$

If  $\mathbf{V}^*$  was one of the shapes used to construct the SSM, then it can be estimated perfectly using all non-zero modes of variation. However, generally some number of modes,  $n_m < n_s$ , is used to estimate shapes as long as the error in estimation is below some acceptable threshold. This reduces the amount of computational as well as storage overhead.

SSMs built using the described method require highly accurate segmentations in order to capture correct and meaningful variation in the sample population. The segmentation pipeline described in Sec. 2.1 computes highly accurate segmentations. However, the segmentation improvement using GVF moves vertices in each shape independent of other shapes in the dataset resulting in errors in point correspondences between the shapes. Methods have been presented that are able to improve correspondences between shapes. Seshamani et al.<sup>2</sup> use the initial point correspondences to build an SSM using  $n_s - 1$  shapes, and estimate the left-out shape using Eqs. 2.1 and 2.2. The vertices on the left-out shape can then be moved along the surface towards the corresponding vertices on the estimated mesh<sup>2</sup> (Fig. 2.6). This process is repeated for each shape, and once vertices on all the shapes are updated, a new SSM is computed using the set of shapes with updated vertices (Fig. 2.5, Alg. 2.4).

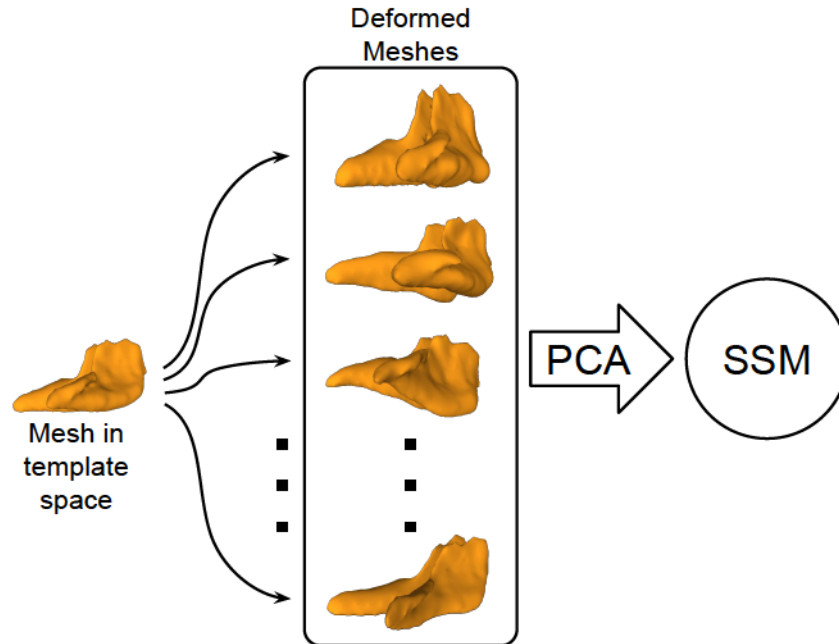


**Figure 2.4:** Given correspondences between shapes in a dataset, PCA can be used to understand the mean and variance in the dataset.<sup>1</sup>

---

**Algorithm 2.3:** Build SSM

---

**Input** : Template CT image

Mesh representing hand-segmented ROI in template CT image

**Output:** SSM

1 **for** *each patient CT image* **do**

2     Deformably register patient CT image to the template CT image

3     Use resulting deformation field to deform mesh in template coordinate frame to patient coordinate frame

**end**

5 Use PCA on the set of patient shapes obtained to build SSM<sup>1</sup>

---

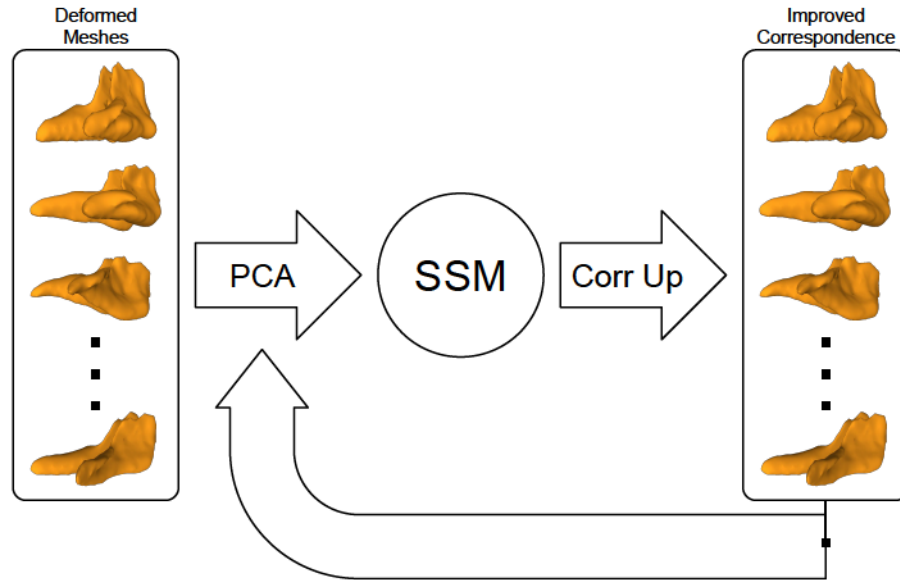


Figure 2.5: Correspondence improvement algorithm presented by Seshamani et al.<sup>2</sup> using the middle turbinate as an example shape.

---

**Algorithm 2.4:** Correspondence improvement

---

**Input** : Set of shapes with correspondences

**Output:** Set of shapes with improved correspondences

```

1 while not converged do
2   for  $i \leftarrow 1$  to  $n_s$  do
3     Build an SSM using  $n_s - 1$  shapes leaving out patient  $i$ 
4     Estimate left out shape using the SSM (Eqs. 2.1, 2.2)
5     Move the vertices on the left-out shape along the surface in the
      direction of the corresponding vertices on the estimated shape2
   end
end
end

```

---



This process can be repeated several times until a desired quality of vertex correspondence is achieved. This can be measured by computing the per vertex distance or the residual surface error between the left-out and estimated shapes at each iteration, averaging over all left out shapes, and testing to check if the mean vertex error or mean residual error is below some specified threshold.

## 2.3 Simultaneous segmentation and correspondence improvement

Instead of first improving segmentation and allowing the correspondences to deteriorate, and then trying to recover the correspondences, perhaps the two, segmentation and correspondences, could be improved simultaneously. That is, segmentation improvement could be performed without compromising the correspondences. This can be achieved using a *constrained GVF* algorithm presented here.<sup>76</sup> In order to maintain correspondence, the GVF algorithm is modified in order to constrain the movement of vertices using an SSM. The original SSM is built using the set of shapes obtained from automatic segmentation via deformable registration (Sec. 2.1). Although this set of shapes contains inaccurate segmentation, the shapes are in correspondence. Therefore, although the SSM built from this set of shapes cannot accurately explain the variability in the population, the SSM is able to estimate the shapes in the current set with small errors. This initial set of shapes is first evolved

using GVF, and the new evolved shapes are then estimated using the current SSM. The vertices on each evolved shape are moved along the surface in the direction of the corresponding vertices on the estimated shape (Fig. 2.6). The new shapes produced using this constrained GVF method exhibit improved segmentations, and retain some amount of correspondence, which can be further improved using the correspondence improvement algorithm described above<sup>2</sup> (Fig. 2.7, Alg. 2.5). Constrained GVF followed by correspondence improvement can be iterated several times until a satisfactory set of segmentations is obtained.

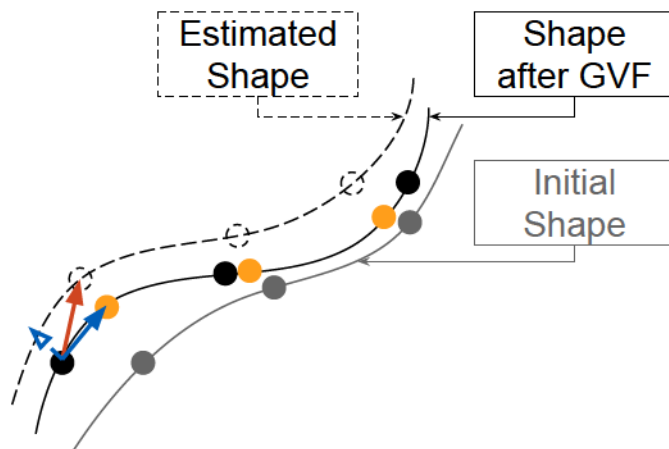


**Figure 2.6:** 2D example illustrating the constrained GVF algorithm: Initial shape (gray curve) is evolved to new updated shape (black curve), which is then estimated using an SSM (dashed curve). Vertices (black dots) on the updated shape are moved along the surface toward corresponding vertices on the estimated shape to obtain new vertex positions (yellow dots) that preserve correspondence between the update shape and SSM.

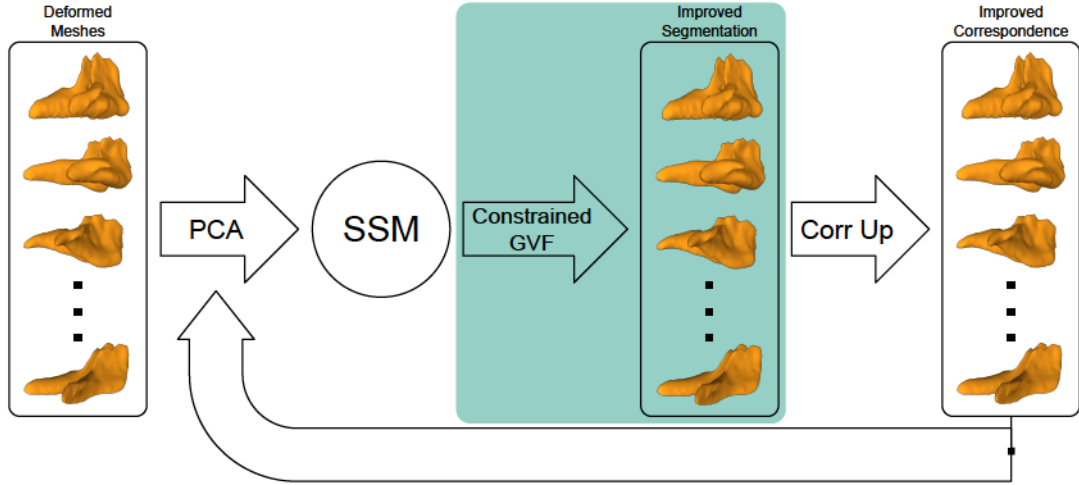


**Figure 2.7:** Simultaneous segmentation and correspondence improvement using the middle turbinate as an example shape. The middle (green) section performs the constrained segmentation improvement which is followed by the correspondence improvement method presented by Seshamani et al.<sup>2</sup>

---

**Algorithm 2.5:** Simultaneous segmentation and correspondence improvement

---

**Input** : Set of shapes with correspondences  
 Number of GVF iterations:  $P$  (default: 5)  
 Number of correspondence improvement iterations:  $Q$  (default: 3)

**Output:** Set of shapes with improved segmentation and correspondences

- 1 Build SSM using input set of shapes
- 2 **while** *not converged* **do**
- 3     **for** *each shape* **do**
- 4         Use GVF to move vertices towards edges in the corresponding image for  $P$  iterations.
- 5         Estimate updated shape using the current SSM (Eqs. 2.1, 2.2)
- 6         Move vertices on updated shape along the surface in the direction of the corresponding vertices on the estimated shape<sup>2</sup> (Fig. 2.6)
- end**
- 8     Build SSM using updated set of shapes
- 9     Improve correspondences for  $Q$  iterations
- end**

---

## 2.4 Experimental results and discussion

A publicly available head CT image dataset<sup>91–94</sup> containing 52 CT images and the template CT image built using this dataset were used to build SSMs for various structures and ROIs in the nasal cavity and sinuses. The resolution of all CT scans was  $1 \times 1 \times 1 \text{ mm}^3$  and the dimensions were  $308 \times 210 \times 272 \text{ mm}^3$  (axial  $\times$  sagittal  $\times$  coronal). The algorithms were implemented in C++ and segmentation and shape modeling results were evaluated using the maxillary sinus (Fig. 1.2), one of the four paranasal sinuses.

### 2.4.1 GVF experiment

In order to assess the efficacy of the sampling technique presented in Sec. 2.1, segmentation improvement using GVF is evaluated first. In order to evaluate the improvement between segmentations obtained automatically using deformable registration and segmentations improved using GVF, the segmentations produced are compared to corresponding manual segmentations in 6 CT scans using the Hausdorff distance metric.<sup>95</sup> Results show that GVF improves the original segmentations obtained using deformable registration (Table 2.1). Deformable registration is unable to capture fine details, but these details are captured using GVF (Fig. 2.8) resulting in lower segmentation errors (Fig. 2.9). The improvement in segmentation errors shows that the spiral sampling technique can be used to efficiently construct snake splines

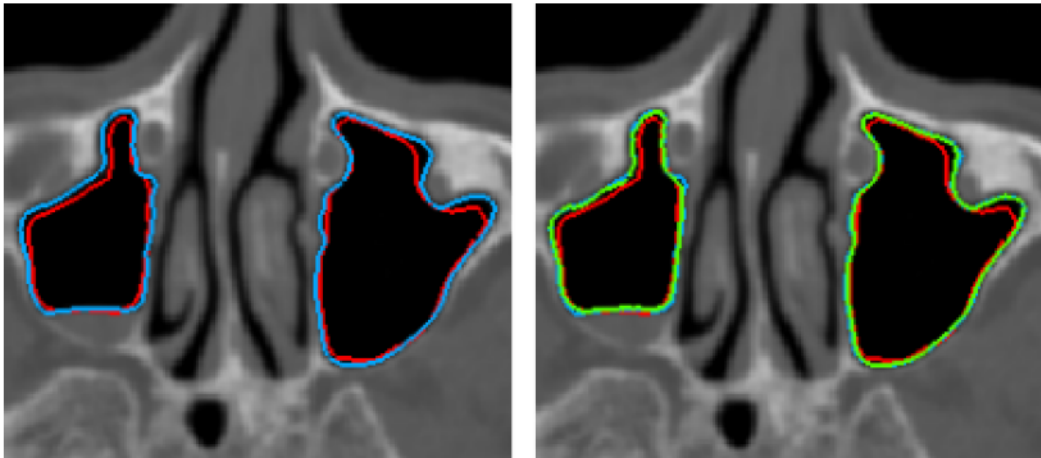


**Figure 2.8:** Left: contours of hand-segmented (blue) and deformedly registered (red) left and right maxillary sinuses. Right: contours after GVF (green) overlap almost perfectly with the hand-segmented contours.

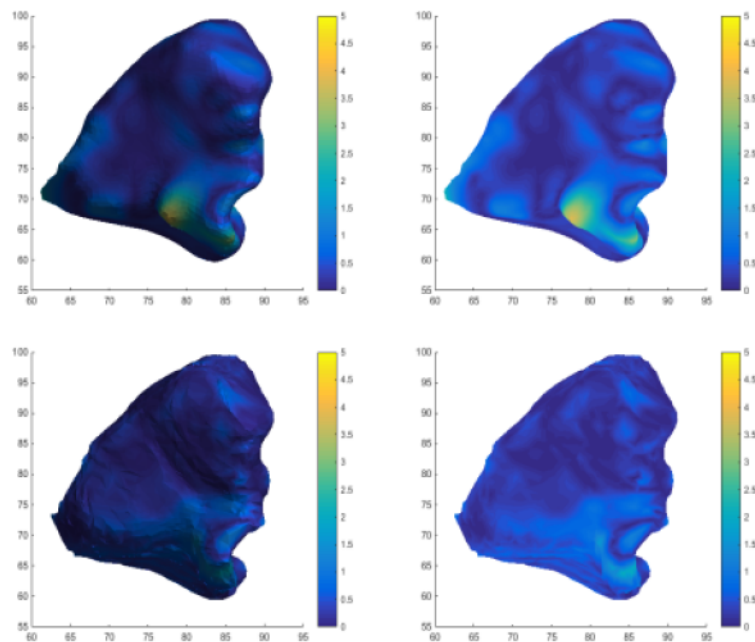


**Figure 2.9:** Top: errors from deformable registration visualized on the right maxillary sinus mesh with lighting (left) to show structure and without lighting (right) to focus on errors without distractions from specularities or shadows. Bottom: errors after GVF, visualized similarly as above.

that can be used along with GVF to evolve meshes.

## 2.4.2 Constrained GVF experiment

In this experiment, the constrained GVF algorithm is evaluated to assess the simultaneous improvement in segmentation and correspondences between the segmentations. The constrained GVF algorithm was iterated 5 times before termination. Within each iteration, GVF was repeated for 5 iterations followed by correspondence improvement for 3 iterations. Each iteration took about 10 seconds per shape, with the majority of the time spent in computing GVF in the CT volumes. As before, in order to evaluate the improvement between segmentations obtained using deformable registration and segmentations improved using constrained GVF, the segmentations produced are compared to corresponding manual segmentations in 6 CT scans using the Hausdorff distance metric.<sup>95</sup> Results show that constrained GVF improves the original segmentations obtained via deformable registration. Further, constrained GVF is able to match or improve the segmentations produced by traditional GVF (Fig. 2.10). Table 2.1 shows cumulative errors in segmentation over all trials.

Next, in order to evaluate the improvement in correspondence between shapes, a leave-one-out analysis was performed using SSMs built from shapes obtained from deformable registration, shapes after traditional GVF, and shapes after constrained GVF. The left-out shape was estimated using an increasing number of modes and errors between the left-out and estimated shapes were computed using the Haus-

## CHAPTER 2. SEGMENTATION AND STATISTICAL MODELING

dorff distance metric.<sup>95</sup> Mean errors over all left-out shapes are shown in Fig. 2.11. Residual errors are seen to deteriorate when GVF is used to improve segmentation. Interestingly, with fewer than 30 modes, segmentations produced using constrained GVF show similar some deterioration in residual error compared to the original segmentations from deformable registration. This occurs because the original segmentations do not capture fine details resulting in a smoothed approximation of the correct shape. Therefore, although SSMs built using these shapes may estimate left-out shapes more accurately using few modes, the shapes being estimated do not capture the real anatomy accurately. By improving the segmentations, high frequency details in the objects being segmented are captured reducing segmentation error, but also requiring more modes to accurately estimate these details. With more than 30 modes, the residual errors using constrained GVF in the leave-one-out analysis show

**Table 2.1:** Segmentation errors computed using the Hausdorff distance metric: GVF and constrained GVF (C-GVF) both produce comparable improvement over deformable registration (DR). C-GVF has the added advantage of maintaining correspondences (Figure 2.11).

	Mean error $\pm$ std. dev. (mm)	Max error (mm)
DR	$0.333 \pm 0.315$	2.338
GVF	$0.113 \pm 0.132$	1.155
C-GVF	$0.099 \pm 0.128$	1.036

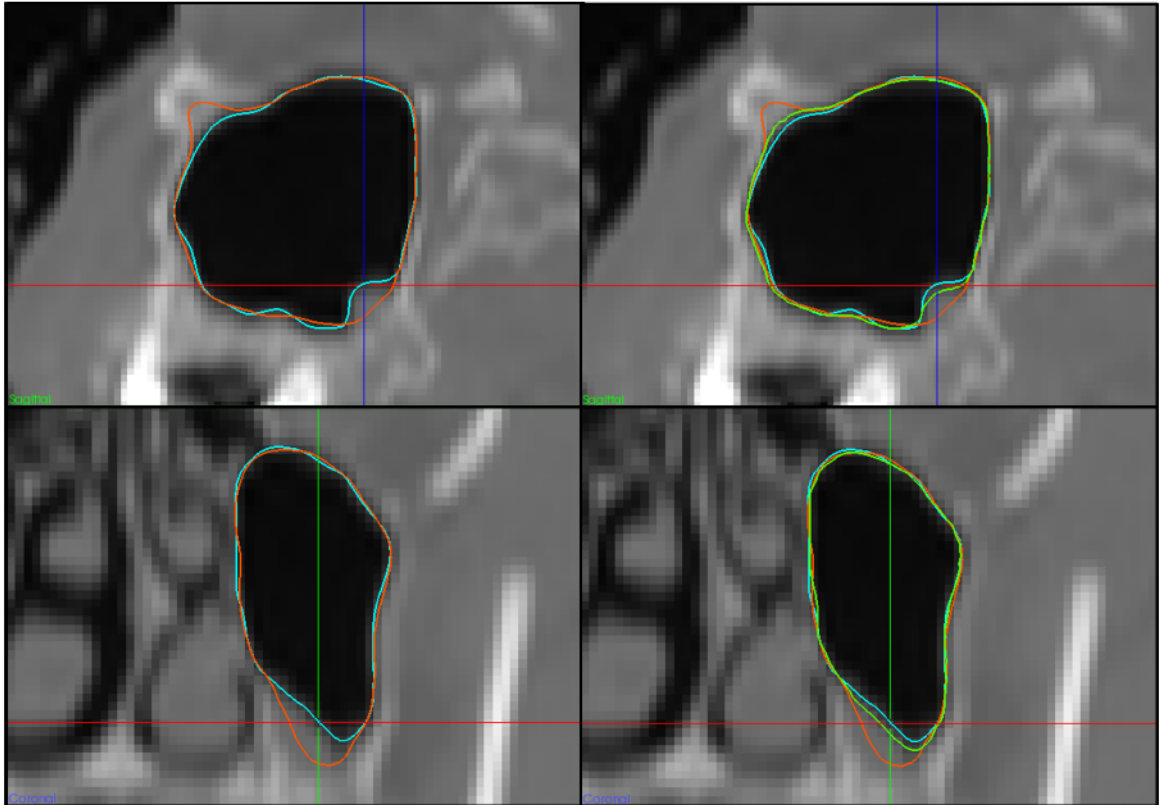


**Figure 2.10:** Left: Initial segmentation (red) of the maxillary sinus using deformable registration does not capture details such as sharp corners, therefore introducing errors when compared with hand-segmented gold standard (blue). Right: Constrained GVF is able to capture these details (green).



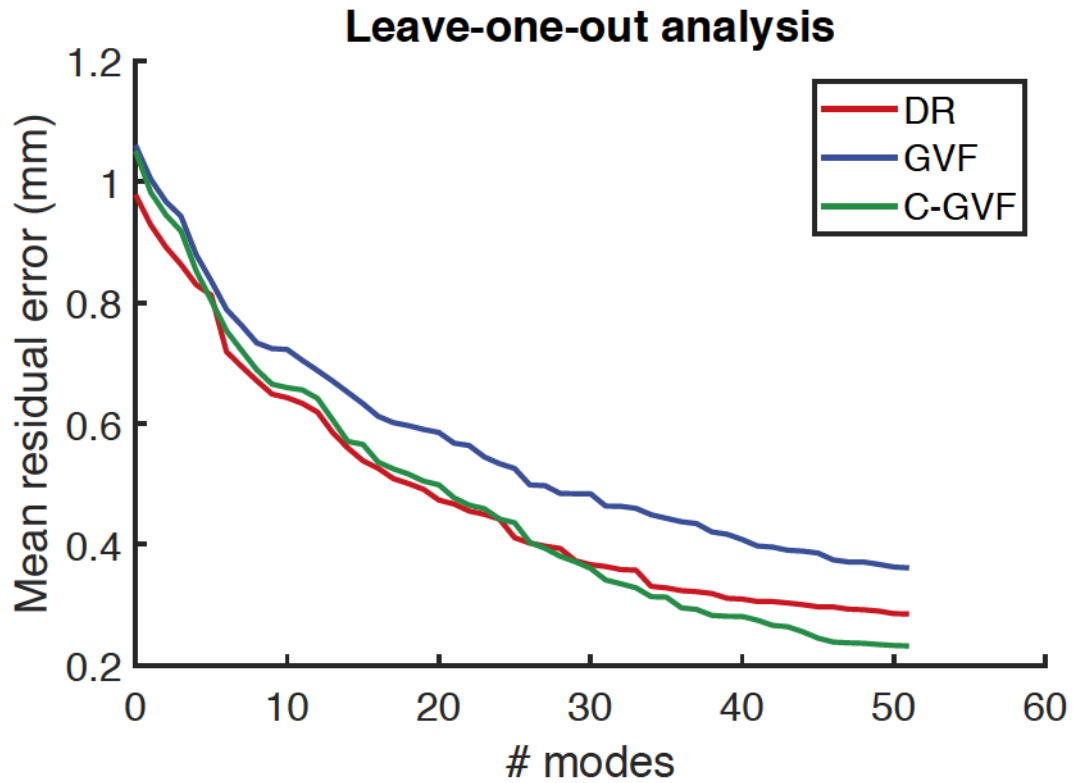


**Figure 2.11:** Residual surface errors from leave-one-out analysis: since the shapes produced by constrained GVF (C-GVF) contain more detail than those produced by deformable registration (DR) (Figure 2.10), it is hard to estimate shapes with few modes. However, with more than roughly 30 modes, shape estimation errors for segmentations improved using C-GVF show improvement (green) over the original shapes obtained using DR (red). On the other hand, segmentations improved using traditional GVF (purple) do not maintain correspondence between shapes, as reflected in the deteriorating mean residual errors.

improvement over both the original shapes obtained from deformable registration and the shapes after GVF. These results show that constrained GVF is able to improve both segmentation and correspondences.

Additionally, by restricting the movement of vertices during segmentation improvement using constrained GVF, the resulting shapes represented as triangular meshes exhibit better triangle quality than when traditional GVF is used. Meshes obtained using GVF can cause high concentration of vertices at corners and regions with strong gradients, creating skinny triangles which lead to pinching artifacts in meshes. However, by restricting the movement of vertices using SSMs, this concentration of vertices and problems arising from it, like pinching artifacts and triangle flipping, are avoided producing more stable meshes (Fig. 2.12).

## 2.5 Concluding Remarks

A novel method for simultaneous improvement of segmentation per shape and correspondences between a set of shapes is presented. This method leverages the advantages presented by GVF and SSMs to segment structures accurately while maintaining correspondences between shapes in a dataset, which other segmentation methods fail to do. By maintaining correspondences, more accurate SSMs that better represent the mean and variance in the dataset can be built. These SSMs are able to estimate shapes with higher fidelity than both a) models constructed using initial shapes

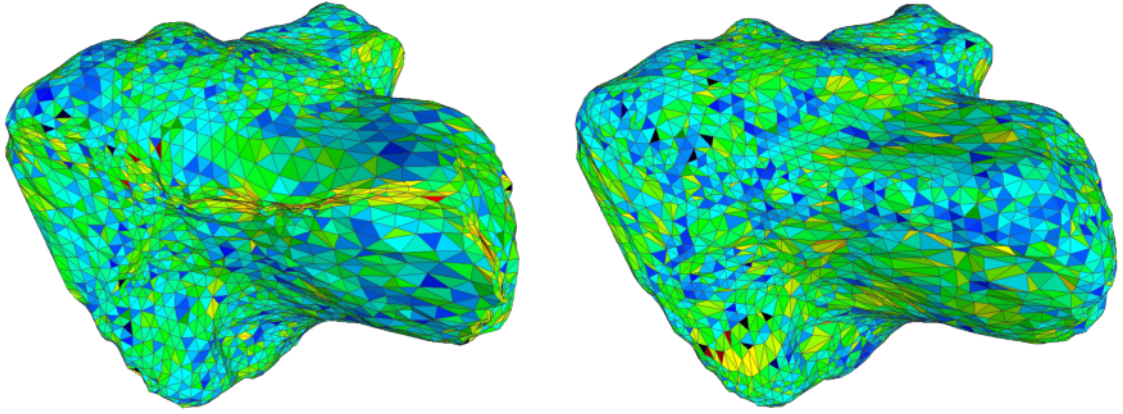


**Figure 2.12:** Meshes obtained using GVF (left) can contain skinny triangles near corners causing pinching artifacts and flipped triangles, whereas meshes obtained using constrained GVF (right) avoid these problems producing more stable meshes.

obtained from deformable registration that do not capture the anatomy accurately, and b) models constructed using shapes after segmentation improvement using traditional GVF because the quality of correspondences deteriorates during this process. Constrained GVF is able to overcome both of these problems, and also produce more stable triangular meshes with fewer skinny triangles. Better mesh quality reduces the chances of pinching artifacts and triangle flipping.

High quality SSMs of sinonasal anatomy have several advantages. These SSMs enable a clear and quantitative understanding of the types and extents of variation in anatomical structures. Periodic changes in anatomy, for instance in the nasal

turbinates, and other changes between preoperative and intraoperative imaging can be compensated for using these models. Further, SSMs built from a normal population can be exploited to quantitatively measure the extent of disease by computing its deviation from the normal range of variation.

### 2.6 Contributions

The contributions of this chapter include:

1. A novel method for simultaneous improvement of segmentation and correspondences among a set of shapes in order to build better statistical shape models.<sup>76</sup>

### 2.7 Published Work

Material from this chapter appeared in the following publications:

1. A. Sinha, S. Leonard, A. Reiter, M. Ishii, R. H. Taylor, G. D. Hager, “Automatic segmentation and statistical shape modeling of the paranasal sinuses to estimate natural variations,” Proc. SPIE 9784, Medical Imaging 2016: Image Processing, 97840D (2016)
2. A. Sinha, A. Reiter, S. Leonard, M. Ishii, G. D. Hager, R. H. Taylor, “Simultaneous segmentation and correspondence improvement using statistical modes,” Proc. SPIE 10133, Medical Imaging 2017: Image Processing, 101331B (2017)

## Chapter 3

# The deformable most-likely-point paradigm

Statistical shape models (SSMs) not only facilitate a better understanding of the variation present in a given population, but can also be used to inform how different shapes may be allowed to deform. Since PCA-based models are generative models, new instances of shapes can be estimated using PCA-based SSMs, making these models extremely powerful tools. One area that can benefit tremendously from generative models is the field of medicine. Ease of access to medical imaging technologies has created an abundance of medical images in many different modalities, including CT scans, making it possible to build large scale SSMs of various structures. This begs the question of whether these existing images can be used to build a framework that can be used to estimate the anatomy of new patients.

## CHAPTER 3. THE DEFORMABLE MOST-LIKELY-POINT PARADIGM

In this chapter, a new deformable registration paradigm, known here on as the *deformable most-likely-point paradigm*, is introduced. This framework computes deformations based on SSMS by restricting deformations to the statistical modes of variation. The purpose of this paradigm is to enable registration between a point cloud and a statistically derived target shape while deforming the target shape using statistical modes to reflect the shape represented by the point cloud. This paradigm is built upon the *most-likely-point paradigm*,<sup>51</sup> and extends it to include deformations based on statistics in the optimization in addition to transformation parameters. This paradigm is explained here at a high level which will enable the development of several different deformable registration algorithms using different features, noise models, and statistical shape models.

Deformable registration is an active area of research, and a large amount of prior work has been presented in this area. Crum et al.<sup>33</sup> present an overview of the various different deformable registration methods. Deformable registration methods can vary significantly based on the type of transformation applied to deform a given shape. The *similarity* and *affine transformation*, which apply a global scaling or general linear mapping to a shape, respectively, are two of the simplest deformations that can be applied. Several less constrained and more complex forms of deformation that apply local variations and allow different regions of the shape to vary differently have been studied.<sup>96</sup> Many of these methods typically compute transformations with several parameters, like deformation fields, and attempt to restrict the deformations

### CHAPTER 3. THE DEFORMABLE MOST-LIKELY-POINT PARADIGM

to be locally smooth by embedding a regularization term in the cost function, for instance.

Some important deformable registration methods include deformable versions of the iterative closest point (ICP) algorithm<sup>35,97</sup> Coherent point drift is a standard deformable registration algorithm and takes a maximum likelihood approach to registration.<sup>50</sup> It uses expectation maximization (EM) to find the best deformation to align two point sets. The thin plate spline robust point matching (TPS-RPM) algorithm computes a joint estimate of pose and correspondence to register two point sets.<sup>98</sup> Deformable registration has several important clinical applications as well, and methods for computing deformable registration between CT volumes and video features, for instance, have been studied for various applications.<sup>99</sup>

Deformable registration can play a critical role in improving surgical navigation during FESS. As explained earlier, minimally invasive procedures like FESS require high resolution preoperative CT scans due to the thinness and pseudo stochastic growth pattern of the ethmoid bones.<sup>100</sup> However, CT image acquisition exposes patients to high doses of ionizing radiation and can have adverse effects. The head contains several important organs , and minimizing radiation to these organs is vital. Therefore, reducing or eliminating the use of CT images is an important goal. Instead, the paradigm developed below employs deformable registration between SSMs of target anatomical structures along with points extracted from intraoperative endoscopic video of corresponding structures to accurately estimate patient anatomy.

### CHAPTER 3. THE DEFORMABLE MOST-LIKELY-POINT PARADIGM

This is a reasonable approach since there are a limited number of genes that govern bone growth. Therefore, although the number of dimensions in bone development may be large enough to appear pseudostochastic to a human, they are likely not to be an SSM.

The paradigm developed here is a general paradigm that can be used in several applications. For instance, statistical shape models can be used to identify the modes that account for deformations resulting from the natural nasal cycle,<sup>6</sup> and deformable registration can be used to account for changes caused by these deformations between preoperative and intraoperative image acquisitions. Further, deformations that occur during procedures such as those caused by insufflation of the abdomen, breathing activity, cutting or pressing from surgical tools can also be compensated for via deformable registration in order to provide accurate surgical navigation.

Other procedures like orthopedic interventions can also take advantage of this paradigm. Most orthopedic procedures require preoperative CT scans because the high contrast between bone and soft tissue exhibited by CT images allows for easy bone segmentation and surface extraction, which can then be used for preoperative planning and intraoperative surgical navigation. Orthopedic procedures involving the hip or femoral head often require a full pelvic CT scan, which is detrimental to the reproductive health of patients, especially women of reproductive age.<sup>101</sup> Often partial CT scans of hips are acquired to protect reproductive organs. Therefore, the ability to estimate full patient shape from partial data without exposing vital organs to ion-



### CHAPTER 3. THE DEFORMABLE MOST-LIKELY-POINT PARADIGM

izing radiation is critical. Other medical applications include registering anatomical structures from different patients to establish correspondences, or registering structures from the same patient extracted from CT images taken over time to monitor changes.

This paradigm has applications outside the medical field as well. For instance, SSMs can be used to learn the range of human expression and pose. Since there are limited number of expressions and poses that humans can achieve, SSMs are expected to learn the range facial expressions and human poses with enough shapes and the right type of statistical modeling. Therefore, although it may be hard to visualize these when represented as point clouds, the emotion or actioned being rendered can be inferred by deformably registering a statistically derived shape to the point cloud and reconstructing the expression simultaneously.

In the following sections, the general probabilistic models for shape deformation and deformable registration using a PCA-based SSM are developed, and the deformable correspondence and registration phases are explained. These ideas were first developed by Billings,<sup>78</sup> and are repeated here for ease of reference since they serve as foundations for the ideas developed in the following chapters.

### 3.1 Probabilistic model

SSMs can be used to describe shape deformation by establishing some statistically derived shape, like the mean shape, as the statistically most likely shape, that can be deformed according to the statistical modes of variation. The probabilistic models developed below use PCA-based SSMs, which are explained earlier. As a reminder, these SSMs are built from different shapes that represent different instances of some object (e.g., an anatomical structure like the middle turbinate or the femur), have the same topology, and are homologous (i.e., in correspondence with each other). The process for building an SSM is described in Chapter 2. PCA-based SSMs are generative models and, for ease of reference, the equation that allows an estimate of a homologous shape,  $\mathbf{V}^*$ , to be constructed using such SSMs is repeated here:

$$\tilde{\mathbf{V}}^* = \bar{\mathbf{V}} + \sum_{i=1}^{n_m} b_i \mathbf{m}_i, \quad (3.1)$$

where  $\bar{\mathbf{V}}$  is the mean shape,  $\mathbf{m}_i$  are the orthonormal set of eigenvectors that represent the modes of variation,  $n_m < n_s$  is a user selected number of modes, and  $b_i$  are the mode weights or shape parameters, which can be computed as

$$b_i = \mathbf{m}_i^T (\mathbf{V}^* - \bar{\mathbf{V}}). \quad (3.2)$$

In the following discussions, the shape parameters are converted to units of stan-

dard deviation relative to the SSM covariance by rewriting Eq. 2.1 as

$$\tilde{\mathbf{V}}^* = \bar{\mathbf{V}} + \sum_{i=1}^{n_m} s_i \mathbf{w}_i, \quad (3.3)$$

where  $\mathbf{w}_i = \sqrt{\lambda_i} \mathbf{m}_i$  are the weighted modes of variation, and  $s_i$  are the shape parameters in units of standard deviation, which can be computed by projecting the mean subtracted  $\mathbf{V}^*$  onto the weighted modes:

$$s_i = \mathbf{w}_i^T (\mathbf{V}^* - \bar{\mathbf{V}}). \quad (3.4)$$

### 3.1.1 Probabilistic model for shape deformation

Using these  $s_i$ , an expression is formulated in this section for assuming a probability on an instance of a model shape generated from an SSM. This allows the shape deformation parameters to be optimized directly within the probabilistic framework of the algorithms developed under the *most-likely-point paradigm*.<sup>78</sup>

Assuming a Gaussian distribution on the deformation from the mean shape, the likelihood of a deformed vertex is defined by

$$f_{\text{vertex}}(\mathbf{v}; \mathbf{s}) = \prod_{i=1}^{n_m} \frac{1}{(2\pi)^{3/2}} \cdot e^{-\frac{\|\mathbf{s}_i\|_2^2}{2}}. \quad (3.5)$$

Since, the weighted shape parameters,  $\mathbf{s} = \{s_i\}$ , are already in units of standard devi-

### CHAPTER 3. THE DEFORMABLE MOST-LIKELY-POINT PARADIGM

ation, a variance parameter is not required for the Gaussian distribution in Eq. 3.5. In other words, the variation is simply equal to one. Another point to note is that only the shape parameters,  $\mathbf{s}$ , are required in the calculation of the vertex probability, the vertex position,  $\mathbf{v}$ , is not required. However,  $\mathbf{v}$  is included in  $f_{\text{vertex}}(\mathbf{v}; \mathbf{s})$  in order to signify that the expression represents the probability of the vertex *given* parameters from an SSM-based deformation model for that vertex.<sup>78</sup>

Assuming that the deformation at each vertex comprising a shape is independent, the likelihood of a complete shape can be defined by the following *shape likelihood function*:

$$f_{\text{shape}}(\mathbf{V}; \mathbf{s}) = \prod_{i=1}^{n_v} f_{\text{vertex}}(\mathbf{v}_i; \mathbf{s}). \quad (3.6)$$

Although, this assumption is not entirely accurate, since there is likely some local dependence between the deformations of vertices representing a particular shape, this assumption allows for a tractable formulation of the shape deformation probability.<sup>78</sup> Further, this assumption becomes more valid as the sparsity of the vertices representing the shape increases.<sup>78</sup> This assumption may also become more valid when used within the context of the full probabilistic model for deformable registration,<sup>78</sup> as presented in the following section.

### 3.1.2 Probabilistic model for deformable registration

Given the shape deformation probability model derived in Sec. 3.1.1, a probability model that combines the shape likelihood with the match likelihoods of registration algorithms can now be derived.<sup>78</sup> Assuming independence between the matches found between data points,  $\mathbf{x}$ , and model shape,  $\mathbf{y}$ , and the deformation of the model shape, the following *deformable match likelihood function* can be formulated:<sup>77</sup>

$$f_{\text{match\_deformable}}(\mathbf{x}, \mathbf{y}; \theta, \mathbf{s}, \bar{\mathbf{V}}, \mathbf{W}) = f_{\text{match}}(\mathbf{x}; \mathbf{T}_{\text{ssm}}(\mathbf{y}, \mathbf{s}), \theta) \cdot f_{\text{shape}}(\mathbf{T}_{\text{ssm}}(\mathbf{y}, \mathbf{s}); \mathbf{s}), \quad (3.7)$$

where  $f_{\text{match}}$  is any point to point or point to shape match likelihood function with  $\theta$  representing the distribution parameters of a particular match likelihood function, which vary by algorithm,  $f_{\text{shape}}$  depends on the type of model used to compute shape statistics, and  $\mathbf{s}$  represents the shape parameters that define an instance of the SSM. The expression for the probability of a vertex, and consequently for  $f_{\text{shape}}$ , could also be adapted to other non-SSM-based shape deformations by appropriately changing the definition of  $\mathbf{s}$ .

The expression for  $\mathbf{T}_{\text{ssm}}(\mathbf{y}, \mathbf{s})$  also depends on the type of statistical model being used. Since, the statistics in consideration here are computed on shapes represented by triangular meshes, each matched point,  $\mathbf{y}$ , can be assumed to reside within the convex hull of the triangle face it is matched to. Therefore, it can be represented as

the weighted sum of the triangle vertices,

$$\mathbf{y} = \sum_{j=1}^3 \mu^{(j)} \mathbf{v}^{(j)} \quad \text{subject to} \quad \sum_{j=1}^3 \mu^{(j)} = 1, \quad (3.8)$$

where  $\{\mathbf{v}^{(1)}, \mathbf{v}^{(2)}, \mathbf{v}^{(3)}\}$  are the three triangle vertices.  $\mu^{(j)}$  can be computed as the barycentric coordinates of  $\mathbf{y}$ . If statistics are computed directly on a point cloud, then each matched point would simply equal a vertex in the point cloud,  $\mathbf{y} = \mathbf{v}$ .

Each matched point,  $\mathbf{y}_i$ , can be defined to be the point on the mean shape,  $\bar{\mathbf{V}}$ , and homologous to the actual point of correspondence,  $\mathbf{T}_{\text{ssm}}(\mathbf{y}_i, \mathbf{s})$ , on the deformed shape. Every time the model shape is deformed using the current shape parameters during optimization, the deformed matched point can be estimated using the vertex weights,  $\mu^{(j)}$ , along with the current vertex positions:

$$\mathbf{T}_{\text{ssm}}(\mathbf{y}_i, \mathbf{s}) = \sum_{j=1}^3 \mu_i^{(j)} \mathbf{T}_{\text{ssm}}(\mathbf{v}_i^{(j)}, \mathbf{s}), \quad (3.9)$$

where  $\mathbf{v}_i^{(j)}$  is the  $i$ th vertex of the mesh triangle on which the  $i$ th matched point,  $\mathbf{y}_i$ , is located, and  $\mu_i^{(j)}$  are the corresponding vertex weights. Again, if statistics were computed on a point cloud, then the deformed matched point could be computed directly as  $\mathbf{T}_{\text{ssm}}(\mathbf{y}_i, \mathbf{s}) = \mathbf{T}_{\text{ssm}}(\mathbf{v}_i, \mathbf{s})$ . Other representations of model shapes can also be accommodated with appropriate assumptions.

How the vertices are deformed is dependent on the shape model being used to estimate the deformation. Using a generative PCA model, the deformed vertex positions

are computed as

$$\mathbf{T}_{\text{ssm}}(\mathbf{v}_i, \mathbf{s}) = \bar{\mathbf{v}}_i + \sum_{j=1}^{n_m} s_j \mathbf{w}_j^{(i)}, \quad (3.10)$$

where  $\mathbf{w}_j^{(i)}$  is the component of the weighted mode,  $\mathbf{w}_j = [\mathbf{w}_j^{(1)} \dots \mathbf{w}_j^{(n_v)}]^T$ , that corresponds to the  $i$ th vertex,  $\mathbf{v}_i$ . As before, the expression for the deformed vertex position can be adapted to other SSM-based or non-SSM-based shape deformations.

Taking a product over all the data points, the *total deformable match likelihood function* can be formulated as

$$f_{\text{match\_deformable}}(\mathbf{X}, \mathbf{Y}; \theta, \mathbf{s}, \bar{\mathbf{V}}, \mathbf{W}) = \left( \prod_{i=1}^{n_{\text{data}}} f_{\text{match}}(\mathbf{x}_i; \mathbf{T}_{\text{ssm}}(\mathbf{y}_i, \mathbf{s}), \theta_i) \right) \cdot f_{\text{shape}}(\mathbf{T}_{\text{ssm}}(\mathbf{Y}, \mathbf{s}); \mathbf{s}), \quad (3.11)$$

where the matrix of weighted modes,  $\mathbf{W}$ , and the mean shape,  $\bar{\mathbf{V}}$ , represent the SSM.

Unlike Eq. 3.5, Eqs. 3.11 and 3.11 define the likelihood of shape deformation based on the current set of matches,  $\mathbf{Y}$ , rather than all the vertices,  $\mathbf{V}$ , in the model shape. This formulation for the shape deformation probability has the advantage of normalizing the influence of the shape likelihood component compared to the influence of the match likelihood component of the features being registered.<sup>78</sup> If all the vertices of the model shape were used, then the influence of the shape likelihood component within the registration could be easily increased by simply increasing the sampling density of the vertices comprising the model shape. This is not a desired outcome. Further, if the data points are more sparsely sampled than the model shape, which is

often the case, then, again, the assumption of independence between the deformations of the vertices comprising the model shape becomes more valid.<sup>78</sup>

## 3.2 Correspondence phase

With the probabilistic models set up, the discussion can now move to the two phases of the registration framework: correspondence phase and registration phase. In this section, the implementation of the correspondence phase of the deformable most-likely-point paradigm is discussed. The feature matches between the data points and the current model shape are computed during the correspondence phase by maximizing the match likelihood function. This computation is represented by the *deformable most likely point correspondence operator*:

$$\mathbf{y} = \mathbf{C}_{\text{DMLP}}(\mathbf{x}, \Psi) = \underset{\mathbf{y} \in \Psi}{\operatorname{argmax}} f_{\text{match}}(\mathbf{x}, \mathbf{y}). \quad (3.12)$$

This results in the computation of a matched point on the current deformed model shape for every data point. The deformable version of the correspondence phase is similar to the correspondence phase in the corresponding rigid registration algorithms, except that at each iteration, matched points are computed on the current deformed shape rather than the initial shape. The details of the correspondence phase for these algorithms will not be repeated here, with the focus strictly on the additional details required in the deformable setting. The corresponding rigid algorithm for each



## CHAPTER 3. THE DEFORMABLE MOST-LIKELY-POINT PARADIGM

deformable algorithm we develop in the following chapters will be referenced.

The rigid algorithms use principal direction (PD) trees<sup>51</sup> to efficiently search for the most likely match, and the PD tree construction and search techniques remain the same for the deformable algorithms. The PD tree can be constructed using the model shape vertices defined by an initial set of values for the shape parameters,  $\mathbf{s}$ , which are initialized by the user. The default shape parameters,  $\mathbf{s}$ , can be set to 0, which results in simply the statistically mean shape. However, at the beginning of each correspondence phase, the positions of the vertices of the model shape are recomputed based on the current  $\mathbf{s}$ . Therefore, since the vertices of the model shape move from their prior locations at each iteration, the PD tree must also be updated at every iteration.

Since the topology of the model shape does not change with deformation, the PD-tree does not need to be reconstructed at every iteration. Instead, only the positions of the vertices of the model shape within the PD-tree and the extents of the bounding boxes that bound these vertices within each PD-tree node need to be updated. This update is performed recursively, starting at the vertices and progressing up the PD-tree, updating the extents of the bounding boxes at each node until the extents of the bounding box at the root node are updated. In order to optimize the updates, only the extents of the bounding boxes need to be updated even for oriented bounding boxes, leaving the orientations of the bounding boxes unchanged, since small deformations of the model shape should not drastically affect the bounding box orientations. In

case the deformations are large enough, then the bounding box orientations could be updated if the accumulated deformation over several iterations results in changes that are greater than some user-defined threshold.<sup>78</sup>

### 3.3 Registration phase

Once matched points are found, a transformation to align corresponding points is computed during the registration phase. In this section, the details of this registration phase of the deformable registration paradigm are discussed. During this phase, the total deformable match likelihood of Eq. 3.11 is maximized over all corresponding points with respect to both the data transformation parameters and the deformable shape parameters. This is different from rigid registration algorithms in that rigid registration algorithms would maximize some total match likelihood function only with respect to the data transformation parameters.

Maximizing the total deformation match likelihood function of Eq. 3.11 is equivalent to minimizing its negative log, reducing the minimization to the *total deformable match error function*:

$$E_{\text{match\_deformable}}(\mathbf{X}, \mathbf{Y}; \theta, \mathbf{s}) = \sum_{i=1}^{n_{\text{data}}} E_{\text{match}}(\mathbf{T}(\mathbf{x}_i); \mathbf{T}_{\text{ssm}}(\mathbf{y}_i, \mathbf{s}), \theta_i, \mathbf{s}) + \frac{1}{2} \sum_{j=1}^{n_{\text{m}}} \|s_j\|_2^2, \quad (3.13)$$

where  $E_{\text{match}}(\cdot)$  is the negative log of the corresponding match likelihood function of the rigid registration algorithm serving as the foundation for the deformable registra-

## CHAPTER 3. THE DEFORMABLE MOST-LIKELY-POINT PARADIGM

tion algorithm. Each of these rigid registration algorithms will be reviewed briefly as the corresponding deformable registration algorithms are developed in the following chapters.  $T(\mathbf{x}_i)$  represents the standard transformation applied to the data points,  $\mathbf{x}_i$ , which may be a rigid transformation or a similarity transformation, etc.  $T_{\text{ssm}}(\mathbf{y}_i, \mathbf{s})$  is the SSM-based deformable transformation applied to the matched point,  $\mathbf{y}_i$ , as defined earlier in Eq. 3.9. Finally, as explained earlier,  $\theta$  are the distribution parameters of a particular match likelihood function, which depend, again, on the rigid registration algorithm, and  $s_j \in \mathbf{s}$  are the deformable shape parameters that control how the model shape deforms.

For PCA-based SSMs, the underlying distribution that the data used to build the SSM is drawn from is assumed to be Gaussian. Therefore, when optimizing over the deformable shape parameters,  $\mathbf{s}$ , each shape parameter may be constrained to some realistic range, for instance,  $\pm 3$  standard deviations from the mean shape since this interval covers 99.7% of variations. In the following chapters, three deformable registration algorithms are developed upon these foundations. For each of these algorithms,  $\mathbf{s}$  is initialized to 0, meaning the registration starts with the mean shape. However,  $\mathbf{s}$  may be initialized differently.

### 3.4 Concluding remarks

In this chapter, a general approach for incorporating an SSM-based deformable registration component within any probabilistic registration algorithm is developed, as was in Billings.<sup>78</sup> Implementation details for three different algorithms are covered in the following three chapters of this dissertation. It is possible to incorporate non-SSM-based deformation models into this framework as well. The general approach remains the same. What changes is the method for assuming a likelihood on the shape being deformed based on some deformation parameters. Once this likelihood is defined, it can simply be plugged into the total deformable match likelihood function of Eq. 3.11.<sup>77</sup>

Further, it is possible to incorporate deformable models into both the data points as well as model shapes.<sup>78</sup> Such a formulation would be useful, for instance, if the deformations in the two feature sets follow different statistical distributions that could be modeled using two independent SSMs, or if the deformations could be modeled in a different way, not limited to SSMs. If it possible to also formulate this paradigm as an expectation maximization (EM) problem. The current formulation would translate to a hard EM problem, where an SSM is already built and being utilized to align new objects with the SSM via deformable registration. This formulation could also be modified and extended into a soft EM problem, where an SSM is not necessarily given, but the registration framework optimizes over both aligning a set of shapes and also building or improving SSMs using the aligned shapes' correspondences by

minimizing the error produced by the SSM in estimating correspondences.

## 3.5 Contributions

The contributions of this chapter include:

1. The improvement and implementation of the *deformable most-likely-point paradigm*, a general probabilistic paradigm for incorporating deformable shape transformations within a probabilistic registration framework that was first introduced conceptually by Billings.<sup>78</sup> This framework enables the development of deformable registration algorithms for registering sample points to a deformable model shape that is characterized by an SSM, where the shape deformations computed by the registration are driven by the modes of the SSM<sup>77,78</sup>
2. An extension to the software architecture developed by Billings<sup>78</sup> to incorporate deformable probabilistic registration algorithms
3. A user friendly command line interface to perform registrations with different datasets using several algorithms including but not limited to ICP, directional ICP, the deformable registration algorithms presented in this dissertation, and their corresponding rigid counterparts.

## 3.6 Published work

Material from this chapter appeared in the following publication:

1. A. Sinha, S. D. Billings, A. Reiter, X. Liu, M. Ishii, G. D. Hager, R. H. Taylor, “The deformable most-likely-point paradigm,” *submitted to Medical Image Analysis* (2018)

## Chapter 4

# Deformable iterative most likely point (D-IMLP) algorithm

This chapter presents the deformable extension of the iterative most likely point (IMLP) algorithm, which is an algorithm that can register positional data characterized by unconstrained uncertainty, that is, uncertainty that could be isotropic or anisotropic.<sup>51</sup> The deformable algorithm, called the deformable most likely point (D-IMLP) algorithm, is built upon the paradigm explained in the previous chapter, and can deformably register positional shape data characterized by unconstrained uncertainty.

Allowing the noise model to be anisotropic is motivated by anisotropic measurement uncertainties, which are common in several real world applications, especially in medical applications. For example, intra-slice resolution of CT images is often lower

## CHAPTER 4. D-IMLP ALGORITHM

than inter-slice spacing, which cause anisotropic position uncertainty in models segmented from CT images. Similarly, points reconstruction from 2D images, like frames from endoscopic video, will produce higher uncertainty in the depth direction because depth is harder to estimate. This is also true for other non-medical stereo-vision based reconstructions. Other applications outside the medical field include points obtained from range imaging, which are also characterized by anisotropic measurement error.

Much research has been conducted to investigate probabilistic registration methods to improve upon the basic ICP algorithm, which is not built to handle noise in measurements. Several of these registration algorithms compute rigid or similarity transformations. Some of the deformable registration algorithms are reviewed in the previous chapter. Here, IMLP will be briefly reviewed, and its deformable extension, D-IMLP, will then be developed.

### 4.1 Probabilistic model

As a reminder, the probabilistic model of IMLP incorporates a generalized Gaussian noise model that is able to account for anisotropic noise in both the data points and the model shape.<sup>51</sup> Assuming the errors in the measurements of these points to be independent, zero-mean, multivariate Gaussian distributed with unconstrained covariance, the match likelihood function for each data point,  $\mathbf{x}$ , transformed by a



## CHAPTER 4. D-IMLP ALGORITHM

current *rigid* registration estimate,  $[\mathbf{R}, \mathbf{t}]$ , is defined as

$$f_{\text{match}}(\mathbf{x}; \mathbf{y}, \Sigma_{\mathbf{x}}, \Sigma_{\mathbf{y}}, \mathbf{R}, \mathbf{t}) = \frac{1}{\sqrt{(2\pi)^3 |\mathbf{R}\Sigma_{\mathbf{x}}\mathbf{R}^T + \Sigma_{\mathbf{y}}|}} \cdot e^{-\frac{1}{2}(\mathbf{y}-\mathbf{R}\mathbf{x}-\mathbf{t})^T(\mathbf{R}\Sigma_{\mathbf{x}}\mathbf{R}^T+\Sigma_{\mathbf{y}})^{-1}(\mathbf{y}-\mathbf{R}\mathbf{x}-\mathbf{t})}, \quad (4.1)$$

where  $\mathbf{y}$  is the point on the model shape,  $\Psi$ , assumed to be in correspondence with data point,  $\mathbf{x} \in \mathbf{X}$ , and  $\Sigma_{\mathbf{x}}$  and  $\Sigma_{\mathbf{y}}$  are measurement error covariances for  $\mathbf{x}$  and  $\mathbf{y}$ , respectively.<sup>51</sup> This is the match likelihood function that is maximized during the correspondence phase of the IMLP algorithm in order to find the matched points,  $\mathbf{y}$ . The same likelihood function is maximized during the correspondence phase of the D-IMLP algorithm. The only difference in the correspondence phase of D-IMLP is that the matched points are found on the current deformed shape.

Similarly, the match likelihood function for each  $\mathbf{x}$  transformed by a *similarity* registration estimate,  $[a, \mathbf{R}, \mathbf{t}]$ , is defined as

$$f_{\text{match}}(\mathbf{x}; \mathbf{y}, \Sigma_{\mathbf{x}}, \Sigma_{\mathbf{y}}, a, \mathbf{R}, \mathbf{t}) = \frac{1}{\sqrt{(2\pi)^3 |\mathbf{R}\Sigma_{\mathbf{x}}\mathbf{R}^T + \Sigma_{\mathbf{y}}|}} \cdot e^{-\frac{1}{2}(\mathbf{y}-a\mathbf{R}\mathbf{x}-\mathbf{t})^T(\mathbf{R}\Sigma_{\mathbf{x}}\mathbf{R}^T+\Sigma_{\mathbf{y}})^{-1}(\mathbf{y}-a\mathbf{R}\mathbf{x}-\mathbf{t})}, \quad (4.2)$$

where  $a$  is the scale variable. Since the two registration problems are similar, the focus of the derivations will remain on derivations from Eq. 4.1, with technical differences between the two pointed out wherever needed. Maximizing the likelihood of Eq. 4.1 is equivalent to minimizing its negative log likelihood, resulting in the following *match*

## CHAPTER 4. D-IMLP ALGORITHM

*error function:*<sup>51</sup>

$$E_{\text{IMLP}}(\mathbf{x}, \mathbf{y}, \Sigma_{\mathbf{x}}, \Sigma_{\mathbf{y}}, \mathbf{R}, \mathbf{t}) = \log |\mathbf{R}\Sigma_{\mathbf{x}}\mathbf{R}^{\text{T}} + \Sigma_{\mathbf{y}}| + (\mathbf{y} - \mathbf{R}\mathbf{x} - \mathbf{t})^{\text{T}}(\mathbf{R}\Sigma_{\mathbf{x}}\mathbf{R}^{\text{T}} + \Sigma_{\mathbf{y}})^{-1}(\mathbf{y} - \mathbf{R}\mathbf{x} - \mathbf{t}). \quad (4.3)$$

The registration phase of this algorithm is where the transformation that maximizes the total match likelihood function is solved for.<sup>51</sup> This can also be achieved by minimizing the *total match error function* with respect to the transformation parameters:<sup>51</sup>

$$\begin{aligned} \mathbf{T} = \underset{[\mathbf{R}, \mathbf{t}]}{\operatorname{argmin}} \sum_{i=1}^{n_{\text{data}}} & \left( \log |\mathbf{R}\Sigma_{\mathbf{x}_i}\mathbf{R}^{\text{T}} + \Sigma_{\mathbf{y}_i}| \right. \\ & \left. + (\mathbf{y}_i - \mathbf{R}\mathbf{x}_i - \mathbf{t})^{\text{T}}(\mathbf{R}\Sigma_{\mathbf{x}_i}\mathbf{R}^{\text{T}} + \Sigma_{\mathbf{y}_i})^{-1}(\mathbf{y}_i - \mathbf{R}\mathbf{x}_i - \mathbf{t}) \right), \end{aligned} \quad (4.4)$$

which can be simplified by dropping the log term to the *registration cost function:*<sup>51</sup>

$$\mathbf{T} = \underset{[\mathbf{R}, \mathbf{t}]}{\operatorname{argmin}} \sum_{i=1}^{n_{\text{data}}} (\mathbf{y}_i - \mathbf{R}\mathbf{x}_i - \mathbf{t})^{\text{T}}(\mathbf{R}\Sigma_{\mathbf{x}_i}\mathbf{R}^{\text{T}} + \Sigma_{\mathbf{y}_i})^{-1}(\mathbf{y}_i - \mathbf{R}\mathbf{x}_i - \mathbf{t}). \quad (4.5)$$

Substituting  $f_{\text{match}}$  from Eq. 4.1 into the total deformable match likelihood function of Eq. 3.11 enables the derivation of the *deformable registration cost function* for

the D-IMLP algorithm:

$$\mathbf{T} = \underset{[\mathbf{R}, \mathbf{t}], \mathbf{s}}{\operatorname{argmin}} \left( \frac{1}{2} \sum_{i=1}^{n_{\text{data}}} \left( (\mathbf{T}_{\text{ssm}}(\mathbf{y}_i, \mathbf{s}) - \mathbf{R}\mathbf{x}_i - \mathbf{t})^{\mathbf{T}} (\mathbf{R}\boldsymbol{\Sigma}_{\mathbf{x}_i}\mathbf{R}^{\mathbf{T}})^{-1} (\mathbf{T}_{\text{ssm}}(\mathbf{y}_i, \mathbf{s}) - \mathbf{R}\mathbf{x}_i - \mathbf{t}) \right) + \frac{1}{2} \sum_{j=1}^{n_{\text{m}}} \|s_j\|_2^2 \right), \quad (4.6)$$

where a factor of  $\frac{1}{2}$ , which was excluded from  $E_{\text{IMLP}}$  in Eq. 4.3 for simplification, is added back, and the model shape covariances,  $\boldsymbol{\Sigma}_{\mathbf{y}_i}$ , are assumed to be zero since the focus here is on the derivatives introduced by the shape deformations during optimization.

## 4.2 Algorithm overview

In this section, a high level overview with pseudocode explaining the registration pipeline is described. Several details that were developed along with the IMLP algorithm will be referenced and not repeated, maintaining the focus on differences due to the additional deformable aspect of the registration. Algorithm 4.1 provides a summary of the D-IMLP algorithm in the same style as that of IMLP in Billings et al.,<sup>51</sup> and will be referenced throughout this section. Underlined variables in Alg. 4.1 indicate optional variables that would be needed when solving additionally for scale.

The inputs to the algorithm are straightforward and include data points,  $\mathbf{X}$ , and



---

**Algorithm 4.1: D-IMLP** (*continued...*)

---

- 11 Update the transformation and shape to align the point cloud and the corresponding points on the shape (Eq. 4.6 or 4.14):
- $$[\underline{a}, \mathbf{R}, \mathbf{t}], \mathbf{s} \leftarrow \underset{[\underline{a}, \mathbf{R}, \mathbf{t}], \mathbf{s}}{\operatorname{argmin}} \left( \frac{1}{2} \sum_{i=1}^{n_{\text{data}}} \left( (\mathbf{T}_{\text{ssm}}(\mathbf{y}_i, \mathbf{s}) - \underline{a}\mathbf{R}\mathbf{x}_i - \mathbf{t})^{\mathbf{T}} (\mathbf{R}\Sigma_{\mathbf{x}_i}\mathbf{R}^{\mathbf{T}})^{-1} \right. \right. \\ \left. \left. (\mathbf{T}_{\text{ssm}}(\mathbf{y}_i, \mathbf{s}) - \underline{a}\mathbf{R}\mathbf{x}_i - \mathbf{t}) \right) + \frac{1}{2} \sum_{j=1}^{n_{\text{m}}} \|\mathbf{s}_j\|_2^2 \right)$$
- 12 Based on computed  $\mathbf{s}$ , update the vertices of the model shape (Eq. 3.10):
- $$\Psi_{\text{iter}} \leftarrow \mathbf{T}_{\text{ssm}}(\mathbf{v}_i, \mathbf{s})$$
- 13 Update extents of PD-tree bounding boxes based on  $\Psi_{\text{iter}}$  (Sec. 3.2)
- 14  $\text{iter}++$
- end
- 15 Detect registration failure using a chi-square test (Eq. 4.11):

Registration is unsuccessful if

$$E_p = \sum_{i=1}^{n_{\text{data}}} E_{\text{SqrMahalDist}}(\mathbf{x}_i, \mathbf{y}_i, \Sigma_{\mathbf{x}_i}, \Sigma_{\mathbf{y}_i} + \sigma_{\text{match}}^2 \mathbf{I}, \underline{a}, \mathbf{R}, \mathbf{t}) > \chi_{\text{thresh\_final}}^2$$


---

model shape,  $\Psi$ . For this implementation,  $\Psi$  is the statistically mean shape with  $\mathbf{s}$  initialized to 0, but can be changed to a different initial shape with a different initial  $\mathbf{s}$ . The SSM associated with the model shape is represented by the vertices of the mean shape,  $\bar{\mathbf{V}} \in \Psi$ , and the corresponding weighted modes of variation,  $\mathbf{w}$ , and is used to update the model shape at each iteration as  $\mathbf{s}$  is updated (Eqs. 3.9, 3.10). The *measurement-error covariances* associated with both the data points and the initial shape are represented by  $\Sigma_{\mathbf{X}}$  and  $\Sigma_{\Psi}$ .  $\Sigma_{\mathbf{Y}} = \{\Sigma_{\mathbf{y}_i}\}$  associated with matched points,  $\mathbf{Y} = \{\mathbf{y}_i\}$ , are drawn from this larger set of covariances,  $\Sigma_{\Psi}$ , which is defined over all the vertices in the model shape, rather than only at the matched points.<sup>51</sup>

## CHAPTER 4. D-IMLP ALGORITHM

Further, it would be impossible to specify  $\Sigma_Y$  as input since the matched points are unknown until the correspondence phase in every iteration. By default,  $\Sigma_X$  and  $\Sigma_\Psi$  are assumed to be generated from an isotropic Gaussian distribution with standard deviation of  $1 \times 1 \text{ mm}^2$  in plane and 1 mm out of plane. However, this can be modified by the user depending on the noise model that is appropriate for the data.

Additionally, *surface-model covariances*,  $\Sigma_{SX}$  and  $\Sigma_{S\Psi}$ , are also specified in order to obtain the complete noise model for each point by modeling the locally-linear surface regions surrounding each point.<sup>51</sup> Introduced as the basis for the generalized ICP (GICP) algorithm,<sup>102</sup> these surface-model covariances are motivated by the aim to increase the variances in the directions parallel to the surface so that match errors distribute along the surface rather than perpendicular to it.<sup>51</sup> This helps achieve closer alignment of the underlying surfaces presented by the point cloud.<sup>51</sup> This concept has since been incorporated in several algorithms, including anisotropic ICP<sup>103</sup> and IMLP.<sup>51</sup> IMLP keeps the measurement-error covariances separate from the surface-model covariances so that the surface-model covariances can be excluded from the outlier detected phase, which improved the algorithm's outlier detection.<sup>51</sup>

Finally, an initial transformation is specified with a guess for an initial rotation, translation, and, optionally, scale which will be applied to the data points, and an initial set of shape parameters to define the initial shape, which is set to 0 or the mean shape, as mentioned earlier. The remaining input parameters will be discussed briefly as they are encountered in equations seen in the algorithm outline (Alg. 4.1). The

## CHAPTER 4. D-IMLP ALGORITHM

discussions will remain brief since many of these terms also appear in Billings et al.,<sup>51</sup> and the reader is directed there for a more thorough explanation. The output of the algorithm is a final transformation that aligns the data points to the final deformed shape, defined by a final set of shape parameters.

The convergence criteria used to terminate this algorithm are dependent on several factors. These factors can be changed by the user, but have some default values. In order for the algorithm to converge, the difference between the values attained by the rotation, translation, scale, *and* shape parameters in the previous iteration and the current iteration must be smaller than 0.01 twice in a row. This threshold as well as the number of times the threshold must be met in a row can be modified by the user. Whether or not scale is being optimized over does not affect the termination conditions since if scale is not being optimized over then the value of scale does not change between iterations. Therefore, scale always satisfies the termination condition, and convergence becomes solely dependent on the remaining parameters, as desired. Further, a cycling detection is added as an additional termination condition.<sup>51</sup> Cycling occurs when the minimal value of the cost function being minimized in the registration phase increases twice within four iterations and if the cost following the second increase is within a small tolerance of the first increase.<sup>51</sup> This is detected by monitoring the value of the cost function. If detected, the algorithm terminates and returns the registration corresponding to the last iteration where the cost function decreased. This enforces computational efficiency since a cycling condition would

## CHAPTER 4. D-IMLP ALGORITHM

otherwise cause termination at the maximum iteration count, which is set to 100<sup>51</sup> but can also be modified by the user. Therefore, if none of these conditions are met in 100 iterations, then the algorithm is forced to terminate and return the registration at the last iteration.

Until convergence is achieved, every iteration computes the correspondences between the data points and the current model shape. Once correspondences are found, the *match-uncertainty term*,  $\sigma_{\text{match}}^2$ , is updated to attempt to account for uncertainty in the matching process.<sup>51</sup> This is achieved by adding isotropic variance to the noise models with a magnitude equal to the estimated amount of misalignment between the correspondences.<sup>51</sup> The misalignment is computed as the average square residual distance over all inlying corresponding points:

$$\sigma_{\text{match}}^2 = \frac{1}{n_{\text{inlier}}} \sum_{i \in \text{inliers}} \|y_i - \underline{a}\mathbf{R}x_i - \mathbf{t}\|_2^2, \quad (4.7)$$

where  $n_{\text{inlier}}$  denotes the number of inliers in the current set of matches. A more detailed analysis of this model for estimating match uncertainty is explored in Sharp et al.<sup>37</sup> Since the match-uncertainty term is isotropic, it has the same effect on the outcome regardless of whether it is added to the data points or the model shape.<sup>51</sup> However, for computational efficiency, the match-uncertainty term is added to the covariances of the data points in the correspondence phase in Step 6 of Alg. 4.1.<sup>51</sup> A fully isotropic noise model is used to initialize correspondences in Step 5, since



## CHAPTER 4. D-IMLP ALGORITHM

computing  $\sigma_{\text{match}}^2$  requires a set of correspondences. For the registration phase, the match-uncertainty term is added to the covariances of the matched points on the model shape in Step 10 since this term intuitively affects the choice of correspondences.<sup>51</sup>

The match-uncertainty term also plays an important role in the chi-square outlier detection test in Steps 8 and 9 by enabling the algorithm to account for large initial misalignments in the noise model, and, therefore, avoid flagging several matches as outliers based on the measurement-error covariances alone.<sup>51</sup> However, in case shapes with partial overlap are being registered, the average square match distance could remain large even when the correct alignment is achieved.<sup>51</sup> The match-uncertainty term is kept from growing too large by defining a *match-uncertainty maximum threshold*,  $\sigma_{\text{max}}^2$ . By default, the maximum threshold is disabled by setting  $\sigma_{\text{max}}^2 = \infty$ .<sup>51</sup>

The chi-square test is used to identify outliers under the assumption of correspondences and generalized Gaussian noise, so that the square Mahalanobis distance between the matched points in 3D space can be assumed to be distributed as the sum of squares of three independent Gaussian distributions, each representing a distribution along a different eigen-vector of the noise covariance matrix.<sup>51</sup> Under these assumptions, the square Mahalanobis match distance has a chi-square distribution with 3 degrees of freedom (DOF), allowing outliers to be detected by comparing the square

## CHAPTER 4. D-IMLP ALGORITHM

Mahalanobis distance for each corresponding pair of points

$$E_{\text{SqrMahalDist}}(\mathbf{x}, \mathbf{y}, \Sigma_x, \Sigma_y, \underline{a}, \mathbf{R}, \mathbf{t}) = (\mathbf{y} - \underline{a}\mathbf{R}\mathbf{x}_i - \mathbf{t})^T (\mathbf{R}\Sigma_x\mathbf{R}^T + \Sigma_y)^{-1} (\mathbf{y} - \underline{a}\mathbf{R}\mathbf{x}_i - \mathbf{t}) \quad (4.8)$$

to the value of the inverse cumulative density function (CDF) of a chi-square distribution with 3 DOF evaluated at some probability,  $p$ ,<sup>51</sup> denoted by  $\text{chi2inv}(p, 3)$ . As a reminder, here  $\mathbf{y}$  denotes a point on the current deformed shape matched to a data point,  $\mathbf{x}$ . If the square Mahalanobis distance for a correspondence exceeds the chi-square inverse CDF value,  $\chi_{\text{thresh}}^2$ ,

$$E_{\text{SqrMahalDist}}(\mathbf{x}, \mathbf{y}, \Sigma_x, \Sigma_y, \underline{a}, \mathbf{R}, \mathbf{t}) > \text{chi2inv}(p, 3) = \chi_{\text{thresh}}^2, \quad (4.9)$$

then that matched point pair  $(\mathbf{x}, \mathbf{y})$ , with corresponding noise covariances,  $\Sigma_x$  and  $\Sigma_y$ , respectively, is considered an outlier.<sup>51</sup> By default,  $\chi_{\text{thresh}}^2$  is set to 7.81, which corresponds to a chi-square inverse CDF probability of  $p = 0.95$ .<sup>51</sup> However, this value can be modified by the user to accommodate different percentages of outliers. A few different values of  $\chi_{\text{thresh}}^2$  depending on different  $p$  values are specified in Table 4.1. Outlier detection can be effectively disabled by setting  $\chi_{\text{thresh}}^2$  to a very large value.<sup>51</sup>

In order to reduce the influence of outliers on the computed registration, a set of *outlier noise-model terms*,  $\{\varphi_i\}$ , are used to further add isotropic variance into the noise of the matches that are identified as outliers.<sup>51</sup> This reduces the influence of outliers in the registration phase (Step 11).  $\{\varphi_i\}$  are set by using the following rule:

$$\varphi_i = \begin{cases} \varphi_{\text{exp}} \|\mathbf{y}_i - \underline{a}\mathbf{R}\mathbf{x}_i - \mathbf{t}\|_2^2 & \text{if } (\mathbf{x}_i, \mathbf{y}_i) \text{ is an outlier,} \\ 0 & \text{otherwise.} \end{cases} \quad (4.10)$$

The default value for the *variance expansion factor*,  $\varphi_{\text{exp}}$  is set to 9, which pulls the outlier match errors within approximately 1/3 standard deviation relative to their noise models.<sup>51</sup> In order to give more or less weight to the outliers, this value can be decreased or increased, respectively, by the user. Alternatively, the registration in Step 11 may be computed using only matches identified as inliers to completely remove the influence from outliers.<sup>51</sup>

Once the algorithm has converged or terminated and a registration computed, a chi-square test similar to that in Eq. 4.9 is used to classify the registration as successful or unsuccessful. The two tests differ in that for failure detection, the test is performed

**Table 4.1:** Different  $\chi_{\text{thresh}}^2$  values based on different values of  $p$  for 3 DOF.

$p$	$\chi_{\text{thresh}}^2$
0.95	7.81
0.975	9.35
0.99	11.34
0.9973	14.16

## CHAPTER 4. D-IMLP ALGORITHM

over the sum of square Mahalanobis distances computed over all corresponding pairs,  $(\mathbf{x}_i, \mathbf{y}_i)$ . That is, a registration is rejected if this sum becomes greater than the value of a chi-square inverse CDF with  $3n_{\text{data}}$  DOF at some probability,  $p$ :

$$E_p = \sum_{i=1}^{n_{\text{data}}} E_{\text{SqMahalDist}}(\mathbf{x}_i, \mathbf{y}_i, \Sigma_{\mathbf{x}_i}, \Sigma_{\mathbf{y}_i}, \underline{a}, \mathbf{R}, \mathbf{t}) > \text{chi2inv}(p, 3n_{\text{data}}) = \chi_{\text{thresh\_final}}^2, \quad (4.11)$$

where  $p$  is again set to 0.95. This test is used because the square Mahalanobis distance normalizes each match residual by its variance along each dimension, therefore accounting for the anisotropy of the noise model used by D-IMLP.<sup>51</sup> This means that the sum is distributed as a chi-square distribution with  $3n_{\text{data}}$  DOF.<sup>51</sup>

### 4.3 Correspondence phase

This section briefly describes the correspondence phase of the D-IMLP algorithm, which is very similar to the correspondences phase of the IMLP algorithm. Therefore, for most of the details, the reader is referred to Billings et al.,<sup>51</sup> while this section will solely focus on the differences introduced by the deformable algorithm. As mentioned before, the correspondence phase computes the most likely matches between the data points and the current model shape at each iteration by minimizing the match error

## CHAPTER 4. D-IMLP ALGORITHM

function of Eq. 4.3, repeated here for ease of reference:

$$E_{\text{IMLP}}(\mathbf{x}, \mathbf{y}, \Sigma_{\mathbf{x}}, \Sigma_{\mathbf{y}}, \mathbf{R}, \mathbf{t}) = \log |\mathbf{R}\Sigma_{\mathbf{x}}\mathbf{R}^T + \Sigma_{\mathbf{y}}| + (\mathbf{y} - \mathbf{R}\mathbf{x} - \mathbf{t})^T (\mathbf{R}\Sigma_{\mathbf{x}}\mathbf{R}^T + \Sigma_{\mathbf{y}})^{-1} (\mathbf{y} - \mathbf{R}\mathbf{x} - \mathbf{t}). \quad (4.12)$$

As is clear from the term  $E_{\text{IMLP}}$ , this expression is the same as that minimized to compute correspondences in the IMLP algorithm.<sup>51</sup> The main difference here is that the matched points,  $\mathbf{y}$ , are computed on a shape that is changing at each iteration. The PD-tree search for the most likely correspondence on the model shape is identical to that in the IMLP algorithm.<sup>51</sup> However, since the model shape deforms according to the the shape parameters,  $\mathbf{s}$ , at every iteration, the algorithm must ensure that the correspondences are computed on the correct shape. This is achieved by updating the position of the vertices of the deformed shape in the PD-tree after the model shape is updated and before correspondences are found at each iteration. Additionally, the bounds of each PD-tree node are also updated to make sure each of the new vertex positions are still accommodated for by the PD-tree. This is a recursive process because in addition to including the new vertex positions within the leaf node bounds, the bounds of each parent node must also be updated to accommodate the new bounds of its child nodes. The process is completed when the bounds of the root node bounding box are updated. For further details, including the building and traversal of the PD-tree, the reader is referred to Billings et al.<sup>51</sup>

## 4.4 Registration phase

Once matched points are found on the current shape in the correspondence phase, the deformable registration cost function for the D-IMLP algorithm (Eq. 4.6) is minimized with respect to both the data transformation parameters and the model shape parameters. This cost function is repeated here for ease of reference:

$$\mathbf{T} = \underset{[\mathbf{R}, \mathbf{t}], \mathbf{s}}{\operatorname{argmin}} \left( \frac{1}{2} \sum_{i=1}^{n_{\text{data}}} \left( (\mathbf{T}_{\text{ssm}}(\mathbf{y}_i, \mathbf{s}) - \mathbf{R}\mathbf{x}_i - \mathbf{t})^{\mathbf{T}} (\mathbf{R}\Sigma_{\mathbf{x}_i}\mathbf{R}^{\mathbf{T}})^{-1} (\mathbf{T}_{\text{ssm}}(\mathbf{y}_i, \mathbf{s}) - \mathbf{R}\mathbf{x}_i - \mathbf{t}) \right) + \frac{1}{2} \sum_{j=1}^{n_{\text{m}}} \|s_j\|_2^2 \right). \quad (4.13)$$

If, instead of computing a rigid transformation between the data points and the corresponding matched points on the model shape, a *similarity* transform is computed, then the cost function changes slightly to incorporate a scale factor,  $a$ :

$$\mathbf{T} = \underset{[a, \mathbf{R}, \mathbf{t}], \mathbf{s}}{\operatorname{argmin}} \left( \frac{1}{2} \sum_{i=1}^{n_{\text{data}}} \left( (\mathbf{T}_{\text{ssm}}(\mathbf{y}_i, \mathbf{s}) - a\mathbf{R}\mathbf{x}_i - \mathbf{t})^{\mathbf{T}} (\mathbf{R}\Sigma_{\mathbf{x}_i}\mathbf{R}^{\mathbf{T}})^{-1} (\mathbf{T}_{\text{ssm}}(\mathbf{y}_i, \mathbf{s}) - a\mathbf{R}\mathbf{x}_i - \mathbf{t}) \right) + \frac{1}{2} \sum_{j=1}^{n_{\text{m}}} \|s_j\|_2^2 \right) \quad (4.14)$$

Before this minimization is performed, barycentric coordinates of the matched points are computed in order to find the vertex weights,  $\mu^{(j)}$ , for  $j = 1, 2, 3$ , as seen in Eq. 3.9, for each matched point. These  $\mu^{(j)}$  will be used during optimization to compute the

## CHAPTER 4. D-IMLP ALGORITHM

deformed matched point,  $T_{\text{ssm}}(\mathbf{y}_i, \mathbf{s})$ , as the shape is recomputed based on different values of  $\mathbf{s}$ .

Both these objective functions can be optimized by computing the gradients with respect to the optimization parameters, and applying a nonlinear quasi-Newton based optimizer. For the implementation described here, the box constrained BFGS quasi-Newton solver available in the dlib open-source C++ software library<sup>80</sup> was used. In order to apply a quasi-Newton solver to minimize either of these equations, the variables being optimized need to be reparametrized to enforce the algebraic constraints of the rotation matrix, that is,  $\mathbf{R}^T \mathbf{R} = \mathbf{I}$  and  $\det(\mathbf{R}) = 1$ .<sup>51</sup> This is accomplished by using Rodrigues' parametrization, which represents a rotation as a 3-vector,  $\mathbf{r} = [r_x, r_y, r_z]$ , whose direction and magnitude signify the axis and angular extent of rotation, respectively.

Additionally, the transformation  $T(\mathbf{x}_i)$  is re-expressed in the reference frame of  $\mathbf{Y}$  as  $T(\mathbf{y}_i)$  in order to keep all transformation in the same space. The deformable registration cost function of Eq. 4.6 can then be re-written as

$$T = \underset{[\mathbf{r}, \mathbf{t}, \mathbf{s}]}{\operatorname{argmin}} \left( \sum_{i=1}^{n_{\text{data}}} C_{\text{match}i} + C_{\text{shape}} \right), \quad (4.15)$$

## CHAPTER 4. D-IMLP ALGORITHM

where

$$\begin{aligned}
 C_{\text{match}i} &= \mathbf{z}_i^T \Sigma_{\mathbf{x}_i}^{-1} \mathbf{z}_i \quad \text{and} \quad C_{\text{shape}} = \mathbf{s}^T \mathbf{s}, \\
 \mathbf{z}_i &= \mathbf{R}(\mathbf{r})^T (\mathbf{T}_{\text{ssm}}(\mathbf{y}_i, \mathbf{s}) - \mathbf{R}(\mathbf{r})\mathbf{x}_i - \mathbf{t}) \\
 &= \mathbf{R}(\mathbf{r})^T (\mathbf{T}_{\text{ssm}}(\mathbf{y}_i, \mathbf{s}) - \mathbf{t}) - \mathbf{x}_i.
 \end{aligned} \tag{4.16}$$

$\mathbf{R}(\mathbf{r})$  is the  $3 \times 3$  rotation matrix corresponding to the Rodrigues' vector,  $\mathbf{r}$ , and is defined as

$$\mathbf{R}(\mathbf{r}) = \mathbf{I} + \sin(\theta) \text{skew}(\alpha) + (1 - \cos(\theta)) \text{skew}(\alpha)^2,$$

where  $\theta = \|\mathbf{r}\|_2$  is the magnitude of  $\mathbf{r}$ , representing the angle of rotation,  $\alpha = \frac{\mathbf{r}}{\|\mathbf{r}\|}$  is the unit vector in the direction of  $\mathbf{r}$ , representing the axis of rotation, and  $\text{skew}(\alpha)$  is the skew symmetric matrix formed using the elements of  $\alpha$ .

Similarly, Eq. 4.14 can be re-written as

$$\mathbf{T} = \underset{[a, \mathbf{r}, \mathbf{t}], \mathbf{s}}{\text{argmin}} \left( \sum_{i=1}^{n_{\text{data}}} C_{\text{match}i} + C_{\text{shape}} \right), \tag{4.17}$$

with a slight modification in the  $C_{\text{match}i}$  term in Eq. 4.16, so that

$$\begin{aligned}
 C_{\text{match}i} &= \mathbf{z}_i^T \Sigma_{\mathbf{x}_i}^{-1} \mathbf{z}_i \quad \text{and} \quad C_{\text{shape}} = \mathbf{s}^T \mathbf{s}, \\
 \mathbf{z}_i &= \mathbf{R}(\mathbf{r})^T (\mathbf{T}_{\text{ssm}}(\mathbf{y}_i, \mathbf{s}) - \mathbf{t}) - a\mathbf{x}_i.
 \end{aligned} \tag{4.18}$$

The gradient,  $\nabla C$ , of the deformable registration cost function of Eq. 4.15 with respect to the transformation parameters  $[\mathbf{r}, \mathbf{t}]$  and the deformable shape parameters,



## CHAPTER 4. D-IMLP ALGORITHM

$\mathbf{s}$ , is discussed next.  $\nabla \mathbf{C}$  is a stacked vector with the data transformation parameters located on top of the deformable shape parameters. The notation  $\mathbf{J}_{a,b}$  is used to express the Jacobian of an expression,  $a$ , with respect to variable,  $b$ . With the notation established,  $\nabla \mathbf{C}$  is expressed as:

$$\nabla \mathbf{C} = \sum_{i=1}^{n_{\text{data}}} \nabla C_{\text{match}i} + \nabla C_{\text{shape}} \quad (4.19)$$

$$\nabla C_{\text{match}i} = [\mathbf{J}_{C_{\text{match}i}, \mathbf{z}_i} \mathbf{J}_{\mathbf{z}_i, \mathbf{r}} , \mathbf{J}_{C_{\text{match}i}, \mathbf{z}_i} \mathbf{J}_{\mathbf{z}_i, \mathbf{t}} , \mathbf{J}_{C_{\text{match}i}, \mathbf{z}_i} \mathbf{J}_{\mathbf{z}_i, \mathbf{s}}]^\mathbf{T}, \quad \text{where}$$

$$\begin{aligned} \mathbf{J}_{C_{\text{match}i}, \mathbf{z}_i} &= 2\mathbf{z}_i^\mathbf{T} \boldsymbol{\Sigma}_{\mathbf{x}_i}^{-1} \\ \mathbf{J}_{\mathbf{z}_i, \mathbf{r}} &= \left[ \frac{\partial \mathbf{R}(\mathbf{r})^\mathbf{T}}{\partial \mathbf{r}_x} (\mathbf{T}_{\text{ssm}}(\mathbf{y}_i, \mathbf{s}) - \mathbf{t}) , \frac{\partial \mathbf{R}(\mathbf{r})^\mathbf{T}}{\partial \mathbf{r}_y} (\mathbf{T}_{\text{ssm}}(\mathbf{y}_i, \mathbf{s}) - \mathbf{t}) , \right. \\ &\quad \left. \frac{\partial \mathbf{R}(\mathbf{r})^\mathbf{T}}{\partial \mathbf{r}_z} (\mathbf{T}_{\text{ssm}}(\mathbf{y}_i, \mathbf{s}) - \mathbf{t}) \right] \\ \mathbf{J}_{\mathbf{z}_i, \mathbf{t}} &= -\mathbf{R}(r)^\mathbf{T} \end{aligned} \quad (4.20)$$

$$\mathbf{J}_{\mathbf{z}_i, \mathbf{s}} = \mathbf{J}_{\mathbf{z}_i, \mathbf{T}_{\text{ssm}}(\mathbf{y}_i, \mathbf{s})} \mathbf{J}_{\mathbf{T}_{\text{ssm}}(\mathbf{y}_i, \mathbf{s}), \mathbf{s}}$$

$$\mathbf{J}_{\mathbf{z}_i, \mathbf{T}_{\text{ssm}}(\mathbf{y}_i, \mathbf{s})} = \mathbf{R}(r)^\mathbf{T}$$

$$\mathbf{J}_{\mathbf{T}_{\text{ssm}}(\mathbf{y}_i, \mathbf{s}), \mathbf{s}} = \sum_{j=1}^3 \mu_i^{(j)} \mathbf{J}_{\mathbf{T}_{\text{ssm}}(\mathbf{v}_i^{(j)}, \mathbf{s}), \mathbf{s}}$$

$$\mathbf{J}_{\mathbf{T}_{\text{ssm}}(\mathbf{v}_i^{(j)}, \mathbf{s}), \mathbf{s}} = [\mathbf{w}_1^p \quad \mathbf{w}_2^p \quad \cdots \quad \mathbf{w}_{\mathbf{n}_m}^p]$$

and

$$\nabla C_{\text{shape}} = [0, 0, 2\mathbf{s}^T]^T \quad (4.21)$$

Here, each of  $\frac{\partial \mathbf{R}(\mathbf{r})^T}{\partial r_x}$ ,  $\frac{\partial \mathbf{R}(\mathbf{r})^T}{\partial r_y}$ , and  $\frac{\partial \mathbf{R}(\mathbf{r})^T}{\partial r_z}$  denote the  $3 \times 3$  matrix of partial derivatives of  $\mathbf{R}(\mathbf{r})$  with respect to the  $x$ ,  $y$ , and  $z$  components of  $\mathbf{r} = [r_x, r_y, r_z]^T$ , respectively. The Jacobian,  $\mathbf{J}_{\mathbf{T}_{\text{ssm}}(\mathbf{v}_i^{(j)}, \mathbf{s}), \mathbf{s}}$ , of a deformed vertex,  $\mathbf{T}_{\text{ssm}}(\mathbf{v}_i^{(j)}, \mathbf{s})$ , with respect to the shape parameters,  $\mathbf{s}$ , is formed by positioning the weighted mode component,  $\mathbf{w}_i^p$ , at the  $i$ th column of a  $3 \times \mathbf{n}_m$  matrix, where  $p$  represents the global vertex index  $\mathbf{v}_i^{(j)}$ .

The gradient,  $\nabla C$ , of the deformable cost function of Eq. 4.17 with respect to the transformation parameters  $[a, \mathbf{r}, \mathbf{t}]$  and the deformable shape parameters,  $\mathbf{s}$ , is almost the same as  $\nabla C$  defined in Eqs. 4.19, 4.20, 4.21, with an additional component in  $\nabla C_{\text{match}i}$  so that

$$\nabla C_{\text{match}i} = [\mathbf{J}_{C_{\text{match}i}, \mathbf{z}_i} \mathbf{J}_{\mathbf{z}_i, \mathbf{r}}, \mathbf{J}_{C_{\text{match}i}, \mathbf{z}_i} \mathbf{J}_{\mathbf{z}_i, \mathbf{t}}, \mathbf{J}_{C_{\text{match}i}, \mathbf{z}_i} \mathbf{J}_{\mathbf{z}_i, a}, \mathbf{J}_{C_{\text{match}i}, \mathbf{z}_i} \mathbf{J}_{\mathbf{z}_i, \mathbf{s}}]^T, \quad (4.22)$$

where the new term is simply

$$\mathbf{J}_{\mathbf{z}_i, a} = -\mathbf{x}_i. \quad (4.23)$$

The  $\nabla C_{\text{shape}}$  term simply gains an additional zero component so that

$$\nabla C_{\text{shape}} = [0, 0, 0, 2\mathbf{s}^T]^T. \quad (4.24)$$

The dimensions of  $\nabla C$  is dependent on the number of shape parameters being used to estimate the shape. The sizes of the rotation, translation and scale (when being used) components are fixed at 3, 3 and 1, respectively. So the total size of  $\nabla C$  is 6 + number of shape parameters, or 7 + number of shape parameters, when additionally optimizing over scale. Once the optimization has computed the current transformation and shape parameters, the data points are transformed by the computed  $\mathbf{R}$ ,  $\mathbf{t}$  and, optionally,  $a$ , and the model shape is deformed by the computed  $\mathbf{s}$  (Eq. 3.10).

## 4.5 Experimental results and discussion

Several different experiments were performed in order to evaluate the robustness of D-IMLP. These experiments were performed using several different datasets:

1. 42 mesh pelvis dataset<sup>104</sup>
2. 53 mesh sinus dataset<sup>91-94</sup>
3. 385 mesh human expression dataset<sup>105</sup>
4. 100 mesh human pose dataset<sup>106</sup>

When ground truth is available, registration results can be evaluated based on how well the transformation and shape parameters are recovered. Errors in rotation and translation can be evaluated by comparing the initial offset applied and the final

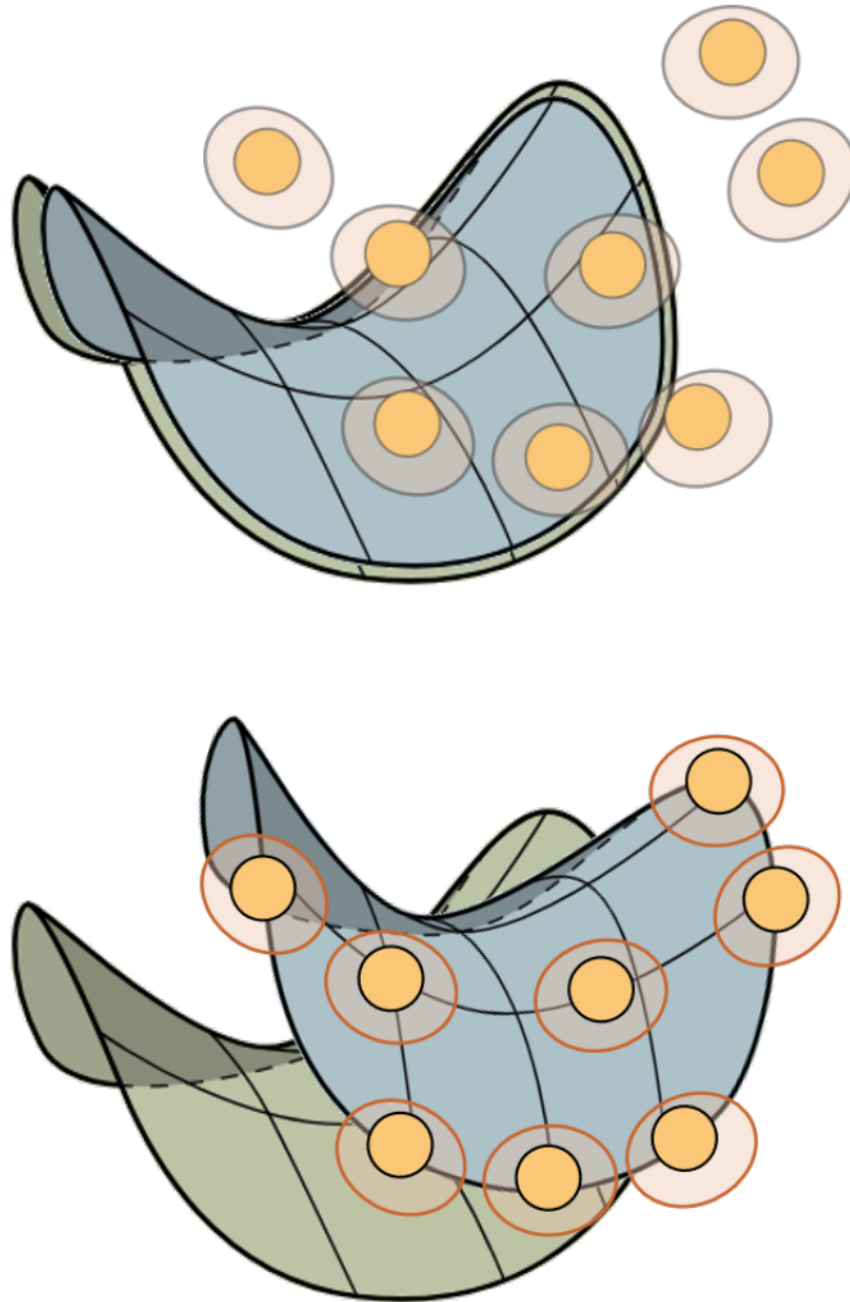


**Figure 4.1:** Registration metrics: TSE (top) measures the Hausdorff distance between the ground truth shape (green) and the shape estimated by our algorithm in shape space (blue), not taking the final transformation computed by the algorithm into consideration. TRE (bottom) measures the Hausdorff distance between the ground truth shape (green) and the estimated shape (blue) transformed to sample point space, therefore also adding the transformation computed by our algorithms into the error metric.

transformation produced. The errors in shape parameter recovery can be measured by computing the difference between the known shape parameters and those estimated by D-IMLP, or by computing the Hausdorff distance between the shape from which points were sampled and the shape recovered by D-IMLP (Fig. 4.1, top). This metric is called the total shape error (TSE). Another metric that can be used is the total registration error (TRE), which is the Hausdorff distance between the shape from which sample points are generated and the shape recovered by our algorithms transformed into sample point space (Fig. 4.1, bottom).

### 4.5.1 Sample size experiment

This experiment was performed in order to evaluate the performance of D-IMLP with increasing number of sample points. A synthetic dataset was generated using the mean shape and SSM from the pelvis dataset. The mean pelvis shape was deformed by known shape parameters sampled within  $\pm 3$  standard deviations (SD), and oriented points were sampled from the deformed shapes. Although this algorithm does not make use of orientation, oriented points were sampled so that other algorithms that use orientation (presented in the following chapters) can use the same data during experiments for fair comparison. Known transformations within realistic intervals were applied to the sampled points.

Experiments were run with 1000, 1500 and 2000 sample points. For each set of sample points, 3 sets of experiments were run with 0, 5 and 10 modes used to deform

## CHAPTER 4. D-IMLP ALGORITHM

the mean shape. In this experiment, the same number of modes were used by D-IMLP to estimate the deformed shape as were used to generate the deformed shape from which points were sampled. This was done in order to evaluate the performance of D-IMLP with different number modes without bias since it can be assumed that if fewer modes are used to estimate the shape from which points are sampled, the performance will be worse than if that same number of modes are used. However, how the performance of D-IMLP will be affected as the number of parameters to optimize over increases is not known. When 0 modes are used, D-IMLP is effectively IMLP, performing registration between the mean shape and points sampled from it. 10 registrations were performed in each set with known transformations sampled from the intervals  $[0, 15]$  mm and  $[0, 9]^\circ$  for translational and rotational offsets, respectively, and applied to points sampled from the deformed shapes. Noise was added to both the position and orientation of the sampled points, and two experiments were designed based on different noise models. In this experiment, the noise assumptions made by D-IMLP are identical to the noise in the generated data. In this chapter, the focus will be on positional noise, and details of orientation noise added will be covered in later chapters, where they are relevant.

### 4.5.1.1 Experiment 1: Isotropic position noise

For the first experiment, an isotropic noise model with SD of 1 mm in each direction in plane and 1 mm out of plane ( $1 \times 1 \times 1 \text{ mm}^3$ ) for positional noise was used.

## CHAPTER 4. D-IMLP ALGORITHM

D-IMLP produced small errors in recovering the shape and registering the sampled points to the recovered shape for the different number of samples (Fig. 4.2). It also showed an increase in successful registrations with increasing number of sample points (Fig. 4.3, Table. 4.2), where success is defined as registrations producing TRE less than 1 mm. A majority of the registrations performed were successful. Further, cues from the algorithm, like the objective function (total match error) or the residual error (Mahalanobis distance), show correlation with the TRE (Fig. 4.5, left). Therefore, empirically chosen thresholds can be used to determine which trials succeeded and which did not using the residual error. This is done retrospectively in the simulated experiments because of availability of ground truth and to learn how to associate residuals errors with measures of confidence or success in clinical or other experiments where ground truth is not available. Using empirically found thresholds such that there were no false positives, D-IMLP was able to correctly detect successful registrations with high percentages (Table. 4.2).

### 4.5.1.2 Experiment 2: Anisotropic position noise

Second, an anisotropic noise model with 1 mm SD in each direction in plane and 2 mm out of plane was used for positional noise (or,  $1 \times 1 \times 2 \text{ mm}^3$ ). Using anisotropic positional noise, D-IMLP produced higher errors than with isotropic noise due to the increased uncertainty along one of the dimensions (Fig. 4.4). Only about half the trials produced successful registrations (Table. 4.2). However, again, the objective

CHAPTER 4. D-IMLP ALGORITHM

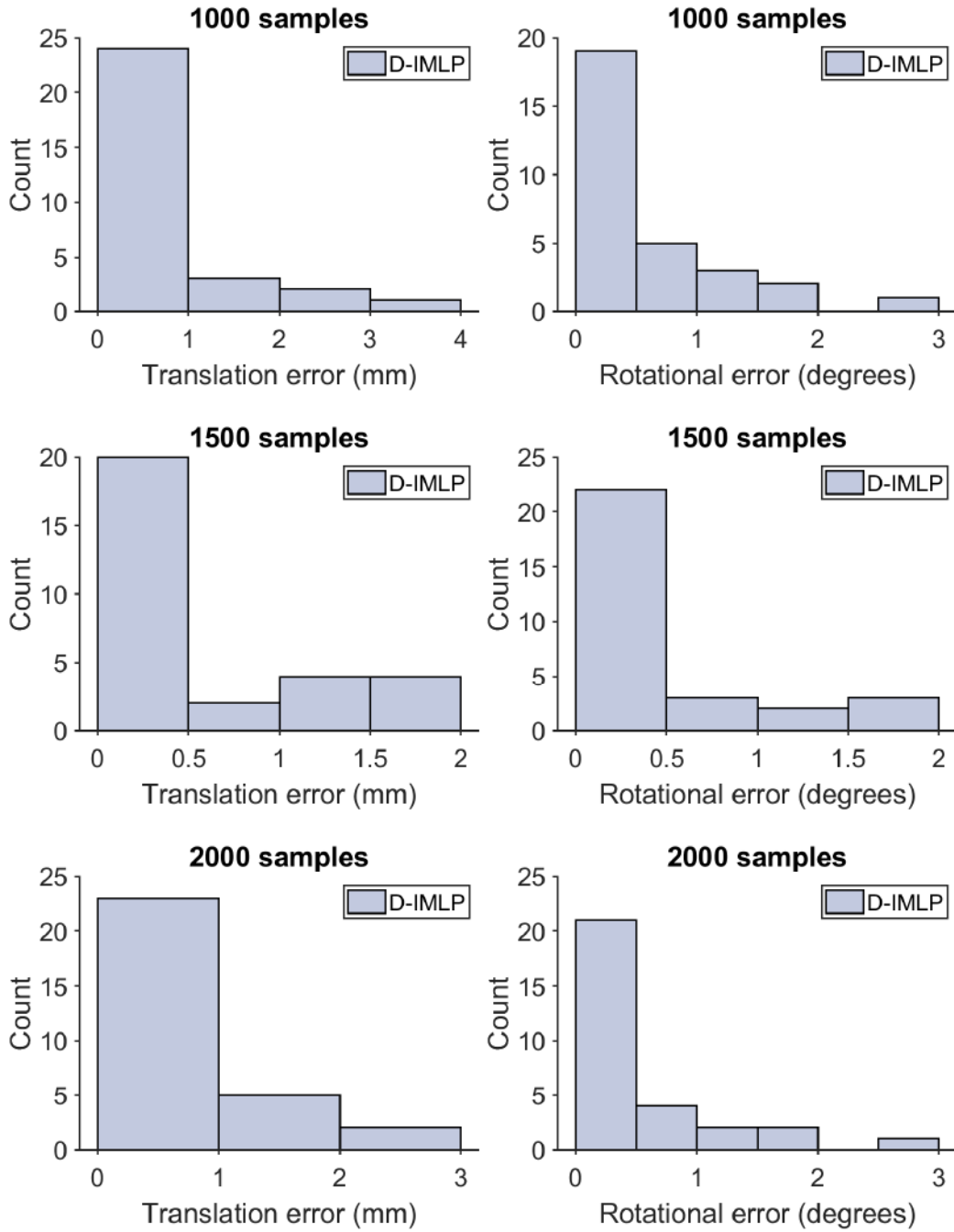


**Figure 4.2:** Sample size experiment: translation (left) and rotation (right) errors produced using, from top to bottom, 1000, 1500 and 2000 data points sampled from the pelvis model in Exp. 1 (Sec. 4.5.1.1)



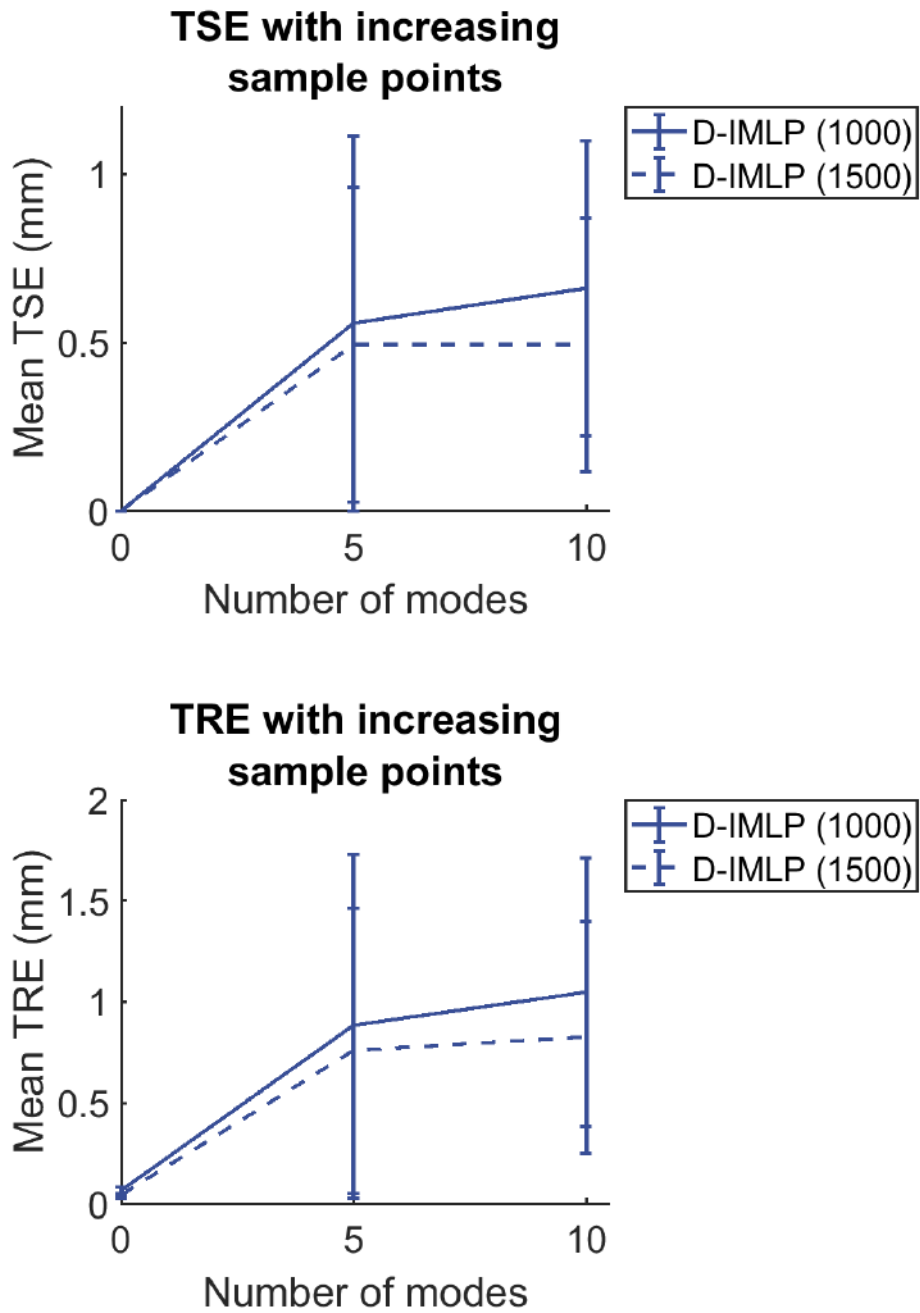


**Figure 4.3:** Sample size experiment: increasing TSE (top) and TRE (bottom) with increasing number of sample points in Exp. 1 (Sec. 4.5.1.1). Note that errors are increasing with increasing modes because for this experiment the number of modes used to estimate the shapes equals the number of modes used to simulate a new shape from which points were sampled.

**Table 4.2:** Sample size experiment: percent successful registration runs, i.e., runs producing TREs less than 1 mm and, in parentheses, percent successful runs correctly detected as successful using residual errors.

	# samples	D-IMLP (%)
Experiment 1	1000	73.33 (100.00)
	1500	76.67 (86.96)
	2000	80.00 (100.00)
Experiment 2	1000	56.67 (100.00)
	1500	46.67 (100.00)
	2000	56.67 (100.00)

function and residual error showed correlation with TRE (Fig. 4.5, right), and using empirically found thresholds on the residual errors, D-IMLP was able to automatically classify almost all successful registrations as successful (Table. 4.2).

## 4.5.2 Regularization term experiment

The cost function that is minimized to compute a registration using D-IMLP (Eq. 4.6) contains an L2 regularization term,  $\frac{1}{2} \sum_{j=1}^{n_m} \|s_j\|_2^2$ , that comes from the assumption that the shapes used to build the SSM used to drive the deformations in the registration are sampled from a Gaussian distribution (Eq. 3.5). The effect of this regularization term can be evaluated by computing registrations with and without this term. Therefore, experiments using the same data generated for Exp. 4.5.1.1 using

## CHAPTER 4. D-IMLP ALGORITHM

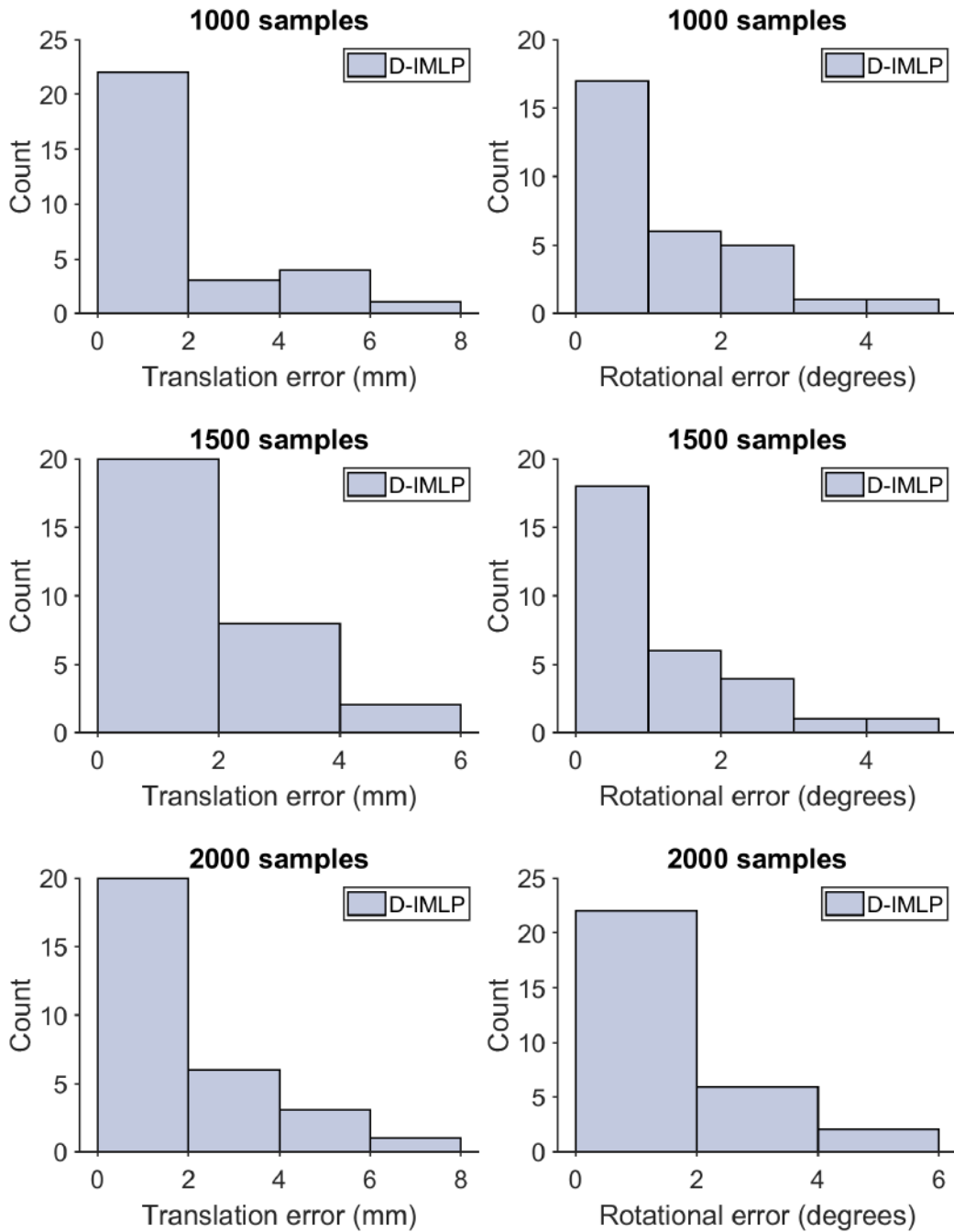


**Figure 4.4:** Sample size experiment: translation (left) and rotation (right) errors produced using, from top to bottom, 1000, 1500 and 2000 data points sampled from the pelvis model in Exp. 2 (Sec. 4.5.1.2)

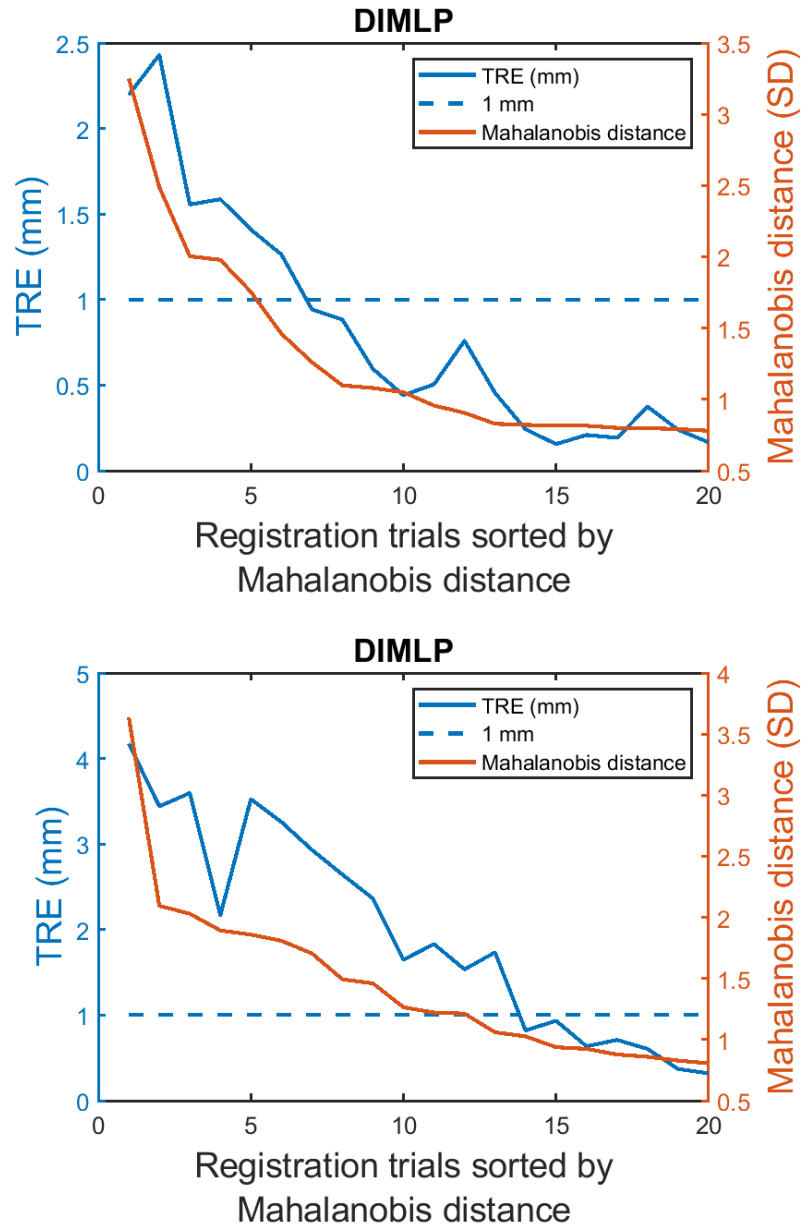


**Figure 4.5:** Sample size experiment: residual errors compared against TRE using 2000 sample points in Exp. 1 (left) and Exp. 2 (right). The two measures exhibit correlation in both experiments 1 and 2 with correlation coefficients of 0.95 and 0.88, respectively.

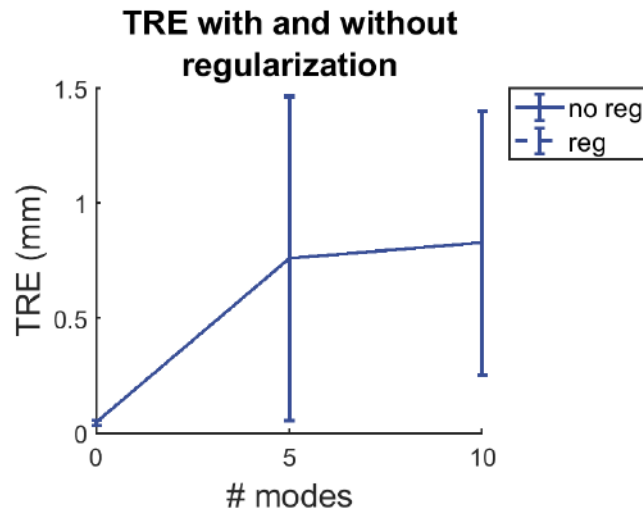


**Figure 4.6:** Regularization term experiment: registrations produced by D-IMLP in the presence of small noise were unaffected by the absence of the regularization term.

1500 sample points were repeated without the regularization term. Results showed that removing the regularization term had no effect on results produced by D-IMLP (Fig. 4.6). The noise in these data samples was small ( $1 \times 1 \times 1 \text{ mm}^3$ ) and, therefore, the algorithm did not suffer from fitting to noise in the absence of the regularization term. However, with more noise in the data, performance could deteriorate without this term.

### 4.5.3 Noise model experiment

This experiment was designed to evaluate the stability of D-IMLP with different noise models. A synthetic dataset was generated using the pelvis data in a similar way as described in Sec. 4.5.1. The differences are that experiments in this section were run with a fixed sample size of 500, and for each algorithm, 11 sets of 25 experiments each were run with increasing number of modes used to deform the mean shape in each set, starting at 0 and going up to 10 modes. Again, the same number of modes are used by D-IMLP to recover the deformed shape as were used to generate the deformed shape. Different noise models were used to add noise to both the position and orientation of the sampled points, and the same noise models were assumed by our algorithms. Again, focusing on positional noise, three experiments were designed based on how the noise models were varied.

#### 4.5.3.1 Experiment 1: Varying isotropic position noise

For the first experiment, 5 isotropic noise models with SDs of  $1 \times 1 \times 1 \text{ mm}^3$ ,  $2 \times 2 \times 2 \text{ mm}^3$ ,  $3 \times 3 \times 3 \text{ mm}^3$ ,  $4 \times 4 \times 4 \text{ mm}^3$ , and  $5 \times 5 \times 5 \text{ mm}^3$  for positional noise were used. D-IMLP showed a general trend of increasing TRE with increasing noise SD (Fig. 4.7) due to the increase in uncertainty in the sample points. The objective function and the residual errors are again found to be strongly correlated with the TRE, which can be used to distinguish between successful and unsuccessful registrations (Fig. 4.8).

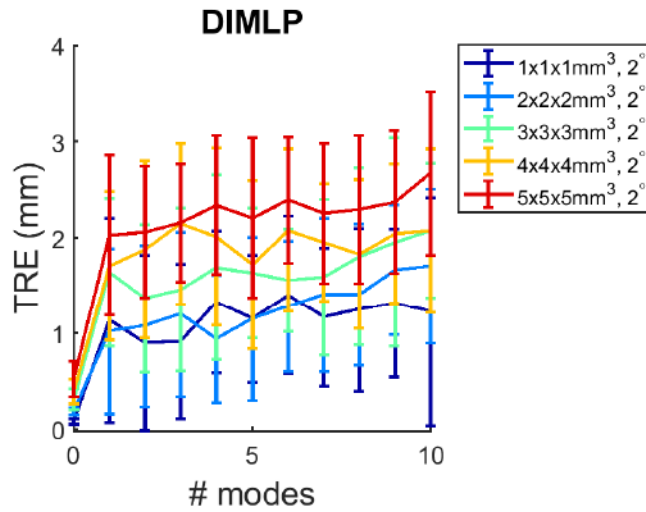


**Figure 4.7:** Noise model experiment: a general trend of increasing TRE as the uncertainty in the sample points increases. Note that errors are increasing with increasing modes because for this experiment the number of modes used to estimate the shapes equals the number of modes used to simulate a new shape from which points were sampled.

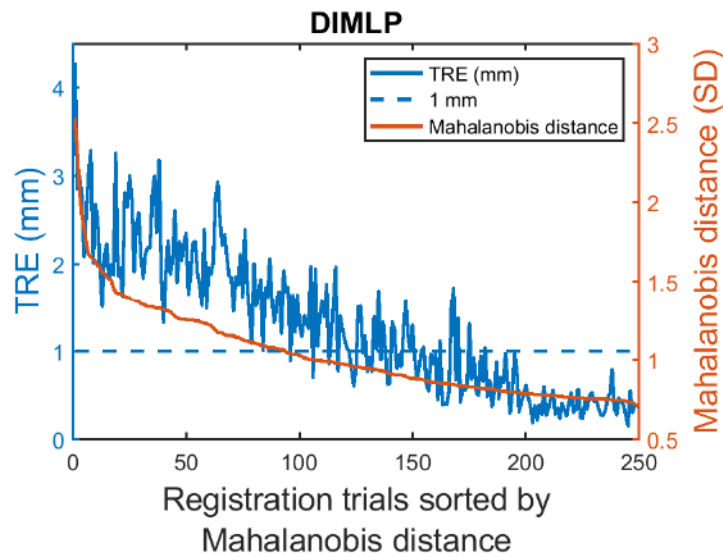


**Figure 4.8:** Noise model experiment: residual errors compared against TRE using 500 sample points with  $2 \times 2 \times 2 \text{ mm}^3$  SD positional noise and  $2^\circ$  SD angular noise in Exp. 1 of the noise model experiment (Sec. 4.5.3.1). The two measures exhibit correlation with correlation coefficient of 0.86.

### 4.5.3.2 Experiment 2: Varying anisotropic position noise

For the second experiment, anisotropic noise models with SDs of  $1 \times 1 \times 2 \text{ mm}^3$ ,  $2 \times 2 \times 3 \text{ mm}^3$ ,  $3 \times 3 \times 4 \text{ mm}^3$ ,  $3 \times 3 \times 5 \text{ mm}^3$ , and  $4 \times 4 \times 5 \text{ mm}^3$  for positional noise were used. Errors produced by D-IMLP showed the same trend as with varying isotropic noise. That is, the TRE showed an increasing trend as the uncertainty in the sample points increased (Fig. 4.9). Again, both the objective function and residual errors again showed correlation with the TRE, which can be used to assign confidence to the resulting registrations (Fig. 4.10).

### 4.5.3.3 Experiment 3: Noise parameter sweep

In the final experiment, the sample points were generated with a particular noise model. However, it was assumed that this noise model is unknown to D-IMLP. Sample points were generated with anisotropic position noise with SD  $2 \times 2 \times 4 \text{ mm}^3$ . Then, a hyper-parameter sweep was performed and the D-IMLP algorithm was deployed with different isotropic and anisotropic position noise assumptions to evaluate how well D-IMLP performs with inaccurate noise model assumptions.

The results show that D-IMLP is unaffected by changing orientation noise, which is expected since D-IMLP does not take orientation into account. TREs using D-IMLP are either stable or show a gradual trend downward as position noise becomes more conservative. Another noticeable trend is that D-IMLP performs slightly worse as the anisotropy in the noise estimates increases (Fig. 4.11).



CHAPTER 4. D-IMLP ALGORITHM

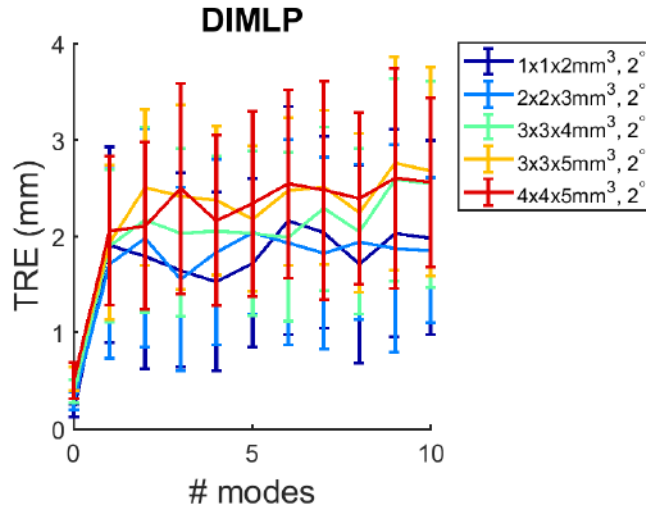


**Figure 4.9:** Noise model experiment: a general trend of increasing TRE as the uncertainty in the sample points increases. Note that errors are increasing with increasing modes because for this experiment the number of modes used to estimate the shapes equals the number of modes used to simulate a new shape from which points were sampled.

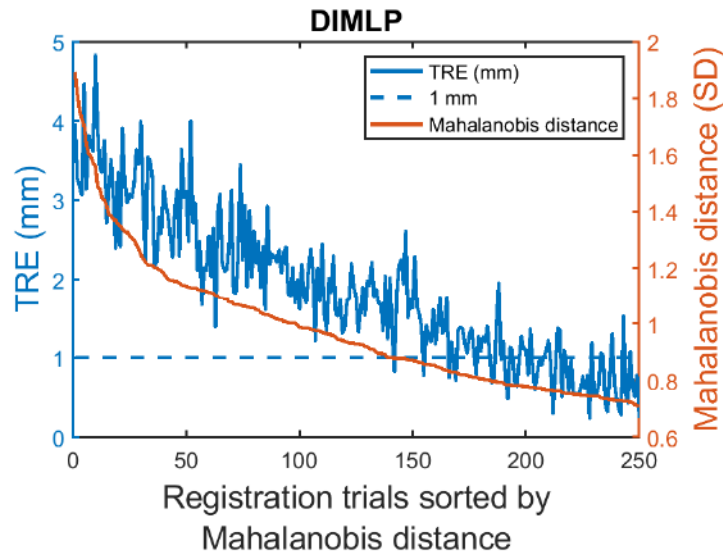


**Figure 4.10:** Noise model experiment: residual errors compared against TRE using 500 sample points with  $2 \times 2 \times 3 \text{ mm}^3$  SD positional noise and  $2^\circ$  SD angular noise in Exp. 2 of the noise model experiment (Sec. 4.5.3.2). The two measures exhibit correlation with correlation coefficient of 0.87.

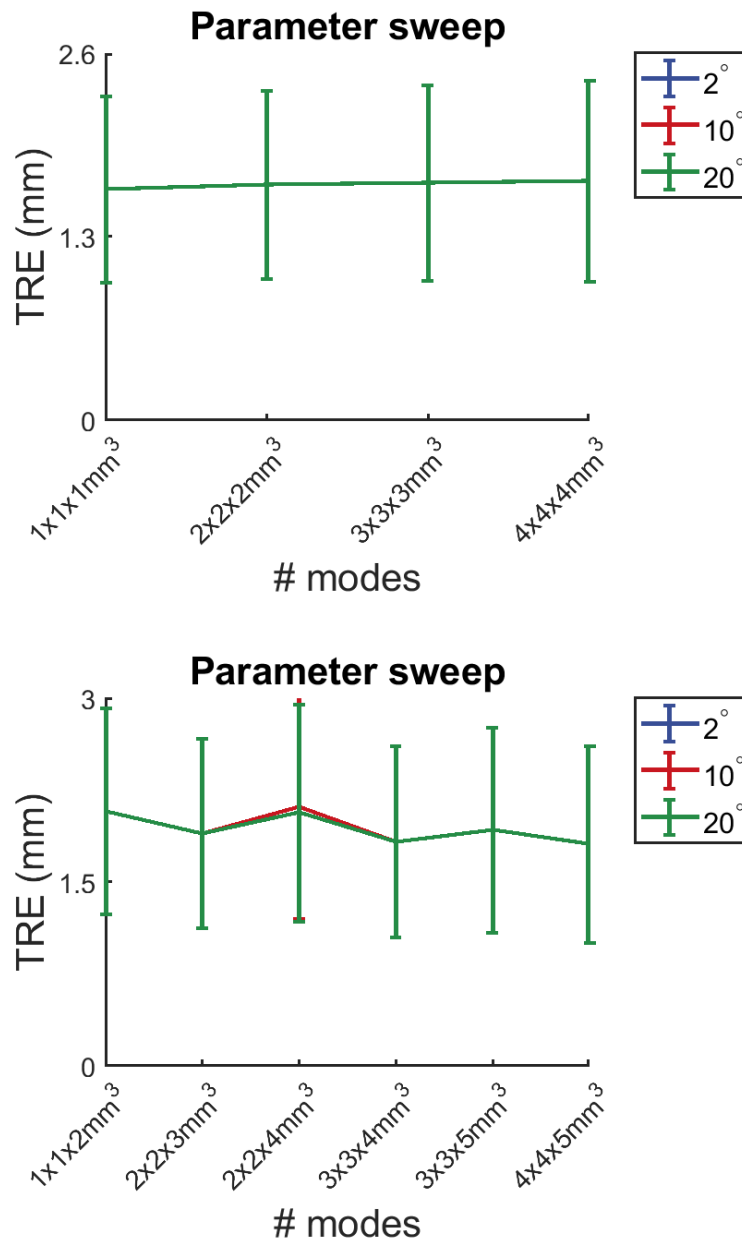


**Figure 4.11:** Noise model experiment: parameter sweep results show that D-IMLP is unaffected by changing angular noise assumptions since orientations are not taken into account by D-IMLP. Therefore, only the last plot (20°) is visible since the plots overlap almost perfectly. Errors are also stable (top) or gradually decreasing (bottom) under changing position noise assumptions, although increasing anisotropy tends to increase TRE (bottom).

#### 4.5.4 Outlier experiment

Using a synthetic dataset generated using the right nasal cavity model from the sinus dataset, the robustness of D-IMLP to outliers is evaluated. This dataset was, again, generated similarly as described in Sec. 4.5.1; the difference being that here 6 sets of 10 experiments each are performed. The number of modes used to deform the mean shape increases by 2 in each set, starting at 0 and going up to 10 modes. Again, the same number of modes are used to estimate the deformed shape using D-IMLP as were used to generate the deformed shape. All sample points were generated with isotropic noise in position data with  $1 \times 1 \times 1 \text{ mm}^3$  SD. Experiments were conducted with 0%, 10%, and 20% outliers in the generated point samples. Outliers were generated by perturbing the position of a specified number of samples randomly in the range  $[2, 5] \text{ mm}$ .

Outliers were identified and rejected using the chi-square test as described in Sec. 4.2. As a reminder, for position data, a match is rejected if the square Mahalanobis distance is greater than the value of the chi-square inverse CDF with 3 DOF at  $p = 0.95$ . Since the square Mahalanobis distance normalizes each match residual error by its variance along each dimension, the sum of the square Mahalanobis distance over all data points,  $n_{\text{data}}$ , is distributed as a chi-square distribution with  $3n_{\text{data}}$  DOF.<sup>107</sup> This knowledge is used to reject a registration outcome if this sum exceeds the value of a chi-square inverse CDF with  $3n_{\text{data}}$  DOF at  $p = 0.95$ . Using this outlier rejection criterium, D-IMLP is able to produce submillimeter registrations even in

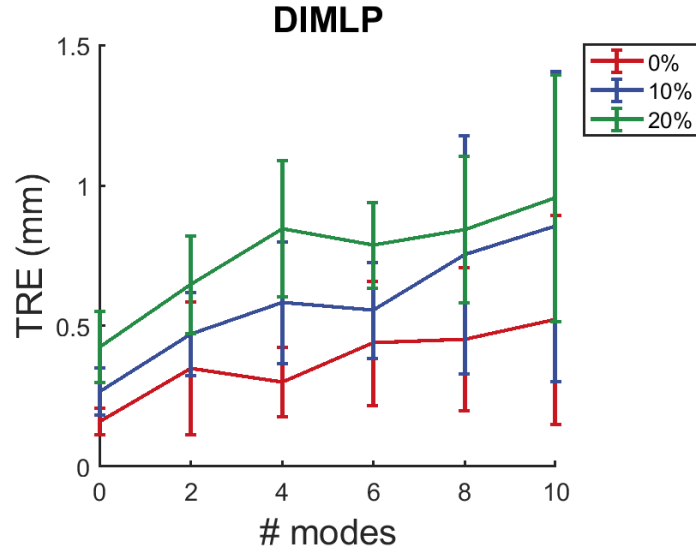


**Figure 4.12:** Outlier experiment: mean TRE with different number of outliers using D-IMLP. Note that errors are increasing with increasing modes because for this experiment the number of modes used to estimate the shapes equals the number of modes used to simulate the deformed shape from which points were sampled.

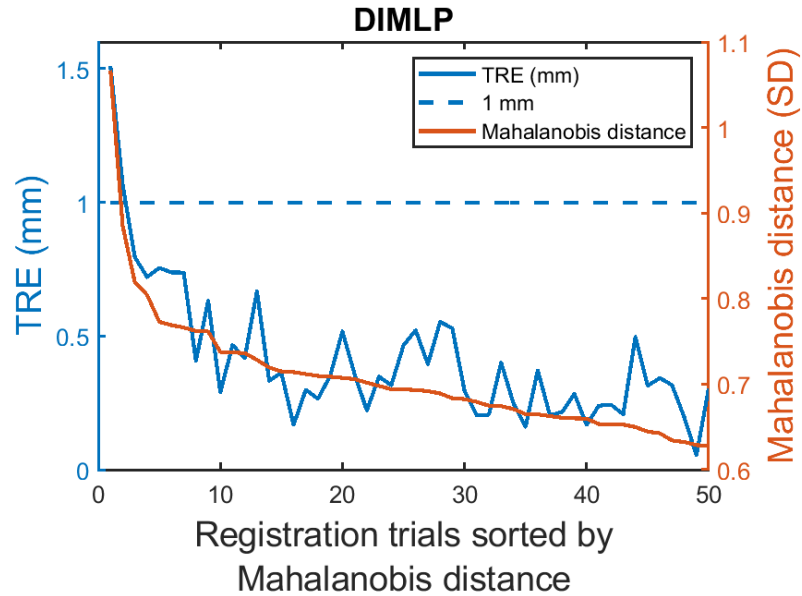


**Figure 4.13:** Residual errors compared against TRE using the right nasal cavity meshes in the outlier experiment with 0% outliers. The two measures exhibit correlation with a correlation coefficient of 0.88.

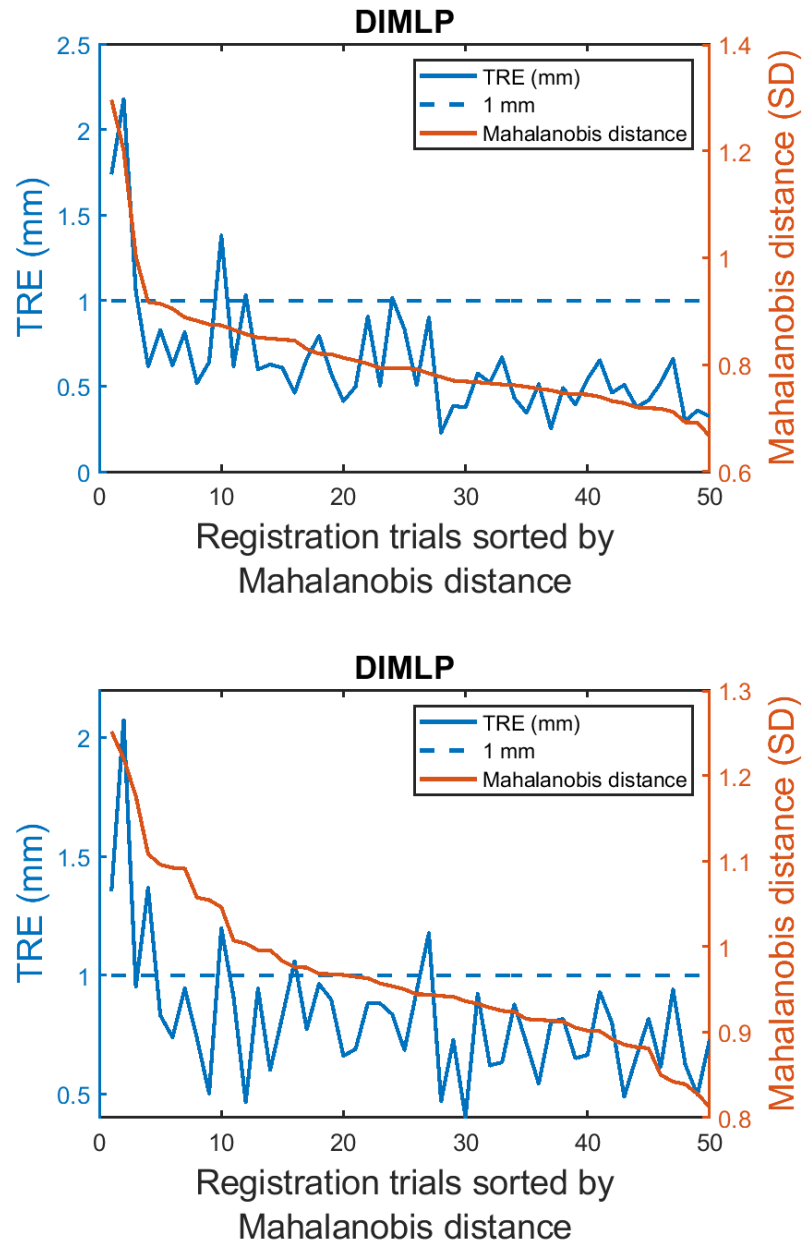


**Figure 4.14:** Residual errors compared against TRE using the right nasal cavity meshes in the outlier experiment with 10% (top) and 20% (bottom) outliers. The two measures exhibit high correlation when the sample points contain 10% outliers with a correlation coefficient of 0.81, and weak correlation with the sample points contain 20% outliers with a correlation coefficient of 0.59.

the presence of outliers in the sample points (Fig. 4.12). Although the performance is slightly worse as the percentage of outliers in the sample points increases, D-IMLP is able to detect them, as explained in Sec. 4.2, and limit their effect on errors. Even with 20% outliers in the sample points, the mean TRE produced by D-IMLP remains below 1 mm. Further, although the correlation between the TRE and residual errors degrades with increasing number of outliers, the residual errors are still able to discriminate between successful and unsuccessful registrations (Figs. 4.13, 4.14).

### 4.5.5 Scale experiment

In this experiment, the ability of D-IMLP to recover scale in addition to rotation, translation, and shape parameters is evaluated. The dataset generated in Sec. 4.5.4 with 0% outliers was reused for this experiment. However, the sample points were scaled by some amount in the range  $[0.7, 1.3]$ . D-IMLP was executed with scale optimization enabled, and the output scale was compared to the initial scale applied to the sample points. D-IMLP was able to estimate scale in addition to rotation, translation, and shape parameters well, but it performs better when optimization over scale is not required (Fig. 4.15). This is due to the lack of sufficient information in position features, causing ambiguity in matches and leading to convergence at local minima. However, errors in scale estimation and TREs remain roughly stable as the number of shape parameters to optimize over increases (Fig. 4.16).

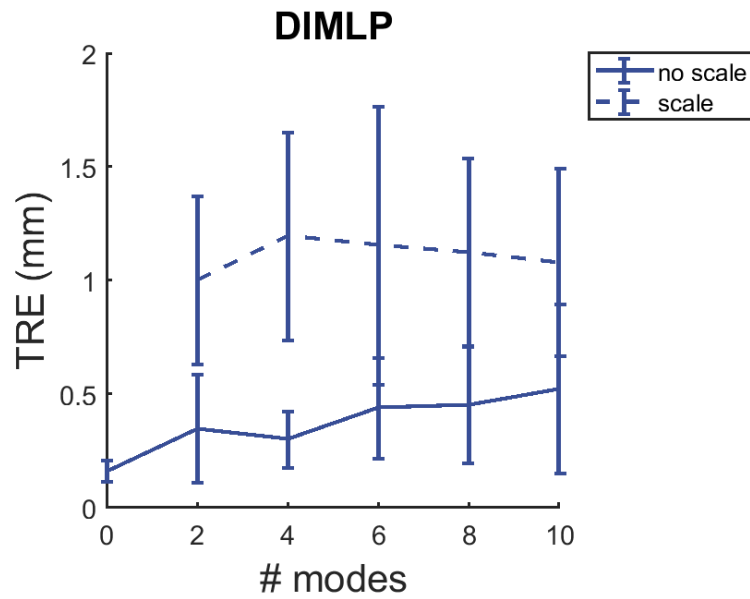


**Figure 4.15:** Scale experiment: additional scale optimization increases TRE as compared to when scale optimization is not required.



**Figure 4.16:** Scale experiment: errors in scale estimation using D-IMLP with increasing number of modes remain stable.

### 4.5.6 Leave-one-out experiment

The leave-one-out experiment was designed by building  $n_s$  SSMs in a  $n_s$  mesh dataset, with a different shape in the dataset left out for each SSM construction. This resulted in 53 different SSMs for the sinus dataset. The left out shape was then estimated in two ways:

1. by projecting the left out shape onto the SSM to obtain mode weights, and then using different numbers of modes along with the mode weights in Eq. 2.1, and
2. by using D-IMLP with different numbers of modes.

The left out shapes were estimated using 11 different number of modes, starting at 0 and increasing at increments of 5 upto 50 modes, producing a total of 1749 runs. This experiment enabled the evaluational of D-IMLP in the presence of shapes not seen before by the shape model. The errors produced by D-IMLP in estimating the left out shapes were compared to ground truth since the left out shapes are known, and also to errors produced by the SSM estimates of the left out shapes. The SSM estimates of the left out shapes represent the upper bound for how well D-IMLP can perform. This experiment enables us to relate the errors produced by D-IMLP to how representative the SSM used was of the shapes being estimated. 1000 sample points were generated for each experiment by uniformly sampling from the left out shape. An isotropic positional noise model with a SD of  $1 \times 1 \times 1 \text{ mm}^3$  was used, since the CT volumes used to segment the sinus structures had a resolution of  $1 \times 1 \times 1 \text{ mm}^3$ .



D-IMLP assumed the same noise model as was used to generate the sample points.

#### 4.5.6.1 Experiment 1: Middle turbinates

In the first experiment, the middle turbinate models from the sinus dataset were used to generate sample points. Registrations are also computed using deformable coherent point drift (CPD), a standard deformable registration algorithm,<sup>50</sup> for comparison. Since deformable CPD produces a deformation field that moves the vertices from the mean shape towards to the sample points to fit the samples and does not produce a transformation matrix, a TRE cannot be computed. However, since the original offset transformation applied to the sample points is known, the final mesh produced by CPD can be transformed by the inverse of the original transformation to compute the TSE. In order to produce a transformation matrix, rigid or affine CPD can be performed first, followed by deformable CPD. However, this is not as time efficient. Note that since CPD does not use different numbers of modes to compute its registration, results from CPD are shown as a baseline

Of the 1749 registrations, D-IMLP was able to recover the left out shape and the transformation offset applied successfully (with mean TRE less than 1 mm) 76.39% of the time. However, as the number of shape parameters increased, the performance of D-IMLP deteriorated since the position component of the sample points is insufficient information as the number of parameters to optimize over increases (Fig. 4.17). This leads to slower convergence with increasing shape parameters. Therefore, when D-

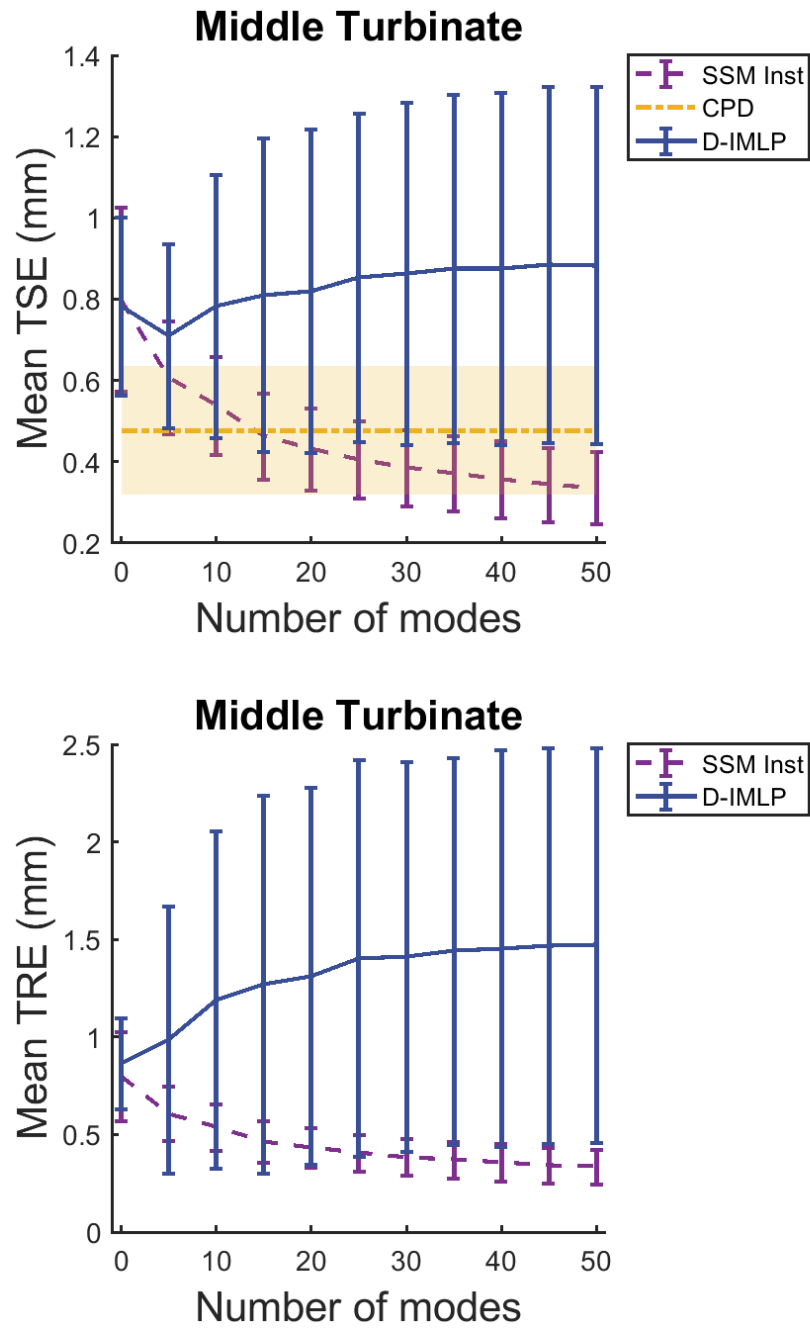


**Figure 4.17:** Leave-one-out experiment: TSE (top) and TRE (bottom) produced by D-IMLP compared against that produced by CPD and SSM using the middle turbinate meshes in the leave-one-out experiment.

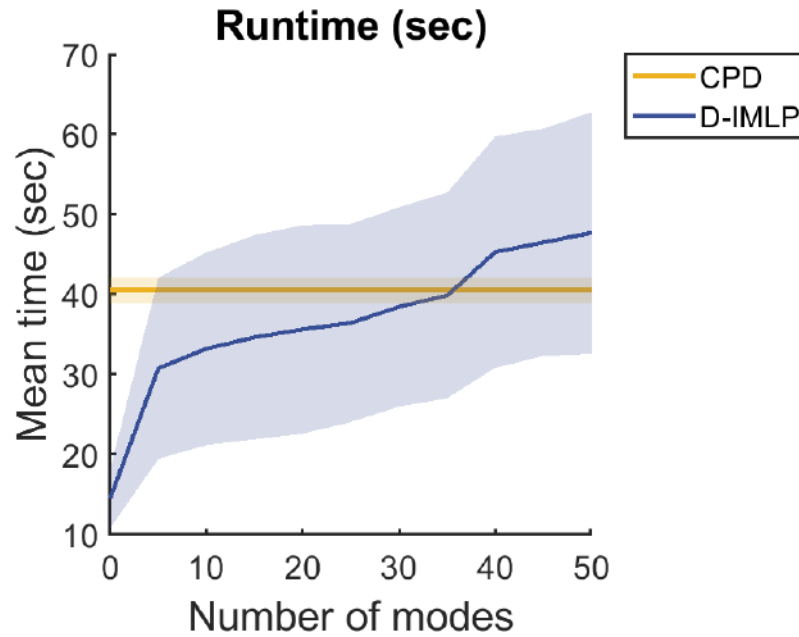


**Figure 4.18:** Leave-one-out experiment: runtime comparison between CPD and D-IMLP.

IMLP terminates at the maximum number of iterations allowed, the final alignment is worse with increasing number of shape parameters. D-IMLP was outperformed by CPD and the computation time for both were comparable. The average time required by CPD to perform registrations was 40.55s, as compared to 47.69s required by D-IMLP when using 50 modes (Fig. 4.18). As before, the error metrics produced by D-IMLP show correlation with the TRE, allowing it to accept or reject the registrations produced (Fig. 4.20), while errors produced by CPD does not show correlation with

the TSE (Fig. 6.18). Therefore, errors produced by CPD cannot be used to assign confidence to or detect success or failure of the produced registration.

#### 4.5.6.2 Experiment 2: Right nasal airway

Since both turbinates would generally not be visible at the same time during an endoscopic procedure, in the second experiment, the right nasal airway models were used to generate sample points. Apart from this difference, the experiment is set up and evaluated identically to the previous experiment (Sec. 4.5.6.1). The performance of D-IMLP in this experiment was similar to the one before with results deteriorating as the number of parameters to optimize over becomes too large for the limited information provided by the position components (Fig. 4.19). As explained before, lack of sufficient information causes slower rate of convergence, meaning that D-IMLP terminates at an earlier stage in the registration as the number of shape parameters increases. However, of the 1749 runs, 82.39% of the D-IMLP runs were still able to recover the left out mesh with mean TRE less than 1 mm. These results were not compared to CPD because the machine used for these computations was unable to handle the memory requirements of CPD with larger meshes. CPD computes a  $n_v \times n_v$  matrix, where  $n_v$  is the number of vertices in the deformable mesh. This results in extremely large memory overhead even for medium sized meshes, a drawback that D-IMLP does not suffer from. Again, the residual errors produced by D-IMLP were in correlation with the TRE (Fig. 4.21).

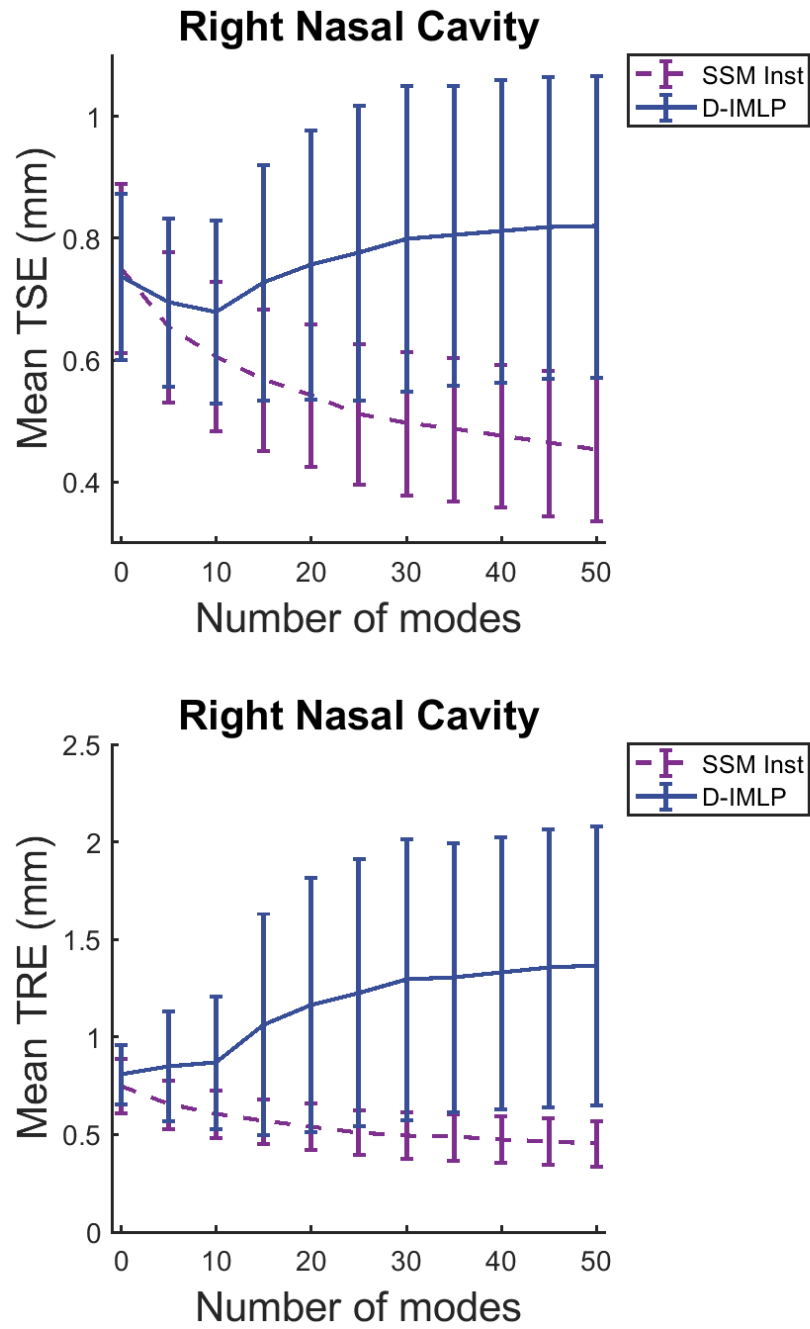


**Figure 4.19:** Leave-one-out experiment: TSE (top) and TRE (bottom) produced by D-IMLP compared against that produced by the SSM estimate using the right nasal cavity meshes in the leave-one-out experiment.

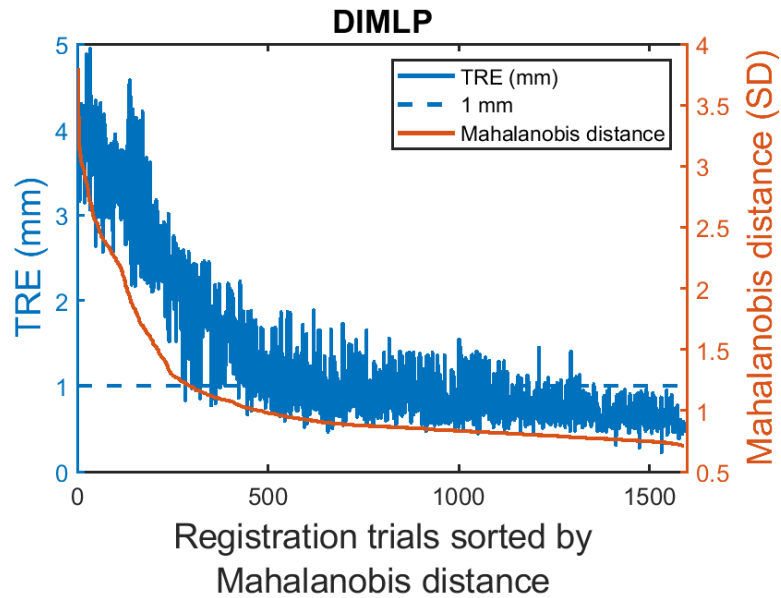


**Figure 4.20:** Leave-one-out experiment: residual errors compared against TRE using the middle turbinate meshes in the leave-one-out experiment. The two measures exhibit correlation with correlation coefficients of 0.91.

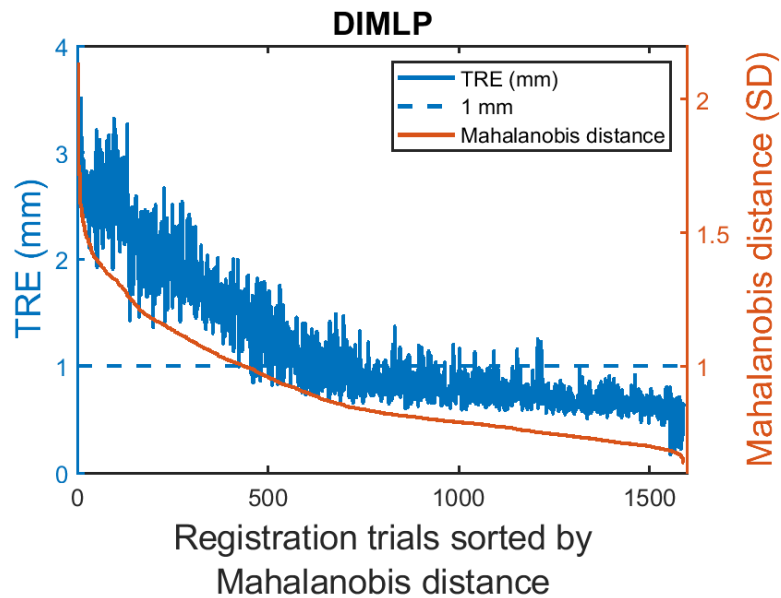


**Figure 4.21:** Leave-one-out experiment: residual errors compared against TRE using the right nasal cavity meshes in the leave-one-out experiment. The two measures exhibit correlation with correlation coefficients of 0.95.

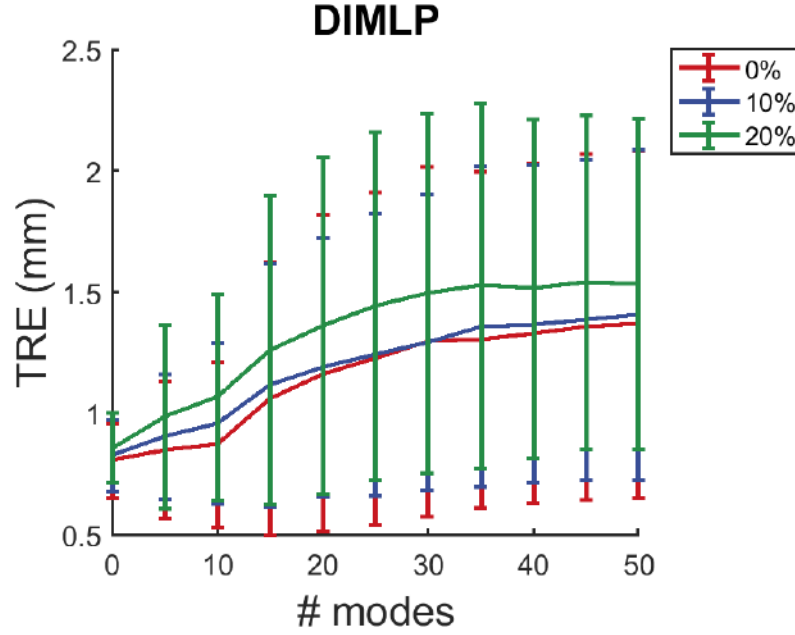


**Figure 4.22:** Leave-one-out experiment: TRE produced by D-IMLP with 0%, 10% and 20% outliers in the data points sampled from the right nasal cavity meshes in the leave-one-out experiment.

### 4.5.6.3 Experiment 3: Right nasal airway with outliers

Since real data will most likely contain several outliers, the previous experiment using the right nasal cavity data was modified slightly to introduce outliers in the sampled data points. The experiment was set up identically to that in Sec. 4.5.6.2, with the same number of data points sampled and the same offset applied to the sampled points. However, 10% and 20% of the samples were perturbed to simulate outliers in the generated data. The perturbation was similar to that explained in the

previous outlier experiment (Sec. 4.5.4) and outliers were detected as explained in Sec. 4.2. Results show that the TREs produced when there are 10% outliers in the data samples is almost identical to those produced when there are no outliers, and TREs are slightly worse with 20% outliers in the data samples (Fig. 4.22).

### 4.5.7 Partial data experiment

This experiment was set up similarly to the leave-one-out experiments. However, in order to simulate more realistic scenarios, the pelvis and right nasal cavity SSMs were used to generate point samples from *part* of the left out shape, rather than uniformly from the entire mesh, for each registration (Fig 4.23). The part of the meshes that points were generated from was dependent on the procedure being simulated. We designed two experiments simulating two different procedures. For both experiments, 2000 points were sampled from the candidate regions of the meshes with appropriate amounts of noise added to the sampled points. Although results using CPD are not computed for this experiment due to computational limitations of CPD with relatively large meshes, it can be assumed that it will not perform as well in recovering the shape because only the parts of the mesh that the sample points are matched to will be deformed by CPD.



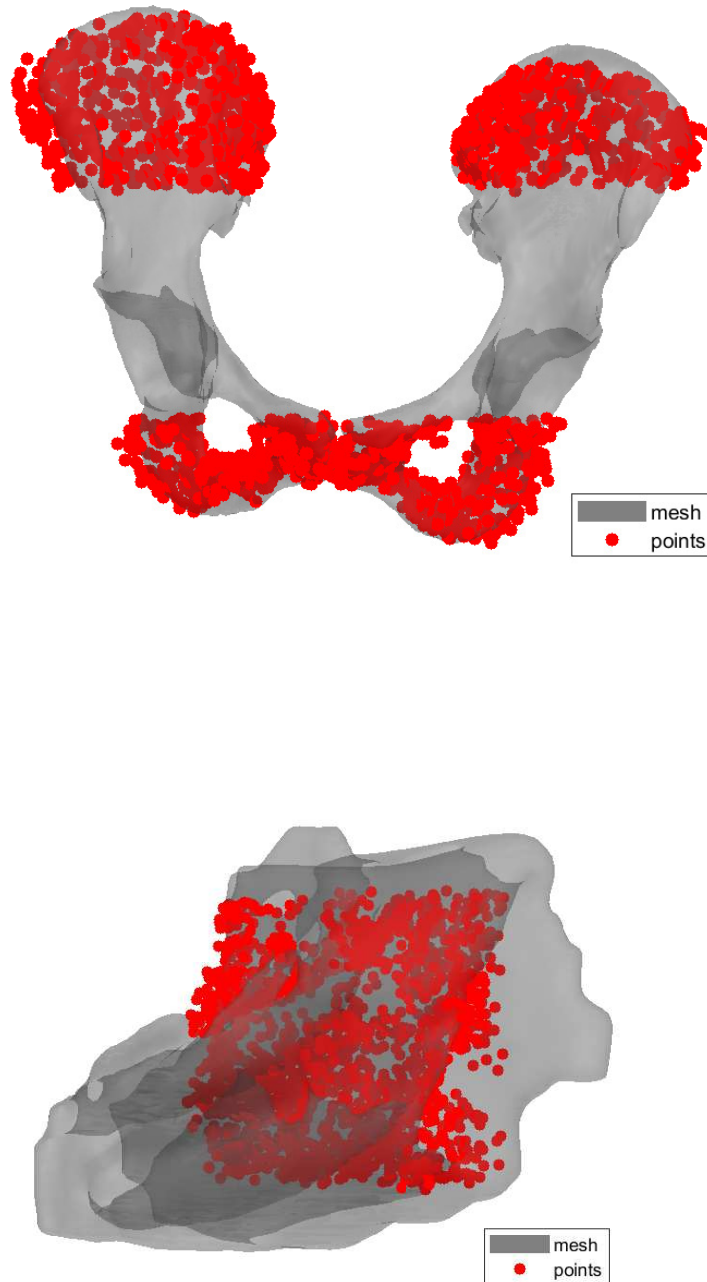


**Figure 4.23:** Partial data experiment: An example of data generated for the partial data experiment: (top) points are sampled only from the ilium and ischium on the pelvis mesh, and (bottom) points are sampled from the front section of the right nostril which include parts of the septum and middle and inferior turbinates.

### 4.5.7.1 Experiment 1: Pelvis

Simulating a situation in which only a partial CT scan of the pelvis is obtained to prevent radiation exposure to reproductive organs, points were sampled only from the ilium and ischium (Fig 4.23, top) regions of the pelvis model. Anisotropic noise with SD  $1 \times 1 \times 2 \text{ mm}^3$  was added to position data. An instance of the pelvis is then estimated by D-IMLP using these sampled points and a generous noise assumption with SD  $2 \times 2 \times 3 \text{ mm}^3$  for position data. Results from this experiment show a big improvement in both transformation parameters and TSE from 0 to 10 modes (Fig. 4.24). However, with over 10 modes, the improvement in transformation parameters stabilizes, and only a gradual improvement in TSE is observed, although the trend followed by the TSE is similar to that followed by the error between the left out shape and the SSM instance of the left out shape (Fig. 4.24). The resulting mean TRE falls below 2 mm with only 10 modes (Fig. 4.24), which is the desired accuracy for pelvis registrations. The improvement in the TRE is also reflected in the residual errors produced by D-IMLP (Fig. 4.26, top), although the correlation is weaker than in the previous experiments.

### 4.5.7.2 Experiment 2: Right nasal airway

In order to simulate nasal endoscopy, points were sampled only from parts of the nasal cavity that would be visible to the endoscope when inserted into the right nostril (Fig 4.23, bottom). Anisotropic noise with SD  $0.5 \times 0.5 \times 1 \text{ mm}^3$  was added to position

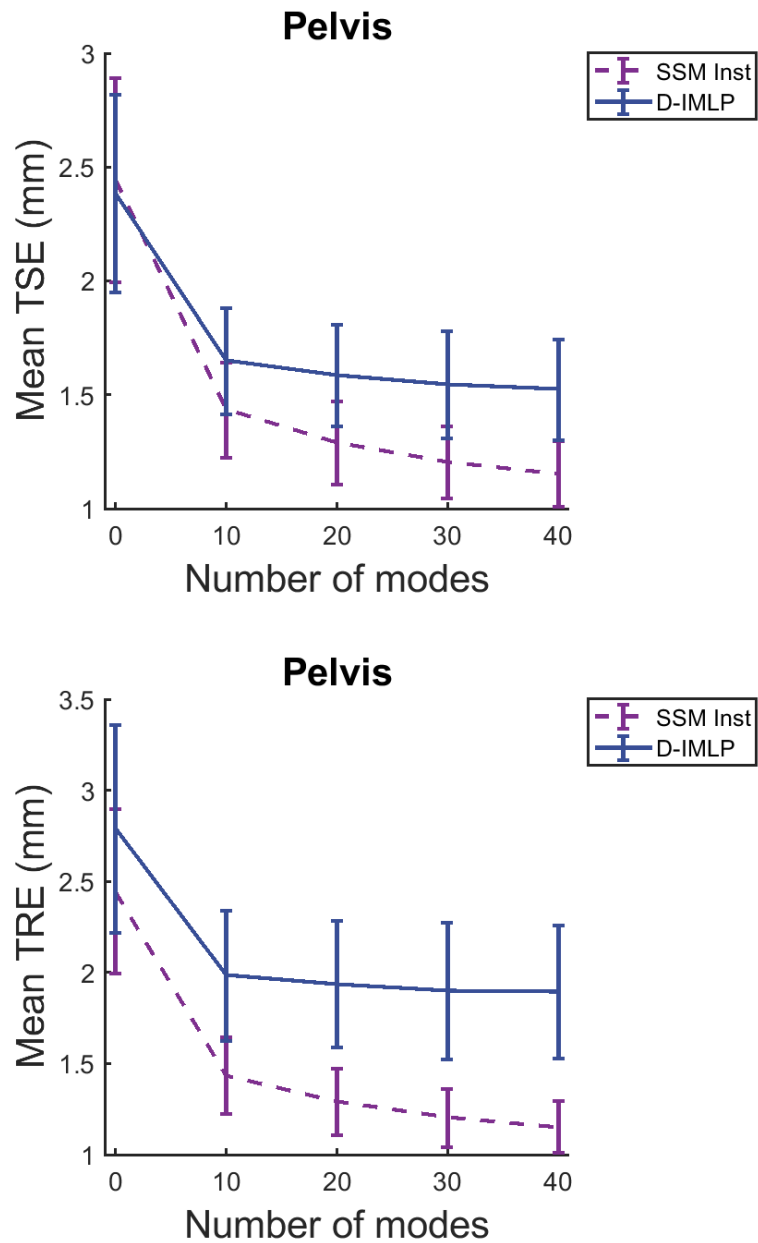


**Figure 4.24:** Partial data experiment: TSE (top) and TRE (bottom) produced by D-IMLP compared against that produced by the SSM estimate using the pelvis meshes.

## CHAPTER 4. D-IMLP ALGORITHM

data since this produced point clouds that resembled reconstructions obtained from in vivo data using the method described in the chapter 7. Position noise in the generated samples has a larger standard deviation in the z-direction since depth is harder to estimate from video data. The left out nasal cavity was then estimated using these sampled points and a noise model assumption with SD  $1 \times 1 \times 2 \text{ mm}^3$  for position data. This experiment yielded slightly different results due to the increased complexity of the right nasal airway models. Although the transformation errors either remained stable or showed slight improvement with increasing number of modes, the TSE increased from 0 to 10 modes and stabilized or showed slight improvement beyond that. Although, the mean TSE remained below 1 mm, the mean TRE for all modes remained above 1 mm (Fig. 4.25). The results indicate that for complex structures like the nasal cavity, position information is not sufficient to accurately estimate both the registration and shape parameters. The TRE and residual errors, again, show weak correlation (Fig. 4.26, bottom).

### 4.5.8 Failure detection experiment

In this experiment, the success or failure of the registrations produced are compared to the outcome predicted by D-IMLP using the chi-square inverse test explained in Sec. 4.2. A registration is considered successful if the TRE is below 1 mm. Two experiments are designed based on whether or not the algorithm has knowledge of the noise model used to generate the data samples.

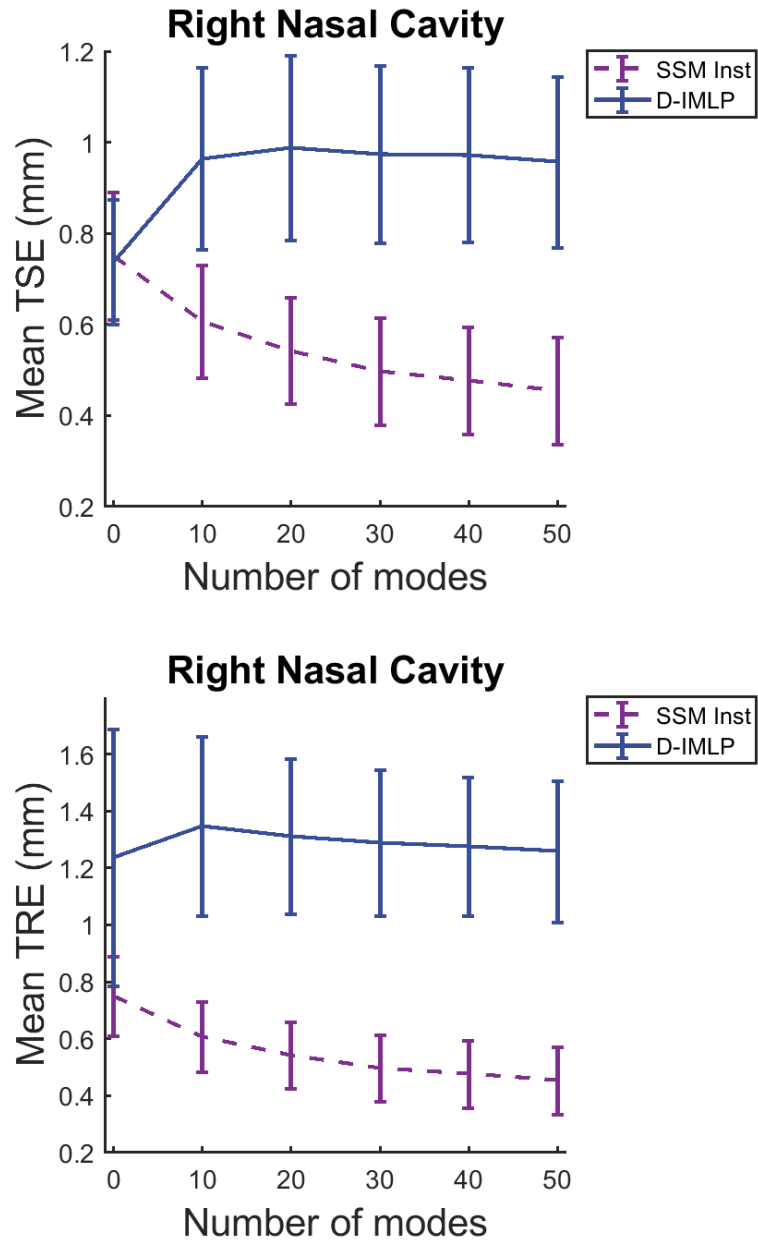


**Figure 4.25:** Partial data experiment: TSE (top) and TRE (bottom) produced by D-IMLP compared against that produced by the SSM estimate using the right nasal airway meshes.

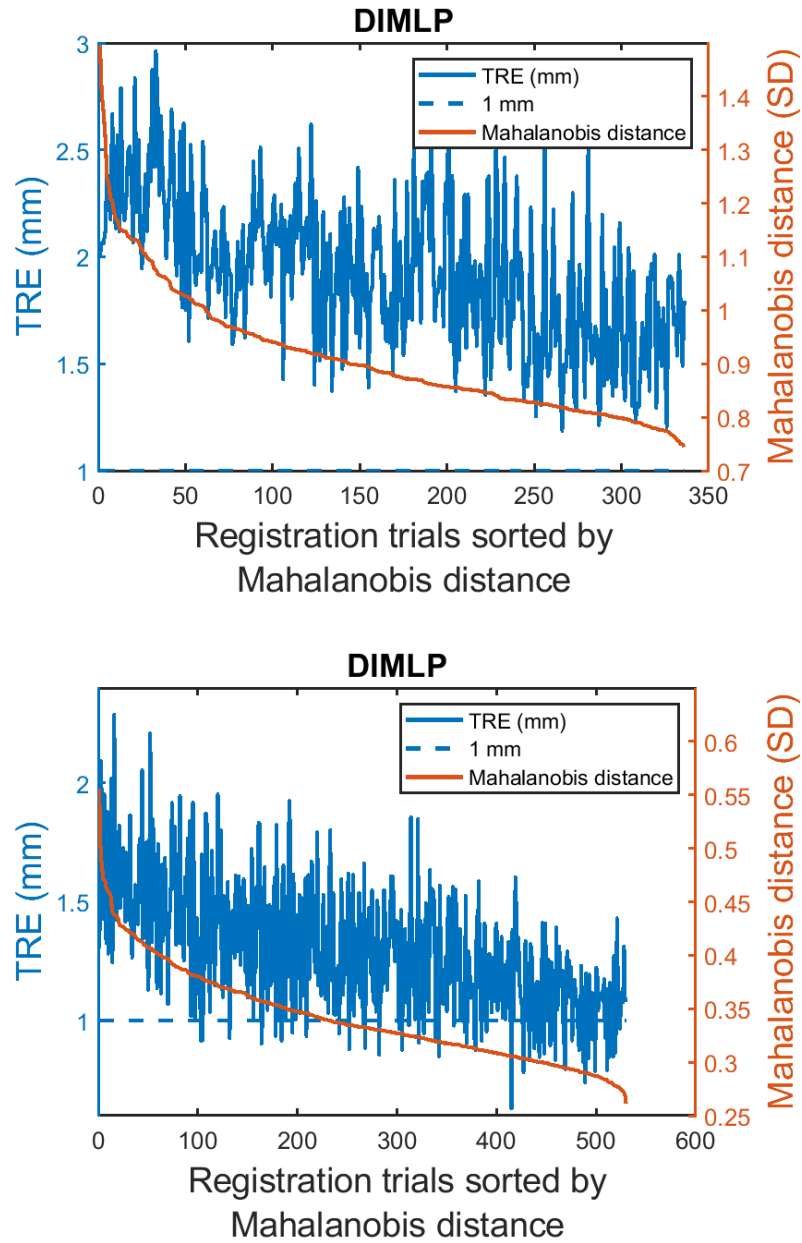


**Figure 4.26:** Partial data experiment: residual errors compared against TRE using the pelvis (top) and right nasal airway (bottom) meshes. The two measures exhibit weak correlation in both experiments 1 and 2 with correlation coefficients of 0.52 and 0.56, respectively.

### 4.5.8.1 Experiment 1: Known noise

This setup for this experiment is the same as the setup for the leave-one-out experiment with right nasal airway data (Sec. 4.5.6.2). As in Sec. 4.5.6.2, this experiment assumes the same position noise SD as was used to generate the data samples. Results from the chi-square test at  $p = 0.95$  show that although the test is successfully able to detect registrations that were successful by the  $\text{TRE} < 1$  mm criterium, the test is not as successful at rejecting unsuccessful registrations (Fig. 4.27, top). This is because registrations that only use position data can often find good incorrect sets of correspondences. This leads to small residual errors although the registered pose is incorrect. Since  $E_p$  is simply the sum over the residual errors from all corresponding point pairs, this sum may remain below the  $\chi_{\text{thresh\_final}}^2$  threshold for registrations producing TREs  $> 1$  mm. However, just like the mean residual error, the total residual error,  $E_p$ , is found to be correlated with the TRE (Fig. 4.27, bottom). Therefore, although the  $\chi_{\text{thresh\_final}}^2$  threshold may not be able to discriminate between successful and unsuccessful registrations, a different threshold can be found that is better able to reject unsuccessful registration or assign degrading confidence to the registrations based on  $E_p$ .

### 4.5.8.2 Experiment 2: Unknown noise

The setup for this experiment is similar to the partial data experiment setup for the right nasal airway data (Sec. 4.5.7.2) with some differences to simulate a more

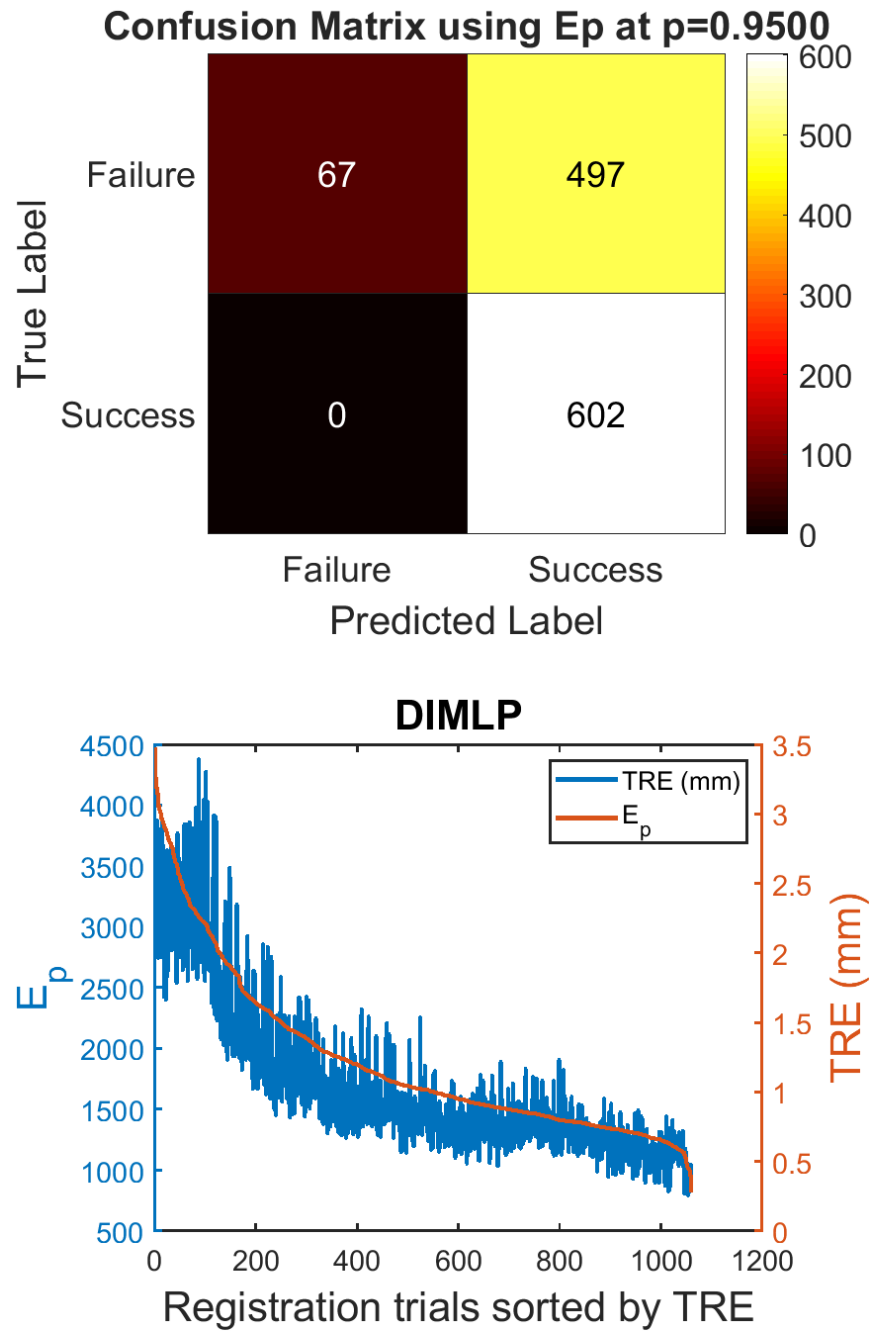


**Figure 4.27:** Failure detection experiment: Confusion matrix (top) and correlation between  $E_p$  and TRE (bottom) with a correlation coefficient of 0.90 when the noise in the data is known.



## CHAPTER 4. D-IMLP ALGORITHM

realistic scenario. 3000 points were sampled from the nasal cavity region of the left out shape, and anisotropic noise with SD  $0.5 \times 0.5 \times 0.75 \text{ mm}^3$  was added to the position component of the sampled points. A rotation, translation and scale are applied to these sampled points in the interval  $[0, 10] \text{ mm}$ ,  $[0, 10]^\circ$  and  $[0.95, 1.05]$ , respectively. 2 offsets are produced in this interval for each left out shape. This experiment assumes that it does not have knowledge of the noise model used to generate the data samples. Therefore, D-IMLP makes slightly more generous noise assumptions with SD  $1 \times 1 \times 2 \text{ mm}^3$  for position noise, and restricts scale optimization to within  $[0.9, 1.1]$ . In this more realistic scenario, the performance of the chi-square test at  $p = 0.95$  is worse than in the previous experiment. This is expected since in this experiment, a more limited amount of data is available to the registration algorithm as compared to the previous experiment (Sec. 4.5.8.1). With only position information, it is likely that the optimization will get trapped in local minima leading to low  $E_p$  for incorrect registrations. In addition, since the square Mahalanobis distance normalizes each match residual by its variance along each dimension, assuming a larger noise SD than the actual noise SD further lowers  $E_p$ . Therefore, the  $\chi_{\text{thresh\_final}}^2$  threshold is unable to detect any failed registration produced in this experiment (Fig. 4.28, top). Further,  $E_p$  and TRE only show weak correlation making it hard for the algorithm to make decisions on the success or failure of the produced registration (Fig. 4.28, bottom).

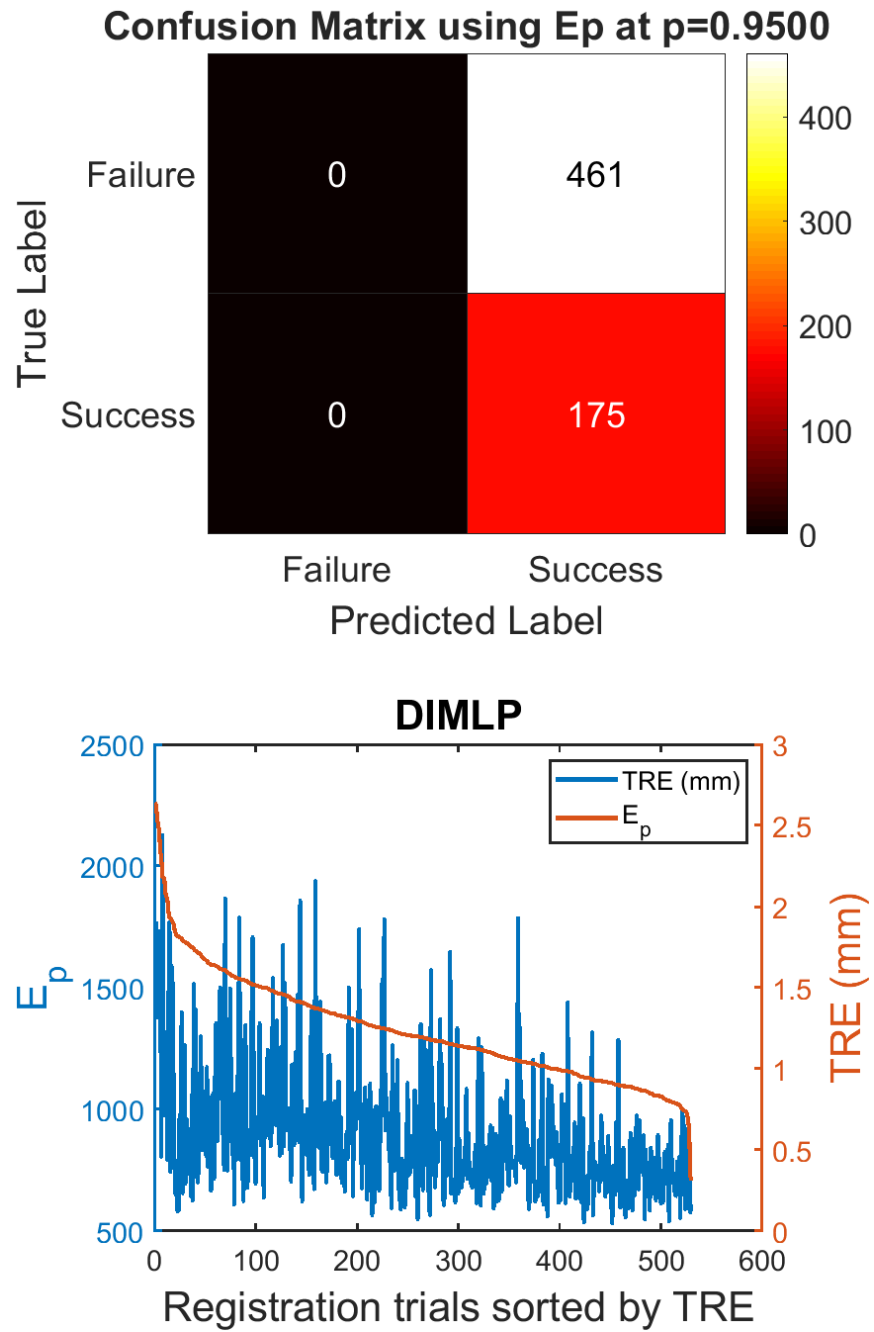


**Figure 4.28:** Failure detection experiment: Confusion matrix (top) and weak correlation between  $E_p$  and TRE (bottom) with a correlation coefficient of 0.46 when the noise in the data is unknown.

### 4.5.9 Non-medical data experiment

The previous experiments evaluate the generalizability of D-IMLP within the medical field. The following experiments evaluate D-IMLP on some non-medical data to test its generalizability beyond the medical field. We used human expression and human pose datasets in separate leave- $n$ -out experiments by dividing the datasets into training and test sets. We used the training set to build a shape model, and estimated the meshes in the test set using the two methods described in Sec. 4.5.6.

This, and other registration algorithms presented in this thesis, are not expected to perform well on this dataset because the assumption that facial expression or human pose are Gaussian distributed is likely an incorrect assumption depending on the dataset.<sup>108</sup> Further, the limited number of data points in our dataset was not enough to explain well the complex variations that can exist in human expression and pose. The deformable registration paradigm presented in this dissertation should still, however, be applicable to this type of data as long as enough shapes are used to build the SSM and an appropriate statistical model is used to explain the variation present in the dataset.

#### 4.5.9.1 Experiment 1: Human expression

For the human expression dataset, 300 meshes were used in the training set to build an SSM for expressions from a single individual. The remaining 86 meshes, also from the same individual, were reserved for the test set. 1000 points were sampled

## CHAPTER 4. D-IMLP ALGORITHM

from meshes in the test set with anisotropic positional noise with SD  $1 \times 1 \times 2 \text{ mm}^3$ . This simulates a realistic situation in which a scan of a head is obtained using a depth camera, where error is larger in the depth direction. D-IMLP was executed with a slightly more relaxed noise assumption, assuming that the position noise model has a SD of  $2 \times 2 \times 4 \text{ mm}^3$ . D-IMLP performed relatively well on this challenging dataset. It was able to deformably register the mean face mesh to points sampled from test faces to produce low TSEs, although improvement with increasing number of modes stabilized quickly (Fig. 4.29, top). TREs showed a gradual trend up but mean TREs remained below 2 mm (Fig. 4.29, bottom). Again, these results indicate that for higher accuracy, more information in the form of larger number of samples or orientation components might be required. The residual errors produced by our algorithms correlate with the TRE, indicating that D-IMLP has the ability to handle such data (Fig. 4.31, left).

### 4.5.9.2 Experiment 2: Human pose

For the human pose dataset, 80 meshes were used in the training set to build an SSM of poses. The remaining 20 meshes were reserved for the test set. As with the previous experiment setup, in order to simulate a realistic pose capture system, 1000 points were sampled with the same anisotropic position noise model as before. D-IMLP was deployed with a more relaxed noise assumption where the SD of the position noise model was assumed to be  $2 \times 2 \times 4 \text{ mm}$ . The search space for shape parameters,

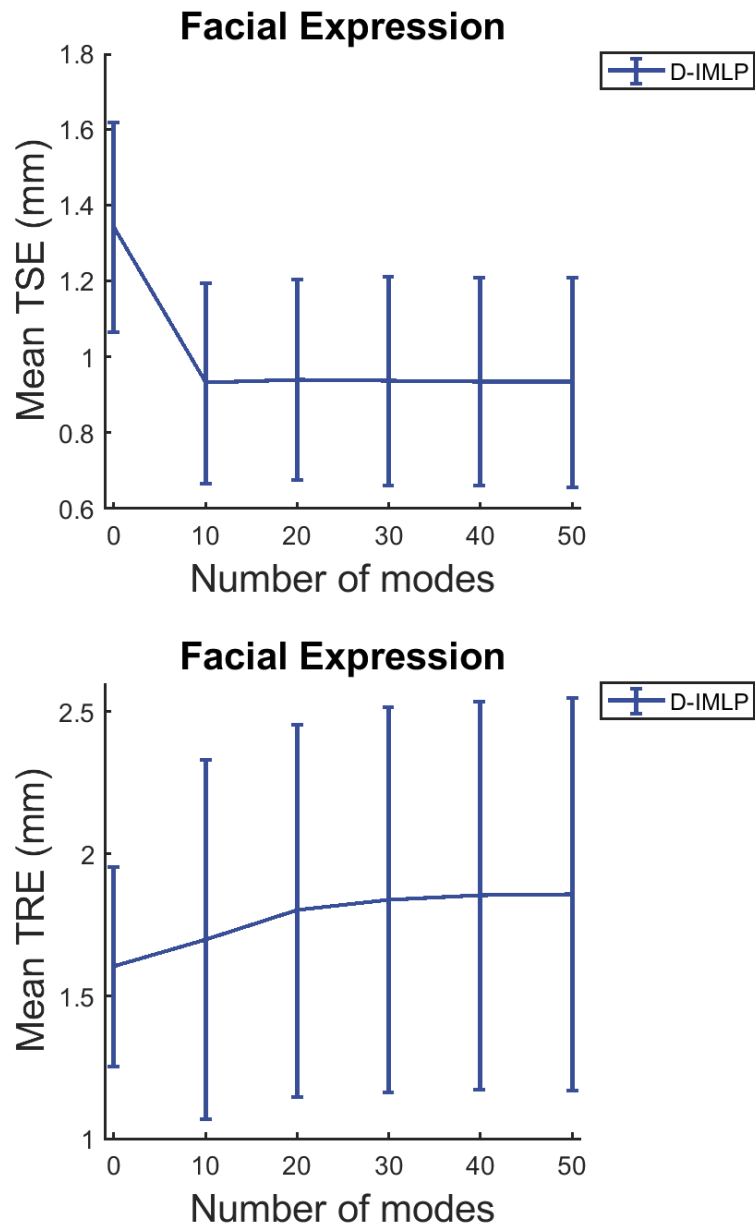


**Figure 4.29:** Leave- $n$ -out experiment: TSE (top) and TRE (bottom) produced by D-IMLP.

s, in this case was restricted to  $\pm 1$  SD. The human pose dataset proved to be the failure case for D-IMLP, as is clear from the high TREs and TSEs (Fig. 4.30). This was expected since the limited data available and perhaps the linearity assumptions made by PCA-based models are not sufficient to explain the complex variations observed in different poses. The failure of D-IMLP to accommodate this dataset is also clear from the absence of correlation between residual errors and TREs (Fig. 4.31).

## 4.6 Concluding remarks

A novel deformable variant of IMLP, known as the deformable iterative most likely point (D-IMLP) algorithm, is presented in this chapter. This method is able to compute an alignment between a mean shape and data samples and simultaneously deform the mean shape to fit the data samples. The accuracy of this method increases with data samples, but is not significantly affected by inaccurate noise assumptions. Further, the performance shows only slight degradation in the presence of outliers. These features are advantageous for real world applications where data will likely contain both outliers and noise, and only an estimate of the noise can be made. Although CPD outperforms D-IMLP in terms of errors, D-IMLP is faster than CPD with fewer than  $\sim 35$  modes and comparable with more modes. The biggest advantage D-IMLP has over CPD is that D-IMLP has a lower memory requirement than CPD, allowing D-IMLP to compute registrations using large meshes and several

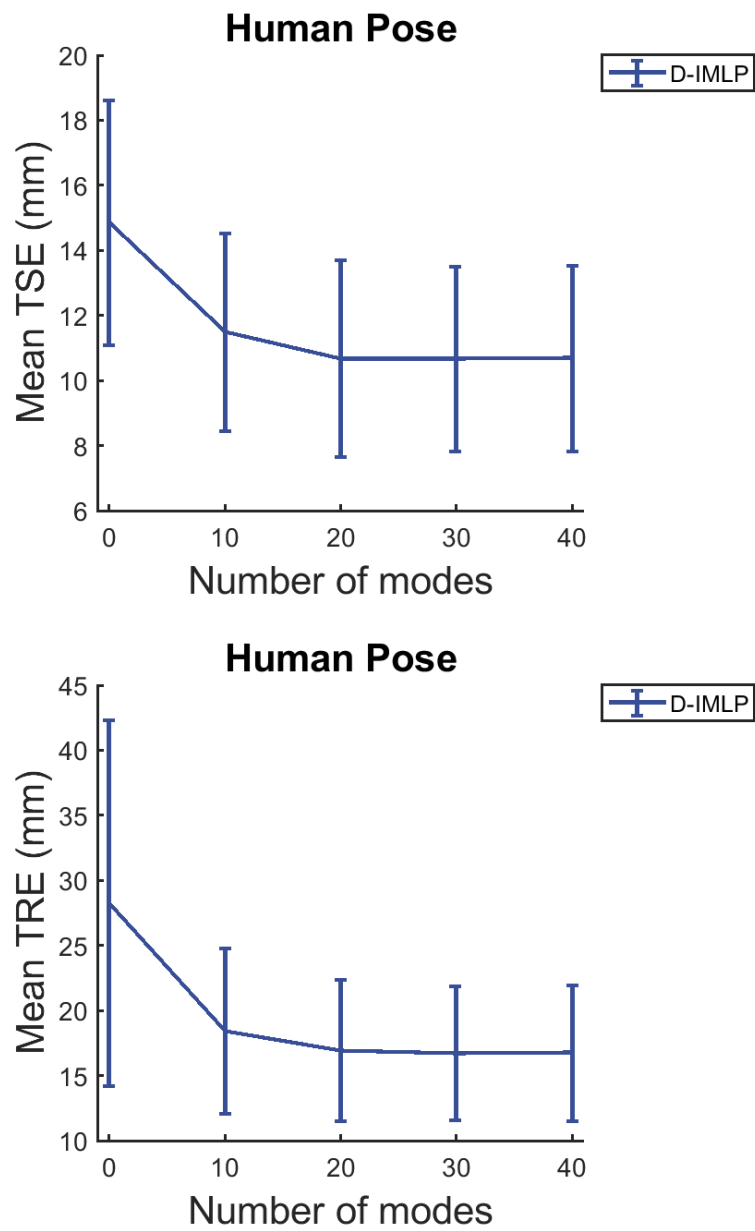


**Figure 4.30:** Leave- $n$ -out experiment: TSE (top) and TRE (bottom) produced by D-IMLP.

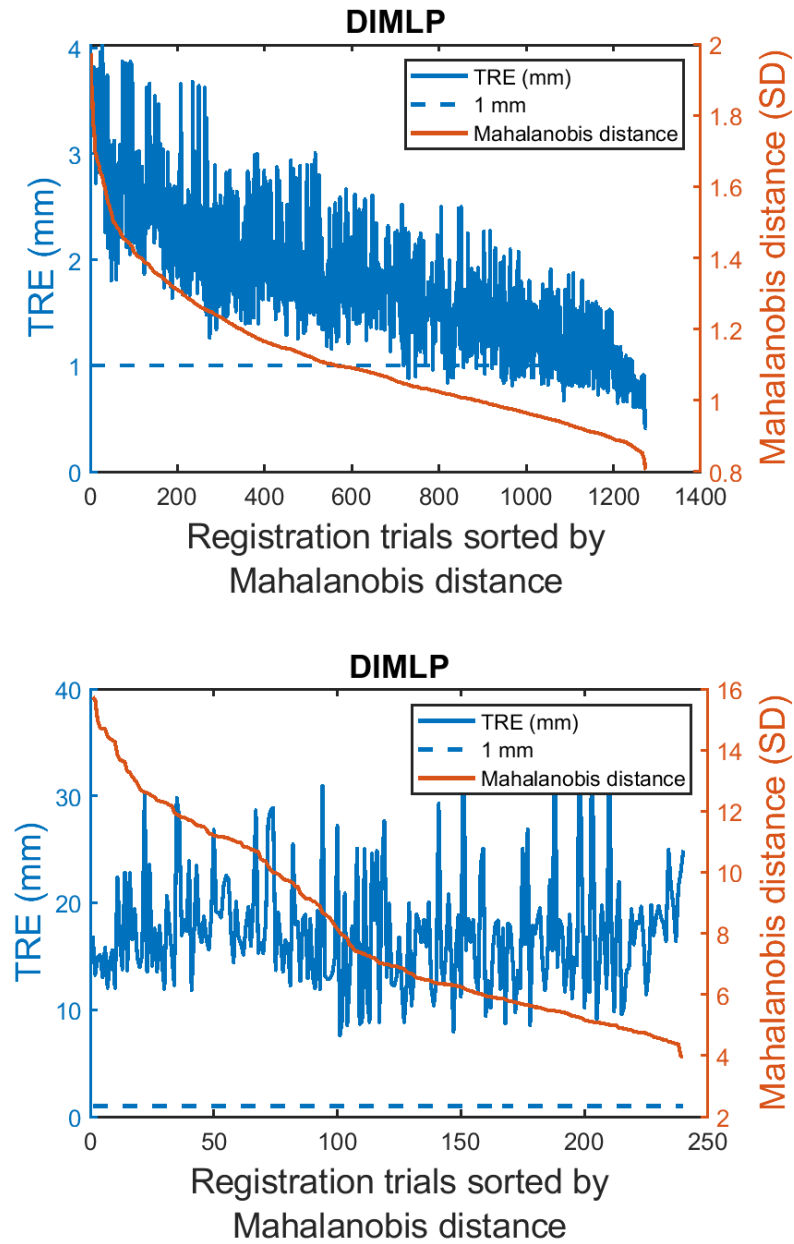


**Figure 4.31:** Leave- $n$ -out experiment: residual errors compared against TRE show that the two measures exhibit high correlation using the facial expression data with a correlation coefficient of 0.81 (top), and no correlation using the human pose data with a correlation coefficient of 0.03 (bottom).



data samples. Further, unlike CPD, residual errors produced by D-IMLP correlate with the TSEs and TREs computed allowing some assignment of confidence to the registrations produced based on the residual errors.

However, since D-IMLP only makes use of position information, it does suffer from convergence to local minima that do not represent the optimal solution due to the lack of sufficient information to prevent such convergence. Additional information like orientation, for instance, can help reject matches where position components produce good alignment but the corresponding normals do not.

## 4.7 Contributions

The contributions of this chapter include:

1. The improvement, implementation and evaluation of the deformable iterative most likely point (D-IMLP) algorithm<sup>77,78</sup> which
  - (a) incorporates deformable shape transformations using SSMs within a probabilistic registration algorithm that uses point features with associated unconstrained or anisotropic noise
  - (b) performs an efficient implementation of PD-tree update to accommodate a deforming model shape
  - (c) computes a gradient-based solution to the optimization problem using an off-the-shelf nonlinear box-constrained BFGS quasi-Newton optimizer<sup>80</sup>

## CHAPTER 4. D-IMLP ALGORITHM

(d) incorporates a mechanism for autonomously evaluating a registration in order to assign confidence to the resulting alignment

Although many of these ideas were introduced by Billings,<sup>78</sup> they were refined during implementation to accurately compute the gradients during optimization and to include scale as an optional optimization parameter.

### 4.8 Published work

Material from this chapter appeared in the following publication:

1. A. Sinha, S. D. Billings, A. Reiter, X. Liu, M. Ishii, G. D. Hager, R. H. Taylor, “The deformable most-likely-point paradigm,” *submitted to Medical Image Analysis* (2018)

## Chapter 5

# Deformable iterative most likely oriented point (D-IMLOP) algorithm

This chapter presents an extension to the D-IMLP algorithm which is inspired by the iterative most likely oriented point (IMLOP) algorithm.<sup>52</sup> IMLOP is an algorithm that can register oriented data characterized by isotropic uncertainty not only in position data, but also in orientation data.<sup>52</sup> The deformable algorithm presented here, called the deformable most likely oriented point (D-IMLOP) algorithm, is built upon the paradigm presented in Chapter 3, and incorporates a probabilistic framework to combine the position and orientation information of features and deformably registers these features. D-IMLOP can incorporate features characterized

## CHAPTER 5. D-IMLOP ALGORITHM

by unconstrained uncertainty in the positional elements and constrained, or isotropic, uncertainty in the orientation elements.

Algorithms that are able to use both position and orientation data are beneficial for data samples that have orientation components along with position components. In the medical field, surface normals can be computed on surface models extracted from 3D volumes like CT or MRI scans to estimate the surface orientation per vertex and/or per triangle. In other modalities, like videos from endoscopy or laparoscopy, extracting surface models is not trivial. However, a large amount of research has been dedicated to estimating structure from such data. Structure from motion<sup>109</sup> algorithms of several varieties are able to compute sparse point clouds representing structure seen in a sequence of video frames. A surface that fits this structure can be approximated and surface normals can be computed for every vertex in the point cloud.<sup>110</sup> Procedures that allow for physical probing like total hip replacement (THR) surgery can compute normals directly on the surface using tracked probes with force or torque sensors, for instance<sup>111,112</sup> When physical probing is not possible, range-imaging techniques can be used to reconstruct a surface and normals.<sup>36</sup> Range-imaging has several applications outside the medical field as well due to its accuracy in capturing surfaces and orientations. They are often used to capture human motion and facial expression, and also to digitize historical artifacts like statues by accurately measuring surfaces and orientations using range-imaging.<sup>113</sup>

ICP based methods that use orientation in addition to position data have been

developed before.<sup>36</sup> However, several of the applications described above also require the registration to be deformable. For instance, medical data from different modalities captured at some time interval will exhibit some amount of differences. These differences can be due to breathing movement or movement of tissues due to pressure from tools during surgery, etc. Outside the medical field, registration may be required between humans in two different poses or faces with different expressions, etc. Some deformable registration algorithms that have been developed are reviewed in Chapter. 3. In this chapter, IMLOP will be briefly reviewed, and its deformable extension, D-IMLOP, will be developed.

## 5.1 Probabilistic model

For ease of reference, a brief description of the probabilistic model for IMLOP is described here. As mentioned earlier, IMLOP incorporates isotropic Gaussian and Fisher distributions<sup>114</sup> to model measurement errors in position and orientation data, respectively, into its probabilistic framework. The Fisher distribution is the analog of the Gaussian distribution on the sphere.<sup>114</sup> Therefore, combining these two distributions to model oriented-point measurement error is analytically convenient.<sup>78</sup> As before, assuming zero-mean, independent, identically distributed (iid) error for both position and orientation data, the *match likelihood function* for an oriented data point,  $\mathbf{x} = (\mathbf{x}_p, \hat{\mathbf{x}}_n)$ , transformed by a current registration estimate,  $[\mathbf{R}, \mathbf{t}]$ , is defined

## CHAPTER 5. D-IMLOP ALGORITHM

as<sup>52</sup>

$$f_{\text{match}}(\mathbf{x}; \mathbf{y}, \sigma^2, \kappa, \mathbf{R}, \mathbf{t}) = \frac{\kappa}{\sqrt{(2\pi\sigma^2)^3} \cdot 2\pi(e^\kappa - e^{-\kappa})} \cdot e^{\kappa\hat{\mathbf{y}}_n\mathbf{R}\hat{\mathbf{x}}_n - \frac{1}{2\sigma^2}\|\mathbf{y}_p - \mathbf{R}\mathbf{x}_p - \mathbf{t}\|_2^2}, \quad (5.1)$$

where  $\mathbf{y} = (\mathbf{y}_p, \mathbf{y}_n)$  is an oriented point on the shape model that is assumed to be in correspondence with the oriented data point,  $\mathbf{x}$ ,  $\sigma^2$  is the *variance* of the positional noise model, and  $\kappa$  is the *concentration parameter* of the orientation noise model.<sup>52</sup> The oriented model point,  $\mathbf{y} \in \Psi$ , is also a parameter of the joint distribution from which the orientation noise is drawn, where  $\hat{\mathbf{y}}_n$  is the central direction and  $\mathbf{y}_p$  is the mean position.<sup>52</sup> This is the match likelihood function that is maximized during the correspondence phase of the IMLOP algorithm in order to find the oriented matched points,  $\mathbf{y}$ , on the model shape,  $\Psi$ .

There are a few differences between this formulation and the formulation in the deformable version of this algorithm. First, D-IMLOP incorporates a generalized Gaussian noise that is able to account for both isotropic and anisotropic noise to model measurement errors in position data. Therefore, the formulation for the *deformable match likelihood function* is slightly different from Eq. 5.1:

$$f_{\text{match}}(\mathbf{x}; \mathbf{y}, \Sigma_x, \Sigma_y, \kappa, \mathbf{R}, \mathbf{t}) = \frac{\kappa}{\sqrt{(2\pi)^3 |\mathbf{R}\Sigma_x\mathbf{R}^T + \Sigma_y|} \cdot 2\pi(e^\kappa - e^{-\kappa})} \cdot e^{\kappa\hat{\mathbf{y}}_n\mathbf{R}\hat{\mathbf{x}}_n - \frac{1}{2}(\mathbf{y}_p - \mathbf{R}\mathbf{x}_p - \mathbf{t})^T(\mathbf{R}\Sigma_x\mathbf{R}^T + \Sigma_y)^{-1}(\mathbf{y}_p - \mathbf{R}\mathbf{x}_p - \mathbf{t})}, \quad (5.2)$$

## CHAPTER 5. D-IMLOP ALGORITHM

where measurement error covariances,  $\Sigma_x$  and  $\Sigma_y$ , are used to describe the positional noise model for  $\mathbf{x}$  and  $\mathbf{y}$ , respectively, instead of  $\sigma^2$ . As in D-IMLP, the oriented matched points in D-IMLOP are also found on the current deformed shape.

Similarly, the deformable match likelihood function for an oriented point,  $\mathbf{x}$ , transformed by a *similarity* registration estimate,  $[a, \mathbf{R}, \mathbf{t}]$ , is defined as

$$f_{\text{match}}(\mathbf{x}; \mathbf{y}, \Sigma_x, \Sigma_y, \kappa, a, \mathbf{R}, \mathbf{t}) = \frac{\kappa}{\sqrt{(2\pi)^3 |\mathbf{R}\Sigma_x\mathbf{R}^T + \Sigma_y|} \cdot 2\pi(e^\kappa - e^{-\kappa})} \cdot e^{\kappa\hat{\mathbf{y}}_n\mathbf{R}\hat{\mathbf{x}}_n - \frac{1}{2}(\mathbf{y}_p - a\mathbf{R}\mathbf{x}_p - \mathbf{t})^T(\mathbf{R}\Sigma_x\mathbf{R}^T + \Sigma_y)^{-1}(\mathbf{y}_p - a\mathbf{R}\mathbf{x}_p - \mathbf{t})}, \quad (5.3)$$

where  $a$  is the scale variable. Since, the two registration problems are similar, the focus of this chapter will be on derivations from Eq. 5.2, with differences between the two pointed out whenever required. Maximizing the likelihood of Eq. 5.2 is equivalent to minimizing its negative log likelihood, resulting in the following *deformable match error function*:

$$E_{\text{D-IMLOP}}(\mathbf{x}, \mathbf{y}, \Sigma_x, \Sigma_y, \kappa, \mathbf{R}, \mathbf{t}) = \frac{1}{2}(\mathbf{y} - \mathbf{R}\mathbf{x} - \mathbf{t})^T(\mathbf{R}\Sigma_x\mathbf{R}^T + \Sigma_y)^{-1}(\mathbf{y} - \mathbf{R}\mathbf{x} - \mathbf{t}) - \kappa\hat{\mathbf{y}}_n\mathbf{R}\hat{\mathbf{x}}_n. \quad (5.4)$$

In the registration phase, IMLOP solves for the rigid transformation that maximizes the total match likelihood function derived from Eq. 5.1. This simplifies to minimizing the *total match error function* with respect to the transformation param-

eters:<sup>52</sup>

$$\mathbb{T} = \operatorname{argmin}_{[\mathbf{R}, \mathbf{t}]} \left( \frac{1}{2\sigma^2} \sum_{i=1}^{n_{\text{data}}} \|\mathbf{y}_{\mathbf{p}_i} - \mathbf{R}\mathbf{x}_{\mathbf{p}_i} - \mathbf{t}\|_2^2 - \kappa \sum_{i=1}^{n_{\text{data}}} \hat{\mathbf{y}}_{\mathbf{n}_i} \mathbf{R} \hat{\mathbf{x}}_{\mathbf{n}_i} \right), \quad (5.5)$$

which is the registration cost function for IMLOP.

Plugging  $f_{\text{match}}$  from Eq. 5.2 into the total deformable match likelihood function of Eq. 3.11, the *deformable registration cost function* for D-IMLOP can be derived as:

$$\mathbb{T} = \operatorname{argmin}_{[\mathbf{R}, \mathbf{t}], \mathbf{s}} \left( \frac{1}{2} \sum_{i=1}^{n_{\text{data}}} (\mathbb{T}_{\text{ssm}}(\mathbf{y}_{\mathbf{p}_i}, \mathbf{s}) - \mathbf{R}\mathbf{x}_{\mathbf{p}_i} - \mathbf{t})^{\mathbf{T}} (\mathbf{R}\Sigma_{\mathbf{x}}\mathbf{R}^{\mathbf{T}})^{-1} (\mathbb{T}_{\text{ssm}}(\mathbf{y}_{\mathbf{p}_i}, \mathbf{s}) - \mathbf{R}\mathbf{x}_{\mathbf{p}_i} - \mathbf{t}) - \kappa \sum_{i=1}^{n_{\text{data}}} \hat{\mathbf{y}}_{\mathbf{n}_i} \mathbf{R} \hat{\mathbf{x}}_{\mathbf{n}_i} + \frac{1}{2} \sum_{j=1}^{n_{\text{m}}} \|\mathbf{s}_j\|_2^2 \right), \quad (5.6)$$

where the model shape covariances,  $\Sigma_{\mathbf{y}_i}$ , are again assumed to be zero since the focus here is on the derivatives introduced by the shape deformations during optimization.

## 5.2 Algorithm overview

In this section, a high level overview of D-IMLOP is presented along with pseudocode explaining the registration pipeline. As before, in order to maintain focus on the new developments made for the D-IMLOP algorithm, in-depth details developed along with the IMLOP algorithm will not be repeated here, but will be referenced whenever necessary. Similarly, details already explained during the development of





---

**Algorithm 5.1:** D-IMLOP (*continued...*)
 

---

11 Update the outlier noise-model terms (Eq. 4.10):

$$\varphi_i \leftarrow \begin{cases} \varphi_{\text{exp}} \|\mathbf{y}_{\mathbf{p}_i} - \underline{a}\mathbf{R}\mathbf{x}_{\mathbf{p}_i} - \mathbf{t}\|_2^2 & \text{if } (\mathbf{x}_i, \mathbf{y}_i) \text{ is an outlier,} \\ 0 & \text{otherwise.} \end{cases}$$

12 Set the noise-model covariances for the registration phase:

$$\Sigma_{\mathbf{x}_i}^* \leftarrow \Sigma_{\mathbf{x}_i} + \Sigma_{\text{Sx}_i} + \frac{\varphi_i}{2}\mathbf{I}, \quad \Sigma_{\mathbf{y}_i}^* \leftarrow \Sigma_{\mathbf{y}_i} + \Sigma_{\text{Sy}_i} + \frac{\varphi_i}{2}\mathbf{I} + \sigma_{\text{match}}^2\mathbf{I}$$

13 Update the transformation and shape to align the point cloud and the corresponding points on the shape (Eq. 5.15 or 5.16):

$$[\underline{a}, \mathbf{R}, \mathbf{t}], \mathbf{s} \leftarrow \underset{[\underline{a}, \mathbf{R}, \mathbf{t}], \mathbf{s}}{\text{argmin}} \left( \frac{1}{2} \sum_{i=1}^{n_{\text{data}}} \left( (\mathbf{T}_{\text{ssm}}(\mathbf{y}_{\mathbf{p}_i}, \mathbf{s}) - \underline{a}\mathbf{R}\mathbf{x}_{\mathbf{p}_i} - \mathbf{t})^{\text{T}} (\mathbf{R}\Sigma_{\mathbf{x}_i}\mathbf{R}^{\text{T}})^{-1} \right. \right. \\ \left. \left. (\mathbf{T}_{\text{ssm}}(\mathbf{y}_{\mathbf{p}_i}, \mathbf{s}) - \underline{a}\mathbf{R}\mathbf{x}_{\mathbf{p}_i} - \mathbf{t}) \right) + \kappa \sum_{i=1}^{n_{\text{data}}} (1 - \hat{\mathbf{y}}_{\mathbf{n}_i} \mathbf{R} \hat{\mathbf{x}}_{\mathbf{n}_i}) + \frac{1}{2} \sum_{j=1}^{n_{\text{m}}} \|s_j\|_2^2 \right)$$

14 Based on computed  $\mathbf{s}$ , update the vertices of the model shape (Eq. 3.10):

$$\Psi_{\text{iter}} \leftarrow \mathbf{T}_{\text{ssm}}(\mathbf{v}_i, \mathbf{s})$$

15 Update extents of PD-tree bounding boxes based on  $\Psi_{\text{iter}}$  (Sec. 3.2)

16 Update orientation noise-model parameters:

$$\kappa = \frac{\bar{R}(3 - \bar{R}^2)}{1 - \bar{R}^2}$$

17  $\text{iter}++$

**end**

18 Detect registration failure using a chi-square test (Eqs. 4.11, 5.13):

Registration is unsuccessful if

$$\sum_{i=1}^{n_{\text{data}}} \text{E}_{\text{SqrMahalDist}}(\mathbf{x}_{\mathbf{p}_i}, \mathbf{y}_{\mathbf{p}_i}, \Sigma_{\mathbf{x}_i}, \Sigma_{\mathbf{y}_i} + \sigma_{\text{match}}^2\mathbf{I}, \underline{a}, \mathbf{R}, \mathbf{t}) \geq \chi_{\text{pos\_thresh\_final}}^2$$

$$\text{OR} \quad \sum_{i=1}^{n_{\text{data}}} \text{E}_{\text{SqrIsoAngRes}}(\hat{\mathbf{x}}_{\mathbf{n}_i}, \hat{\mathbf{y}}_{\mathbf{n}_i}, \kappa, \mathbf{R}) \geq \chi_{\text{ang\_thresh\_final}}^2$$


---

## CHAPTER 5. D-IMLOP ALGORITHM

the D-IMLP algorithm will be referenced and not repeated here. Algorithm 5.1 summarizes the D-IMLOP algorithm, and will be referenced throughout this section. Underlined variables in Alg. 5.1 indicate optional variables that are required when solving additionally for scale.

The inputs to this algorithm are similar to the inputs to the D-IMLP algorithm.  $\mathbf{X}$  and  $\Psi$  represent the data points and the statistically mean model shape, respectively, except that now these features must have an orientation component associated with each position component.  $\mathbf{w}$ , as before, are the mode weights that represent the statistics associated with the model shape. The measurement-error covariances associated with the data points and model shape are represented by  $\Sigma_{\mathbf{x}}$  and  $\Sigma_{\Psi}$ , respectively, and surface-model covariances for the data points and model shape are represented by  $\Sigma_{S\mathbf{x}}$  and  $\Sigma_{S\Psi}$ , respectively. As with D-IMLP,  $\Sigma_{\mathbf{x}}$  and  $\Sigma_{\Psi}$  are assumed to be generated from an isotropic Gaussian with SD  $1 \times 1 \times 1 \text{ mm}^3$ . This default value can be modified by the user based on requirement. The orientation noise is assumed to be drawn from an isotropic Fisher distribution with a default circular SD,  $\sigma_{\text{circ.deg}}$ , of  $2^\circ$ . This value can also be modified by the user based on the application.

An initial transformation consisting of an estimated rotation, translation, and, optionally, scale, and an initial set of shape parameters to define the initial shape, which we set to 0 or the mean shape, must be specified. The orientation noise

## CHAPTER 5. D-IMLOP ALGORITHM

concentration parameter,  $\kappa$ , is initialized based on  $\sigma_{\text{circ\_deg}}$  in radians:

$$\begin{aligned}\sigma_{\text{circ\_rad}} &= \sigma_{\text{circ\_deg}} \frac{\pi}{180} \\ \kappa_0 &= \frac{1}{\sigma_{\text{circ\_rad}}^2}\end{aligned}\tag{5.7}$$

The remaining input parameters will be discussed as they are encountered in the equations seen in the algorithm (Alg. 5.1) with the exception of those that have already been covered in Alg. 4.1. The output of the algorithm is a final transform that aligns the data points to the final deformed shape, defined by the final set of shape parameters.

The convergence criteria for D-IMLOP are identical to those of D-IMLP. Until convergence, every iteration of D-IMLOP computes the correspondences between the oriented data points and the current orientated model shape. After correspondences are found, the match uncertainty term for the position component of the matched points is updated as described in Alg. 4.1. In addition, a threshold,  $\theta_{\text{thresh}}$ , for the orientation component of the matched points is updated using the SD of  $\varphi_{\text{exp}}$  and the circular SD,  $\theta_{\text{circ}}$ , of the average orientation error between inlying matched points.

$$\hat{\mathbf{y}}_{\mathbf{n}_i}^T \hat{\mathbf{x}}_{\mathbf{n}_i} < \cos(\theta_{\text{thresh}})\tag{5.8}$$

is used in addition to  $\chi_{\text{thresh}}^2$  to identify outliers in the orientation and position components of the matched points, respectively. First, correspondences are tested for

## CHAPTER 5. D-IMLOP ALGORITHM

outliers in the position component, and correspondences that are identified as inliers are additionally tested for outliers in the orientation component. This is reasonable since points sampled from surfaces facing opposite directions can have low match error in the position component, but would have an extremely high error in the orientation component. Points that pass both these tests are marked as inliers.

The remaining noise-model updates before registration are identical to those in Alg. 4.1. An additional update is made post registration in order to update the concentration of orientation error,  $\kappa$ , which is estimated using an approximation to its maximum likelihood estimate:<sup>52</sup>

$$\begin{aligned} \kappa &\approx \frac{\bar{R}(3 - \bar{R}^2)}{1 - \bar{R}^2}, \\ \text{where } \bar{R} &= \frac{1 - \omega}{n_{\text{data}}} \sum_{i=1}^{n_{\text{data}}} \hat{y}_{\mathbf{n}_i}^T \mathbf{R} \hat{\mathbf{x}}_{\mathbf{n}_i} + \frac{\omega}{\alpha} \sum_{i=1}^{n_{\text{data}}} \mathbf{y}'_{p_i}{}^T \mathbf{R} \mathbf{x}'_{p_i}, \\ \alpha &= \sum_{i=1}^{n_{\text{data}}} \|\mathbf{y}'_{p_i}\| \cdot \|\mathbf{R} \mathbf{x}'_{p_i}\|, \\ \mathbf{x}'_{p_i} &= \mathbf{x}_{p_i} - \frac{1}{n_{\text{data}}} \sum_{i=1}^{n_{\text{data}}} \mathbf{x}_{p_i}, \quad \mathbf{y}'_{p_i} = \mathbf{y}_{p_i} - \frac{1}{n_{\text{data}}} \sum_{i=1}^{n_{\text{data}}} \mathbf{y}_{p_i}, \end{aligned} \tag{5.9}$$

where  $\omega$  weights the relative importance of the orientation and position data terms used to estimate  $\kappa$ .<sup>52</sup> Both position data and orientation data are used to estimate the distribution of orientation match errors because it is often possible to find good orientation matches for any given orientation for a closed shape model.<sup>52</sup> An extreme case example is a sphere, where any orientation of the shape would result in nearly perfect orientation matches. Therefore, estimating  $\kappa$  based only on the orientation

## CHAPTER 5. D-IMLOP ALGORITHM

component of matches would progressively over-estimate  $\kappa$  by allowing it to grow extremely large.<sup>52</sup> This can result in geometrically inconsistent matches, and to prevent this, rotational misalignment is represented in both the orientation and position components of the matched points when computing  $\bar{R}$ . By default, the orientation and position components are equally weighted using  $\omega = 0.5$ . The user can, however, increase or decrease this value in the interval  $[0, 1]$  based on whether the application allows for low or high confidence in the orientation component, respectively. It may also be desirable to use an alternate formulation for  $\bar{R}$  that restricts the effect of position errors to only decrease orientation confidence:<sup>52</sup>

$$\bar{R} = \min \left( \frac{1}{n_{\text{data}}} \sum_{i=1}^{n_{\text{data}}} \hat{\mathbf{y}}_{\mathbf{n}_i}^T \mathbf{R} \hat{\mathbf{x}}_{\mathbf{n}_i}, \frac{1-\omega}{n_{\text{data}}} \sum_{i=1}^{n_{\text{data}}} \hat{\mathbf{y}}_{\mathbf{n}_i}^T \mathbf{R} \hat{\mathbf{x}}_{\mathbf{n}_i} + \frac{\omega}{\alpha} \sum_{i=1}^{n_{\text{data}}} \mathbf{y}'_{p_i}^T \mathbf{R} \mathbf{x}'_{p_i} \right). \quad (5.10)$$

Once convergence or termination has been reached and a final registration computed, two chi-square tests are used to determine whether the registration produced is successful or unsuccessful. The first test, shown in Step 18 of Alg 5.1, is identical to the test used in D-IMLP (Eq. 4.11). However, this test only evaluates the quality of matches based on the positional components. Since there is an additional orientation component in D-IMLOP, an additional test is performed to evaluate the quality of matches based on the orientation components if the registration is not rejected based on positional components. To evaluate whether the orientations of corresponding points are consistent, a 2D wrapped-Gaussian approximation to the Fisher distribu-

## CHAPTER 5. D-IMLOP ALGORITHM

tion is used to convert the noise model for the orientation residuals to Gaussian form in order to leverage the chi-square test with  $2n_{\text{data}}$  DOF.

A wrapped-Gaussian with zero mean has the form

$$\frac{1}{\sigma\sqrt{2\pi}} \sum_{k=-\infty}^{\infty} e^{-\frac{(\theta_{\mathbf{n}}+2\pi k)^2}{2\sigma^2}}, \quad (5.11)$$

and in its approximation of the Fisher distribution,  $\theta_{\mathbf{n}} = \cos^{-1}(\hat{\mathbf{y}}_{\mathbf{n}}\mathbf{R}\hat{\mathbf{x}}_{\mathbf{n}})$  is the angular residual between  $\hat{\mathbf{x}}_{\mathbf{n}}$  and  $\hat{\mathbf{y}}_{\mathbf{n}}$  and  $\sigma^2 \approx \frac{1}{\kappa}$  is the variance of the Fisher noise model. Under the assumption of correspondence and a wrapped-Gaussian approximation of Fisher noise, the sum of square angular residual errors between the orientations of matched points can be assumed to be distributed as the sum of squares of  $2n_{\text{data}}$  independent wrapped-Gaussian distributions. Therefore, the sum of square angular residual has a chi-square distribution with  $2n_{\text{data}}$  DOF and a registration can be rejected by comparing the sum of square angular residual errors over all corresponding pairs,  $(\mathbf{x}_i, \mathbf{y}_i)$ ,

$$\sum_{i=1}^{n_{\text{data}}} \text{E}_{\text{SqIsoAngRes}}(\hat{\mathbf{x}}_{\mathbf{n}_i}, \hat{\mathbf{y}}_{\mathbf{n}_i}, \kappa, \mathbf{R}) = \sum_{i=1}^{n_{\text{data}}} \kappa (\cos^{-1}(\hat{\mathbf{y}}_{\mathbf{n}_i}^{\text{T}}\mathbf{R}\hat{\mathbf{x}}_{\mathbf{n}_i}))^2 \quad (5.12)$$

to the value of the chi-square inverse CDF with  $2n_{\text{data}}$  DOF at some probability,  $p$ , denoted by  $\text{chi2inv}(p, 2n_{\text{data}})$ . If a registration is not already rejected based on the sum of square Mahalanobis distances computed over all  $(\mathbf{x}_i, \mathbf{y}_i)$ , then the registration

can be rejected if

$$\sum_{i=1}^{n_{\text{data}}} E_{\text{SqrIsoAngRes}}(\hat{\mathbf{x}}_{\mathbf{n}_i}, \hat{\mathbf{y}}_{\mathbf{n}_i}, \kappa, \mathbf{R}) > \text{chi2inv}(p, 2n_{\text{data}}) = \chi_{\text{ang\_thresh\_final}}^2, \quad (5.13)$$

ensuring that the angular residual remains within  $[0, 2\pi)$ . If the registration passes both tests, then the registration is successful.

### 5.3 Correspondence phase

In this section, the implementation of the correspondence phase of the D-IMLOP algorithm is explained. In the correspondence phase, D-IMLOP computes the most likely oriented match on the current model shape for each data point by minimizing the match error function of Eq. 5.4. For the implementation of D-IMLOP, Eq. 5.4 is rewritten with the addition of an extra  $\kappa$  term to ensure that  $E_{\text{D-IMLOP}}$  is always positive (see<sup>78</sup> for justification):

$$E_{\text{D-IMLOP}}(\mathbf{x}, \mathbf{y}, \Sigma_{\mathbf{x}}, \Sigma_{\mathbf{y}}, \mathbf{R}, \mathbf{t}) = (\mathbf{y} - \mathbf{R}\mathbf{x} - \mathbf{t})^{\text{T}}(\mathbf{R}\Sigma_{\mathbf{x}}\mathbf{R}^{\text{T}} + \Sigma_{\mathbf{y}})^{-1}(\mathbf{y} - \mathbf{R}\mathbf{x} - \mathbf{t}) + \kappa(1 - \hat{\mathbf{y}}_{\mathbf{n}}\mathbf{R}\hat{\mathbf{x}}_{\mathbf{n}}). \quad (5.14)$$

As in the correspondence phase of D-IMLP, the main difference here from IMLOP is that the oriented matched points,  $\mathbf{y}$ , lie on a shape that changes at every iteration. The PD-tree construction and search strategies are also similar to that of IMLP,



with differences stemming from the additional orientation component of the features. Therefore, *directional* PD-trees are used for D-IMLOP which contain additional parameters within each node for orientation information. This PD-tree is identical to the PD-tree used in the implementation of IMLOP,<sup>52</sup> and therefore, details of its construction and search strategies will not be repeated here. The difference, as in D-IMLP, is that the PD-tree is updated at each iteration, as described in Sec. 4.3, in order to incorporate the deformations in the model shape at each iteration.

## 5.4 Registration phase

Once correspondences on the current model shape are found, the deformable registration cost function for D-IMLOP (Eq. 5.6) is minimized with respect to the data transformation parameters as well as the model shape parameters to compute the transformation and shape parameters that best align the correspondences. As with the match error function, the deformable registration cost function is rewritten to ensure that it is always positive:

$$\begin{aligned}
 T = \operatorname{argmin}_{[\mathbf{R}, \mathbf{t}], \mathbf{s}} & \left( \frac{1}{2} \sum_{i=1}^{n_{\text{data}}} (\mathbf{T}_{\text{ssm}}(\mathbf{y}_{\mathbf{p}_i}, \mathbf{s}) - \mathbf{R}\mathbf{x}_{\mathbf{p}_i} - \mathbf{t})^T (\mathbf{R}\Sigma_{\mathbf{x}}\mathbf{R}^T)^{-1} (\mathbf{T}_{\text{ssm}}(\mathbf{y}_{\mathbf{p}_i}, \mathbf{s}) - \mathbf{R}\mathbf{x}_{\mathbf{p}_i} - \mathbf{t}) \right. \\
 & \left. + \kappa \sum_{i=1}^{n_{\text{data}}} (1 - \hat{\mathbf{y}}_{\mathbf{n}_i} \mathbf{R} \hat{\mathbf{x}}_{\mathbf{n}_i}) + \frac{1}{2} \sum_{j=1}^{n_{\text{m}}} \|s_j\|_2^2 \right).
 \end{aligned} \tag{5.15}$$

## CHAPTER 5. D-IMLOP ALGORITHM

If, instead, a *similarity* transform is computed between the data points and the corresponding oriented matched points on the current model shape, then the cost function changes slightly to incorporate the scale factor,  $a$ :

$$\mathbf{T} = \underset{[a, \mathbf{R}, \mathbf{t}], \mathbf{s}}{\operatorname{argmin}} \left( \frac{1}{2} \sum_{i=1}^{n_{\text{data}}} (\mathbf{T}_{\text{ssm}}(\mathbf{y}_{\mathbf{p}_i}, \mathbf{s}) - a\mathbf{R}\mathbf{x}_{\mathbf{p}_i} - \mathbf{t})^{\mathbf{T}} (\mathbf{R}\Sigma_{\mathbf{x}}\mathbf{R}^{\mathbf{T}})^{-1} \right. \\ \left. (\mathbf{T}_{\text{ssm}}(\mathbf{y}_{\mathbf{p}_i}, \mathbf{s}) - a\mathbf{R}\mathbf{x}_{\mathbf{p}_i} - \mathbf{t}) + \kappa \sum_{i=1}^{n_{\text{data}}} (1 - \hat{\mathbf{y}}_{\mathbf{n}_i} \mathbf{R} \hat{\mathbf{x}}_{\mathbf{n}_i}) + \frac{1}{2} \sum_{j=1}^{n_{\text{m}}} \|s_j\|_2^2 \right). \quad (5.16)$$

As in the registration phase of D-IMLP, before this minimization is performed, barycentric coordinates of the matched points are computed to find the vertex weights,  $\mu^{(j)}$ , for  $j = 1, 2, 3$ , for each matched point (Eq. 3.9). These  $\mu^{(j)}$  are required during optimization to compute the deformed matched point,  $\mathbf{T}_{\text{ssm}}(\mathbf{y}_{\mathbf{p}_i}, \mathbf{s})$ , as the shape is recomputed for different values of  $\mathbf{s}$ .

Both these objective functions can be optimized by computing gradients with respect to the optimization parameters, and applying a nonlinear quasi-Newton based optimizer. In order to do this, the variables being optimized need to be reparametrized as in the optimization for D-IMLP. Specifically, the constraints of the rotation matrix, that is,  $\mathbf{R}^{\mathbf{T}}\mathbf{R} = \mathbf{I}$  and  $\det(\mathbf{R}) = 1$ , are enforced using Rodrigues' parameterization, which represents rotation as a 3-vector,  $\mathbf{r} = [r_x, r_y, r_z]$ .<sup>51</sup> The direction and magnitude of  $\mathbf{r}$  signify the axis and angular extent of rotation, respectively. Further, the transformation  $\mathbf{T}(\mathbf{x}_{\mathbf{p}_i})$  is re-expressed in the reference frame of  $\mathbf{Y}$  as  $\mathbf{T}(\mathbf{y}_{\mathbf{p}_i})$  in order to

## CHAPTER 5. D-IMLOP ALGORITHM

keep all transformation in the same space. The deformable registration cost function of Eq. 5.15 can then be re-written as

$$\mathbf{T} = \underset{[\mathbf{r}, \mathbf{t}], \mathbf{s}}{\operatorname{argmin}} \left( \sum_{i=1}^{n_{\text{data}}} (C_{\mathbf{p}i} + C_{\mathbf{n}i}) + C_{\text{shape}} \right), \quad (5.17)$$

where

$$\begin{aligned} C_{\mathbf{p}i} &= \mathbf{z}_i^{\mathbf{T}} \Sigma_{\mathbf{x}_i}^{-1} \mathbf{z}_i \quad , \quad C_{\mathbf{n}i} = \kappa(1 - \hat{\mathbf{y}}_{\mathbf{n}i}^{\mathbf{T}} \mathbf{R} \hat{\mathbf{x}}_{\mathbf{n}i}) \quad \text{and} \quad C_{\text{shape}} = \mathbf{s}^{\mathbf{T}} \mathbf{s}, \\ \mathbf{z}_i &= \mathbf{R}(\mathbf{r})^{\mathbf{T}} (\mathbf{T}_{\text{ssm}}(\mathbf{y}_{\mathbf{p}i}, \mathbf{s}) - \mathbf{R}(\mathbf{r}) \mathbf{x}_{\mathbf{p}i} - \mathbf{t}) \\ &= \mathbf{R}(\mathbf{r})^{\mathbf{T}} (\mathbf{T}_{\text{ssm}}(\mathbf{y}_{\mathbf{p}i}, \mathbf{s}) - \mathbf{t}) - \mathbf{x}_{\mathbf{p}i}. \end{aligned} \quad (5.18)$$

$\mathbf{R}(\mathbf{r})$  is the  $3 \times 3$  rotation matrix corresponding to the Rodrigues' vector,  $\mathbf{r}$  (defined previously in Sec. 4.4). Similarly, Eq. 5.16 can be re-written as

$$\mathbf{T} = \underset{[a, \mathbf{r}, \mathbf{t}], \mathbf{s}}{\operatorname{argmin}} \left( \sum_{i=1}^{n_{\text{data}}} (C_{\mathbf{p}i} + C_{\mathbf{n}i}) + C_{\text{shape}} \right), \quad (5.19)$$

with a slight modification in the  $C_{\mathbf{p}i}$  term in Eq. 5.18, so that

$$\begin{aligned} C_{\mathbf{p}i} &= \mathbf{z}_i^{\mathbf{T}} \Sigma_{\mathbf{x}_i}^{-1} \mathbf{z}_i \quad , \quad C_{\mathbf{n}i} = \kappa(1 - \hat{\mathbf{y}}_{\mathbf{n}i}^{\mathbf{T}} \mathbf{R} \hat{\mathbf{x}}_{\mathbf{n}i}) \quad \text{and} \quad C_{\text{shape}} = \mathbf{s}^{\mathbf{T}} \mathbf{s}, \\ \mathbf{z}_i &= \mathbf{R}(\mathbf{r})^{\mathbf{T}} (\mathbf{T}_{\text{ssm}}(\mathbf{y}_{\mathbf{p}i}, \mathbf{s}) - \mathbf{t}) - a \mathbf{x}_{\mathbf{p}i}. \end{aligned} \quad (5.20)$$

Next, the gradient,  $\nabla \mathbf{C}$ , of the deformable registration cost function of Eq. 5.17 with respect to the transformation parameters  $[\mathbf{r}, \mathbf{t}]$  and the deformable shape pa-

## CHAPTER 5. D-IMLOP ALGORITHM

rameters,  $\mathbf{s}$ , is discussed. As for D-IMLP,  $\nabla \mathbf{C}$  is a stacked vector with the data transformation parameters located on top of the deformable shape parameters, and  $\mathbf{J}_{a,b}$  is used to express the Jacobian of an expression,  $a$ , with respect to variable,  $b$ . Using these notations,  $\nabla \mathbf{C}$  is expressed as:

$$\nabla \mathbf{C} = \sum_{i=1}^{n_{\text{data}}} (\nabla C_{p_i} + \nabla C_{n_i}) + \nabla C_{\text{shape}} \quad (5.21)$$

$$\nabla C_{p_i} = [\mathbf{J}_{C_{p_i}, \mathbf{z}_i} \mathbf{J}_{\mathbf{z}_i, \mathbf{r}} , \mathbf{J}_{C_{p_i}, \mathbf{z}_i} \mathbf{J}_{\mathbf{z}_i, \mathbf{t}} , \mathbf{J}_{C_{p_i}, \mathbf{z}_i} \mathbf{J}_{\mathbf{z}_i, \mathbf{s}}]^\mathbf{T}, \quad \text{where}$$

$$\begin{aligned} \mathbf{J}_{C_{p_i}, \mathbf{z}_i} &= 2\mathbf{z}_i^\mathbf{T} \Sigma_{\mathbf{x}_i}^{-1} \\ \mathbf{J}_{\mathbf{z}_i, \mathbf{r}} &= \left[ \frac{\partial \mathbf{R}(\mathbf{r})^\mathbf{T}}{\partial \mathbf{r}_x} (\mathbf{T}_{\text{ssm}}(\mathbf{y}_{\mathbf{p}_i}, \mathbf{s}) - \mathbf{t}) , \frac{\partial \mathbf{R}(\mathbf{r})^\mathbf{T}}{\partial \mathbf{r}_y} (\mathbf{T}_{\text{ssm}}(\mathbf{y}_{\mathbf{p}_i}, \mathbf{s}) - \mathbf{t}) , \right. \\ &\quad \left. \frac{\partial \mathbf{R}(\mathbf{r})^\mathbf{T}}{\partial \mathbf{r}_z} (\mathbf{T}_{\text{ssm}}(\mathbf{y}_{\mathbf{p}_i}, \mathbf{s}) - \mathbf{t}) \right] \\ \mathbf{J}_{\mathbf{z}_i, \mathbf{t}} &= -\mathbf{R}(r)^\mathbf{T} \end{aligned} \quad (5.22)$$

$$\mathbf{J}_{\mathbf{z}_i, \mathbf{s}} = \mathbf{J}_{\mathbf{z}_i, \mathbf{T}_{\text{ssm}}(\mathbf{y}_{\mathbf{p}_i}, \mathbf{s})} \mathbf{J}_{\mathbf{T}_{\text{ssm}}(\mathbf{y}_{\mathbf{p}_i}, \mathbf{s}), \mathbf{s}}$$

$$\mathbf{J}_{\mathbf{z}_i, \mathbf{T}_{\text{ssm}}(\mathbf{y}_{\mathbf{p}_i}, \mathbf{s})} = \mathbf{R}(\mathbf{r})^\mathbf{T}$$

$$\mathbf{J}_{\mathbf{T}_{\text{ssm}}(\mathbf{y}_{\mathbf{p}_i}, \mathbf{s}), \mathbf{s}} = \sum_{j=1}^3 \mu_i^{(j)} \mathbf{J}_{\mathbf{T}_{\text{ssm}}(\mathbf{v}_i^{(j)}, \mathbf{s}), \mathbf{s}}$$

$$\mathbf{J}_{\mathbf{T}_{\text{ssm}}(\mathbf{v}_i^{(j)}, \mathbf{s}), \mathbf{s}} = [\mathbf{w}_1^p \quad \mathbf{w}_2^p \quad \cdots \quad \mathbf{w}_{\mathbf{n}_m}^p],$$

$$\nabla C_{n_i} = [\mathbf{J}_{C_{n_i}, \mathbf{r}} , 0 , 0]^\mathbf{T} \quad (5.23)$$

CHAPTER 5. D-IMLOP ALGORITHM

$$\mathbf{J}_{C_{n_i}, \mathbf{r}} = \left[ -\kappa \hat{\mathbf{y}}_{n_i}^T \frac{\partial \mathbf{R}(\mathbf{r})^T}{\partial \mathbf{r}_x} \hat{\mathbf{x}}_{n_i}, -\kappa \hat{\mathbf{y}}_{n_i}^T \frac{\partial \mathbf{R}(\mathbf{r})^T}{\partial \mathbf{r}_y} \hat{\mathbf{x}}_{n_i}, -\kappa \hat{\mathbf{y}}_{n_i}^T \frac{\partial \mathbf{R}(\mathbf{r})^T}{\partial \mathbf{r}_z} \hat{\mathbf{x}}_{n_i} \right]$$

and

$$\nabla C_{\text{shape}} = [0, 0, 2\mathbf{s}^T]^T \quad (5.24)$$

The partial derivatives and Jacobians introduced here are identical to those introduced in Eqs. 4.19 and 4.20. The gradient,  $\nabla C$ , of the deformable cost function of Eq. 5.19 with respect to the transformation parameters  $[a, \mathbf{r}, \mathbf{t}]$  and the deformable shape parameters,  $\mathbf{s}$ , is almost the same as  $\nabla C$  defined in Eqs. 5.21, 5.22, 5.23, and 5.24, with an additional component in  $\nabla C_{p_i}$  so that

$$\nabla C_{p_i} = [\mathbf{J}_{C_{p_i}, z_i} \mathbf{J}_{z_i, \mathbf{r}}, \mathbf{J}_{C_{p_i}, z_i} \mathbf{J}_{z_i, \mathbf{t}}, \mathbf{J}_{C_{p_i}, z_i} \mathbf{J}_{z_i, a}, \mathbf{J}_{C_{p_i}, z_i} \mathbf{J}_{z_i, \mathbf{s}}]^T, \quad (5.25)$$

where the new term  $\mathbf{J}_{z_i, a}$  turns out to be

$$\mathbf{J}_{z_i, a} = -\mathbf{x}_{p_i}. \quad (5.26)$$

The  $\nabla C_{n_i}$  and  $\nabla C_{\text{shape}}$  terms simply gain additional zero components so that

$$\nabla C_{n_i} = [\mathbf{J}_{C_{n_i}, \mathbf{r}}, 0, 0, 0]^T \quad (5.27)$$

and

$$\nabla C_{\text{shape}} = [0, 0, 0, 2\mathbf{s}^T]^T. \quad (5.28)$$

As with  $\nabla C$  computed for the deformable registration cost function of D-IMLP,  $\nabla C$  computed here is also dependent on both the number of components in the data transformation parameters and the number of shape parameters. Therefore, the total size of  $\nabla C$  is either 6 + number of shape parameters when the data transformation is a rigid transformation, or 7 + number of shape parameters when the data transformation parameters also include scale in the case of a similarity transformation.

## 5.5 Experimental results and discussion

The experimental design for D-IMLOP was identical to that of D-IMLP. Therefore, the reader is directed to Sec. 4.5 for details about the experiment design and the motivation for each experiment. However, additional details introduced due to the added features of D-IMLOP will be specified here. For instance, the noise model used to generate noisy orientation data, which was not described in the previous chapter since D-IMLP does not make use of orientation information, will be described for each experiment.

### 5.5.1 Sample size experiment

The same setup used and data generated for the experiment designed to evaluate D-IMLP (Sec. 4.5.1 is used here to evaluate D-IMLOP.

#### 5.5.1.1 Experiment 1: Isotropic position noise

As in the previous chapter, the noise model for positional data in this experiment is isotropic with SD of  $1 \times 1 \times 1 \text{ mm}^3$ . For orientation noise, an isotropic noise model with SD of  $2^\circ$  was used. D-IMLOP produced smaller errors compared to D-IMLP in recovering the shape and registering the sampled points to the recovered shape for the different number of samples due to the added information provided by the orientation component of the sample points (Figs. 5.1). In fact, all registration trials resulted in TREs less than 1 mm (Table. 5.1), with TREs decreasing further with increasing number of sample points (Fig. 5.2) As with D-IMLP, the residual error produced by D-IMLOP showed correlation with the TRE (Fig. 5.4). Therefore, using empirically chosen thresholds such that there were no false positives, D-IMLOP was able to detect correct registrations with some success (Table. 5.1).

#### 5.5.1.2 Experiment 2: Anisotropic position noise

An anisotropic noise model with SD  $1 \times 1 \times 2 \text{ mm}^3$  was used for positional noise. For orientation noise, the parameters were the same as in Exp. 5.5.1.1. As in the results from D-IMLP, errors for anisotropic positional noise were slightly higher than those

CHAPTER 5. D-IMLOP ALGORITHM

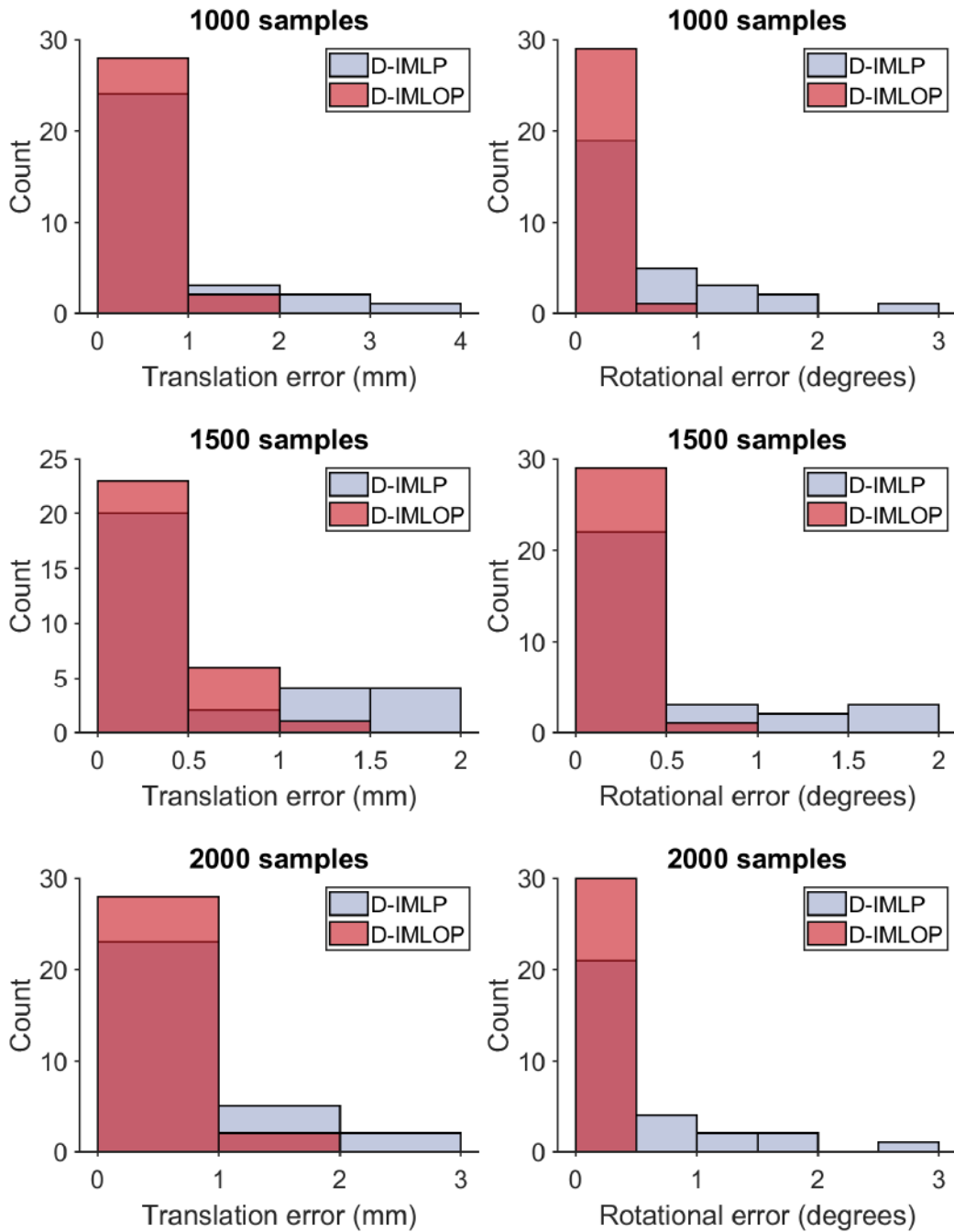


**Figure 5.1:** Sample size experiment: translation (left) and rotation (right) errors produced using, from top to bottom, 1000, 1500 and 2000 data points sampled from the pelvis model in Exp. 1 (Sec. 5.5.1.1)



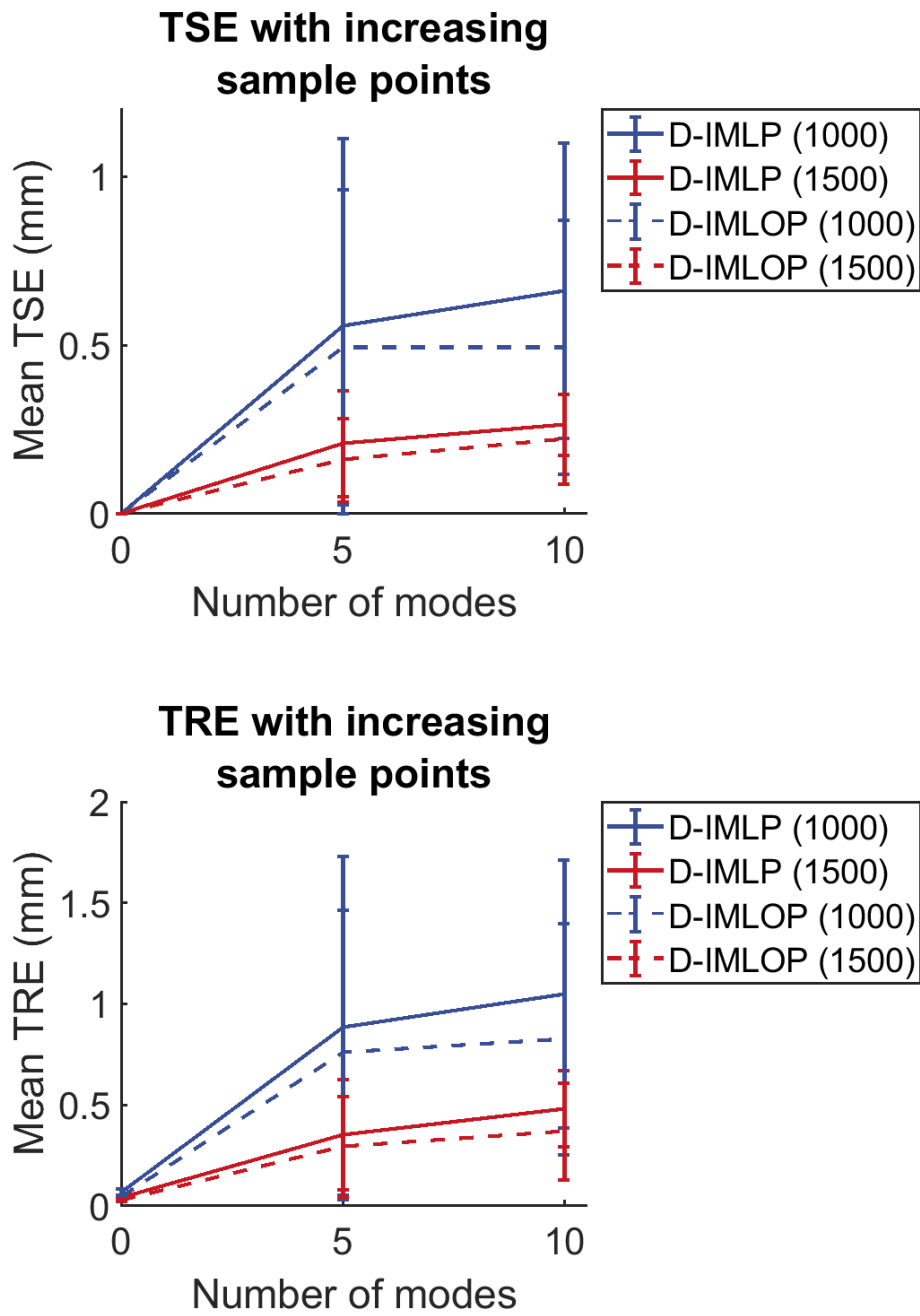


**Figure 5.2:** Sample size experiment: increasing TSE (top) and TRE (bottom) with increasing number of sample points in Exp. 1.

CHAPTER 5. D-IMLOP ALGORITHM

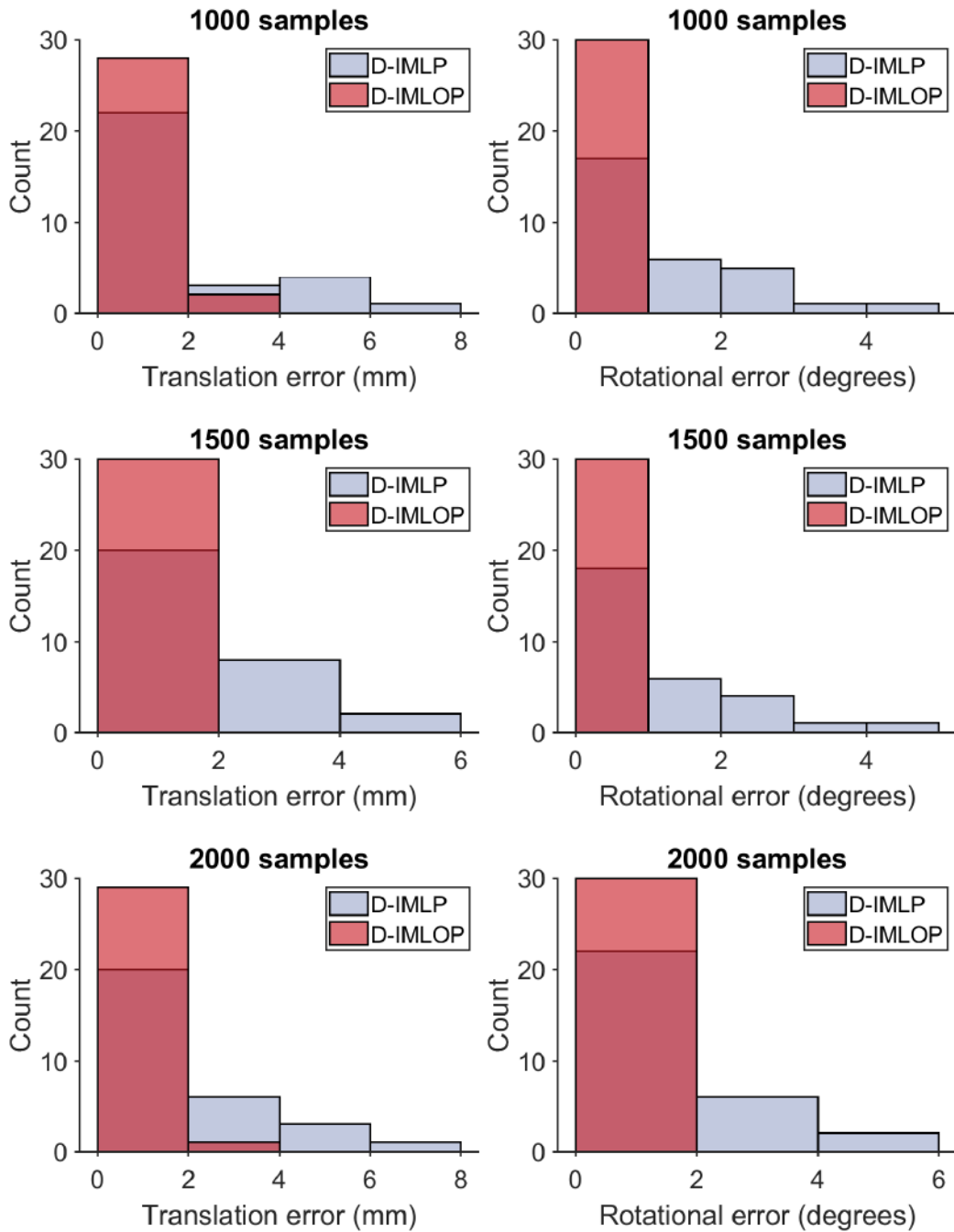


**Figure 5.3:** Sample size experiment: translation (left) and rotation (right) errors produced using, from top to bottom, 1000, 1500 and 2000 data points sampled from the pelvis model in Exp. 2 (Sec. 5.5.1.2)

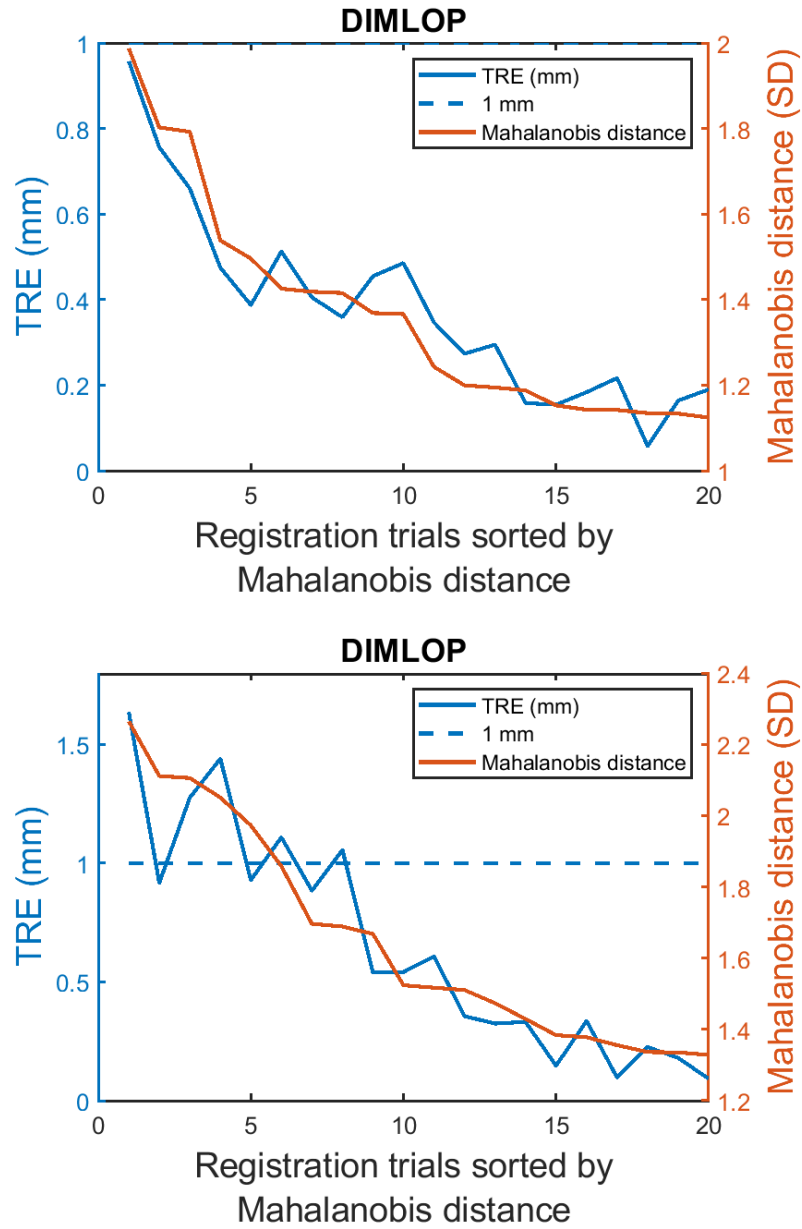


**Figure 5.4:** Sample size experiment: residual errors compared against TRE using 2000 sample points in Exp. 1 (left) and Exp. 2 (right). The two measures exhibit correlation in both experiments 1 and 2 with correlation coefficients of 0.96 and 0.94, respectively.

**Table 5.1:** Sample size experiment: percent successful registration runs, i.e., runs producing TREs less than 1 mm and, in parentheses, percent successful runs correctly detected as successful using residual errors.

	# samples	D-IMLP (%)	D-IMLOP (%)
Experiment 1	1000	73.33 (100.00)	100.00 (66.67)
	1500	76.67 (86.96)	100.00 (63.33)
	2000	80.00 (100.00)	100.00 (66.67)
Experiment 2	1000	56.67 (100.00)	86.67 (100.00)
	1500	46.67 (100.00)	96.67 (100.00)
	2000	56.67 (100.00)	83.33 (88.00)

with isotropic noise (Fig. 5.3). However, a majority of the registrations performed were able to produce successful registrations (Table. 5.1). Using empirically found thresholds, D-IMLOP is more successfully able to use the residual errors produced to correctly classify successful registrations than in the previous experiment (Table. 5.1).

## 5.5.2 Regularization term experiment

As with D-IMLP, the cost function that is minimized to compute a registration using D-IMLOP (Eq. 5.6) contains an L2 regularization term,  $\frac{1}{2} \sum_{j=1}^{n_m} \|s_j\|_2^2$ . The effect of this regularization term is again evaluated by computing registrations without this term on the data generated for Exp. 5.5.1.1 using 1500 sample points. Results showed that removing the regularization term started to show a deteriorating effect on

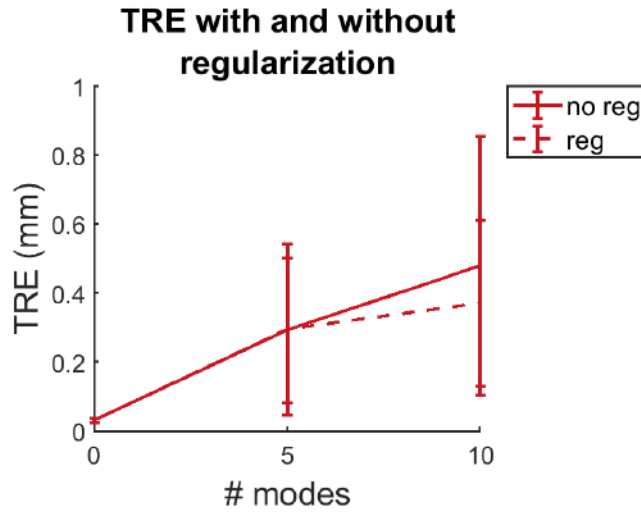


**Figure 5.5:** Regularization term experiment: registrations produced by D-IMLOP without the regularization term showed deterioration with increasing shape parameters.

results produced by D-IMLOP as the number of shape parameters increased (Fig. 5.5).

Therefore, as the optimization becomes harder, the regularization term allows D-IMLOP to generalize better.

### 5.5.3 Noise model experiment

#### 5.5.3.1 Experiment 1: Varying isotropic position noise

As in D-IMLP, 5 isotropic noise models with SDs of  $1 \times 1 \times 1 \text{ mm}^3$ ,  $2 \times 2 \times 2 \text{ mm}^3$ ,  $3 \times 3 \times 3 \text{ mm}^3$ ,  $4 \times 4 \times 4 \text{ mm}^3$ , and  $5 \times 5 \times 5 \text{ mm}^3$  for position noise were used.

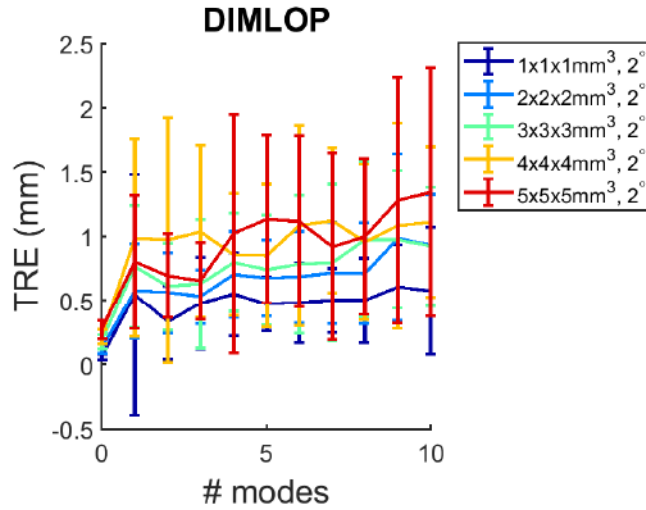


**Figure 5.6:** Noise model experiment: a general trend of increasing TRE as the uncertainty in the sample points increases. Note that errors are increasing with increasing modes because for this experiment the number of modes used to estimate the shapes equals the number of modes used to simulate a new shape from which points were sampled.

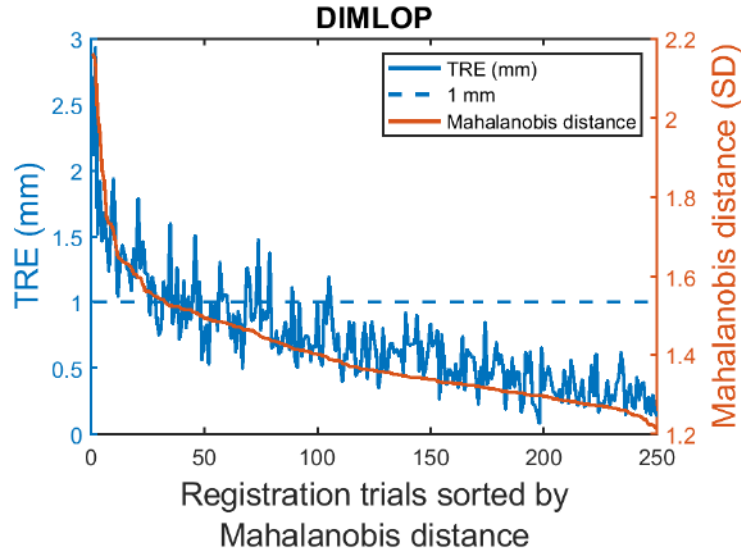


**Figure 5.7:** Noise model experiment: residual errors compared against TRE using 500 sample points with  $2 \times 2 \times 2 \text{ mm}^3$  SD positional noise and  $2^\circ$  SD angular noise in Exp. 1 of the noise model experiment (Sec. 5.5.3.1). The two measures exhibit correlation with correlation coefficient of 0.87.

## CHAPTER 5. D-IMLOP ALGORITHM

An isotropic noise model with SD of  $2^\circ$  for orientation noise was used. As with D-IMLP, D-IMLOP showed a general trend of increasing TRE as the SD of noise increases (Fig. 5.6). However, the TREs produced by D-IMLOP were lower than those produced by D-IMLP. The residual errors were again found to be strongly correlated with the TRE, which again can be used to distinguish between successful and unsuccessful registrations (Fig. 5.7).

### 5.5.3.2 Experiment 2: Varying anisotropic position noise

Anisotropic noise models with SDs of  $1 \times 1 \times 2 \text{ mm}^3$ ,  $2 \times 2 \times 3 \text{ mm}^3$ ,  $3 \times 3 \times 4 \text{ mm}^3$ ,  $3 \times 3 \times 5 \text{ mm}^3$ , and  $4 \times 4 \times 5 \text{ mm}^3$  for positional noise were used. For orientation noise, the parameters were the same as in Exp. 1. Results from this experiment show the same trends as those for isotropic noise (Fig. 5.8), with residual errors again showing strong correlation with the TRE (Fig. 5.9).

### 5.5.3.3 Experiment 3: Varying orientation noise

In the third experiment, one isotropic noise model and one anisotropic noise model with SDs of  $1 \times 1 \times 1 \text{ mm}^3$  and  $1 \times 1 \times 2 \text{ mm}^3$ , respectively, for positional noise were used, and orientation noise models with SDs of  $2^\circ$ ,  $4^\circ$ ,  $6^\circ$ ,  $8^\circ$  and  $10^\circ$  for each positional noise model were used. Results show that changing angular noise does not affect registration results using D-IMLOP significantly since the large number of samples overwhelms the small change in the noise model (Fig. 5.10). D-IMLOP was also com-

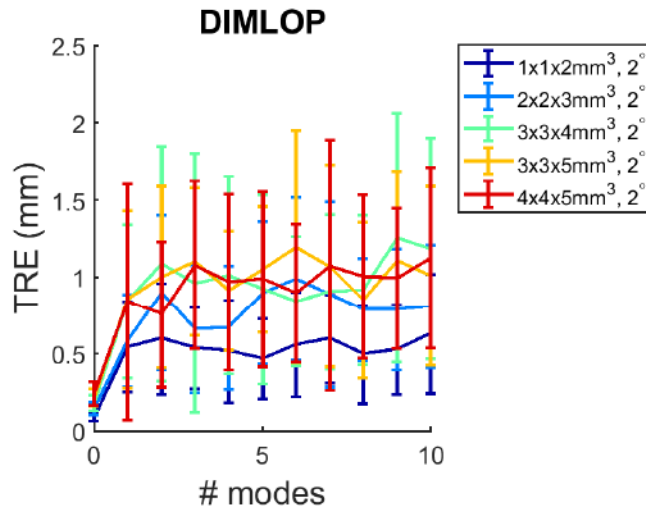


**Figure 5.8:** Noise model experiment: a general trend of increasing TRE as the uncertainty in the sample points increases. Note that errors are increasing with increasing modes because for this experiment the number of modes used to estimate the shapes equals the number of modes used to simulate a new shape from which points were sampled.

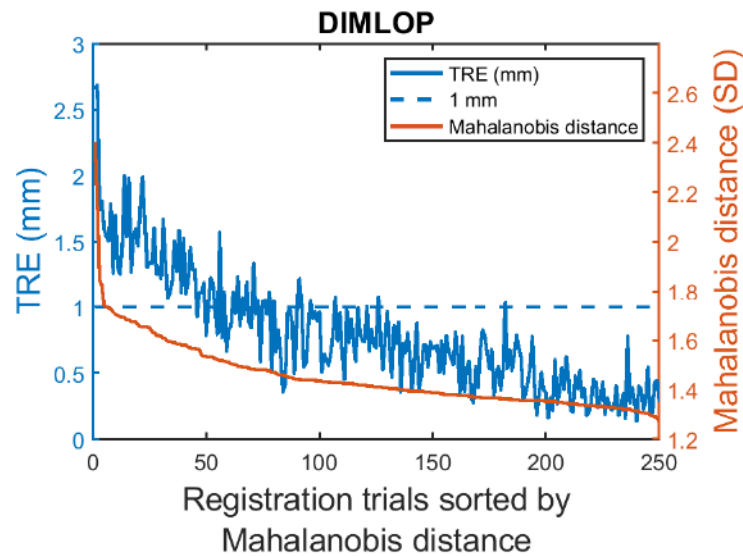


**Figure 5.9:** Noise model experiment: residual errors compared against TRE using 500 sample points with  $2 \times 2 \times 3 \text{ mm}^3$  SD positional noise and  $2^\circ$  SD angular noise in Exp. 2 of the noise model experiment (Sec. 5.5.3.2). The two measures exhibit correlation with correlation coefficient of 0.88.



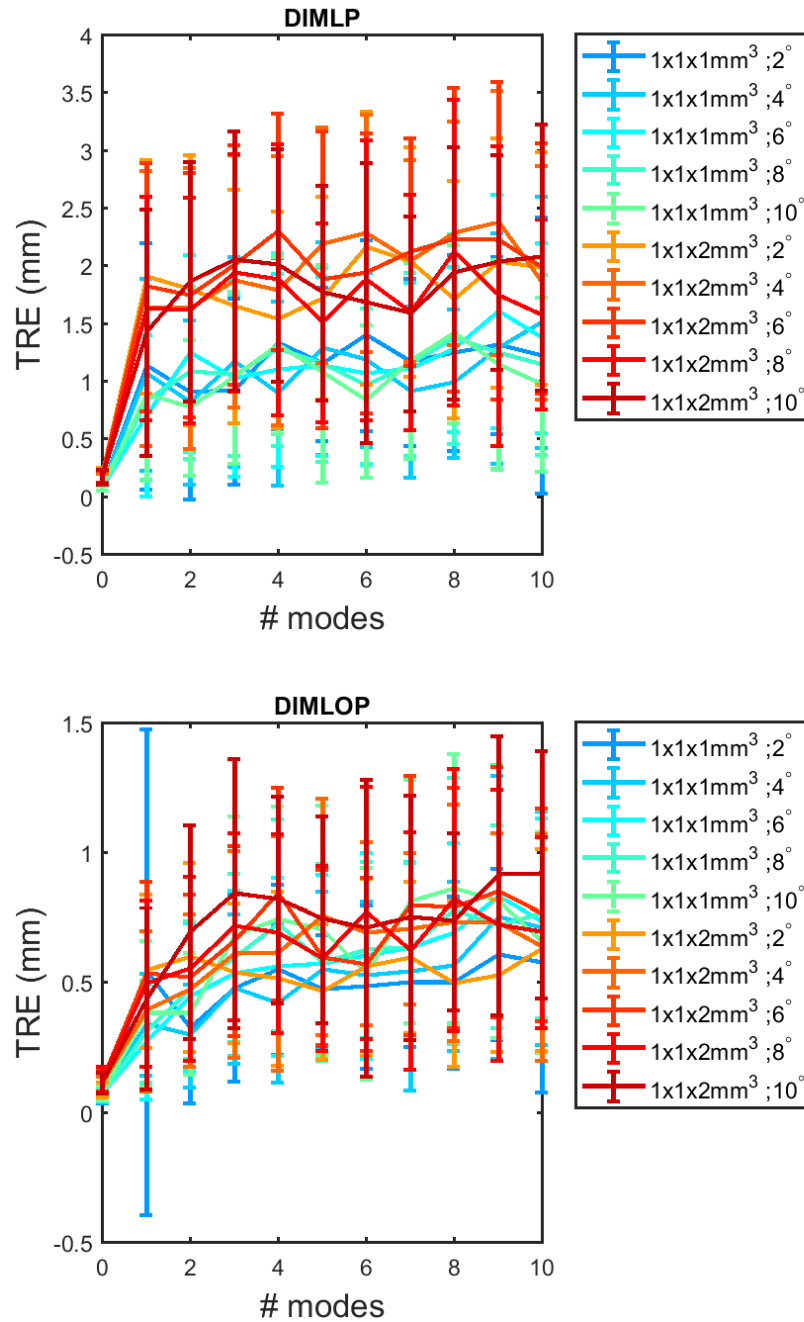


**Figure 5.10:** Noise model experiment: mean TREs produced by D-IMLP (top) and D-IMLOP (bottom) in Exp. 3 show that small changes in orientation noise do not have large influence on registration result. Note that the errors are increasing with increasing modes only because for this experiment the number of modes used to estimate the shapes equals the number of modes used to simulate a new shape from which points were sampled.

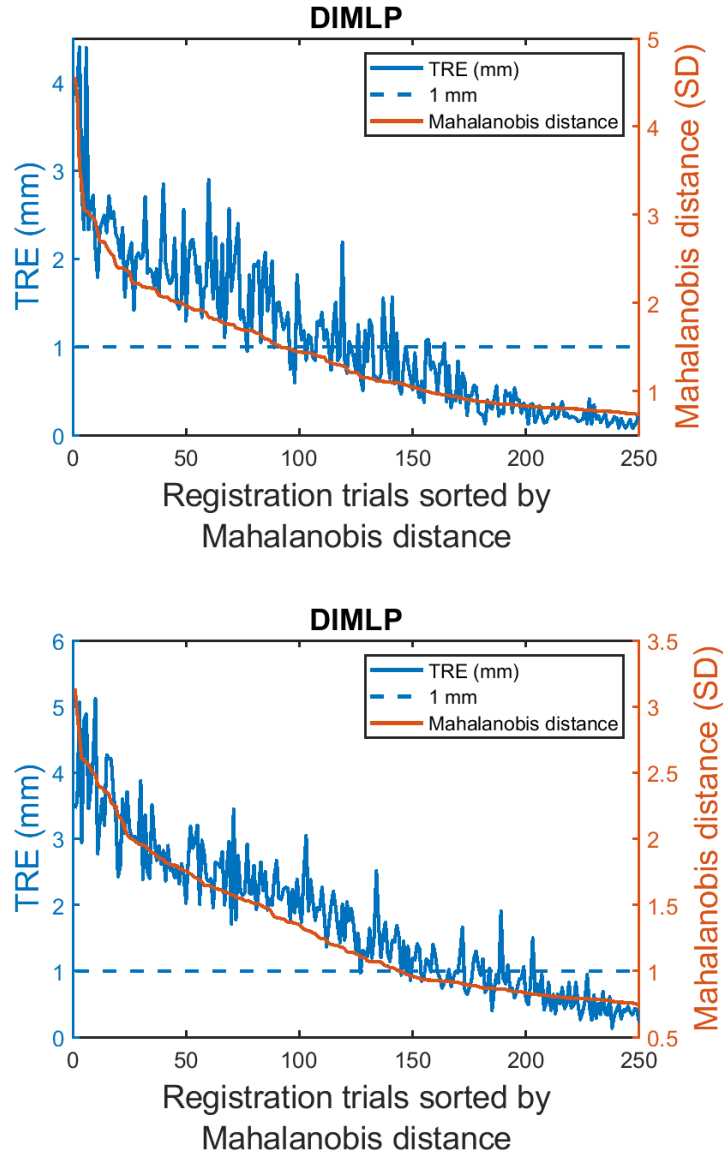


**Figure 5.11:** Noise model experiment: residual errors compared against TRE using 500 sample points with  $1 \times 1 \times 1 \text{ mm}^3$  SD positional noise,  $4^\circ$  SD angular noise (top), and  $1 \times 1 \times 2 \text{ mm}^3$  SD positional noise,  $8^\circ$  SD angular noise (bottom) in Exp. 3 of the noise model experiment. The two measures exhibit correlation for both isotropic and anisotropic position noise with correlation coefficient of 0.91 and 0.92, respectively.

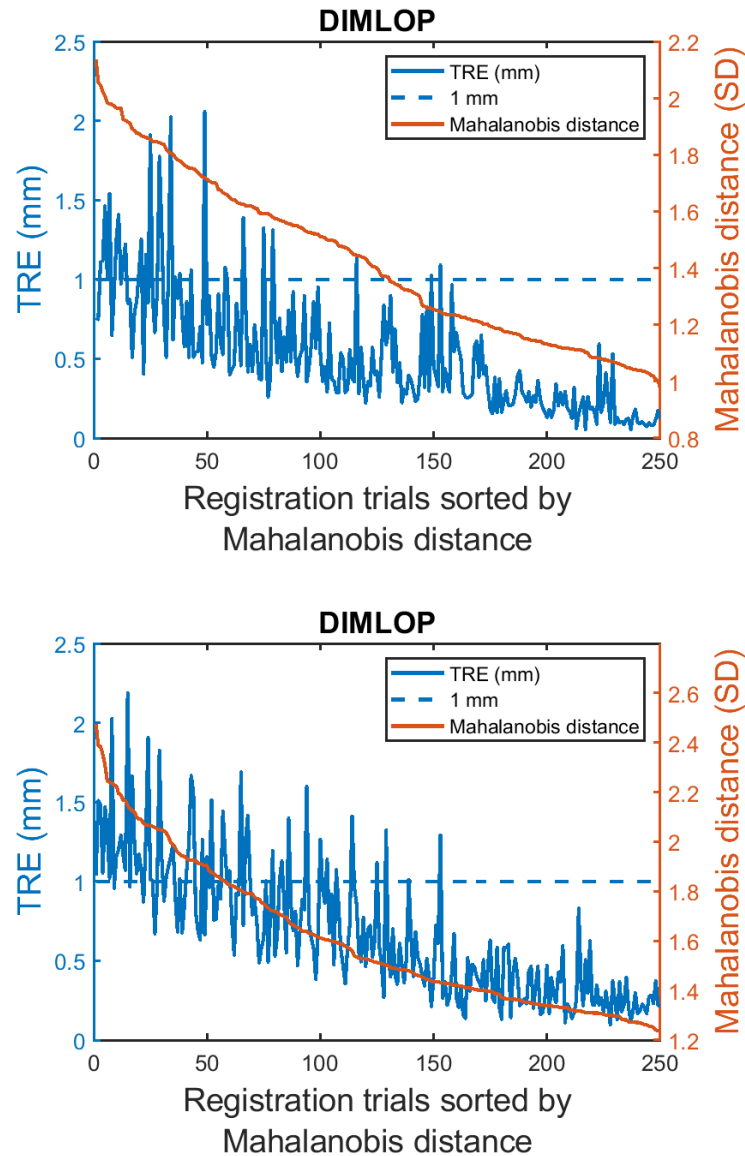


**Figure 5.12:** Noise model experiment: residual errors compared against TRE using 500 sample points with  $1 \times 1 \times 1 \text{ mm}^3$  SD positional noise,  $4^\circ$  SD angular noise (top), and  $1 \times 1 \times 2 \text{ mm}^3$  SD positional noise,  $8^\circ$  SD angular noise (bottom) in Exp. 3 of the noise model experiment. The two measures exhibit correlation for both isotropic and anisotropic position noise with correlation coefficient of 0.72 and 0.78, respectively.

pared to D-IMLP, which was also unaffected by the changing orientation noise models since does not take orientation information into consideration. However, D-IMLP registration trials with isotropic positional noise produce slightly lower TREs than those with anisotropic noise, as was seen in the previous chapter (Sections 4.5.3.1, 4.5.3.2). Errors produced by D-IMLOP were smaller than those produced by D-IMLP due to the added orientation information. However, errors produced by both algorithms were correlated with the TRE (Figures 5.11, 5.12).

#### 5.5.3.4 Experiment 4: Noise parameter sweep

In the final experiment, the sample points were generated with a fixed noise model for both position and orientation components with SDs  $2 \times 2 \times 4 \text{ mm}^3$  and  $10^\circ$ , respectively. However, it was assumed that this noise model is unknown to D-IMLOP. How the anisotropy is added to the orientation noise is covered in the next chapter (Ch. 6) since D-IMLOP cannot make anisotropic orientation noise assumptions. A hyperparameter sweep was then performed and the D-IMLOP algorithm was deployed with different isotropic and anisotropic position and isotropic orientation noise assumptions to evaluate how well D-IMLOP performs with inaccurate noise assumptions. This experiment shows that D-IMLOP performs better when the noise assumption is optimistic, but as the noise assumption becomes more pessimistic, its performance degrades. Therefore, TREs for D-IMLOP do not show stabilization with increasingly conservative noise estimates (Fig. 5.13).

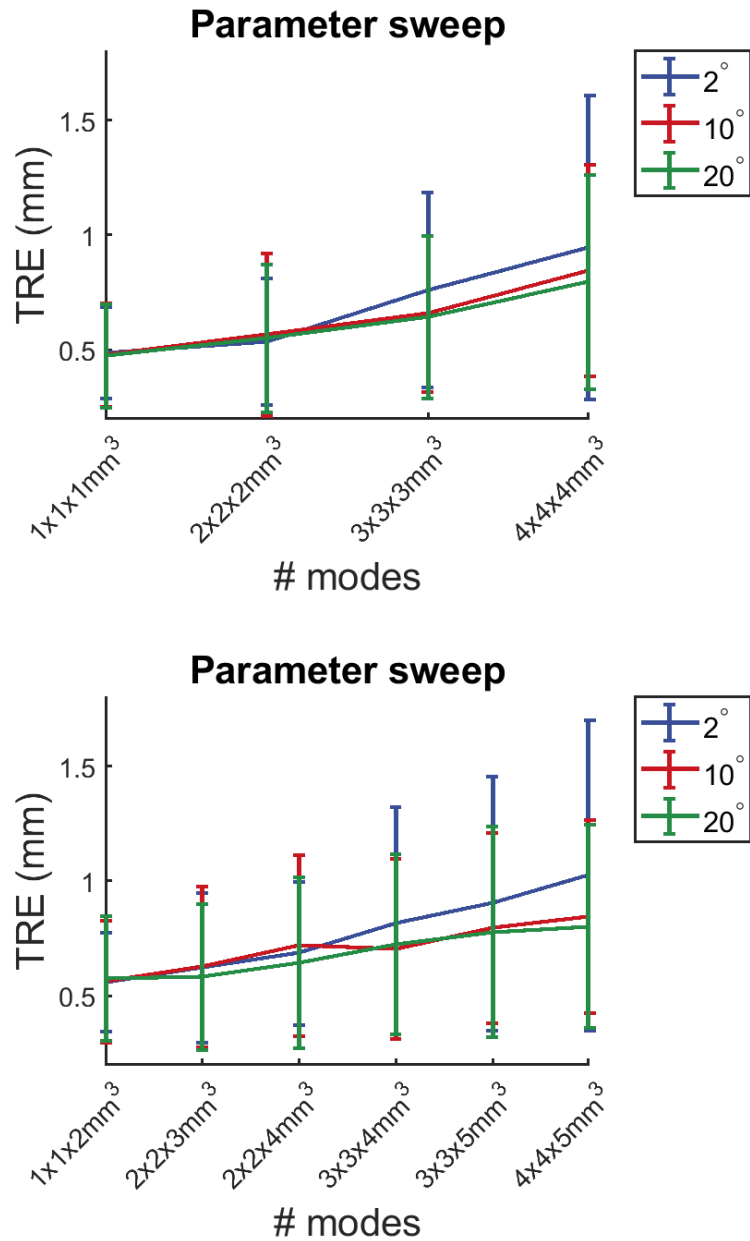


**Figure 5.13:** Noise model experiment: parameter sweep results show that D-IMLOP produces lower errors when the noise assumptions are optimistic, and errors increase as noise assumptions become more pessimistic.

### 5.5.4 Outlier experiment

Sample points for this experiment were generated with isotropic noise in position data with SD  $1 \times 1 \times 1 \text{ mm}^3$  and anisotropic noise in orientation data with  $2^\circ$  SD. Outliers were generated by perturbing the position and orientation components of different amount of samples in the range  $[2, 5] \text{ mm}$  and  $[2, 5]^\circ$ , respectively. Three experiments were designed where different numbers of samples, 0%, 10%, and 20%, were perturbed. Outliers were identified and rejected using the chi-square test, as described earlier in Sec. 5.2, as well as in Billings et al.<sup>51,53</sup> For position data, a match is rejected if the square Mahalanobis distance is greater than the value of the chi-square inverse CDF with 3 DOF at  $p = 0.95$ . Since the square Mahalanobis distance normalizes each match residual error by its variance along each dimension, the sum of the square Mahalanobis distance over all data points,  $n_{\text{data}}$ , is distributed as a chi-square distribution with  $3n_{\text{data}}$  DOF.<sup>107</sup> Similarly, for orientation data, a chi-square test with  $2n_{\text{data}}$  DOF is applied by converting the Fisher noise model for the orientation match residual into Gaussian form.<sup>114</sup>

As with D-IMLP, D-IMLOP is able to perform well even in the presence of outliers. Although the performance is slightly worse in the presence of outliers, D-IMLOP is able to detect them, as explained in Sec. 5.2, and limit their effect on errors. As shown in Fig. 5.14, the errors from 10% and 20% outliers in the sampled points are comparable. Further, despite increasing number of outliers, the residual errors are still correlated with the TREs and, therefore, able to discriminate between successful

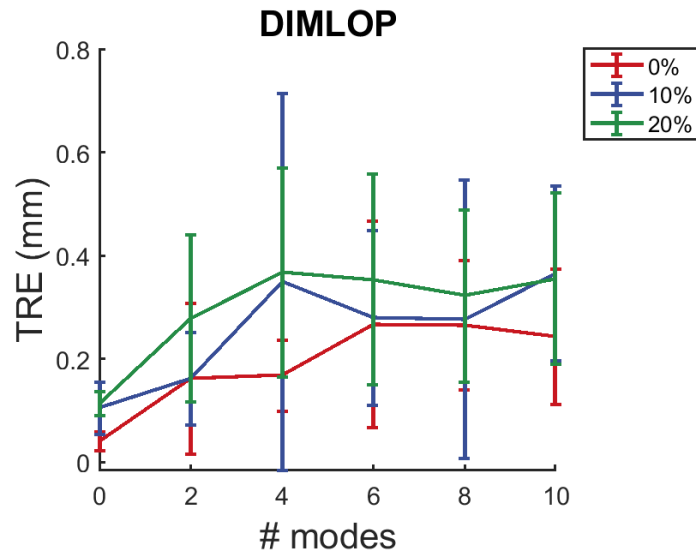


**Figure 5.14:** Outlier experiment: mean TRE with different number of outliers using D-IMLOP. Note that errors are increasing with increasing modes because for this experiment the number of modes used to estimate the shapes equals the number of modes used to simulate the deformed shape from which points were sampled.

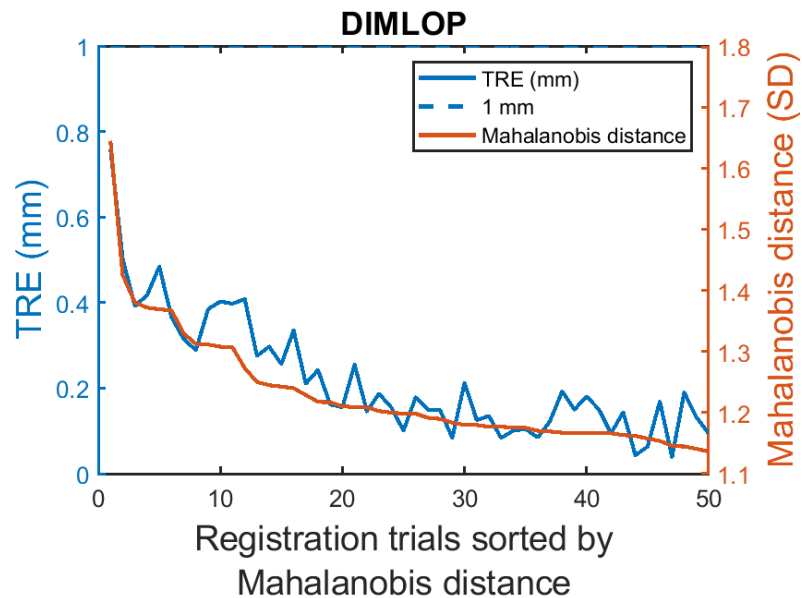


**Figure 5.15:** Outlier experiment: residual errors compared against TRE using the right nasal cavity meshes with 0% outliers. The two measures exhibit correlation with a correlation coefficient of 0.93.

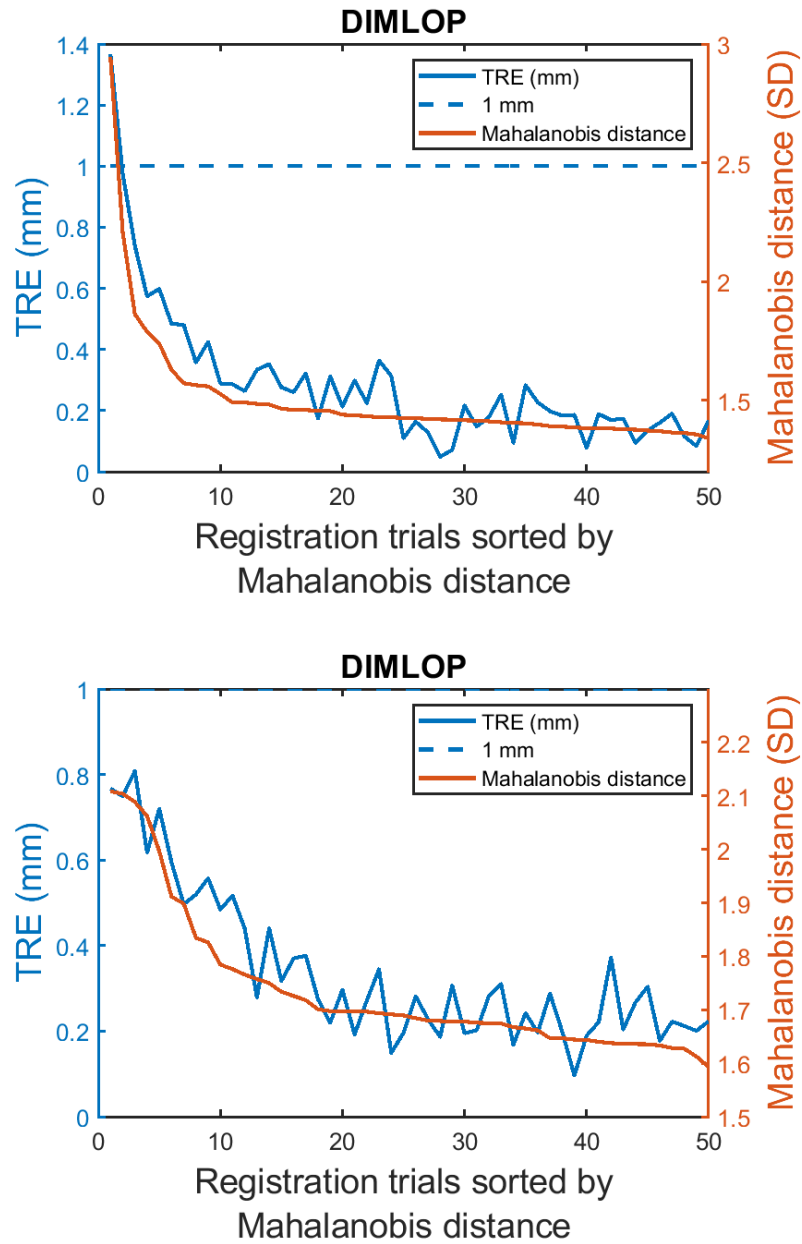


**Figure 5.16:** Outlier experiment: residual errors compared against TRE using the right nasal cavity meshes with 10% (top) and 20% (bottom) outliers. The two measures exhibit high correlation in both experiments with correlation coefficients of 0.95 and 0.92, respectively.



and unsuccessful registrations (Figs. 5.15, 5.16).

### 5.5.5 Scale experiment

The dataset generated in Sec. 5.5.4 with 0% outliers was reused for this experiment. The sample points were scaled by some known amount in the range  $[0.7, 1.3]$ , as mentioned in Sec. 4.5.5. D-IMLOP is able estimate scale in addition to rotation, translation, and shape parameters well, outperforming D-IMLP. D-IMLOP also performs better when there is one fewer parameter to optimize over (Fig. 5.17). The errors produced by D-IMLOP, however, are more irregular than those produced by D-IMLP. This could possibly be due to a few outliers in the registrations produced by D-IMLOP due to its inaccurate noise assumptions, as can be seen in the histogram (Fig. 5.18) showing the distribution of errors produced by our methods. These outliers can be detected and rejected by D-IMLOP.

### 5.5.6 Leave-one-out experiment

For this experiment, an isotropic positional noise model with a SD of  $1 \times 1 \times 1 \text{ mm}^3$  was used to generate data samples, since the CT volumes used to segment the sinus structures had a resolution of  $1 \times 1 \times 1 \text{ mm}^3$ . Further, an anisotropic orientation noise model with  $20^\circ$  SD was used. D-IMLOP assumed the same noise model as was used to generate the data.

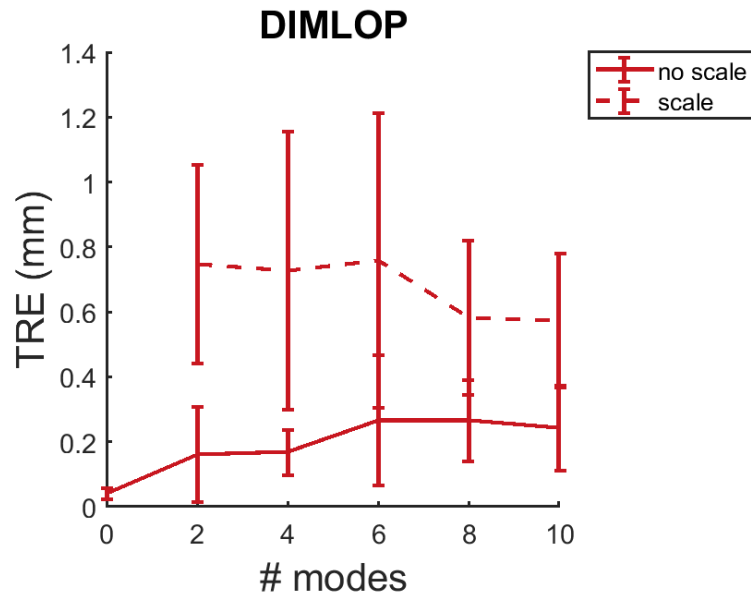


**Figure 5.17:** Scale experiment: additional scale optimization increases TRE as compared to when scale optimization is not required.

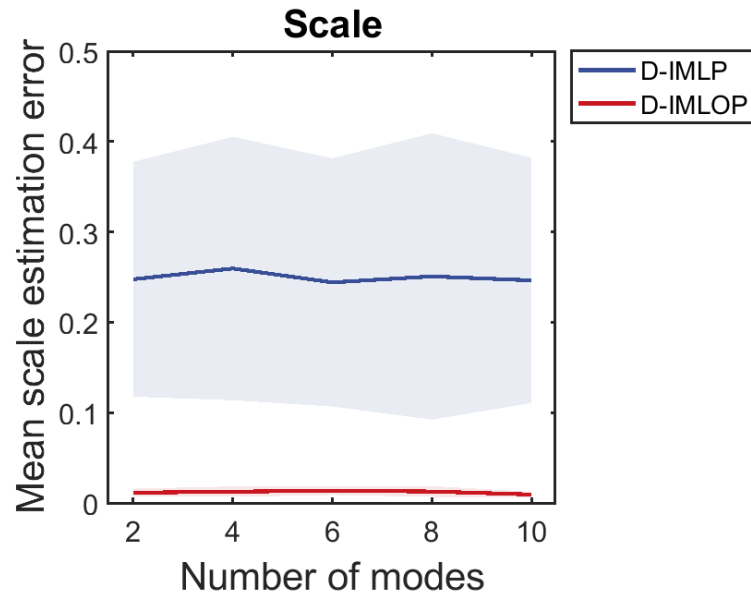


**Figure 5.18:** Scale experiment: errors in scale estimation using D-IMLOP with increasing number of modes remain stable, and are lower than those produced using D-IMLP.

### 5.5.6.1 Experiment 1: Middle turbinates

The middle turbinate models from the sinus dataset were used to generate sample points for this experiment. D-IMLOP was able to recover the left out shape and the transformation offset applied successfully (with mean TRE less than 1 mm) in 88.85% of the 1749 registrations performed. As the number of shape parameters increased, shape estimation errors using D-IMLOP quickly stabilized (Fig. 5.19, top) around 15 modes, while registration parameters either remained stable or deteriorated slightly leading to slowly degrading TREs (Fig. 5.19, bottom). This is likely because the incorrect noise assumptions cause slower convergence rate with increasing number of shape parameters. Although, D-IMLOP was outperformed by CPD in recovering the left out shape, D-IMLOP was considerably faster than CPD. D-IMLOP required only 8.96s average time to converge at its slowest (using 50 modes), while CPD required 40.55s (Fig. 5.20). Again, unlike CPD (Fig. 6.18), error metrics produced by D-IMLOP show correlation with the TRE, allowing it to accept or reject or assign some confidence to the registrations produced (Fig. 5.22).

### 5.5.6.2 Experiment 2: Right nasal airway

The right nasal airway models, also from the sinus dataset, were used to generate sample points for this experiment. Of the 1749 runs, 94.57% of the D-IMLOP runs recovered the left out mesh with mean TRE less than 1 mm. As with the middle turbinate experiment, shape estimation errors show gradual improvement up to about

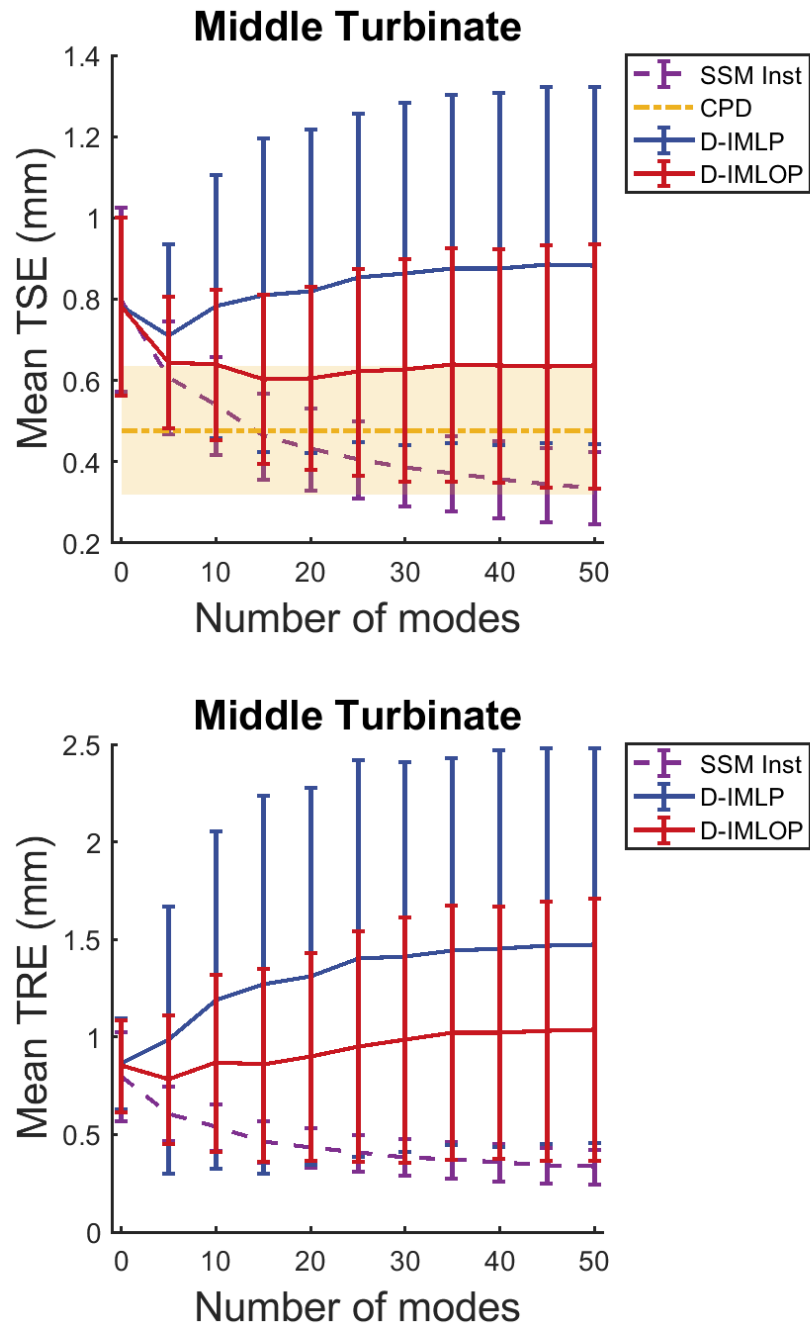


**Figure 5.19:** Leave-one-out experiment: TSE (top) and TRE (bottom) produced by D-IMLOP compared against that produced by CPD and SSM using the middle turbinate meshes in the leave-one-out experiment.

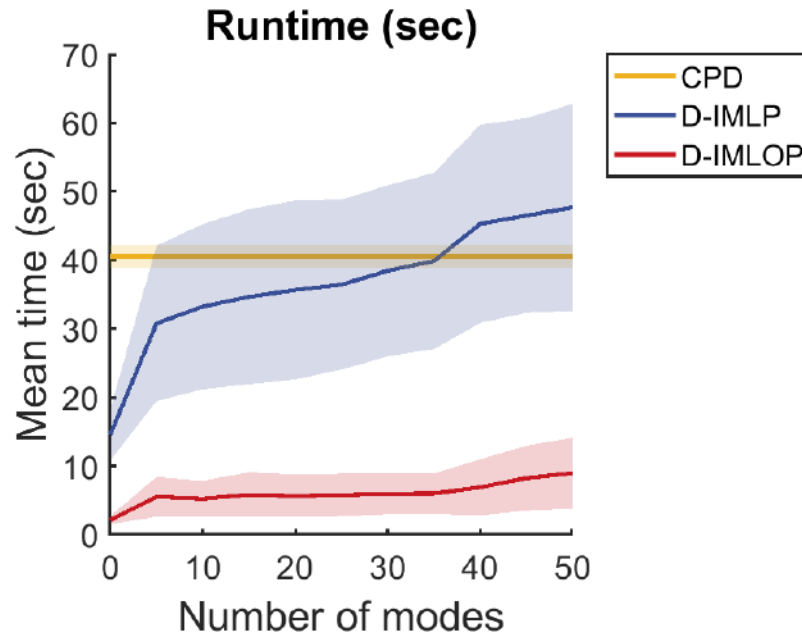
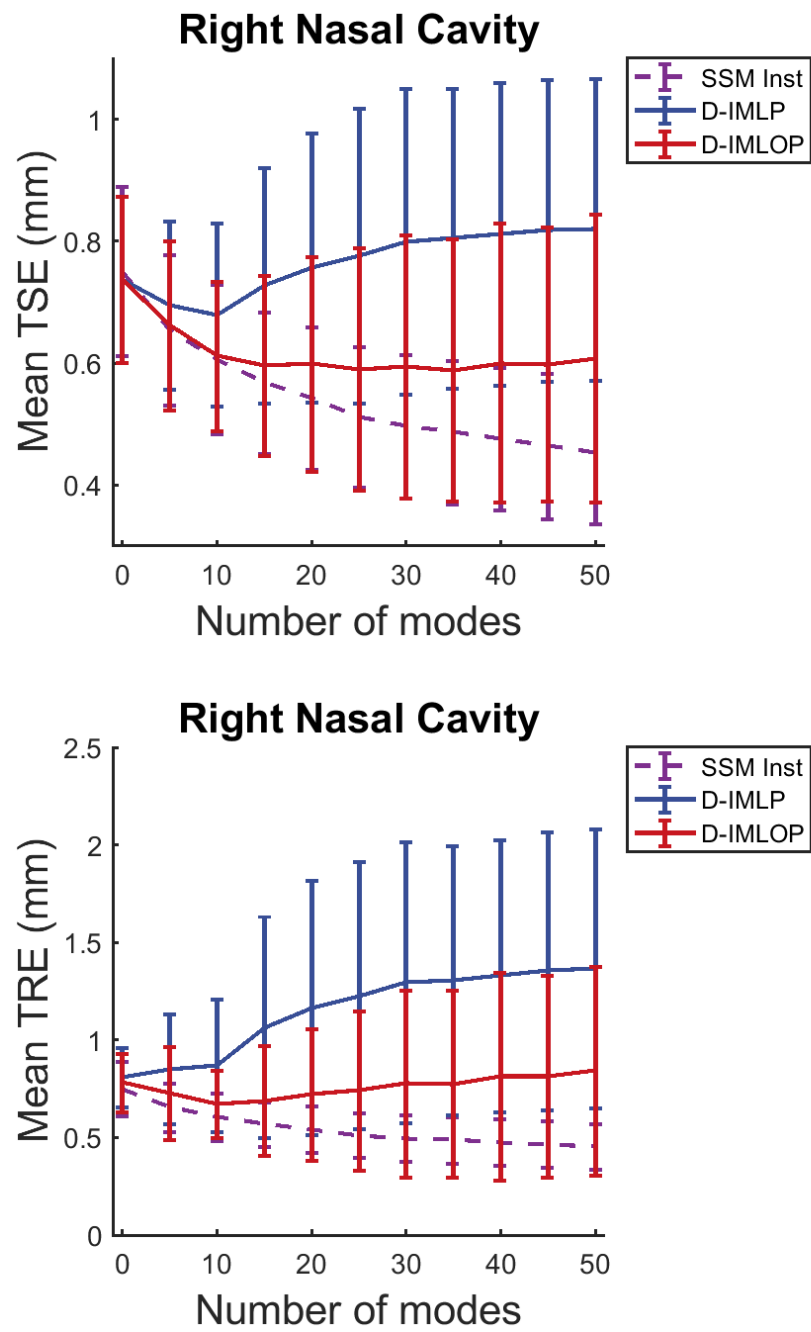
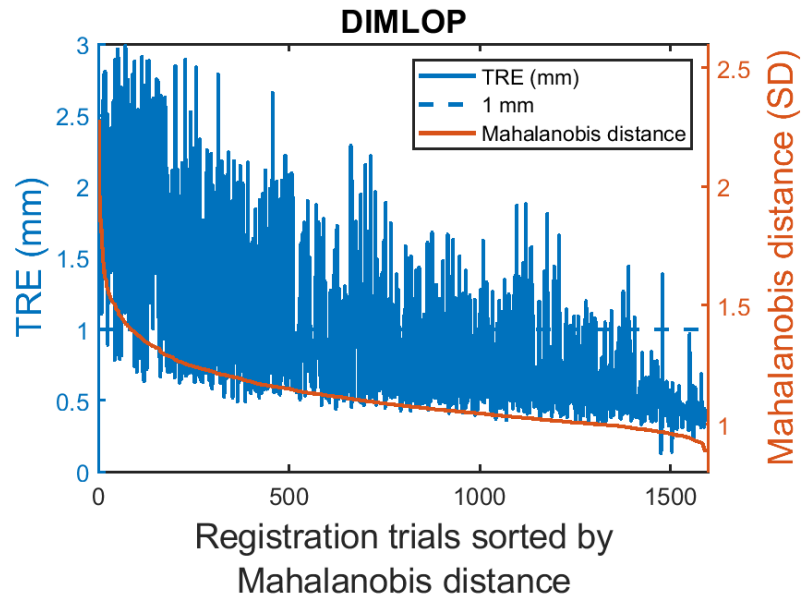


Figure 5.20: Leave-one-out experiment: runtime comparison between CPD, D-IMLP and D-IMLOP.

15 modes and stabilization beyond 15 modes (Fig. 5.21, top), while registration parameters either remain stable or deteriorate slightly leading to slowly degrading TREs with increasing modes (Fig. 5.21, bottom). The reason for this, as in the previous experiment, is slower convergence rate with increasing number of shape parameters likely due to incorrect noise assumptions. As before, the residual errors produced showed correlation with the TRE (Fig. 5.23).



**Figure 5.21:** Leave-one-out experiment: TSE (top) and TRE (bottom) produced by D-IMLOP compared against that produced by the SSM estimate using the right nasal cavity meshes in the leave-one-out experiment.



**Figure 5.22:** Leave-one-out experiment: residual errors compared against TRE using the middle turbinate meshes in the leave-one-out experiment. The two measures exhibit correlation with correlation coefficients of 0.65.

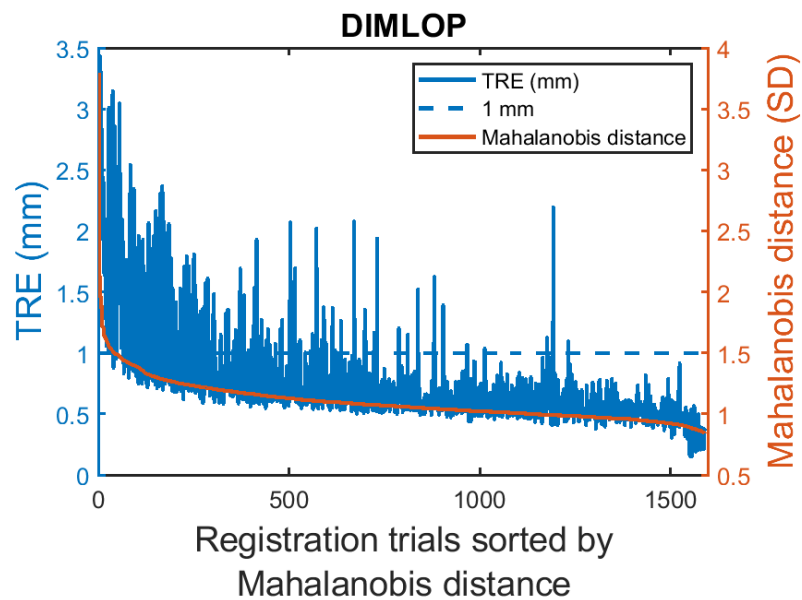


**Figure 5.23:** Leave-one-out experiment: residual errors compared against TRE using the right nasal cavity meshes in the leave-one-out experiment. The two measures exhibit correlation with correlation coefficients of 0.75.

### 5.5.6.3 Experiment 3: Right nasal airway with outliers

As in Sec. 4.5.6.3, D-IMLOP is evaluated on more realistic data containing outliers. This experiment is set up similarly as the previous experiment (Sec. 5.5.6.2), but with 10% and 20% of the sample points perturbed to simulate outliers. The perturbation is similar to that in Sec. 5.5.4, and outliers are detected using the techniques described in Sec. 5.2. Results show that adding outliers did not have a large effect on registration. Results were comparable with 10% outliers and only slightly worse with 20% outliers in the sample points. Despite up to 20% outliers in the data, mean TREs for all modes remained below 1 mm (Fig. 5.24).

## 5.5.7 Partial data experiment

### 5.5.7.1 Experiment 1: Pelvis

Anisotropic noise with SD  $1 \times 1 \times 2 \text{ mm}^3$  and  $10^\circ$  was used to generate sampled position and orientation data, respectively, from a partial CT scan of the pelvis. An instance of the full pelvis is then estimated by D-IMLOP using these sampled points and a generous noise assumption with SD  $2 \times 2 \times 3 \text{ mm}^3$  and  $30^\circ$  for position data and orientation data, respectively. D-IMLOP results follow similar trends as D-IMLP, showing big improvement in both transformation parameters and TSE from 0 to 10 modes (Fig. 5.25), but stabilizing or only showing gradual improvement in errors beyond 10 modes due to slower convergence rate with increasing number of shape



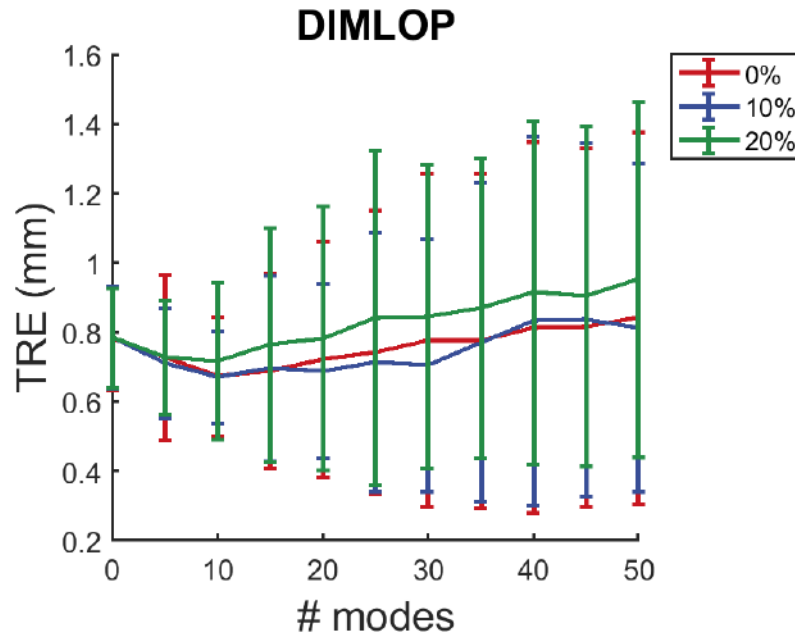


**Figure 5.24:** Leave-one-out experiment: TRE produced by D-IMLOP with 0%, 10% and 20% outliers in the data points sampled from the right nasal cavity meshes in the leave-one-out experiment.

parameters. The trend followed by the TSE is similar to that followed by the error between the left out shape and the SSM instance of the left out shape (Fig. 5.25), with the mean TRE falling below 2 mm with only 10 modes (Fig. 5.25), which is the desired accuracy for pelvis registrations. The improvement in these errors is also reflected in the residual errors produced by D-IMLOP (Fig. 5.27, top), although the correlation between these errors is weaker than in previous experiments.

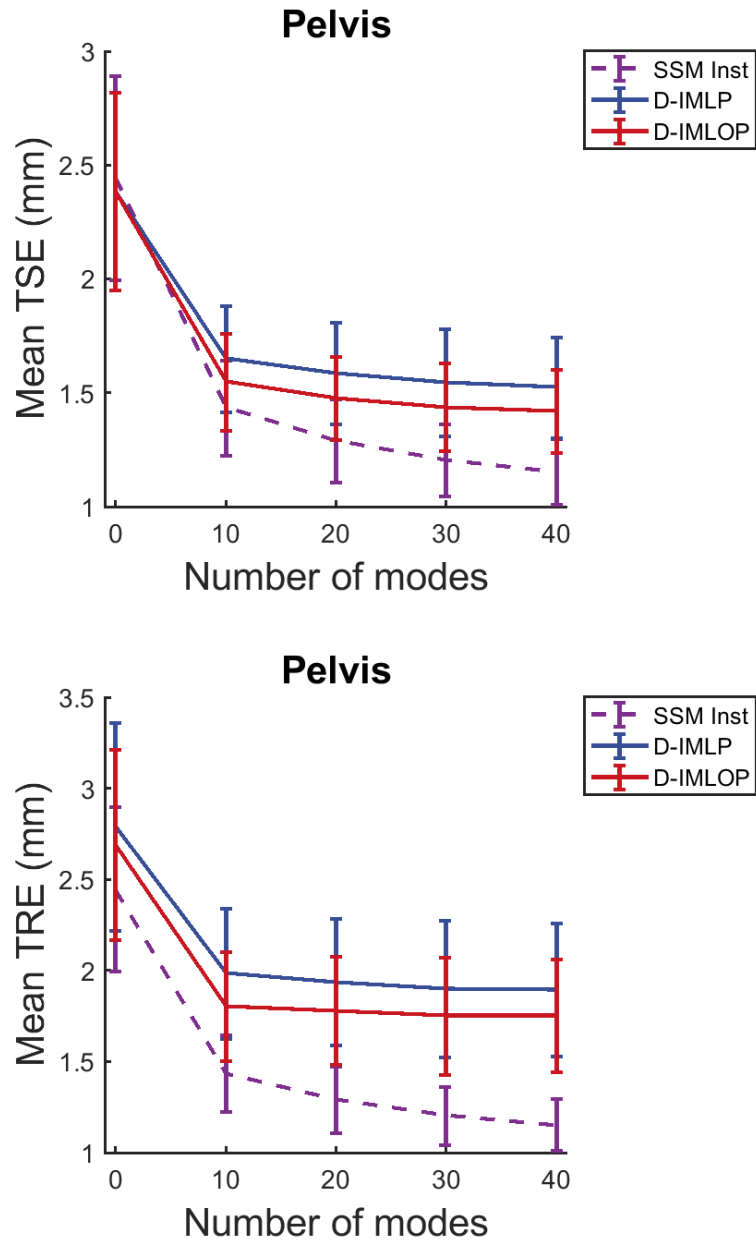


**Figure 5.25:** Partial data experiment: TSE (top) and TRE (bottom) produced by D-IMLOP compared against that produced by the SSM estimate using the pelvis meshes.

### 5.5.7.2 Experiment 2: Right nasal airway

Anisotropic noise with SD  $0.5 \times 0.5 \times 1 \text{ mm}^3$  and  $10^\circ$  was added to position data and orientation data, respectively, since this produced point clouds that resembled reconstructions obtained from in-vivo data using the method described in the chapter 7. The left out nasal cavity was then estimated using these sampled points and a noise model assumption with SD  $1 \times 1 \times 2 \text{ mm}^3$  and  $30^\circ$  for position data and orientation data, respectively. Due to the increased complexity of the right nasal airway models, results from this experiment showed slightly different trends. Other than translational error, all errors stabilized quickly. Translational error, however, continued to gradually degrade with increasing modes (Fig. 5.26). The degradation in translational error might stem from the fact that the nasal cavity is a roughly cylindrical passage. Therefore, translations along the z-direction yield several locations where both the position and orientation components produce good matches leading to convergence at suboptimal local minima. The overall TREs, however, were stable with the mean TRE remaining either below or near 1 mm, and showed weak correlation with the residual errors (Fig. 5.27, bottom).

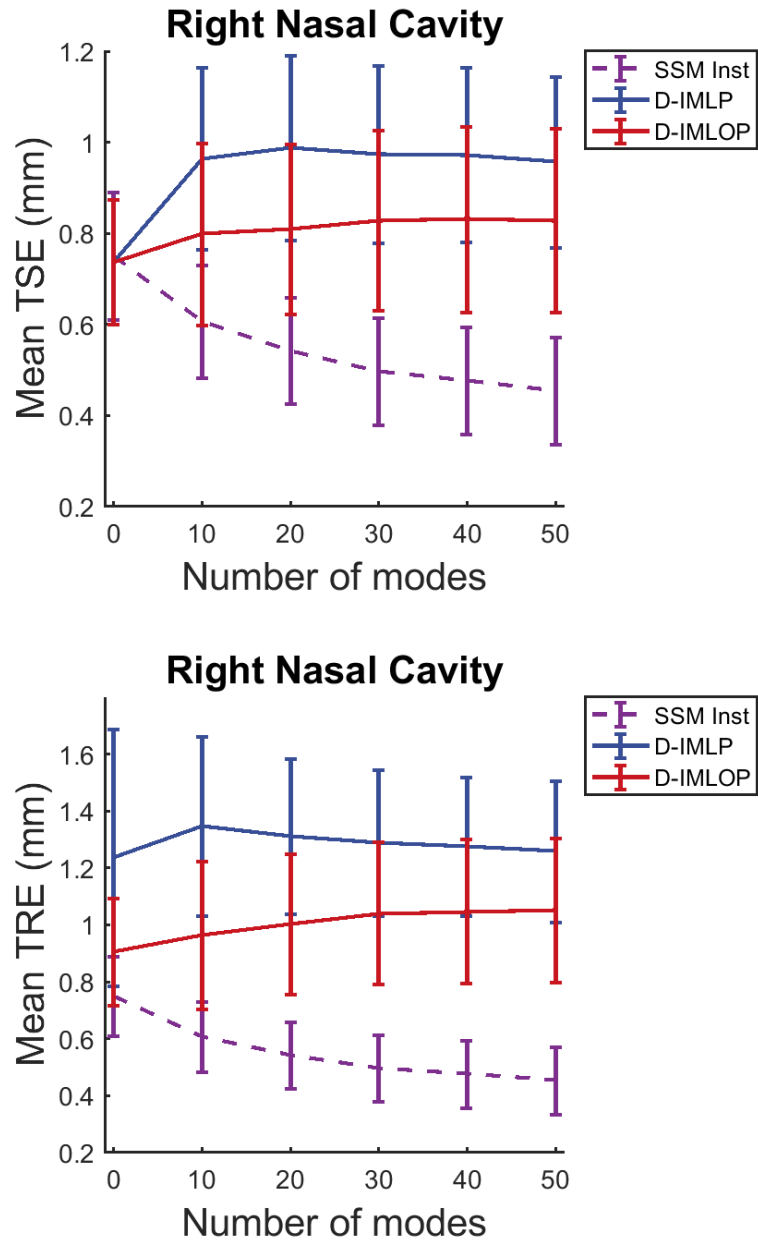


**Figure 5.26:** Partial data experiment: TSE (top) and TRE (bottom) produced by D-IMLOP compared against that produced by the SSM estimate using the right nasal airway meshes.

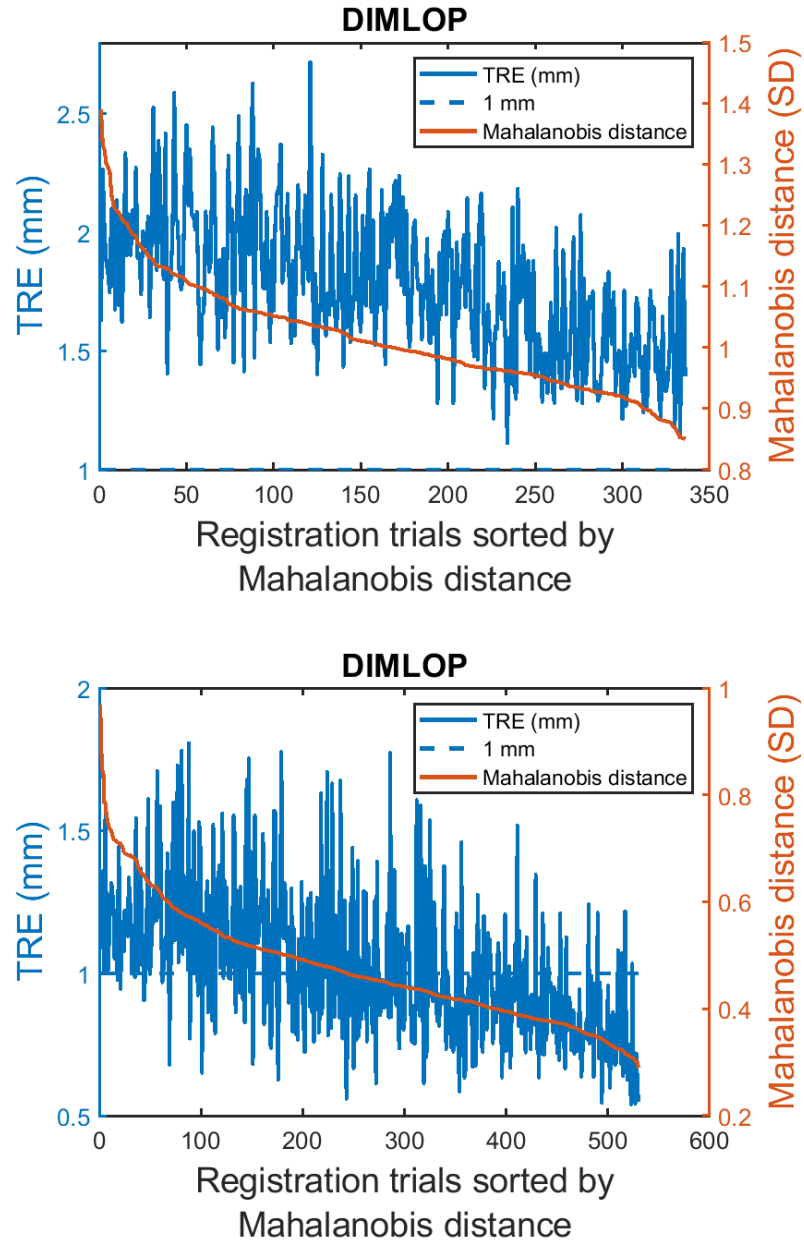


**Figure 5.27:** Partial data experiment: residual errors compared against TRE using the pelvis (top) and right nasal airway (bottom) meshes. The two measures exhibit weak correlation with correlation coefficients of 0.49 in both experiments.

## 5.5.8 Failure detection experiment

### 5.5.8.1 Experiment 1: Known noise

This setup for this experiment is the same as the setup for the leave-one-out experiment with right nasal airway data (Sec. 5.5.6.2). As in Sec. 5.5.6.2, this experiment assumes the same position noise SD as was used to generate the data samples. However, since D-IMLOP cannot accommodate anisotropic orientation noise, it assumes isotropic orientation noise with the same SD as the anisotropic noise used in data generation. The chi-square tests using  $E_p$  at  $p = 0.95$  on the registrations produced in this experiment show that the test is able to detect almost all successful registrations (Fig. 5.28, top). However, over half of the failed registrations are also labeled successful. Using the additional  $E_o$  test along with the  $E_p$  test, about 10% of the unsuccessful registrations are incorrectly labeled as successful, although more successful registrations are also incorrectly labeled as unsuccessful (Fig. 5.28, bottom). However, this is a promising result because such systems are preferred more pessimistic rather than optimistic because labeling an incorrect registration as successful can mislead surgeons during an intervention and cause harm to the patient. On the other hand, if a successful registration is labeled unsuccessful, the system can simply attempt to produce a better registration. Further, both  $E_p$  and  $E_o$  show correlation with the TREs, meaning that confidence can be assigned to computed registrations based on these values (Fig. 5.29).

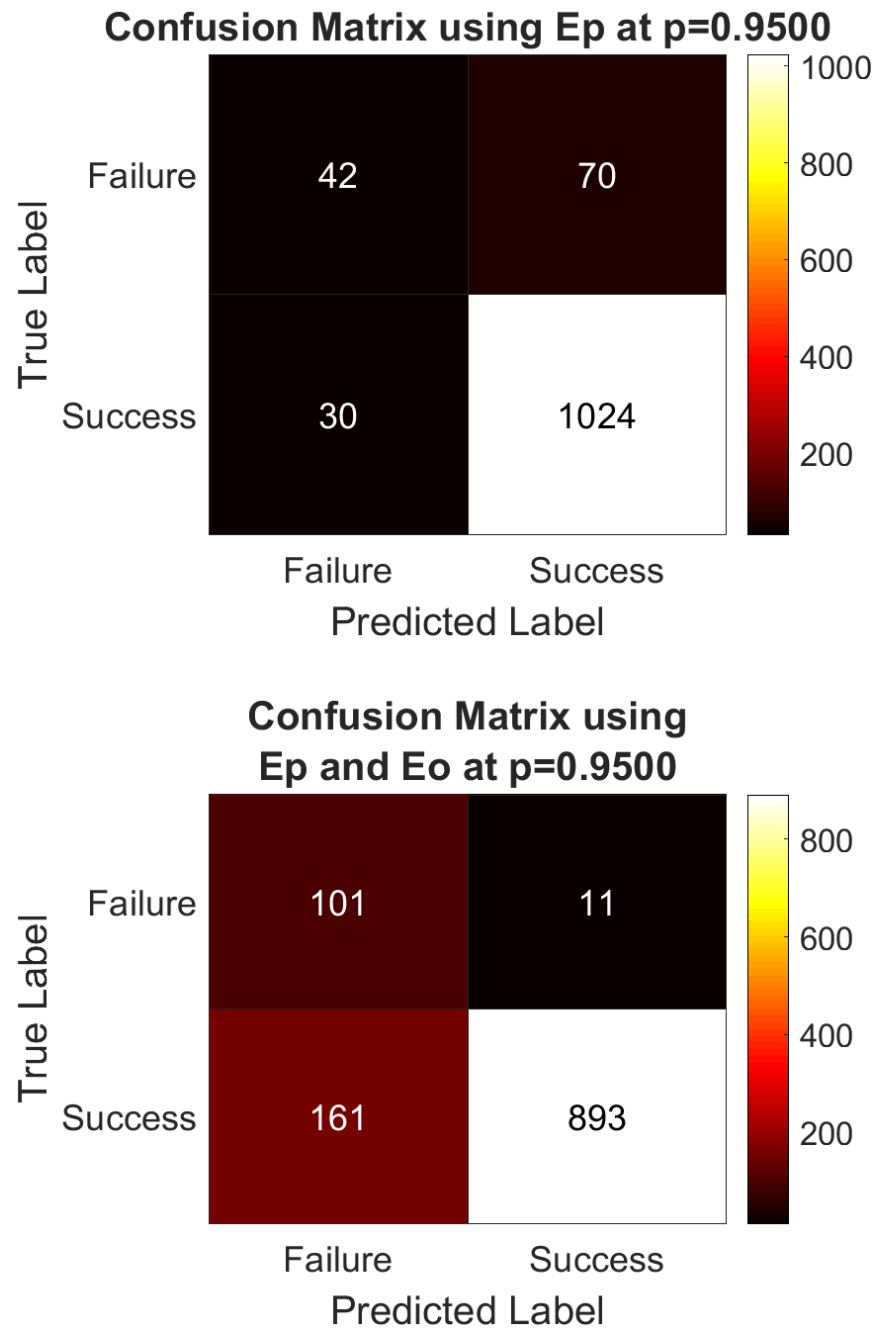


**Figure 5.28:** Failure detection experiment: confusion matrix using  $E_p$  alone (top) and both  $E_p$  and  $E_o$  (bottom).

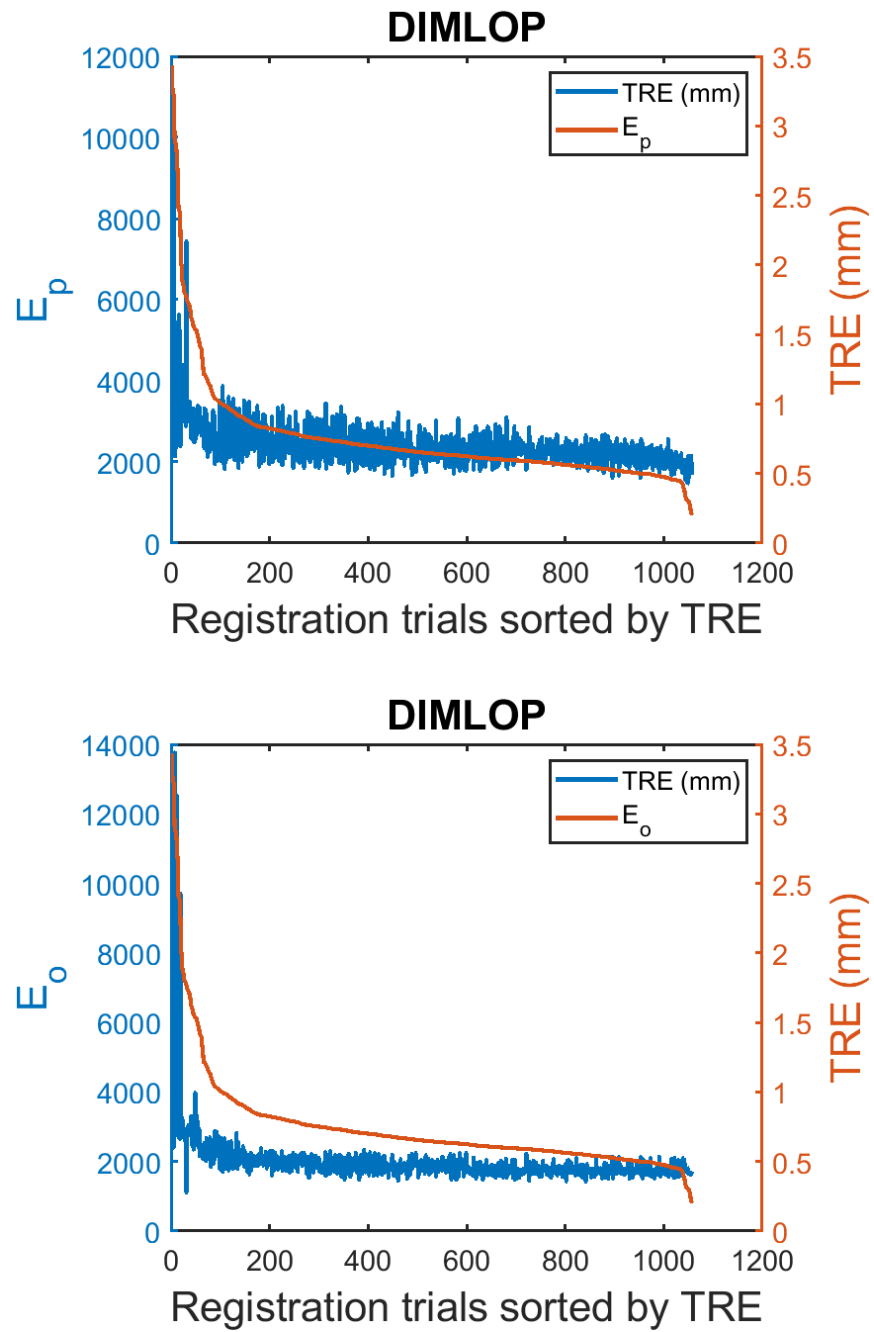


**Figure 5.29:** Failure detection experiment: both  $E_p$  (top) and  $E_o$  (bottom) are correlated with the TRE with correlation coefficients of 0.73 and 0.62, respectively, when the noise in the data is known.



### 5.5.8.2 Experiment 2: Unknown noise

This experiment is set up as described in Sec. 4.5.8. The anisotropic noise in the sampled points has a SD of  $0.5 \times 0.5 \times 0.75 \text{ mm}^3$  and  $10^\circ$  in the position and orientation components, respectively. The anisotropy in the orientation component will be explained in the next chapter. D-IMLOP makes more generous noise assumptions with SDs  $1 \times 1 \times 2 \text{ mm}^3$  and  $30^\circ$  for position and orientation data, respectively. As with D-IMLP, in this more realistic scenario, the performance of the chi-square tests at  $p = 0.95$  is worse than in the previous experiment (Sec. 5.5.8.1). As in the previous experiment, the algorithm is able to correctly detect almost all successful registrations using  $E_p$ , but is not able to reject unsuccessful registrations (Fig. 5.30, top). With the additional  $E_o$  tests, more unsuccessful registrations are correctly rejected than when only  $E_p$  is used. However, unlike the previous experiment, the percentage of successful registrations incorrectly labeled as successful is still very high (Fig. 5.30, bottom). This difference most likely stems from the incorrect noise assumptions made by this experiment. Further, although  $E_p$  and TRE are correlated to each other,  $E_o$  and TRE are not, making it difficult to assign confidence to the registrations produced (Fig. 5.31).

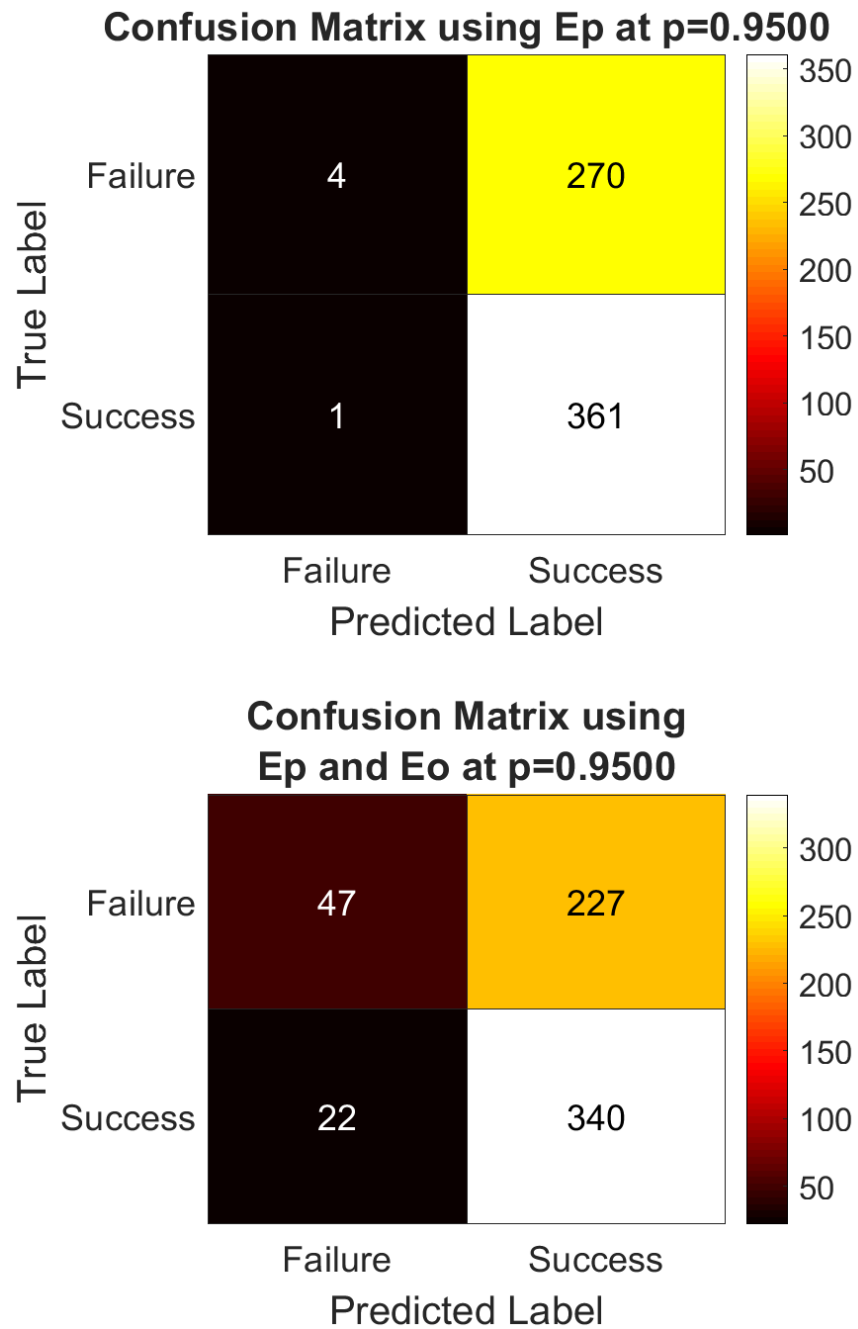


**Figure 5.30:** Failure detection experiment: confusion matrix using  $E_p$  alone (top) and both  $E_p$  and  $E_o$  (bottom).

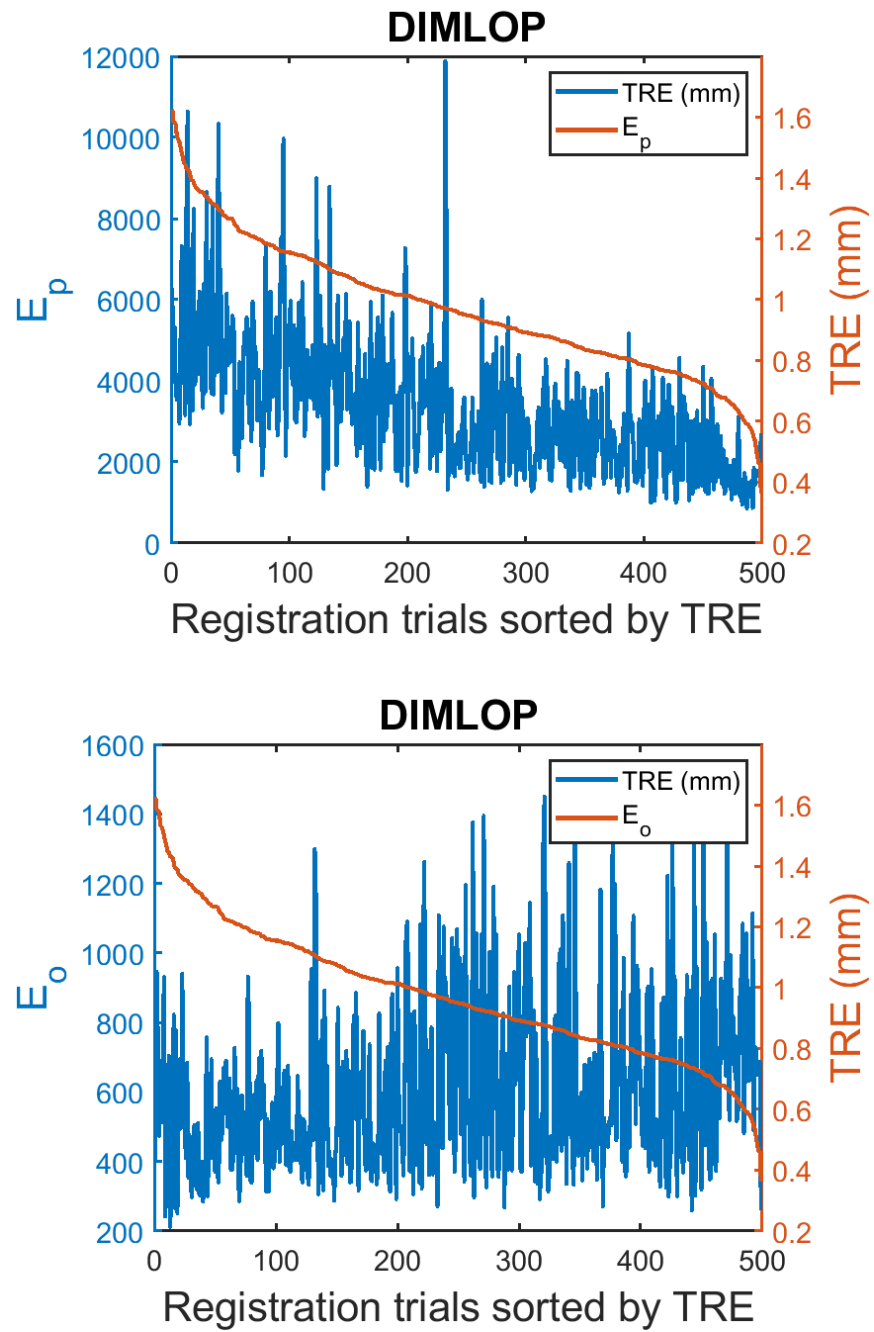


**Figure 5.31:** Failure detection experiment: although  $E_p$  is weakly correlated with the TRE (top) with a correlation coefficient of 0.58,  $E_o$  does not show correlation with the TRE (bottom) when the noise in the data is unknown.

## 5.5.9 Non-medical data experiment

### 5.5.9.1 Experiment 1: Human expression

Points were sampled from meshes in the test set with anisotropic position noise and orientation noise with SD  $1 \times 1 \times 2 \text{ mm}^3$  and  $10^\circ$ , respectively. D-IMLOP was executed with a slightly more relaxed noise assumption, assuming that the position and orientation noise model has a SD of  $2 \times 2 \times 4 \text{ mm}^3$  and  $20^\circ$ , respectively. As with D-IMLP, D-IMLOP was able to deformably register the mean face mesh to points sampled from test faces to produce relatively low TREs and TSEs (Fig. 5.32). However, errors stabilize after 20 modes and do not show further improvement. The residual errors produced by D-IMLOP correlate with the TRE, indicating that D-IMLOP is able to handle such data (Fig. 5.34).

### 5.5.9.2 Experiment 2: Human pose

For this experiment, points were sampled with the same anisotropic position and orientation noise model as before. D-IMLOP was, again, deployed with a more relaxed noise assumption where the SD of the position and orientation noise model was assumed to be  $2 \times 2 \times 4 \text{ mm}$  and  $30^\circ$ , respectively. The search space for shape parameters,  $\mathbf{s}$ , in this case was restricted to  $\pm 1$  SD. D-IMLOP failed to produce meaningful reconstructions and alignments with this dataset, as is clear from the high TREs and TSEs (Fig. 5.33). As explained in the previous chapter, this is expected since the lim-

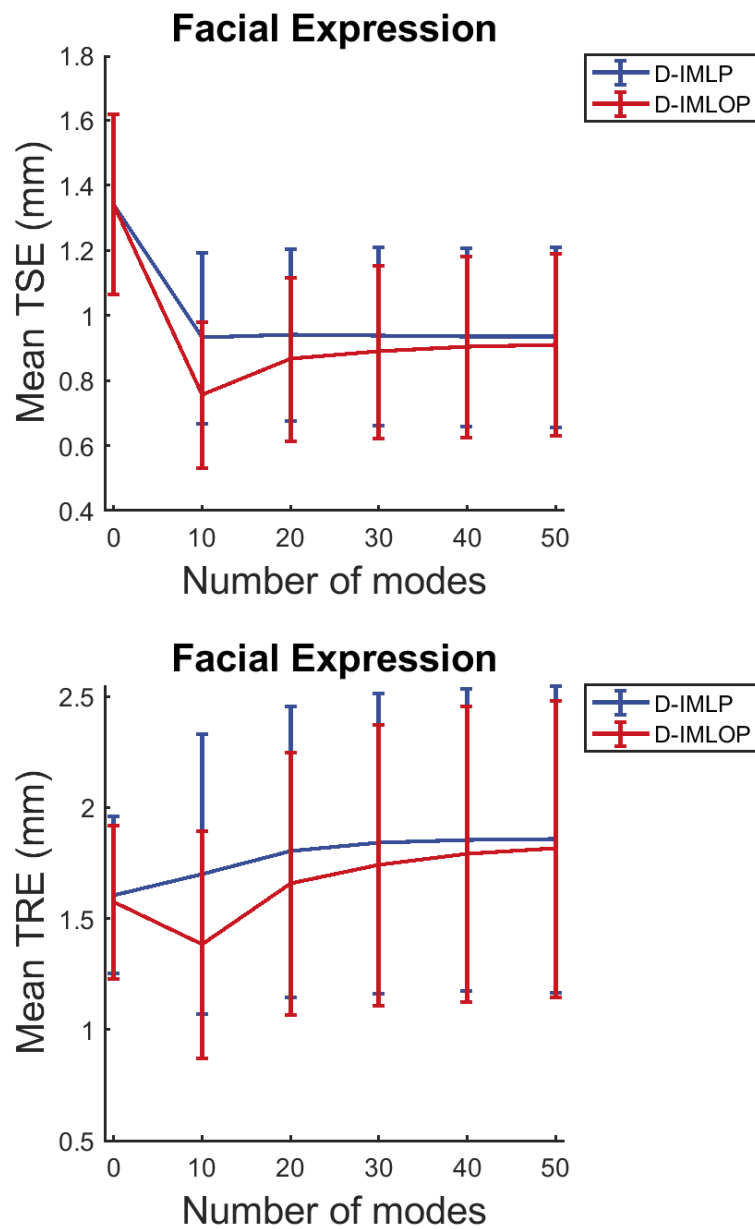


**Figure 5.32:** Leave- $n$ -out experiment: TSE (top) and TRE (bottom) produced by D-IMLOP.

ited data available and perhaps the linearity assumptions made by PCA-based models are not sufficient to explain the complex variations observed in different poses. However, the weak correlation between residual errors and TREs produced by D-IMLOP could be an indication that with sufficient data, the performance of D-IMLOP could show improvement (Fig. 5.34).

## 5.6 Concluding remarks

A novel deformable variant of IMLOP, known as the deformable iterative most likely orientated point (D-IMLOP) algorithm, is presented in this chapter. D-IMLOP can accurately compute an alignment between a mean shape and data samples while simultaneously deforming the mean shape to estimate the shape represented by the data samples. Its accuracy increases as the number of data samples increases, and its performance only degrades slightly with increasing number of outliers. CPD outperforms D-IMLOP in terms of errors, but is about 5–8× slower than D-IMLOP in terms of runtime. Further, CPD’s memory requirements become prohibitively large very quickly, whereas D-IMLOP does not suffer from this problem. Further, errors produced by CPD do not correlate well with ground truth error, whereas those produced by D-IMLOP do, allowing it to make confidence assignments to the registrations based on these errors. However, D-IMLOP is only capable of making isotropic noise assumptions in the orientation component, which is often not able to model noise in

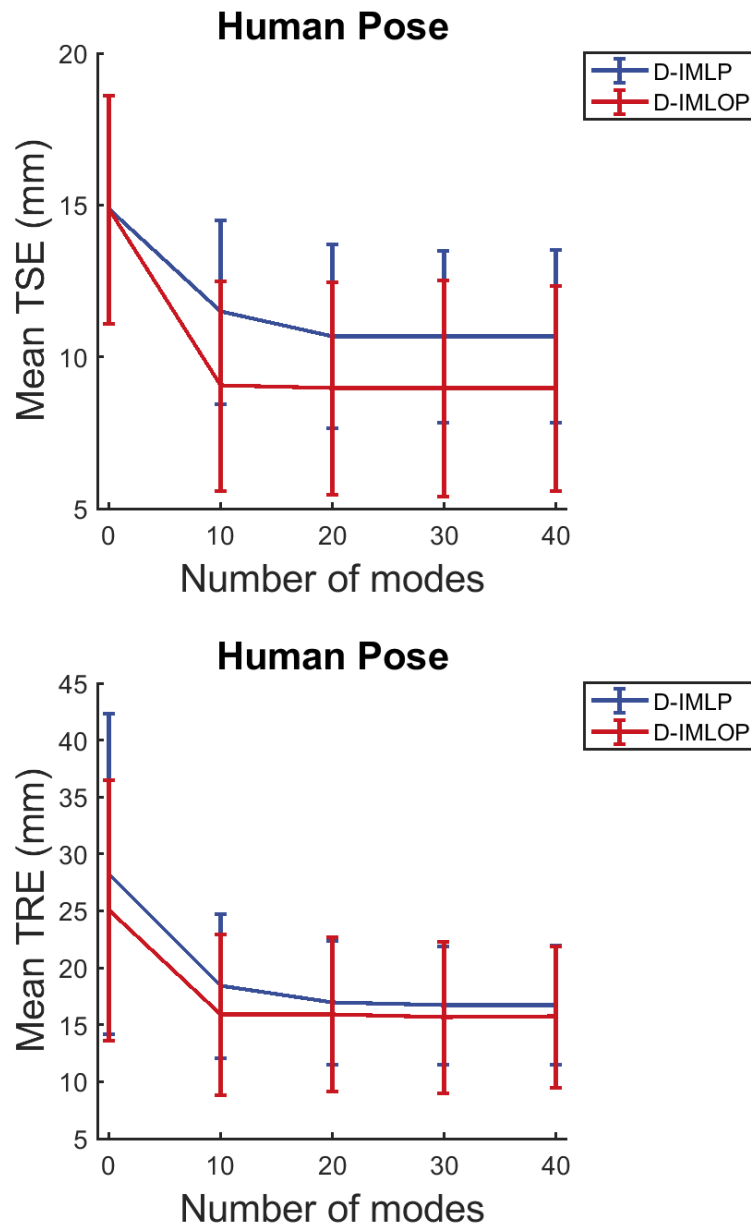


**Figure 5.33:** Leave- $n$ -out experiment: TSE (top) and TRE (bottom) produced by D-IMLOP.

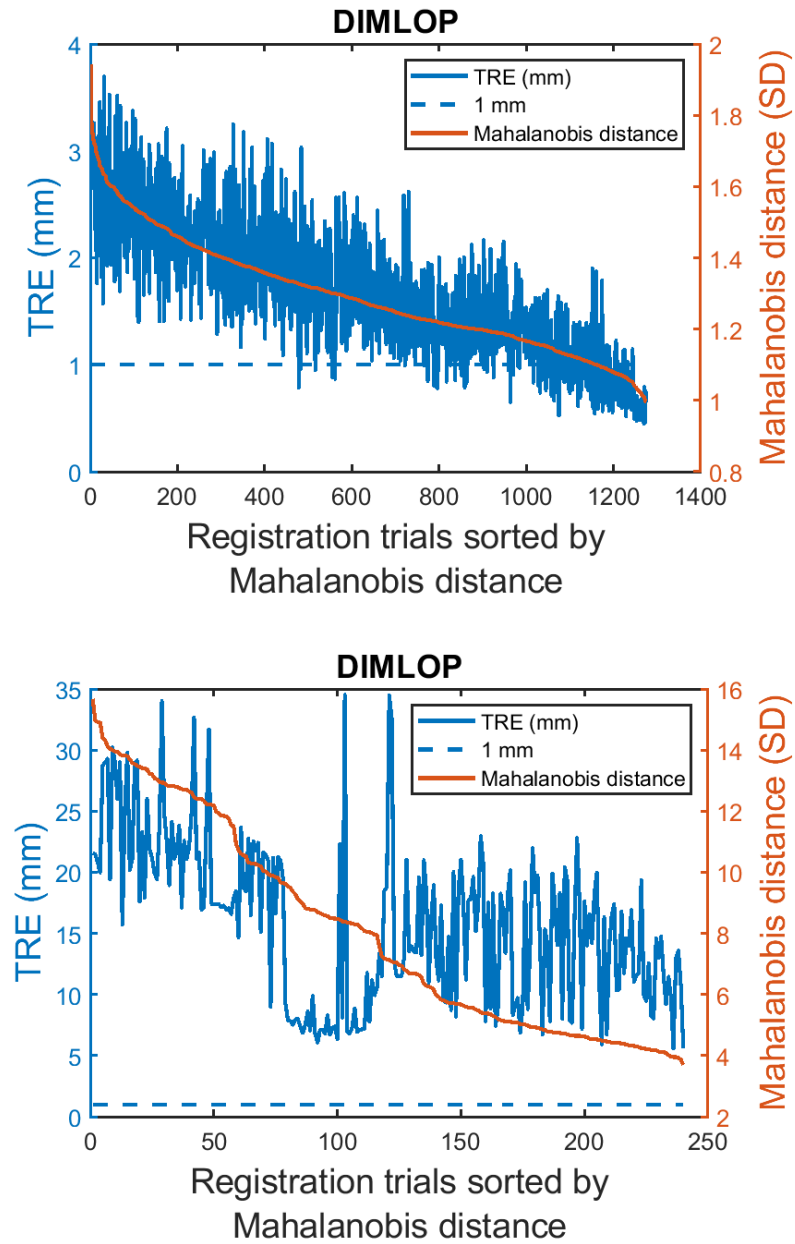


**Figure 5.34:** Leave- $n$ -out experiment: residual errors compared against TRE show that the two measures exhibit high correlation using the facial expression data with a correlation coefficient of 0.81 (top), and weak correlation using the human pose data with a correlation coefficient of 0.51 (bottom).



data from real world applications which may contain anisotropic noise.

## 5.7 Contributions

The contributions of this chapter include:

1. The development, implementation and evaluation of the deformable iterative most likely oriented point (D-IMLOP) algorithm<sup>77</sup> which
  - (a) incorporates deformable shape transformations using SSMs within a probabilistic registration algorithm that uses point features with unconstrained noise along with orientation features with constrained or isotropic noise
  - (b) performs an efficient implementation of PD-tree update to accommodate a deforming model shape
  - (c) computes a gradient-based solution to the optimization problem using an off-the-shelf nonlinear box-constrained BFGS quasi-Newton optimizer<sup>80</sup>
  - (d) incorporates a mechanism for autonomously evaluating a registration in order to assign confidence to the resulting alignment

## 5.8 Published work

Material from this chapter appeared in the following publication:

## CHAPTER 5. D-IMLOP ALGORITHM

1. A. Sinha, S. D. Billings, A. Reiter, X. Liu, M. Ishii, G. D. Hager, R. H. Taylor, “The deformable most-likely-point paradigm,” *submitted to Medical Image Analysis* (2018)

## Chapter 6

# Generalized deformable iterative most likely oriented point (GD-IMLOP) algorithm

This Chapter further extends the D-IMLOP algorithm, described in Chapter 5, drawing inspiration from the generalized iterative most likely oriented point (G-IMLOP).<sup>53</sup> This Chapter describes the generalized deformable most likely oriented point (GD-IMLOP) algorithm, which, like the G-IMLOP algorithm, incorporates anisotropic noise models for both the position and orientation components, and can deformably register oriented features characterized by anisotropic uncertainty in position and orientation data. Like the algorithms presented in the previous two Chapters, D-IMLP and D-IMLOP, GD-IMLOP is also an ICP-based method built on the frame-

## CHAPTER 6. GD-IMLOP ALGORITHM

work described in Chapter 3 that incorporates a probabilistic framework to combine the position and orientation information of the features and deformably registered them.

As with the rigid algorithm, the anisotropic extension will allow GD-IMLOP to achieve higher accuracy when registering realistic data that is often characterized by anisotropic noise in the measured positions and orientations. Anisotropic noise is present in features extracted from video, since error in the depth direction tends to be larger, and also in features extracted from volumetric medical images, which tend to have a lower out of plane resolution. Other sources of anisotropic measurement uncertainties in medical and non-medical data were previously discussed in Chapter 4, and sources of orientation data were discussed in Chapter 5.

### 6.1 Probabilistic model

For ease of reference during the development of the probabilistic model for GD-IMLOP, a brief description of the probabilistic model for GD-IMLOP is repeated here. G-IMLOP incorporates a probabilistic framework formulated using anisotropic Gaussian and Kent distributions to model the measurement errors in the position and orientation data, respectively.<sup>53</sup> Similar to the isotropic Fisher distribution that was used in the previous chapter (Ch. 5), the anisotropic Kent distribution is the analog on the unit sphere of a multivariate Gaussian distribution with unconstrained covari-

## CHAPTER 6. GD-IMLOP ALGORITHM

ance, that is, covariance that may be isotropic or anisotropic. Assuming zero-mean, independent, identically distributed (iid) error for both the position and orientation components, the *match likelihood function* for an oriented data point,  $\mathbf{x} = (\mathbf{x}_p, \hat{\mathbf{x}}_n)$ , transformed by a current registration estimate,  $[\mathbf{R}, \mathbf{t}]$ , is defined as<sup>53</sup>

$$f_{\text{match}}(\mathbf{x}; \mathbf{y}, \Sigma, \kappa, \beta, \hat{\gamma}_1, \hat{\gamma}_2, \mathbf{R}, \mathbf{t}) = \frac{1}{\sqrt{(2\pi)^3 |\Sigma|} \cdot c(\kappa, \beta)} \cdot e^{\kappa \hat{\mathbf{y}}_n^T \mathbf{R} \hat{\mathbf{x}}_n + \beta \left( (\hat{\gamma}_1^T \mathbf{R} \hat{\mathbf{x}}_n)^2 - (\hat{\gamma}_2^T \mathbf{R} \hat{\mathbf{x}}_n)^2 \right) - \frac{1}{2} (\mathbf{y}_p - \mathbf{R} \mathbf{x}_p - \mathbf{t})^T \mathbf{R} \Sigma^{-1} \mathbf{R}^T (\mathbf{y}_p - \mathbf{R} \mathbf{x}_p - \mathbf{t})}, \quad (6.1)$$

where  $\mathbf{y} = (\mathbf{y}_p, \mathbf{y}_n)$  is an oriented point on the shape model that is assumed to be in correspondence with the oriented data point,  $\mathbf{x}$  and  $\Sigma$  is the *covariance matrix* of the positional noise model.<sup>53</sup>  $\kappa$ , the *concentration parameter*,  $\beta$  ( $0 \leq 2\beta < \kappa$ ), the *ellipticity parameter*, and  $\hat{\gamma}_1$  and  $\hat{\gamma}_2$ , the *major* and *minor axes* which define the direction of the elliptical level sets of the Kent distribution on the unit sphere, together define the orientation noise model.<sup>53</sup> The major and minor axes are orthogonal to each other as well as to  $\hat{\mathbf{y}}_n$ , which is the *central direction*. The *central position* is represented by  $\hat{\mathbf{y}}_p$ . The ellipticity parameter,  $\beta$ , controls the amount of anisotropy in the orientation noise model.<sup>53</sup> Larger values of  $\beta$  increase the anisotropy, while a value of 0 reduces the expression to the isotropic Fisher distribution used by the IMLOP algorithm, described in Chapter 5.<sup>53</sup>  $c(\kappa, \beta)$  is the normalizing constant of the Kent distribution, and consists of a complex expression of modified Bessel functions.<sup>114</sup> In the correspondence phase of G-IMLOP, this is the match likelihood function that is maximized in order to find the oriented matched points,  $\mathbf{y}$ , on the model shape,  $\Psi$ .

## CHAPTER 6. GD-IMLOP ALGORITHM

One small difference in the formulation of the deformable algorithm is that GD-IMLOP incorporates generalized Gaussian noise to account for unconstrained noise in the position component of both the data points and model shape. Therefore, Eq. 6.1 is rewritten slightly differently as:

$$f_{\text{match}}(\mathbf{x}; \mathbf{y}, \Sigma_{\mathbf{x}}, \Sigma_{\mathbf{y}}, \kappa, \beta, \hat{\gamma}_1, \hat{\gamma}_2, \mathbf{R}, \mathbf{t}) = \frac{1}{\sqrt{(2\pi)^3} |\mathbf{R}\Sigma_{\mathbf{x}}\mathbf{R}^{\mathbf{T}} + \Sigma_{\mathbf{y}}| \cdot c(\kappa, \beta)} \cdot e^{\kappa \hat{\mathbf{y}}_{\mathbf{n}} \mathbf{R} \hat{\mathbf{x}}_{\mathbf{n}} + \beta \left( (\hat{\gamma}_1^{\mathbf{T}} \mathbf{R} \hat{\mathbf{x}}_{\mathbf{n}})^2 - (\hat{\gamma}_2^{\mathbf{T}} \mathbf{R} \hat{\mathbf{x}}_{\mathbf{n}})^2 \right) - \frac{1}{2} (\mathbf{y}_{\mathbf{p}} - \mathbf{R} \mathbf{x}_{\mathbf{p}} - \mathbf{t})^{\mathbf{T}} (\mathbf{R} \Sigma_{\mathbf{x}} \mathbf{R}^{\mathbf{T}} + \Sigma_{\mathbf{y}})^{-1} (\mathbf{y}_{\mathbf{p}} - \mathbf{R} \mathbf{x}_{\mathbf{p}} - \mathbf{t})}, \quad (6.2)$$

where measurement error covariances,  $\Sigma_{\mathbf{x}}$  and  $\Sigma_{\mathbf{y}}$ , are used to describe the positional noise model for  $\mathbf{x}$  and  $\mathbf{y}$ , respectively. In the correspondence phase of GD-IMLOP, as in the previous two deformable algorithms, this match likelihood function is maximized to find the oriented matched points,  $\mathbf{y}$ , on the current deformed shape. Similarly, the match likelihood function for each  $\mathbf{x}$  transformed by a *similarity* registration estimate,  $[a, \mathbf{R}, \mathbf{t}]$ , where  $a$  is the scale variable, can be defined as

$$f_{\text{match}}(\mathbf{x}; \mathbf{y}, \Sigma, \kappa, \beta, \hat{\gamma}_1, \hat{\gamma}_2, a, \mathbf{R}, \mathbf{t}) = \frac{1}{\sqrt{(2\pi)^3} |\mathbf{R}\Sigma_{\mathbf{x}}\mathbf{R}^{\mathbf{T}} + \Sigma_{\mathbf{y}}| \cdot c(\kappa, \beta)} \cdot e^{\kappa \hat{\mathbf{y}}_{\mathbf{n}} \mathbf{R} \hat{\mathbf{x}}_{\mathbf{n}} + \beta \left( (\hat{\gamma}_1^{\mathbf{T}} \mathbf{R} \hat{\mathbf{x}}_{\mathbf{n}})^2 - (\hat{\gamma}_2^{\mathbf{T}} \mathbf{R} \hat{\mathbf{x}}_{\mathbf{n}})^2 \right) - \frac{1}{2} (\mathbf{y}_{\mathbf{p}} - a \mathbf{R} \mathbf{x}_{\mathbf{p}} - \mathbf{t})^{\mathbf{T}} (\mathbf{R} \Sigma_{\mathbf{x}} \mathbf{R}^{\mathbf{T}} + \Sigma_{\mathbf{y}})^{-1} (\mathbf{y}_{\mathbf{p}} - a \mathbf{R} \mathbf{x}_{\mathbf{p}} - \mathbf{t})}, \quad (6.3)$$

As before, since the two registration problems are similar, the focus of the derivations will remain on derivations from Eq. 6.2. Technical differences between the two registration problems will be pointed out wherever necessary. Maximizing the likelihood function of Eq. 6.2 is equivalent to minimizing its negative log likelihood, producing

## CHAPTER 6. GD-IMLOP ALGORITHM

the following *match error function*:

$$\begin{aligned}
 E_{\text{D-IMLOP}}(\mathbf{x}, \mathbf{y}, \Sigma_{\mathbf{x}}, \Sigma_{\mathbf{y}}, \kappa, \beta, \hat{\gamma}_1, \hat{\gamma}_2, \mathbf{R}, \mathbf{t}) \\
 = \frac{1}{2}(\mathbf{y} - \mathbf{R}\mathbf{x} - \mathbf{t})^{\text{T}}(\mathbf{R}\Sigma_{\mathbf{x}}\mathbf{R}^{\text{T}} + \Sigma_{\mathbf{y}})^{-1}(\mathbf{y} - \mathbf{R}\mathbf{x} - \mathbf{t}) \\
 - \kappa\hat{\mathbf{y}}_{\mathbf{n}}\mathbf{R}\hat{\mathbf{x}}_{\mathbf{n}} - \beta \left( (\hat{\gamma}_1^{\text{T}}\mathbf{R}\hat{\mathbf{x}}_{\mathbf{n}})^2 - (\hat{\gamma}_2^{\text{T}}\mathbf{R}\hat{\mathbf{x}}_{\mathbf{n}})^2 \right).
 \end{aligned} \tag{6.4}$$

Since the major and minor axes,  $\hat{\gamma}_1$  and  $\hat{\gamma}_2$ , are perpendicular to the central direction,  $\hat{\mathbf{y}}_{\mathbf{n}}$ , of the matched point,  $\mathbf{y}$ , this formulation would require recomputing  $\hat{\gamma}_1$  and  $\hat{\gamma}_2$  for every oriented model point that is tested for correspondence.<sup>53</sup> To avoid this computational inefficiency, Eq. 6.4 can be reformulated to an equivalent match error function where  $\hat{\gamma}_1$  and  $\hat{\gamma}_2$  are redefined to be perpendicular to the orientation,  $\hat{\mathbf{x}}_{\mathbf{n}}$ , of the data point,  $\mathbf{x}$ :

$$\begin{aligned}
 E_{\text{D-IMLOP}}(\mathbf{x}, \mathbf{y}, \Sigma_{\mathbf{x}}, \Sigma_{\mathbf{y}}, \kappa, \beta, \hat{\gamma}_1, \hat{\gamma}_2, \mathbf{R}, \mathbf{t}) \\
 = \frac{1}{2}(\mathbf{y} - \mathbf{R}\mathbf{x} - \mathbf{t})^{\text{T}}(\mathbf{R}\Sigma_{\mathbf{x}}\mathbf{R}^{\text{T}} + \Sigma_{\mathbf{y}})^{-1}(\mathbf{y} - \mathbf{R}\mathbf{x} - \mathbf{t}) \\
 - \kappa\hat{\mathbf{y}}_{\mathbf{n}}\mathbf{R}\hat{\mathbf{x}}_{\mathbf{n}} - \beta \left( (\hat{\gamma}_1^{\text{T}}\mathbf{R}^{\text{T}}\hat{\mathbf{y}}_{\mathbf{n}})^2 - (\hat{\gamma}_2^{\text{T}}\mathbf{R}^{\text{T}}\hat{\mathbf{y}}_{\mathbf{n}})^2 \right).
 \end{aligned} \tag{6.5}$$

Using this formulation,  $\hat{\gamma}_1$  and  $\hat{\gamma}_2$  only need to be defined once with respect to the measured data points, rather than the unknown matched points, and therefore, do not need to be recomputed for every oriented model point that is tested for correspondence.<sup>53</sup> This change is able to reduce the computational overhead of the correspondence phase of GD-IMLOP.

## CHAPTER 6. GD-IMLOP ALGORITHM

In the registration phase, G-IMLOP solves for the transformation that maximizes the total match likelihood function of Eq. 6.1.<sup>53</sup> This simplifies to computing the transformation,  $\mathbf{T}$  that maximizes the following *total match error function* with respect to the transformation parameters:<sup>53</sup>

$$\mathbf{T} = \underset{[\mathbf{R}, \mathbf{t}]}{\operatorname{argmin}} \left( \frac{1}{2} \sum_{i=1}^{n_{\text{data}}} (\mathbf{y}_{\mathbf{p}_i} - \mathbf{R}\mathbf{x}_{\mathbf{p}_i} - \mathbf{t})^{\mathbf{T}} \mathbf{R} \boldsymbol{\Sigma}_i^{-1} \mathbf{R}^{\mathbf{T}} (\mathbf{y}_{\mathbf{p}_i} - \mathbf{R}\mathbf{x}_{\mathbf{p}_i} - \mathbf{t}) - \sum_{i=1}^{n_{\text{data}}} \left( \kappa_i \hat{\mathbf{y}}_{\mathbf{n}_i} \mathbf{R} \hat{\mathbf{x}}_{\mathbf{n}_i} + \beta_i \left( (\hat{\gamma}_{1_i}^{\mathbf{T}} \mathbf{R}^{\mathbf{T}} \hat{\mathbf{y}}_{\mathbf{n}_i})^2 - (\hat{\gamma}_{2_i}^{\mathbf{T}} \mathbf{R}^{\mathbf{T}} \hat{\mathbf{y}}_{\mathbf{n}_i})^2 \right) \right) \right). \quad (6.6)$$

Substituting  $f_{\text{match}}$  from Eq. 6.2 into the total deformable match likelihood function of Eq. 3.11, the *deformable registration cost function* for GD-IMLOP can be derived as:

$$\mathbf{T} = \underset{[\mathbf{R}, \mathbf{t}, \mathbf{s}]}{\operatorname{argmin}} \left( \frac{1}{2} \sum_{i=1}^{n_{\text{data}}} (\mathbf{T}_{\text{ssm}}(\mathbf{y}_{\mathbf{p}_i}, \mathbf{s}) - \mathbf{R}\mathbf{x}_{\mathbf{p}_i} - \mathbf{t})^{\mathbf{T}} (\mathbf{R} \boldsymbol{\Sigma}_{\mathbf{x}} \mathbf{R}^{\mathbf{T}})^{-1} (\mathbf{T}_{\text{ssm}}(\mathbf{y}_{\mathbf{p}_i}, \mathbf{s}) - \mathbf{R}\mathbf{x}_{\mathbf{p}_i} - \mathbf{t}) - \sum_{i=1}^{n_{\text{data}}} \left( \kappa_i \hat{\mathbf{y}}_{\mathbf{n}_i} \mathbf{R} \hat{\mathbf{x}}_{\mathbf{n}_i} + \beta_i \left( (\hat{\gamma}_{1_i}^{\mathbf{T}} \mathbf{R}^{\mathbf{T}} \hat{\mathbf{y}}_{\mathbf{n}_i})^2 - (\hat{\gamma}_{2_i}^{\mathbf{T}} \mathbf{R}^{\mathbf{T}} \hat{\mathbf{y}}_{\mathbf{n}_i})^2 \right) \right) + \frac{1}{2} \sum_{j=1}^{n_{\text{m}}} \|s_j\|_2^2 \right), \quad (6.7)$$

where the model shape covariances,  $\boldsymbol{\Sigma}_{y_i}$ , are again assumed to be zero since the focus here is on the derivatives introduced by the shape deformations during optimization. The redefinition of the major and minor axes,  $\hat{\gamma}_1$  and  $\hat{\gamma}_2$ , as defined above for the correspondence phase is carried through to the registration phase.



## 6.2 Algorithm overview

In this section, a high level overview of the GD-IMLOP algorithm is presented along with pseudocode explaining the registration pipeline. As in the previous two chapters, details developed along with the G-IMLOP algorithm will not be repeated in depth here, but will be referenced whenever required. Similarly, ideas already developed in the previous two chapters will not be repeated here, but referenced whenever needed. Instead, the focus will be on the new developments introduced along with the deformable aspect of GD-IMLOP. Algorithm 6.1 provides a summary of the GD-IMLOP algorithm, and will be referenced throughout this section. Underlined variables in Alg. 6.1 indicate optional variables that are required when solving additionally for scale.

The inputs to GD-IMLOP are, again, similar to both D-IMLP and D-IMLOP.  $\mathbf{X}$  and  $\Psi$  represent the data points and the statistically mean model shape with  $\mathbf{s}$  initialized to 0, respectively.  $\mathbf{s}$  can, as mentioned in the previous chapters, be initialized to different set of values, which would lead to a different initial shape.  $\mathbf{w}$  are the mode weights that represent the statistics associated with the model shape,  $\Sigma_{\mathbf{x}}$  and  $\Sigma_{\Psi}$  represent the measurement-error covariances associated with the data points and model shape, respectively, and  $\Sigma_{S_{\mathbf{x}}}$  and  $\Sigma_{S_{\Psi}}$  represent the surface-model covariances for the data points and model shape, respectively. As with D-IMLP and D-IMLOP,  $\Sigma_{\mathbf{x}}$  and  $\Sigma_{\Psi}$  are assumed to be generated from an isotropic Gaussian with SD  $1 \times 1 \times 1 \text{ mm}^3$ , but the default SD can be modified by the user depending on

---

**Algorithm 6.1:** Generalized Deformable Iterative Most Likely Oriented Point (GD-IMLOP)
 

---

**Input** : Data points as a point cloud:  $\mathbf{X} = \{\mathbf{x}_i\} = \{(\mathbf{x}_{\mathbf{p}_i}, \hat{\mathbf{x}}_{\mathbf{n}_i})\}$   
 Statistically mean model shape,  $\Psi_0$ , and associated SSM  
 Measurement-error covariances:  $\Sigma_{\mathbf{X}} = \{\Sigma_{\mathbf{x}_i}\}, \Sigma_{\Psi}$   
 Surface-model covariances:  $\Sigma_{\mathbf{S}\mathbf{X}} = \{\Sigma_{\mathbf{S}\mathbf{x}_i}\}, \Sigma_{\mathbf{S}\Psi}$   
 Orientation noise-model parameters:  $\{\hat{\gamma}_{1_i}\}, \{\hat{\gamma}_{2_i}\}$   
 Circular SD of sample orientations:  $\sigma_{\text{circ.deg}}$  (default:  $2^\circ$ )  
 Eccentricity of sample orientations:  $e$  (default: 0.5)  
 Upper bound on match uncertainty:  $\sigma_{\text{max}}^2$  (default:  $\infty$ )  
 Chi-square threshold value for position outliers:  $\chi_{\text{thresh}}^2$  (default: 7.81)  
 Outlier variance expansion factor:  $\varphi_{\text{exp}}$  (default: 9)  
 Initial transformation estimate:  $[\underline{a}_0, \mathbf{R}_0, \mathbf{t}_0], \mathbf{s}_0$   
 Initial orientation noise parameter:  $\{\kappa_{i_0}\}, \{\beta_{i_0}\}$

**Output:** Final data transformation,  $[\mathbf{R}, \mathbf{t}]$ , and shape parameters,  $\mathbf{s}$ , that align  $\mathbf{X}$  with deformed  $\Psi$

- 1 Initialize transformation:  $[\underline{a}, \mathbf{R}, \mathbf{t}], \mathbf{s} \leftarrow [\underline{a}_0, \mathbf{R}_0, \mathbf{t}_0], \mathbf{s}_0$
- 2 Initialize noise model parameters:  

$$\{\kappa_i\} \leftarrow \{\kappa_{i_0}\}, \{\beta_i\} \leftarrow \{\beta_{i_0} \leftarrow e \frac{\kappa_{i_0}}{2}\}, \sigma_{\text{match}}^2 \leftarrow 0$$
- 3 **while** *not converged* **do**
- 4     **if**  $iter == 1$  **then**
- 5         Compute initial correspondences on the mean shape (Eq. 3.12):  

$$[\mathbf{y}_{\mathbf{p}_i}, \Sigma_{\mathbf{y}_i}, \Sigma_{\mathbf{S}\mathbf{y}_i}] \leftarrow \mathbf{C}_{\text{MLP}}(\mathbf{x}_{\mathbf{p}_i}, \Psi_0, \mathbf{I}, \mathbf{I}, \kappa_i, \beta_i, \hat{\gamma}_{1_i}, \hat{\gamma}_{2_i}, \underline{a}, \mathbf{R}, \mathbf{t})$$
- 6         **else**
- 7             Update PD-tree based on current shape
- 8             Compute most likely correspondences on the current shape (Eq. 3.12):  

$$[\mathbf{y}_{\mathbf{p}_i}, \Sigma_{\mathbf{y}_i}, \Sigma_{\mathbf{S}\mathbf{y}_i}] \leftarrow \mathbf{C}_{\text{MLP}}(\mathbf{x}_{\mathbf{p}_i}, \Psi_{iter}, \Sigma_{\mathbf{x}_i} + \Sigma_{\mathbf{S}\mathbf{x}_i} + \sigma_{\text{match}}^2 \mathbf{I}, \Sigma_{\Psi} + \Sigma_{\mathbf{S}\Psi}, \kappa_i, \beta_i, \hat{\gamma}_{1_i}, \hat{\gamma}_{2_i}, \underline{a}, \mathbf{R}, \mathbf{t})$$
- 9         **end**
- 10         Update the match-uncertainty noise-model term (Eq. 4.7):  

$$\sigma_{\text{match}}^2 \leftarrow \min \left( \frac{1}{n_{\text{inlier}}} \sum_{i \in \text{inliers}} \|\mathbf{y}_{\mathbf{p}_i} - \underline{a}\mathbf{R}\mathbf{x}_{\mathbf{p}_i} - \mathbf{t}\|_2^2, \sigma_{\text{max}}^2 \right)$$
- 11         Compute mean angle between matched normals:  

$$\rho \leftarrow \frac{1}{n_{\text{inlier}}} \sum_{i \in \text{inliers}} \hat{\mathbf{y}}_{\mathbf{n}_i}^T \mathbf{R} \hat{\mathbf{x}}_{\mathbf{n}_i}$$
- 12         Compute circular standard deviation and update angular threshold:  

$$\theta_{\text{circ}} \leftarrow \sqrt{-2 \ln \rho}, \theta_{\text{thresh}} \leftarrow \sqrt{\varphi_{\text{exp}}} \cdot \theta_{\text{circ}}$$

---

---

**Algorithm 6.1: GD-IMLOP** (*continued...*)
 

---

11 Identify outliers (Eq. 4.8, 5.8):

$$\begin{aligned}
 & (\mathbf{x}_i, \mathbf{y}_i) \text{ is an outlier if} \\
 & E_{\text{SqrMahalDist}}(\mathbf{x}_{\mathbf{p}_i}, \mathbf{y}_{\mathbf{p}_i}, \Sigma_{\mathbf{x}_i}, \Sigma_{\mathbf{y}_i} + \sigma_{\text{match}}^2 \mathbf{I}, \underline{a}, \mathbf{R}, \mathbf{t}) > \chi_{\text{thresh}}^2 \\
 & \text{OR } \hat{\mathbf{y}}_{\mathbf{n}_i}^T \hat{\mathbf{x}}_{\mathbf{n}_i} < \cos(\theta_{\text{thresh}})
 \end{aligned}$$

12 Update the outlier noise-model terms (Eq. 4.10):

$$\varphi_i \leftarrow \begin{cases} \varphi_{\text{exp}} \|\mathbf{y}_{\mathbf{p}_i} - \underline{a}\mathbf{R}\mathbf{x}_{\mathbf{p}_i} - \mathbf{t}\|_2^2 & \text{if } (\mathbf{x}_i, \mathbf{y}_i) \text{ is an outlier,} \\ 0 & \text{otherwise.} \end{cases}$$

13 Set the noise-model covariances for the registration phase:

$$\Sigma_{\mathbf{x}_i}^* \leftarrow \Sigma_{\mathbf{x}_i} + \Sigma_{\text{Sx}_i} + \frac{\varphi_i}{2} \mathbf{I}, \quad \Sigma_{\mathbf{y}_i}^* \leftarrow \Sigma_{\mathbf{y}_i} + \Sigma_{\text{Sy}_i} + \frac{\varphi_i}{2} \mathbf{I} + \sigma_{\text{match}}^2 \mathbf{I}$$

14 Update the transformation and shape to align the point cloud and the corresponding points on the shape (Eq. 6.7 or 6.14):

$$\begin{aligned}
 [\underline{a}, \mathbf{R}, \mathbf{t}], \mathbf{s} \leftarrow \underset{[\underline{a}, \mathbf{R}, \mathbf{t}], \mathbf{s}}{\text{argmin}} & \left( \frac{1}{2} \sum_{i=1}^{n_{\text{data}}} \left( \left( \mathbf{T}_{\text{ssm}}(\mathbf{y}_{\mathbf{p}_i}, \mathbf{s}) - \underline{a}\mathbf{R}\mathbf{x}_{\mathbf{p}_i} - \mathbf{t} \right)^T \left( \mathbf{R}\Sigma_{\mathbf{x}_i}\mathbf{R}^T \right)^{-1} \right. \right. \\
 & \left. \left( \mathbf{T}_{\text{ssm}}(\mathbf{y}_{\mathbf{p}_i}, \mathbf{s}) - \underline{a}\mathbf{R}\mathbf{x}_{\mathbf{p}_i} - \mathbf{t} \right) \right) - \sum_{i=1}^{n_{\text{data}}} \left( \kappa_i \hat{\mathbf{y}}_{\mathbf{n}_i} \mathbf{R} \hat{\mathbf{x}}_{\mathbf{n}_i} \right. \\
 & \left. \left. + \beta_i \left( (\hat{\gamma}_{1_i}^T \mathbf{R} \mathbf{R}^T \hat{\mathbf{y}}_{\mathbf{n}_i})^2 - (\hat{\gamma}_{2_i}^T \mathbf{R} \mathbf{R}^T \hat{\mathbf{y}}_{\mathbf{n}_i})^2 \right) \right) \right. \\
 & \left. \left. + \frac{1}{2} \sum_{j=1}^{n_{\text{m}}} \|s_j\|_2^2 \right)
 \end{aligned}$$

 15 Based on computed  $\mathbf{s}$ , update the vertices of the model shape (Eq. 3.10):

$$\Psi_{\text{iter}} \leftarrow \mathbf{T}_{\text{ssm}}(\mathbf{v}_i, \mathbf{s})$$

 16 Update extents of PD-tree bounding boxes based on  $\Psi_{\text{iter}}$  (Sec. 3.2)

 17  $\text{iter}++$ 
**end**

18 Detect registration failure using a chi-square test (Eqs. 4.11, 6.12):

Registration is unsuccessful if

$$\begin{aligned}
 & \sum_{i=1}^{n_{\text{data}}} E_{\text{SqrMahalDist}}(\mathbf{x}_{\mathbf{p}_i}, \mathbf{y}_{\mathbf{p}_i}, \Sigma_{\mathbf{x}_i}, \Sigma_{\mathbf{y}_i} + \sigma_{\text{match}}^2 \mathbf{I}, \underline{a}, \mathbf{R}, \mathbf{t}) \geq \chi_{\text{pos\_thresh\_final}}^2 \\
 \text{OR } & \sum_{i=1}^{n_{\text{data}}} E_{\text{SqrAnisoAngRes}}(\hat{\mathbf{x}}_{\mathbf{n}_i}, \hat{\mathbf{y}}_{\mathbf{n}_i}, \kappa_i, \beta_i, \hat{\gamma}_{1_i}, \hat{\gamma}_{2_i}, \mathbf{R}) \geq \chi_{\text{ang\_thresh\_final}}^2
 \end{aligned}$$


---

## CHAPTER 6. GD-IMLOP ALGORITHM

the application. Additionally, the major and minor axes,  $\hat{\gamma}_1$  and  $\hat{\gamma}_2$ , representing the ellipticity of the orientation noise-model must be defined for each data point. The orientation noise is assumed to be drawn from an anisotropic Kent distribution with a default circular SD,  $\sigma_{\text{circ.deg}}$ , of  $2^\circ$  and eccentricity,  $e = 0.5$ . These values can also be modified by the user based on the application.

An initial transformation with an initial guess for rotation, translation, and, when applicable, scale, and an initial set of shape parameters must be specified. As mentioned before, the initial shape parameters,  $s$  is set to 0, which describes the statistically mean shape. The concentration parameter,  $\kappa$ , of the orientation noise is initialized using  $\sigma_{\text{circ.deg}}$  in radians as described in Eq. 5.7, while the ellipticity,  $\beta$ , of the orientation noise is initialized using the eccentricity,  $e$ , as

$$\beta = e \frac{\kappa}{2}. \quad (6.8)$$

$\kappa$  and  $\beta$  for all data points are initialized to the same value, but this can be modified by the user by specifying different circular SDs for each data point. The remaining input parameters will be discussed briefly as they are encountered in the equations in Alg. 6.1 with the exception of those that have already been covered in Alg. 4.1 and 5.1. The output of the algorithm is the same as the previous two algorithms, D-IMLP and D-IMLOP, that is, a final transform that aligns the data points to the final deformed model shape, defined by a final set of shape parameters,  $s$ .

## CHAPTER 6. GD-IMLOP ALGORITHM

The convergence criteria for GD-IMLOP are identical to the convergence criteria for D-IMLP and D-IMLOP. Until convergence is achieved, GD-IMLOP computes correspondences between the oriented data points and the current deformed model shape at every iteration. After correspondences are found, the match uncertainty term for the position component of the matched points is updated and the threshold for the orientation component of the matched points is updated as described in Alg. 4.1 and 5.1, respectively. Outliers are identified using the position component of the matched points, followed by the orientation component. The remaining noise-model updates before registration are identical to those in Alg. 4.1. Unlike D-IMLOP,  $\kappa$  is not updated after registration because registration results with and without updates were comparable, and skipping the updates improves the efficiency of our computations. However, the framework allows the user to change the setting to add these updates back.

Once the algorithm converges or terminates and a registration is computed, two chi-square tests are used to classify the registration as successful or unsuccessful. The first test that evaluates the registration based on the positional components of the match points, as shown in Step 18 of Alg. 6.1, is identical to that used in D-IMLP and D-IMLOP (Eq. 4.11). If the registration passes this test, it is further evaluated on the orientation components of the matched points. A 2D wrapped-Gaussian approximation of the Kent distribution is used here to convert the noise model of the angular residuals to Gaussian form. Once in Gaussian form, the chi-

## CHAPTER 6. GD-IMLOP ALGORITHM

square test with 2 DOF can be used to evaluate the quality of the orientation matches.

The wrapped-Gaussian, repeated here for ease of reference,

$$\frac{1}{\sigma\sqrt{2\pi}} \sum_{k=-\infty}^{\infty} e^{-\frac{(\theta_{\mathbf{n}}+2\pi k)^2}{2\sigma^2}},$$

now has slightly different  $\theta_{\mathbf{n}}$  and  $\sigma^2$  to accommodate the anisotropy of the Kent distribution. In this case,  $\theta_{\mathbf{n}}$  is a vector containing the angular residual between the orientation components of corresponding sample points and matched points, and also of corresponding matched points and the major and minor axes of the elliptical level sets of the Kent distribution on the unit sphere:

$$\theta_{\mathbf{n}} = \begin{bmatrix} \cos^{-1}(\hat{\mathbf{y}}_{\mathbf{n}_i}^T \mathbf{R} \hat{\mathbf{x}}_{\mathbf{n}_i}) \\ \sin^{-1}(\hat{\gamma}_1^T \mathbf{R}^T \hat{\mathbf{y}}_{\mathbf{n}}) \\ \sin^{-1}(\hat{\gamma}_2^T \mathbf{R}^T \hat{\mathbf{y}}_{\mathbf{n}}) \end{bmatrix}, \quad (6.9)$$

which implies that  $\theta_{\mathbf{n}}$  is minimized if  $\hat{\mathbf{x}}_{\mathbf{n}}$  and transformed  $\hat{\mathbf{y}}_{\mathbf{n}}$  are aligned as best as possible, meaning that transformed  $\hat{\mathbf{y}}_{\mathbf{n}}$  is as perpendicular as possible to  $\hat{\gamma}_1$  and  $\hat{\gamma}_2$  due to the orthogonality requirement mentioned earlier (Sec. 6.1).  $\sigma^2$  is actually a covariance matrix, which will be represented by  $\Sigma$ .

$\Sigma$  is a  $3 \times 3$  diagonal matrix with each element representing the effective variance of the wrapped-Gaussian along each of the orthogonal axes,  $\hat{\mathbf{y}}_{\mathbf{n}}$ ,  $\hat{\gamma}_1$ , and  $\hat{\gamma}_2$ . As mentioned in Sec. 5.2, the variance along the  $\hat{\mathbf{y}}_{\mathbf{n}}$  direction is approximately  $\frac{1}{\kappa}$ . The

## CHAPTER 6. GD-IMLOP ALGORITHM

variances along the major and minor axes of the Kent distribution are  $\frac{1}{\kappa-2\beta}$  and  $\frac{1}{\kappa+2\beta}$ , resulting in

$$\Sigma = \begin{bmatrix} \frac{1}{\kappa} & 0 & 0 \\ 0 & \frac{1}{\kappa-2\beta} & 0 \\ 0 & 0 & \frac{1}{\kappa+2\beta} \end{bmatrix}. \quad (6.10)$$

Therefore, the sum of square angular residual is now

$$\begin{aligned} \sum_{i=1}^{n_{\text{data}}} E_{\text{SqrAnisoAngRes}}(\hat{\mathbf{x}}_{\mathbf{n}_i}, \hat{\mathbf{y}}_{\mathbf{n}_i}, \kappa_i, \beta_i, \hat{\gamma}_{1_i}, \hat{\gamma}_{2_i}, \mathbf{R}) &= \sum_{i=1}^{n_{\text{data}}} \theta_{\mathbf{n}_i}^{\text{T}} \Sigma_i^{-1} \theta_{\mathbf{n}_i} \\ &= \sum_{i=1}^{n_{\text{data}}} \begin{bmatrix} \cos^{-1}(\hat{\mathbf{y}}_{\mathbf{n}_i}^{\text{T}} \mathbf{R} \hat{\mathbf{x}}_{\mathbf{n}_i}) \\ \sin^{-1}(\hat{\gamma}_{1_i}^{\text{T}} \mathbf{R}^{\text{T}} \hat{\mathbf{y}}_{\mathbf{n}_i}) \\ \sin^{-1}(\hat{\gamma}_{2_i}^{\text{T}} \mathbf{R}^{\text{T}} \hat{\mathbf{y}}_{\mathbf{n}_i}) \end{bmatrix}^{\text{T}} \begin{bmatrix} \kappa_i & 0 & 0 \\ 0 & \kappa_i - 2\beta_i & 0 \\ 0 & 0 & \kappa_i + 2\beta_i \end{bmatrix} \begin{bmatrix} \cos^{-1}(\hat{\mathbf{y}}_{\mathbf{n}_i}^{\text{T}} \mathbf{R} \hat{\mathbf{x}}_{\mathbf{n}_i}) \\ \sin^{-1}(\hat{\gamma}_{1_i}^{\text{T}} \mathbf{R}^{\text{T}} \hat{\mathbf{y}}_{\mathbf{n}_i}) \\ \sin^{-1}(\hat{\gamma}_{2_i}^{\text{T}} \mathbf{R}^{\text{T}} \hat{\mathbf{y}}_{\mathbf{n}_i}) \end{bmatrix}, \end{aligned} \quad (6.11)$$

and has a chi-square distribution with  $2n_{\text{data}}$  DOF. Therefore, a registration that has not already been rejected based on the quality of the positional component of matches can be rejected by comparing  $E_{\text{SqrAnisoAngRes}}(\hat{\mathbf{x}}_{\mathbf{n}_i}, \hat{\mathbf{y}}_{\mathbf{n}_i}, \kappa_i, \beta_i, \hat{\gamma}_{1_i}, \hat{\gamma}_{2_i}, \mathbf{R})$  with the value of the chi-square inverse CDF with  $2n_{\text{data}}$  DOF at some probability,  $p$ , denoted by  $\text{chi2inv}(p, 2n_{\text{data}})$ :

$$\sum_{i=1}^{n_{\text{data}}} E_{\text{SqrAnisoAngRes}}(\hat{\mathbf{x}}_{\mathbf{n}_i}, \hat{\mathbf{y}}_{\mathbf{n}_i}, \kappa_i, \beta_i, \hat{\gamma}_{1_i}, \hat{\gamma}_{2_i}, \mathbf{R}) > \text{chi2inv}(p, 2n_{\text{data}}) = \chi_{\text{ang\_thresh\_final}}^2, \quad (6.12)$$

ensuring that the angular residuals remain within  $[0, 2\pi)$ .

### 6.3 Correspondence phase

In this section, the efficient implementation of the correspondence phase of the GD-IMLOP algorithm is described. In the correspondence phase, GD-IMLOP computes the most likely oriented match on the current model shape for each data point that minimizes the match error function of Eq. 6.5. For the implementation of GD-IMLOP, Eq. 6.5 is reformulated to incorporate an additional  $\kappa$  term so that  $E_{\text{GD-IMLOP}}$  is always positive (see<sup>78</sup> for justification):

$$\begin{aligned}
 E_{\text{D-IMLOP}}(\mathbf{x}, \mathbf{y}, \boldsymbol{\Sigma}_x, \boldsymbol{\Sigma}_y, \kappa, \beta, \hat{\gamma}_1, \hat{\gamma}_2, \mathbf{R}, \mathbf{t}) \\
 = \frac{1}{2}(\mathbf{y} - \mathbf{R}\mathbf{x} - \mathbf{t})^T(\mathbf{R}\boldsymbol{\Sigma}_x\mathbf{R}^T + \boldsymbol{\Sigma}_y)^{-1}(\mathbf{y} - \mathbf{R}\mathbf{x} - \mathbf{t}) \\
 + \kappa(1 - \hat{\mathbf{y}}_n\mathbf{R}\hat{\mathbf{x}}_n) - \beta \left( (\hat{\gamma}_1^T\mathbf{R}^T\hat{\mathbf{y}}_n)^2 - (\hat{\gamma}_2^T\mathbf{R}^T\hat{\mathbf{y}}_n)^2 \right).
 \end{aligned} \tag{6.13}$$

As in the correspondence phases of D-IMLP and D-IMLOP, a PD-tree construction and search strategy is used for efficiency. The PD-tree is constructed in a similar manner as the PD-tree for IMLOP for anisotropic position-based matching and for the incorporation of orientation-based matching. The difference from IMLOP is that the PD-tree must now accommodate anisotropy not just in the position component, but also in the orientation component.<sup>53</sup> A PD-tree search strategy is employed to find the oriented matched point,  $\mathbf{y}$ , on the current deformed shape that minimizes the match error function of G-IMLOP for a given oriented data point,  $\mathbf{x}$ .<sup>53</sup> The details of



the this search strategy are similar to that of G-IMLOP and the reader is directed to Billings et al.<sup>53</sup> for further details. The difference from G-IMLOP is that the oriented matched points,  $\mathbf{y}$ , lie on a shape that is changing at each iteration. Therefore, as for the previous two algorithms, the PD-tree must be updated to accommodate the updated shape before correspondences are found. This update is identical to the update described in Sec. 4.3.

## 6.4 Registration phase

In this section, an implementation for the registration phase of the GD-IMLOP algorithm is presented. The registration phase solves for the transformation,  $\mathbf{T}$ , and the shape parameters,  $\mathbf{s}$ , that best align the correspondences found in the correspondence phase by minimizing the deformable registration cost function for GD-IMLOP (Eq. 6.7), repeated here for ease of reference, with respect to the data transformation parameters and the shape parameters:

$$\begin{aligned} \mathbf{T} = \operatorname{argmin}_{[\mathbf{R}, \mathbf{t}], \mathbf{s}} & \left( \frac{1}{2} \sum_{i=1}^{n_{\text{data}}} (\mathbf{T}_{\text{ssm}}(\mathbf{y}_{\mathbf{p}_i}, \mathbf{s}) - \mathbf{R}\mathbf{x}_{\mathbf{p}_i} - \mathbf{t})^{\mathbf{T}} (\mathbf{R}\boldsymbol{\Sigma}_{\mathbf{x}}\mathbf{R}^{\mathbf{T}})^{-1} (\mathbf{T}_{\text{ssm}}(\mathbf{y}_{\mathbf{p}_i}, \mathbf{s}) - \mathbf{R}\mathbf{x}_{\mathbf{p}_i} - \mathbf{t}) \right. \\ & \left. - \sum_{i=1}^{n_{\text{data}}} \left( \kappa_i \hat{\mathbf{y}}_{\mathbf{n}_i} \mathbf{R} \hat{\mathbf{x}}_{\mathbf{n}_i} + \beta_i \left( (\hat{\gamma}_{1_i}^{\mathbf{T}} \mathbf{R}^{\mathbf{T}} \hat{\mathbf{y}}_{\mathbf{n}_i})^2 - (\hat{\gamma}_{2_i}^{\mathbf{T}} \mathbf{R}^{\mathbf{T}} \hat{\mathbf{y}}_{\mathbf{n}_i})^2 \right) \right) + \frac{1}{2} \sum_{j=1}^{n_{\text{m}}} \|\mathbf{s}_j\|_2^2 \right). \end{aligned}$$

Again, to compute a *similarity* transform between the data points and the corresponding oriented matched points on the current model shape, the cost function changes

## CHAPTER 6. GD-IMLOP ALGORITHM

slightly to incorporate the scale factor,  $a$ :

$$\begin{aligned} \mathbf{T} = \operatorname{argmin}_{[a, \mathbf{R}, \mathbf{t}], \mathbf{s}} & \left( \frac{1}{2} \sum_{i=1}^{n_{\text{data}}} (\mathbf{T}_{\text{ssm}}(\mathbf{y}_{\mathbf{p}_i}, \mathbf{s}) - a\mathbf{R}\mathbf{x}_{\mathbf{p}_i} - \mathbf{t})^{\mathbf{T}} (\mathbf{R}\Sigma_{\mathbf{x}}\mathbf{R}^{\mathbf{T}})^{-1} \right. \\ & \left. (\mathbf{T}_{\text{ssm}}(\mathbf{y}_{\mathbf{p}_i}, \mathbf{s}) - a\mathbf{R}\mathbf{x}_{\mathbf{p}_i} - \mathbf{t}) \right. \\ & \left. - \sum_{i=1}^{n_{\text{data}}} \left( \kappa_i \hat{\mathbf{y}}_{\mathbf{n}_i}^{\mathbf{T}} \mathbf{R} \hat{\mathbf{x}}_{\mathbf{n}_i} + \beta_i \left( (\hat{\gamma}_{1_i}^{\mathbf{T}} \mathbf{R}^{\mathbf{T}} \hat{\mathbf{y}}_{\mathbf{n}_i})^2 - (\hat{\gamma}_{2_i}^{\mathbf{T}} \mathbf{R}^{\mathbf{T}} \hat{\mathbf{y}}_{\mathbf{n}_i})^2 \right) + \frac{1}{2} \sum_{j=1}^{n_{\text{m}}} \|s_j\|_2^2 \right) \right). \end{aligned} \quad (6.14)$$

As in the registration phases of D-IMLP and D-IMLOP, before the deformable registration cost function is minimized, barycentric coordinates of the matched points are computed to find the vertex weights,  $\mu^{(j)}$ , for  $j = 1, 2, 3$ , for each matched point (Eq. 3.9). These  $\mu^{(j)}$  are required during optimization to compute the deformed matched point,  $\mathbf{T}_{\text{ssm}}(\mathbf{y}_{\mathbf{p}_i}, \mathbf{s})$ , as the shape is recomputed for different values of  $\mathbf{s}$ .

As before, there is no closed form solution available to solve this nonlinear cost function. Therefore, the minimization problem requires an iterative optimization approach. Again, a nonlinear quasi-Newton based optimizer is used to minimize either of the two cost functions above (Eq. 6.7 or 6.14). In order to do this, some reparameterization is required to enforce the constraints of the rotation matrix ( $\mathbf{R}^{\mathbf{T}}\mathbf{R} = \mathbf{I}$  and  $\det(\mathbf{R}) = 1$ ). Rodrigues' parameterization, which represents a rotation matrix as a 3-vector,  $\mathbf{r} = [r_x, r_y, r_z]$ ,<sup>51</sup> is used to achieve this. The direction and magnitude of  $\mathbf{r}$  signify the axis and angular extent of rotation, respectively. Further, in order to keep all transformation in the same space, the transformation  $\mathbf{T}(\mathbf{x}_{\mathbf{p}_i})$  is re-expressed

CHAPTER 6. GD-IMLOP ALGORITHM

in the reference frame of  $\mathbf{Y}$  as  $\mathbf{T}(\mathbf{y}_{\mathbf{p}_i})$ . The deformable registration cost function of Eq. 6.7 can then be re-written as

$$\mathbf{T} = \underset{[\mathbf{r}, \mathbf{t}], \mathbf{s}}{\operatorname{argmin}} \left( \sum_{i=1}^{n_{\text{data}}} (C_{\mathbf{p}_i} + C_{\mathbf{n}_i}) + C_{\text{shape}} \right), \quad (6.15)$$

where

$$\begin{aligned} C_{\mathbf{p}_i} &= \mathbf{z}_i^{\mathbf{T}} \boldsymbol{\Sigma}_{\mathbf{x}_i}^{-1} \mathbf{z}_i, \\ \mathbf{z}_i &= \mathbf{R}(\mathbf{r})^{\mathbf{T}} (\mathbf{T}_{\text{ssm}}(\mathbf{y}_{\mathbf{p}_i}, \mathbf{s}) - \mathbf{R}(\mathbf{r}) \mathbf{x}_{\mathbf{p}_i} - \mathbf{t}) \\ &= \mathbf{R}(\mathbf{r})^{\mathbf{T}} (\mathbf{T}_{\text{ssm}}(\mathbf{y}_{\mathbf{p}_i}, \mathbf{s}) - \mathbf{t}) - \mathbf{x}_{\mathbf{p}_i}, \end{aligned} \quad (6.16)$$

$$\begin{aligned} C_{\mathbf{n}_i} &= -\kappa_i \hat{\mathbf{y}}_{\mathbf{n}_i}^{\mathbf{T}} \mathbf{R} \hat{\mathbf{x}}_{\mathbf{n}_i} - \beta_i ((\hat{\gamma}_{1_i}^{\mathbf{T}} \mathbf{R}^{\mathbf{T}} \hat{\mathbf{y}}_{\mathbf{n}_i})^2 - (\hat{\gamma}_{2_i}^{\mathbf{T}} \mathbf{R}^{\mathbf{T}} \hat{\mathbf{y}}_{\mathbf{n}_i})^2), \\ &\text{and } C_{\text{shape}} = \mathbf{s}^{\mathbf{T}} \mathbf{s}. \end{aligned}$$

$\mathbf{R}(\mathbf{r})$  is the  $3 \times 3$  rotation matrix corresponding to the Rodrigues' vector,  $\mathbf{r}$  (defined in Sec. 4.4). Similarly, Eq. 6.14 can be re-written as

$$\mathbf{T} = \underset{[a, \mathbf{r}, \mathbf{t}], \mathbf{s}}{\operatorname{argmin}} \left( \sum_{i=1}^{n_{\text{data}}} (C_{\mathbf{p}_i} + C_{\mathbf{n}_i}) + C_{\text{shape}} \right), \quad (6.17)$$

with a slight modification in the  $C_{\mathbf{p}_i}$  term in Eq. 6.16, so that

$$\begin{aligned} C_{\mathbf{p}_i} &= \mathbf{z}_i^{\mathbf{T}} \boldsymbol{\Sigma}_{\mathbf{x}_i}^{-1} \mathbf{z}_i \\ \mathbf{z}_i &= \mathbf{R}(\mathbf{r})^{\mathbf{T}} (\mathbf{T}_{\text{ssm}}(\mathbf{y}_{\mathbf{p}_i}, \mathbf{s}) - \mathbf{t}) - a \mathbf{x}_{\mathbf{p}_i}, \end{aligned} \quad (6.18)$$

## CHAPTER 6. GD-IMLOP ALGORITHM

and the  $C_{ni}$  and  $C_{\text{shape}}$  terms remain the same as before.

The gradient,  $\nabla C$ , of the deformable registration cost function of Eq. 6.15 with respect to the data transformation parameters  $[\mathbf{r}, \mathbf{t}]$  and the deformable shape parameters,  $\mathbf{s}$ , is explored below. As for D-IMLP and D-IMLOP,  $\nabla C$  is a stacked vector with the data transformation parameters located on top of the deformable shape parameters, and  $\mathbf{J}_{a,b}$  is used to express the Jacobian of an expression,  $a$ , with respect to variable,  $b$ .  $\nabla C$  is expressed as:

$$\nabla C = \sum_{i=1}^{n_{\text{data}}} (\nabla C_{pi} + \nabla C_{ni}) + \nabla C_{\text{shape}} \quad (6.19)$$

$$\nabla C_{pi} = [\mathbf{J}_{C_{pi}, \mathbf{z}_i} \mathbf{J}_{\mathbf{z}_i, \mathbf{r}} , \mathbf{J}_{C_{pi}, \mathbf{z}_i} \mathbf{J}_{\mathbf{z}_i, \mathbf{t}} , \mathbf{J}_{C_{pi}, \mathbf{z}_i} \mathbf{J}_{\mathbf{z}_i, \mathbf{s}}]^\mathbf{T}, \quad \text{where}$$

$$\begin{aligned} \mathbf{J}_{C_{pi}, \mathbf{z}_i} &= 2\mathbf{z}_i^\mathbf{T} \Sigma_{x_i}^{-1} \\ \mathbf{J}_{\mathbf{z}_i, \mathbf{r}} &= \left[ \frac{\partial \mathbf{R}(\mathbf{r})^\mathbf{T}}{\partial \mathbf{r}_x} (\mathbf{T}_{\text{ssm}}(\mathbf{y}_{\mathbf{p}_i}, \mathbf{s}) - \mathbf{t}) , \frac{\partial \mathbf{R}(\mathbf{r})^\mathbf{T}}{\partial \mathbf{r}_y} (\mathbf{T}_{\text{ssm}}(\mathbf{y}_{\mathbf{p}_i}, \mathbf{s}) - \mathbf{t}) , \right. \\ &\quad \left. \frac{\partial \mathbf{R}(\mathbf{r})^\mathbf{T}}{\partial \mathbf{r}_z} (\mathbf{T}_{\text{ssm}}(\mathbf{y}_{\mathbf{p}_i}, \mathbf{s}) - \mathbf{t}) \right] \\ \mathbf{J}_{\mathbf{z}_i, \mathbf{t}} &= -\mathbf{R}(r)^\mathbf{T} \end{aligned} \quad (6.20)$$

$$\mathbf{J}_{\mathbf{z}_i, \mathbf{s}} = \mathbf{J}_{\mathbf{z}_i, \mathbf{T}_{\text{ssm}}(\mathbf{y}_{\mathbf{p}_i}, \mathbf{s})} \mathbf{J}_{\mathbf{T}_{\text{ssm}}(\mathbf{y}_{\mathbf{p}_i}, \mathbf{s}), \mathbf{s}}$$

$$\mathbf{J}_{\mathbf{z}_i, \mathbf{T}_{\text{ssm}}(\mathbf{y}_{\mathbf{p}_i}, \mathbf{s})} = \mathbf{R}(\mathbf{r})^\mathbf{T}$$

$$\mathbf{J}_{\mathbf{T}_{\text{ssm}}(\mathbf{y}_{\mathbf{p}_i}, \mathbf{s}), \mathbf{s}} = \sum_{j=1}^3 \mu_i^{(j)} \mathbf{J}_{\mathbf{T}_{\text{ssm}}(\mathbf{v}_i^{(j)}, \mathbf{s}), \mathbf{s}}$$

CHAPTER 6. GD-IMLOP ALGORITHM

$$\mathbf{J}_{\text{Tssm}(\mathbf{v}_i^{(j)}, \mathbf{s}), \mathbf{s}} = [\mathbf{w}_1^p \quad \mathbf{w}_2^p \quad \cdots \quad \mathbf{w}_{n_m}^p],$$

$$\nabla C_{ni} = [\mathbf{J}_{C_{ni}, \mathbf{r}}, 0, 0]^T \quad (6.21)$$

$$\mathbf{J}_{C_{ni}, \mathbf{r}} = \begin{bmatrix} -\kappa \hat{\mathbf{y}}_{n_i}^T \frac{\partial \mathbf{R}(\mathbf{r})^T}{\partial \mathbf{r}_x} \hat{\mathbf{x}}_{n_i} - 2\beta_i \left( \left( \hat{\gamma}_{1_i}^T \frac{\partial \mathbf{R}(\mathbf{r})^T}{\partial \mathbf{r}_x} \hat{\mathbf{y}}_{n_i} \right) \left( \hat{\gamma}_{1_i}^T \mathbf{R}(\mathbf{r})^T \hat{\mathbf{y}}_{n_i} \right) - \left( \hat{\gamma}_{2_i}^T \frac{\partial \mathbf{R}(\mathbf{r})^T}{\partial \mathbf{r}_x} \hat{\mathbf{y}}_{n_i} \right) \left( \hat{\gamma}_{2_i}^T \mathbf{R}(\mathbf{r})^T \hat{\mathbf{y}}_{n_i} \right) \right), \\ -\kappa \hat{\mathbf{y}}_{n_i}^T \frac{\partial \mathbf{R}(\mathbf{r})^T}{\partial \mathbf{r}_y} \hat{\mathbf{x}}_{n_i} - 2\beta_i \left( \left( \hat{\gamma}_{1_i}^T \frac{\partial \mathbf{R}(\mathbf{r})^T}{\partial \mathbf{r}_y} \hat{\mathbf{y}}_{n_i} \right) \left( \hat{\gamma}_{1_i}^T \mathbf{R}(\mathbf{r})^T \hat{\mathbf{y}}_{n_i} \right) - \left( \hat{\gamma}_{2_i}^T \frac{\partial \mathbf{R}(\mathbf{r})^T}{\partial \mathbf{r}_y} \hat{\mathbf{y}}_{n_i} \right) \left( \hat{\gamma}_{2_i}^T \mathbf{R}(\mathbf{r})^T \hat{\mathbf{y}}_{n_i} \right) \right), \\ -\kappa \hat{\mathbf{y}}_{n_i}^T \frac{\partial \mathbf{R}(\mathbf{r})^T}{\partial \mathbf{r}_z} \hat{\mathbf{x}}_{n_i} - 2\beta_i \left( \left( \hat{\gamma}_{1_i}^T \frac{\partial \mathbf{R}(\mathbf{r})^T}{\partial \mathbf{r}_z} \hat{\mathbf{y}}_{n_i} \right) \left( \hat{\gamma}_{1_i}^T \mathbf{R}(\mathbf{r})^T \hat{\mathbf{y}}_{n_i} \right) - \left( \hat{\gamma}_{2_i}^T \frac{\partial \mathbf{R}(\mathbf{r})^T}{\partial \mathbf{r}_z} \hat{\mathbf{y}}_{n_i} \right) \left( \hat{\gamma}_{2_i}^T \mathbf{R}(\mathbf{r})^T \hat{\mathbf{y}}_{n_i} \right) \right) \end{bmatrix}$$

and

$$\nabla C_{\text{shape}} = [0, 0, 2\mathbf{s}^T]^T \quad (6.22)$$

The partial derivatives and Jacobians used here are identical to those introduced in Eqs. 4.19 and 4.20. The gradient,  $\nabla C$ , of the deformable cost function of Eq. 6.17 with respect to the transformation parameters  $[a, \mathbf{r}, \mathbf{t}]$  and the deformable shape parameters,  $\mathbf{s}$ , is almost the same as  $\nabla C$  defined in Eqs. 6.19, 6.20, 6.21, and 6.22, with an additional component in  $\nabla C_{pi}$  so that

$$\nabla C_{pi} = [\mathbf{J}_{C_{pi}, \mathbf{z}_i} \mathbf{J}_{\mathbf{z}_i, \mathbf{r}}, \mathbf{J}_{C_{pi}, \mathbf{z}_i} \mathbf{J}_{\mathbf{z}_i, \mathbf{t}}, \mathbf{J}_{C_{pi}, \mathbf{z}_i} \mathbf{J}_{\mathbf{z}_i, a}, \mathbf{J}_{C_{pi}, \mathbf{z}_i} \mathbf{J}_{\mathbf{z}_i, \mathbf{s}}]^T, \quad (6.23)$$

where the new term  $\mathbf{J}_{\mathbf{z}_i, a}$  is simply  $\mathbf{J}_{\mathbf{z}_i, a} = -\mathbf{x}_{p_i}$ . The  $\nabla C_{ni}$  and  $\nabla C_{\text{shape}}$  terms simply gain additional zero components so that

$$\nabla C_{ni} = [\mathbf{J}_{C_{ni}, \mathbf{r}}, 0, 0, 0]^T \quad (6.24)$$

and

$$\nabla C_{\text{shape}} = [0, 0, 0, 2\mathbf{s}^T]^T. \quad (6.25)$$

Again, as with  $\nabla C$  in D-IMLP and D-IMLOP, the number of components in  $\nabla C$  above is also dependent on the number of components in the transformation parameters and the number of shape parameters. That is, the size of  $\nabla C$  is  $6 +$  number of shape parameters when the data transformation is a rigid transformation, and  $7 +$  number of shape parameters when the data transformation parameters include an additional scale parameter in the case of a similarity transformation.

## 6.5 Experimental results and discussion

The experimental design for GD-IMLOP is also identical to that of D-IMLP 4.5, and therefore, will not be repeated here. The reader is directed to Sec. 4.5 for details on the motivation and setup for the experiments. Additional details, for instance, the anisotropy of the orientation noise, introduced along with GD-IMLOP will be specified for each experiment below. The anisotropy of the orientation noise is defined using an *eccentricity* factor,  $e$ , which takes values in the interval  $[0, 1)$ . The ellipticity parameter,  $\beta$ , is defined in Eq. 6.8.

## 6.5.1 Sample size experiment

### 6.5.1.1 Experiment 1: Isotropic position noise

The noise model for positional data is as described in Sec. 4.5.1.1, since the data being used here is the same data that was generated for the experiment to evaluate D-IMLP. That is, isotropic noise with SD  $1 \times 1 \times 1 \text{ mm}^3$  was used for position data. The orientation noise used here was slightly different from the orientation noise used in D-IMLOP. Instead of isotropic noise, anisotropic noise with SD of  $2^\circ$  and  $e = 0.5$  was used.

GD-IMLOP outperformed D-IMLP in recovering the shape and registering the sampled points to the recovered shape for different number of sample points due to the added information provided by the normals (Fig. 6.1). GD-IMLOP also produced lower TSEs and TREs than both D-IMLP and D-IMLOP (Fig. 6.2). All registrations using different number of samples produced successful registrations (Table. 6.1). As with D-IMLP and D-IMLOP, the residual error produced by GD-IMLOP showed correlation with the TRE enabling a success or failure or confidence assignment in the registration based on the residual error produced by the algorithm (Fig. 6.4, top). Using empirically chosen thresholds such that there were no false positives, GD-IMLOP was very successfully able to detect correct registrations (Table. 6.1).

CHAPTER 6. GD-IMLOP ALGORITHM

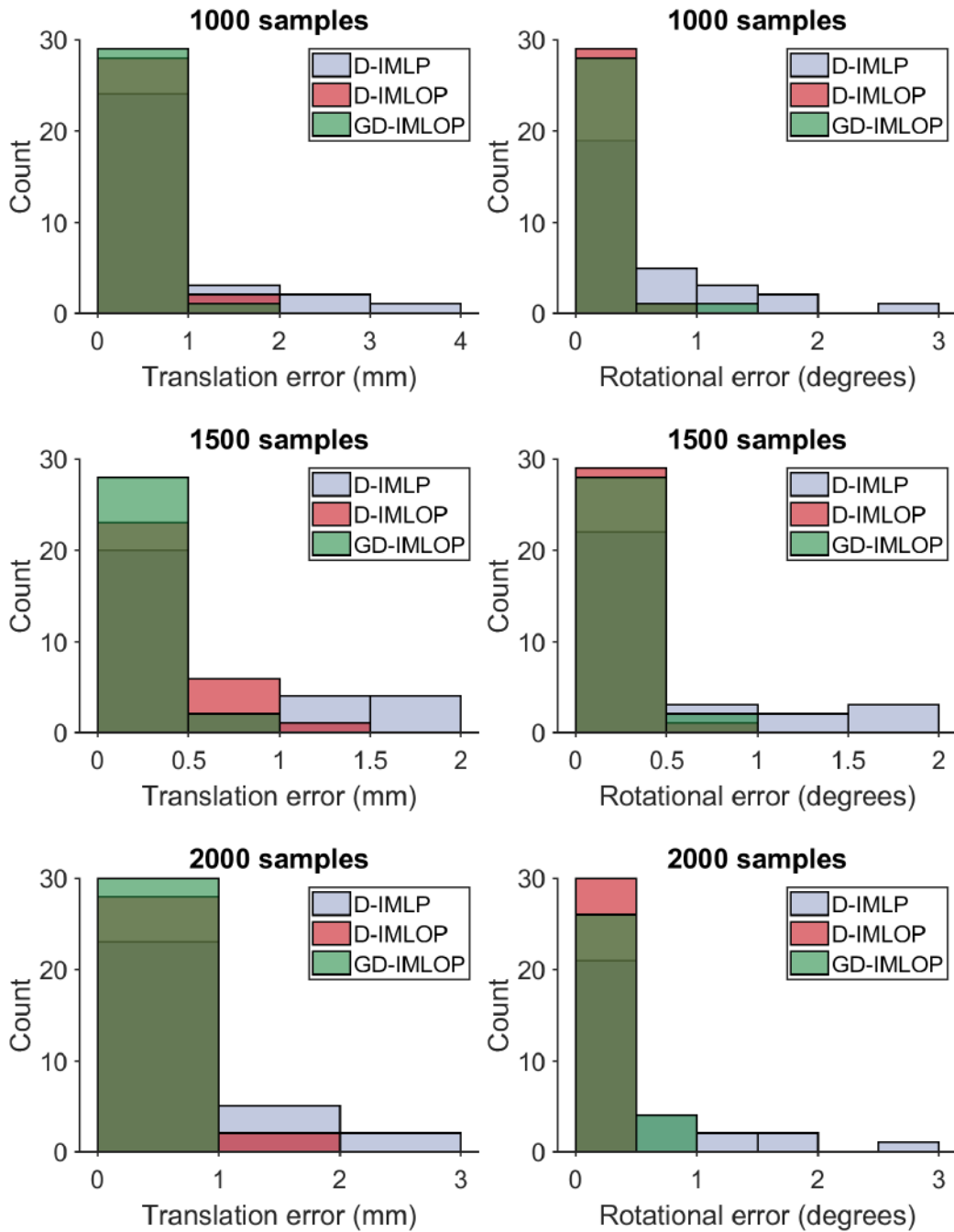


**Figure 6.1:** Sample size experiment: translation (left) and rotation (right) errors produced using, from top to bottom, 1000, 1500 and 2000 data points sampled from the pelvis model in Exp. 1 (Sec. 6.5.1.1)



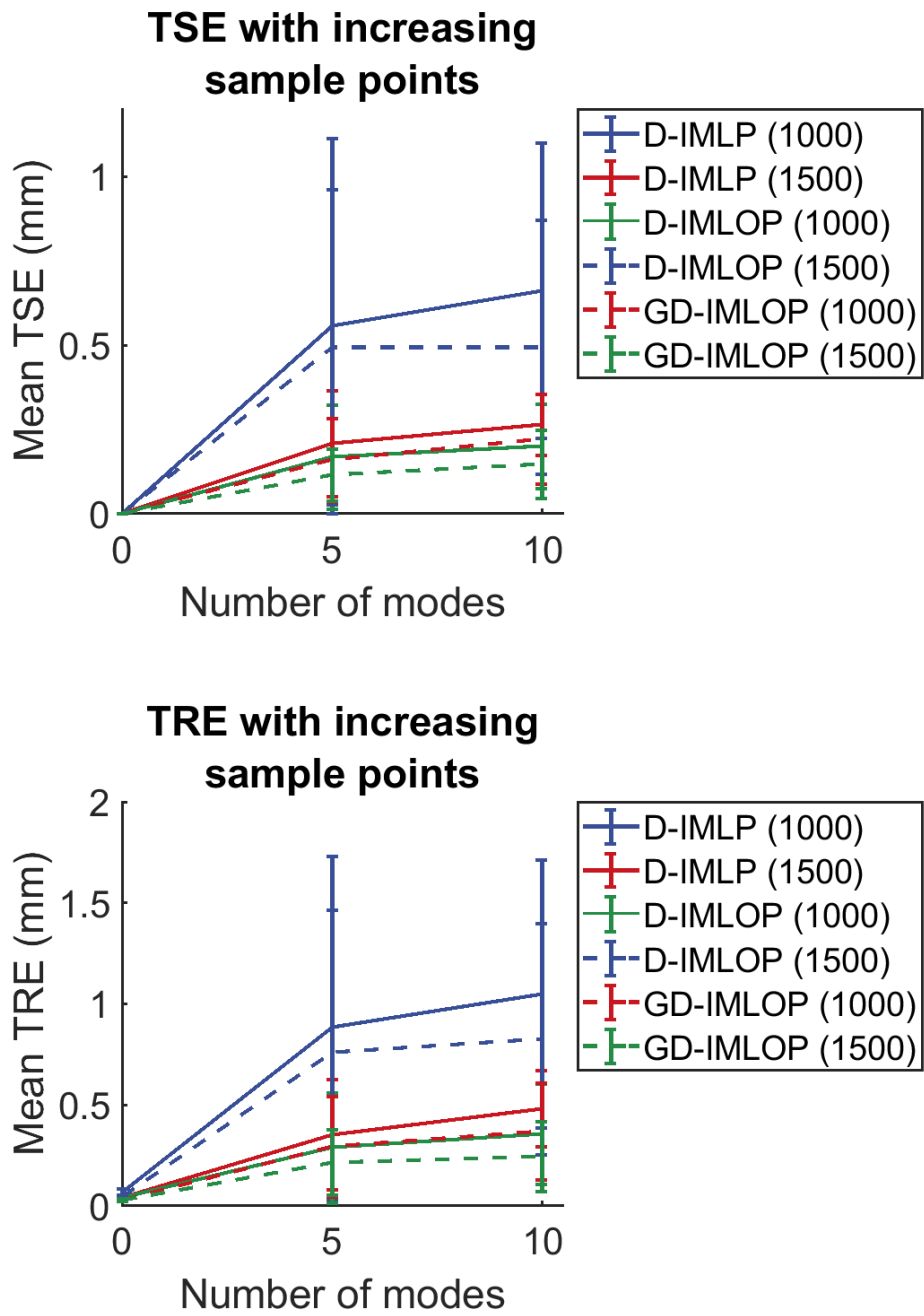


**Figure 6.2:** Sample size experiment: increasing TSE (top) and TRE (bottom) with increasing number of sample points in Exp. 1.

## CHAPTER 6. GD-IMLOP ALGORITHM

**Table 6.1:** Sample size experiment: percent successful registration runs, i.e., runs producing TREs less than 1 mm and, in parentheses, percent successful runs correctly detected as successful using residual errors.

	# samples	D-IMLP (%)	D-IMLOP (%)	GD-IMLOP (%)
Experiment 1	1000	73.33 (100.00)	100.00 (66.67)	100.00 (96.67)
	1500	76.67 (86.96)	100.00 (63.33)	100.00 (96.67)
	2000	80.00 (100.00)	100.00 (66.67)	100.00 (100.00)
Experiment 2	1000	56.67 (100.00)	86.67 (100.00)	96.67 (100.00)
	1500	46.67 (100.00)	96.67 (100.00)	100.00 (93.33)
	2000	56.67 (100.00)	83.33 (88.00)	96.67 (93.10)

### 6.5.1.2 Experiment 2: Anisotropic position noise

An anisotropic noise model with SD  $1 \times 1 \times 2 \text{ mm}^3$  was used for positional noise, whereas for orientation noise, the parameters were the same as in Exp. 6.5.1.1. Errors for anisotropic positional noise were only marginally higher than those with isotropic noise (Fig. 6.3). Again, the residual errors produced by GD-IMLOP were correlated with the TRE allowing the algorithm to accept or reject or assign confidence to the registration produced (Fig. 6.4, bottom). Using empirically found thresholds, GD-IMLOP is again very successfully able to use the residual errors produced to correctly classify successful registrations (Table. 6.1).

CHAPTER 6. GD-IMLOP ALGORITHM

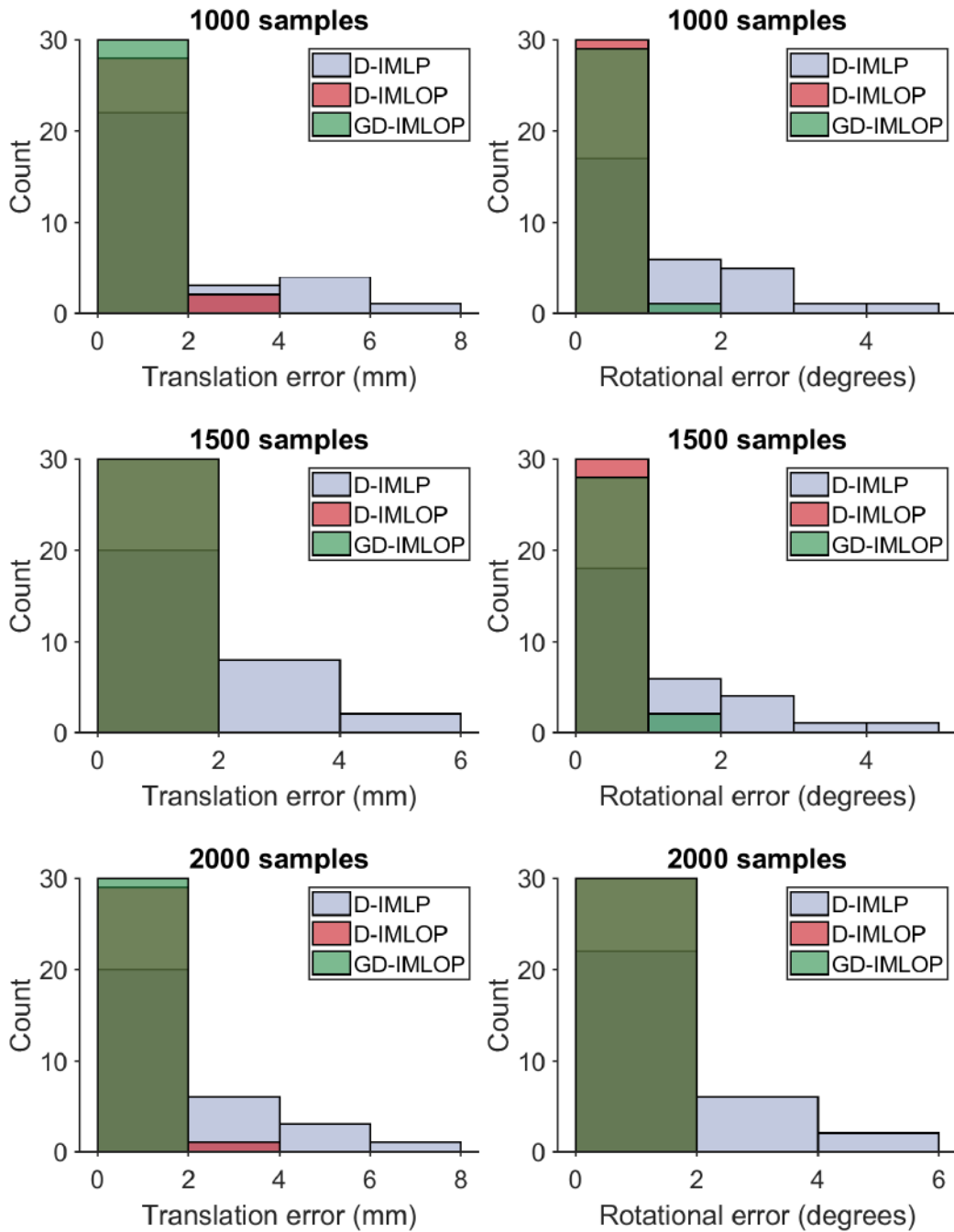


**Figure 6.3:** Sample size experiment: translation (left) and rotation (right) errors produced using, from top to bottom, 1000, 1500 and 2000 data points sampled from the pelvis model in Exp. 2 (Sec. 6.5.1.2)

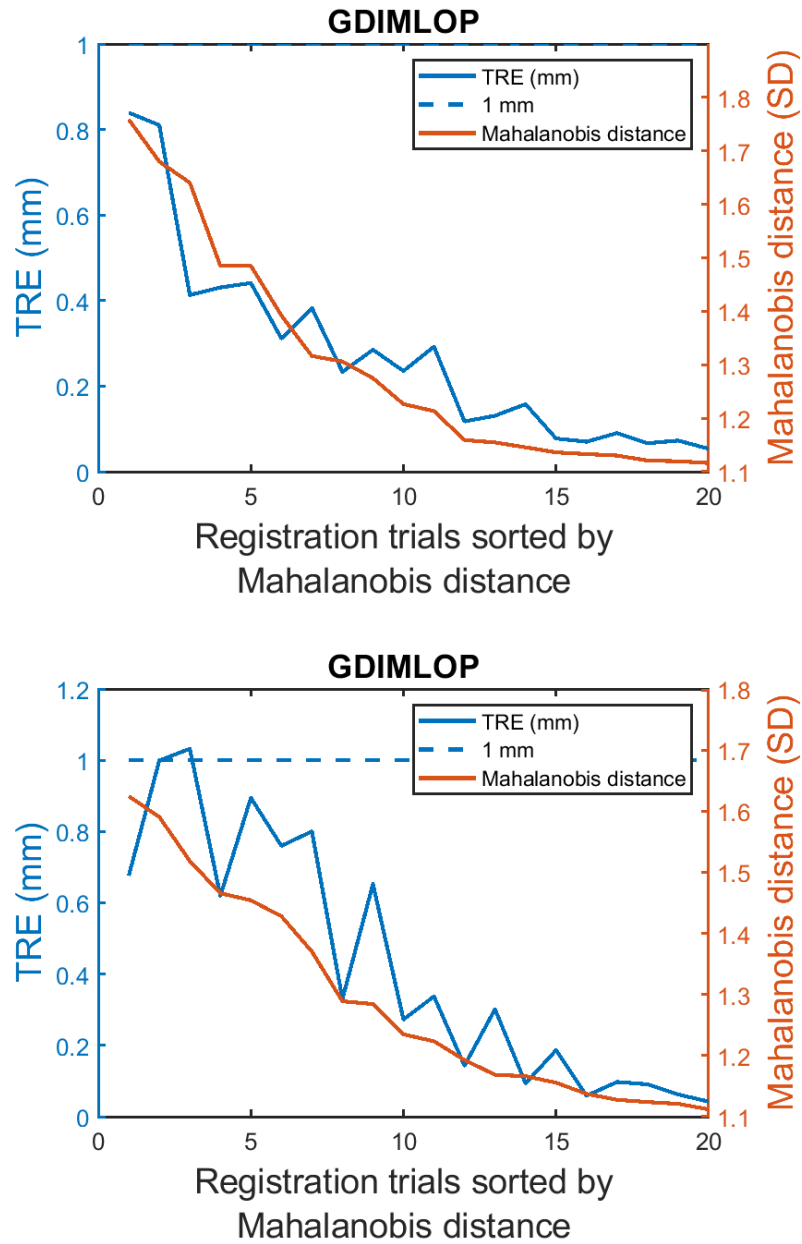


**Figure 6.4:** Residual errors compared against TRE using 2000 sample points in Exp. 1 (left) and Exp. 2 (right) of the sample size experiment. The two measures exhibit correlation in both experiments 1 and 2 with correlation coefficients of 0.94 and 0.91, respectively.

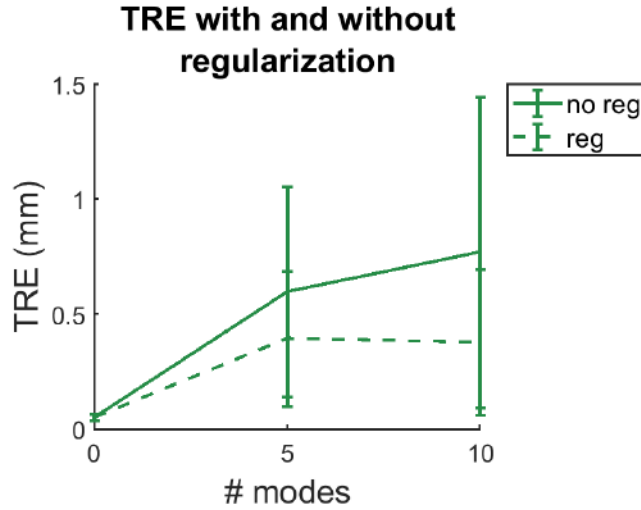


**Figure 6.5:** Regularization term experiment: registrations produced by GD-IMLOP without the regularization term showed larger errors than with the term.

## 6.5.2 Regularization term experiment

As with the previous two algorithms, the cost function that is minimized to compute a registration using GD-IMLOP (Eq. 6.7) contains an L2 regularization term,  $\frac{1}{2} \sum_{j=1}^{n_m} \|s_j\|_2^2$ . The effect of this regularization term is again evaluated by computing registrations without this term on the data generated for Exp. 6.5.1.1 using 1500 sample points. Results showed that removing the regularization showed deteriorating effects on results produced by GD-IMLOP right away (Fig. 6.5). Since, GD-IMLOP solves a harder optimization problem, removing the regularization term makes it more susceptible to noise in the data.

### 6.5.3 Noise model experiment

#### 6.5.3.1 Experiment 1: Varying isotropic position noise

As in D-IMLP, 5 isotropic noise models with SDs of  $1 \times 1 \times 1 \text{ mm}^3$ ,  $2 \times 2 \times 2 \text{ mm}^3$ ,  $3 \times 3 \times 3 \text{ mm}^3$ ,  $4 \times 4 \times 4 \text{ mm}^3$ , and  $5 \times 5 \times 5 \text{ mm}^3$  for position noise were used. An anisotropic noise model with SD of  $2^\circ$  and  $e = 0.5$  was used for orientation noise. GD-IMLOP showed a slight increase TRE as the SD of noise increased. However, TREs for all noise models remained below 1 mm, which was not achieved by D-IMLP or D-IMLOP (Fig. 6.6). The residual errors were found to be strongly correlated with the TRE, which again can be used to distinguish between successful and unsuccessful registrations (Fig. 6.7).

#### 6.5.3.2 Experiment 2: Varying anisotropic position noise

Anisotropic noise models with SDs of  $1 \times 1 \times 2 \text{ mm}^3$ ,  $2 \times 2 \times 3 \text{ mm}^3$ ,  $3 \times 3 \times 4 \text{ mm}^3$ ,  $3 \times 3 \times 5 \text{ mm}^3$ , and  $4 \times 4 \times 5 \text{ mm}^3$  for positional noise were used. For orientation noise, the parameters were the same as in Exp. 1. Results from this experiment show the same trends as those for isotropic noise. Increasing noise SD only introduced small increase in error, with all errors remaining below 1 mm (Fig. 6.8). Residual errors again showed strong correlation with the TRE (Fig. 6.9) allowing the algorithm to detect successful registrations.

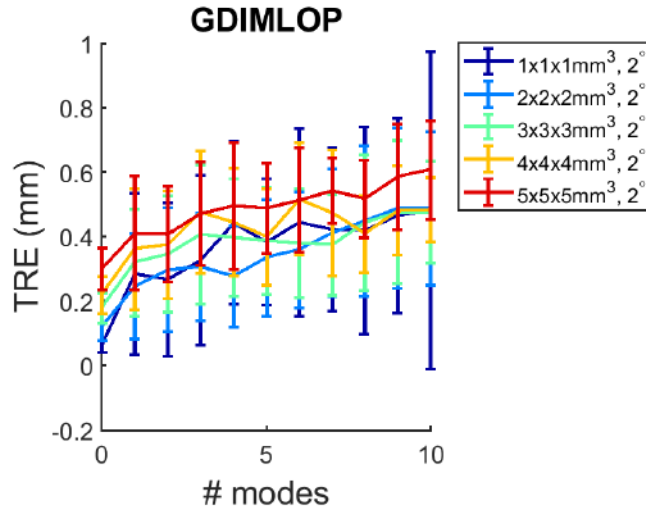


**Figure 6.6:** Noise model experiment: a slight increase in TRE as the uncertainty in the sample points increases. Note that errors are increasing with increasing modes because for this experiment the number of modes used to estimate the shapes equals the number of modes used to simulate a new shape from which points were sampled.

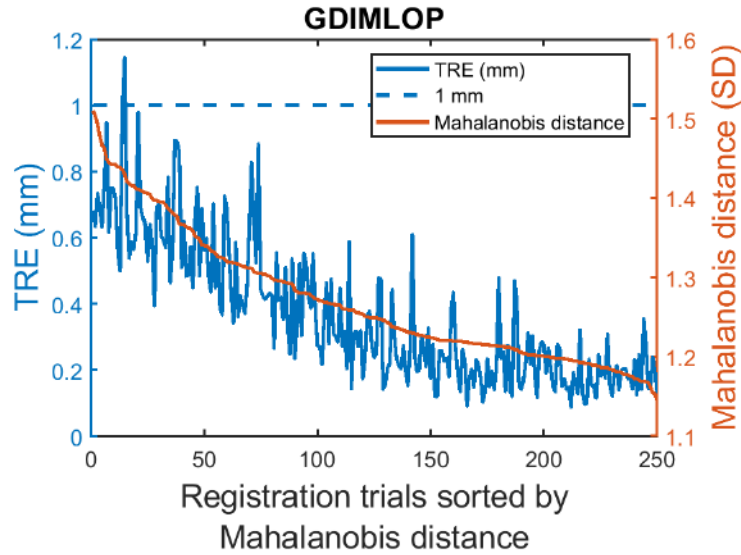


**Figure 6.7:** Sample size experiment: residual errors compared against TRE using 500 sample points with  $2 \times 2 \times 2 \text{ mm}^3$  SD positional noise and  $2^\circ$  SD ( $e = 0.5$ ) angular noise in Exp. 1 of the noise model experiment (Sec. 6.5.3.1). The two measures exhibit correlation with correlation coefficient of 0.83.

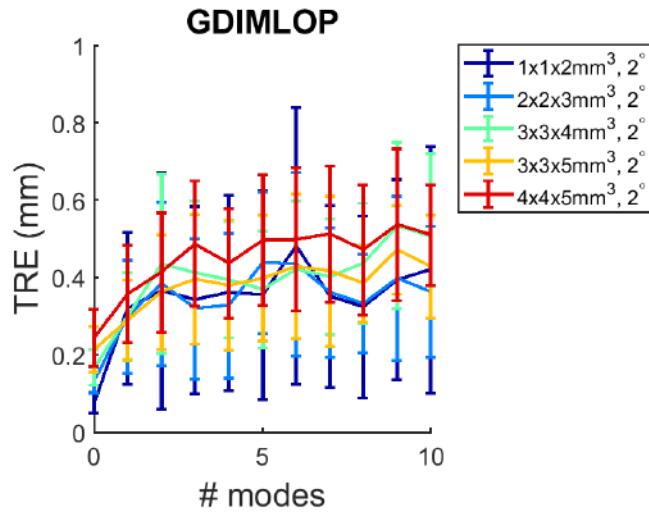


**Figure 6.8:** Noise model experiment: a slight increase in TRE as the uncertainty in the sample points increases. Note that errors are increasing with increasing modes because for this experiment the number of modes used to estimate the shapes equals the number of modes used to simulate a new shape from which points were sampled.

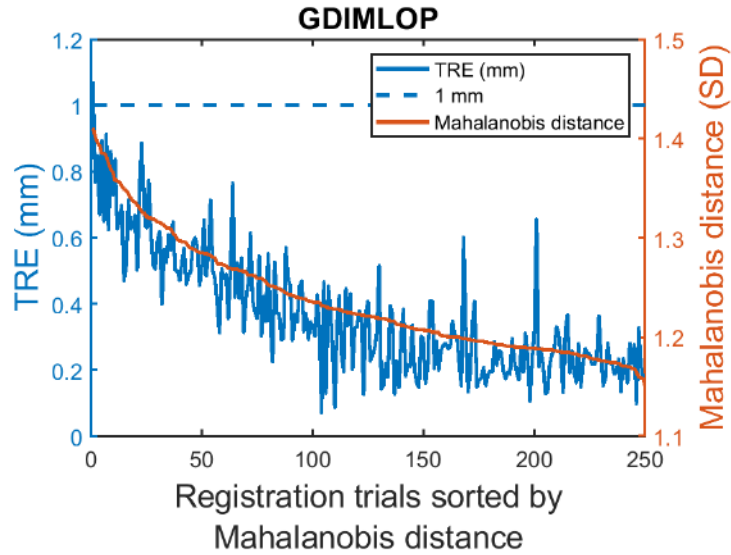


**Figure 6.9:** Noise model experiment: residual errors compared against TRE using 500 sample points with  $2 \times 2 \times 3 \text{ mm}^3$  SD positional noise and  $2^\circ$  SD ( $e = 0.5$ ) angular noise in Exp. 2 of the noise model experiment (Sec. 6.5.3.2). The two measures exhibit correlation with correlation coefficient of 0.85.



### 6.5.3.3 Experiment 3: Varying orientation noise

In the third experiment, one isotropic noise model and one anisotropic noise model with SDs of  $1 \times 1 \times 1 \text{ mm}^3$  and  $1 \times 1 \times 2 \text{ mm}^3$ , respectively, for positional noise were used, and orientation noise models with SDs of  $2^\circ$ ,  $4^\circ$ ,  $6^\circ$ ,  $8^\circ$  and  $10^\circ$  and  $e = 0.5$  for each positional noise model were used. Like D-IMLOP, results show that changing angular noise does not affect registration results using GD-IMLOP significantly since the large number of samples overwhelms the small change in the noise model (Fig. 6.10). GD-IMLOP and D-IMLOP, Fig. 5.10 in the previous chapter, produce comparable errors. The errors produced by GD-IMLOP were, again, found to be correlated with the TREs (Fig. 6.11).

### 6.5.3.4 Experiment 4: Noise parameter sweep

In the final experiment, the sample points were generated with a particular noise model for both position and orientation data. However, it was assumed that this noise model is unknown to GD-IMLOP. Sample points were generated with anisotropic position and orientation noise with SD  $2 \times 2 \times 4 \text{ mm}^3$  and  $10^\circ$  ( $e = 0.5$ ), respectively. A hyper-parameter sweep was then performed and the GD-IMLOP algorithm was deployed with different isotropic and anisotropic position and orientation noise assumptions to evaluate how well GD-IMLOP performs with inaccurate noise model assumptions.

Since the noise in the generated sampled points, anisotropic in both position and

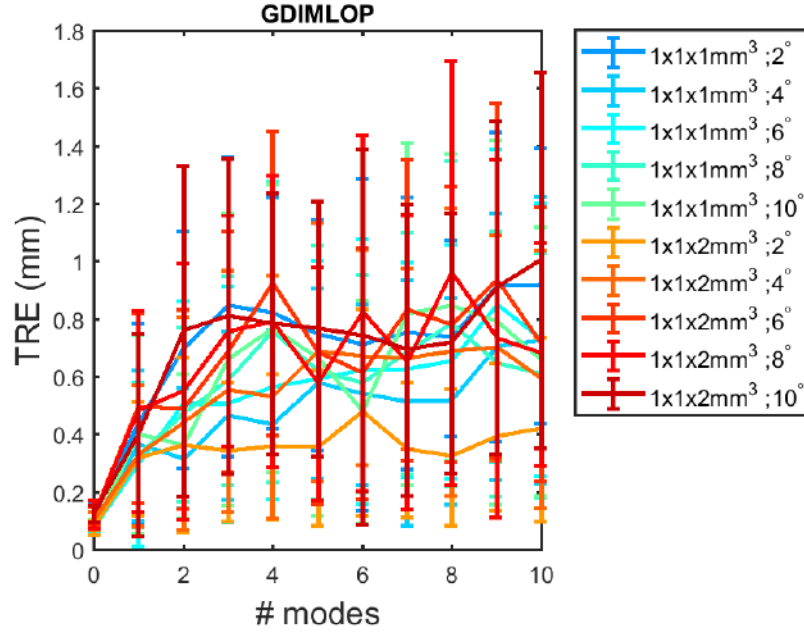


**Figure 6.10:** Noise model experiment: mean TRE produced by GD-IMLOP in Exp. 3. Note that the errors are increasing with increasing modes only because for this experiment the number of modes used to estimate the shapes equals the number of modes used to simulate a new shape from which points were sampled.

orientation ( $2 \times 2 \times 4 \text{ mm}^3$  and  $10^\circ$  ( $e = 0.5$ ), respectively), can be best explained by GD-IMLOP, it is expected to outperform the other two algorithms. As observed in Fig. 6.12, GD-IMLOP does show larger TREs for less conservative noise estimates, with TREs improving or stabilizing with noise models equal to or larger than that of the sampled points. This trend is most clear in the graph with the most conservative orientation noise model with SD of  $20^\circ$  ( $e = 0.5$ ) (Fig. 6.12, bottom). Interestingly,

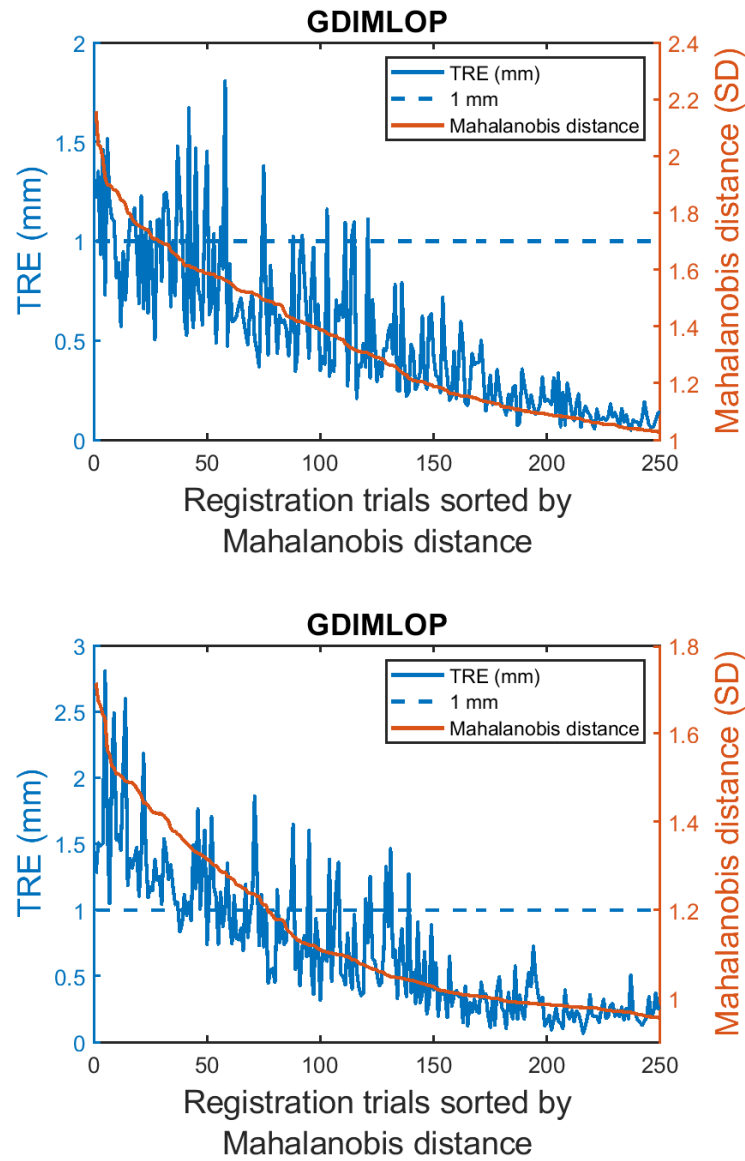


**Figure 6.11:** Noise model experiment: residual errors compared against TRE using 500 sample points with  $1 \times 1 \times 1 \text{ mm}^3$  SD positional noise,  $4^\circ$  SD ( $e = 0.5$ ) angular noise (top), and  $1 \times 1 \times 2 \text{ mm}^3$  SD positional noise,  $8^\circ$  SD ( $e = 0.5$ ) angular noise (bottom) in Exp. 3 of the noise model experiment. The two measures exhibit correlation for both isotropic and anisotropic position noise with correlation coefficient of 0.81 and 0.83, respectively.

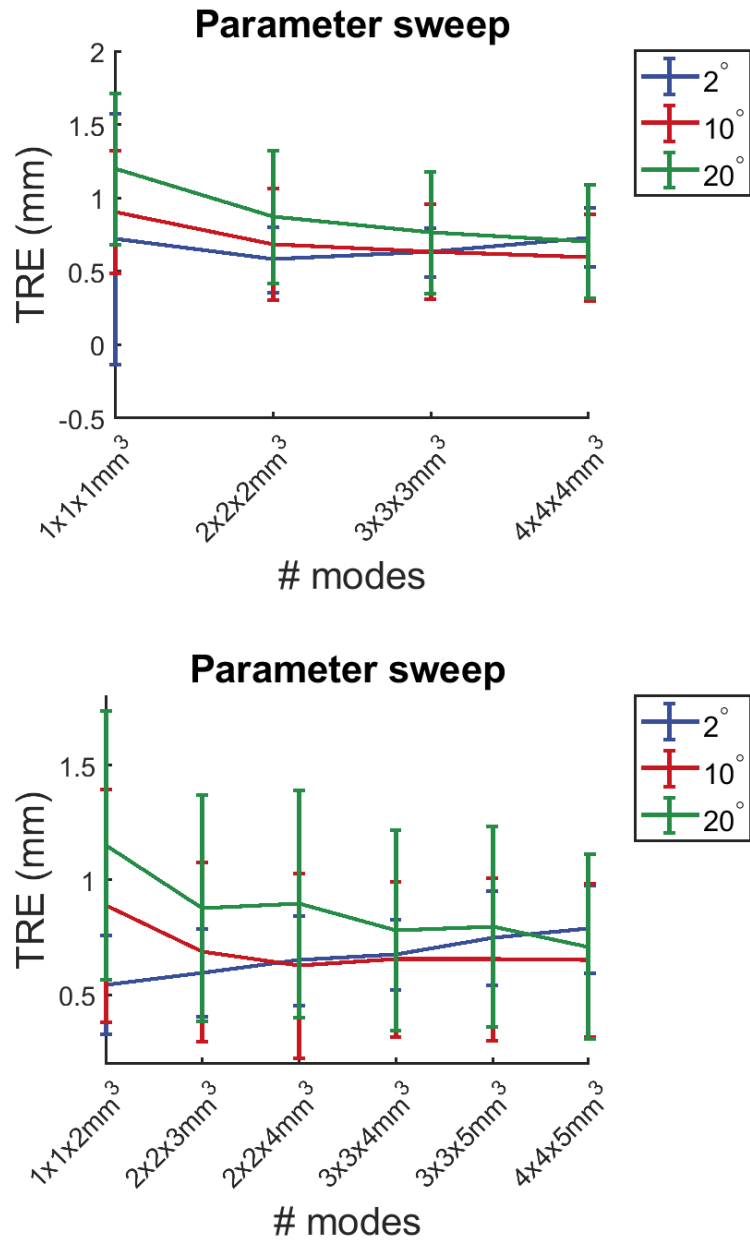


**Figure 6.12:** Noise model experiment: parameter sweep results show that GD-IMLOP produces lower errors as the noise assumptions become more pessimistic

D-IMLOP outperforms GD-IMLOP for less conservative noise estimates. This is also expected since D-IMLOP optimizes a simpler cost function. Therefore, when the noise assumption is optimistic, D-IMLOP converges faster than GD-IMLOP. However, as the noise assumption becomes more pessimistic, GD-IMLOP's performance improves while D-IMLOP's deteriorates since GD-IMLOP models the noise in the sample points more accurately. Therefore, TREs for GD-IMLOP show the stabilization with increasingly conservative noise estimates, but not for D-IMLOP.

### 6.5.4 Outlier experiment

Sample points for this experiment were generated with isotropic noise in position data with SD  $1 \times 1 \times 1 \text{ mm}^3$  and anisotropic noise in orientation data with  $2^\circ$  SD and  $e = 0.5$ . As in the experiment setup for D-IMLOP, outliers were generated by perturbing the position and orientation components of different amount of samples in the range  $[2, 5] \text{ mm}$  and  $[2, 5]^\circ$ , respectively. Three experiments were designed with different numbers of samples, 0%, 10%, and 20%, that were perturbed. Outliers were identified and rejected using the chi-square test, as described earlier in Sec. 5.2 and in Billings et al.<sup>51,53</sup> For position data, a match is rejected if the square Mahalanobis distance is greater than the value of the chi-square inverse CDF with 3 DOF at  $p = 0.95$ . Since the square Mahalanobis distance normalizes each match residual error by its variance along each dimension, the sum of the square Mahalanobis distance over all data points,  $n_{\text{data}}$ , is distributed as a chi-square distribution with  $3n_{\text{data}}$

DOF.<sup>107</sup> Similarly, for orientation data, a chi-square test with  $2n_{\text{data}}$  DOF is applied by converting the Kent noise model for the orientation match residual into Gaussian form,<sup>114</sup> just as was done with the Fisher distribution, since the Kent distribution is simply the Fisher distribution with non-zero ellipticity.

GD-IMLOP perform extremely well in the presence of outliers, outperforming both D-IMLP and D-IMLOP. The degradation in performance with increasing outliers is negligible, since GD-IMLOP is able to detect outliers effectively and reject them, as explained in Sec. 6.2, limiting their effect on errors. As in Fig. 6.13, the errors from 10% and 20% outliers in the sampled points are comparable. Fig. 6.13 shows a very strong result in that although with 10 modes, GD-IMLOP must optimize over 10 extra parameters, the degradation in the TRE between 0 modes and 10 modes is negligible ( $\sim 0.05$  mm) when there are no outliers outliers in the sampled points. The degradation in the presence of outliers is only marginally larger. Results produced by GD-IMLOP in this experiment did not show correlation with the residual errors because all TREs were extremely small and stable with increasing modes and, therefore, did not exhibit any trends.

### 6.5.5 Scale experiment

The dataset generated in Sec. 6.5.4 with 0% outliers was reused for this experiment. The sample points were scaled by some known amount in the range  $[0.7, 1.3]$ , as mentioned in Sec. 4.5.5. GD-IMLOP is successfully able to estimate scale in ad-

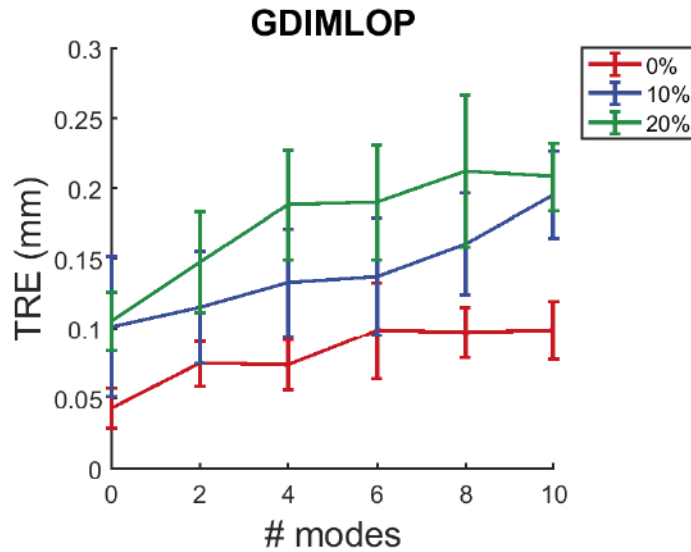


**Figure 6.13:** Outlier experiment: mean TRE with different number of outliers using GD-IMLOP. Note that errors are increasing with increasing modes because for this experiment the number of modes used to estimate the shapes equals the number of modes used to simulate the deformed shape from which points were sampled.

dition to rotation, translation, and shape parameters. The difference between errors produced when one fewer parameter is being estimated and those produced including scale estimation are almost identical and far below 1 mm (Fig. 6.14). GD-IMLOP’s performance also reflects errors in recovering scale, with mean errors  $\sim 0.01$  and  $SD < 0.01$  (Fig. 6.15). This is reasonable given that noise assumptions made by GD-IMLOP best fit the noise in the sampled points. As with D-IMLP and D-IMLOP, GD-IMLOP remains roughly stable as the number of shape parameters to optimize over increases.

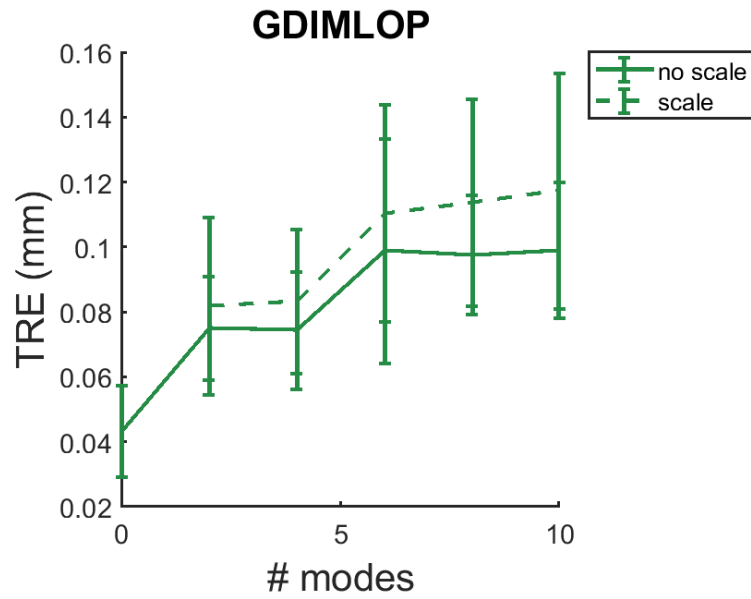


**Figure 6.14:** Scale experiment: additional scale optimization increases TRE as compared to when scale optimization is not required.

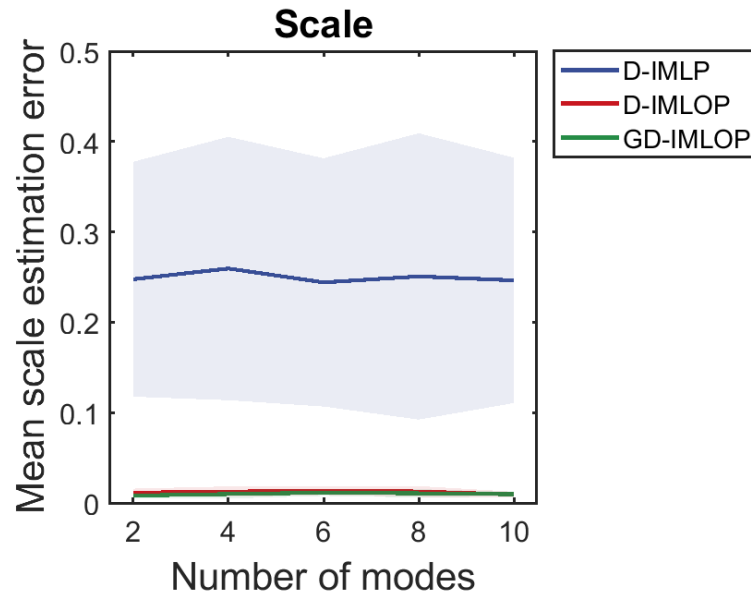


**Figure 6.15:** Scale experiment: errors in scale estimation using GD-IMLOP are similar to those using D-IMLOP and remain stable with increasing number of modes. These errors are lower than those produced using D-IMLP.



### 6.5.6 Leave-one-out experiment

For this experiment, an isotropic positional noise model with a SD of  $1 \times 1 \times 1 \text{ mm}^3$  and an anisotropic orientation noise model with  $20^\circ$  SD ( $e = 0.5$ ) was used to generate data samples. GD-IMLOP assumed the same noise as was used to generate the data.

#### 6.5.6.1 Experiment 1: Middle turbinates

The middle turbinate models from the sinus dataset were used to generate sample points for this experiment. GD-IMLOP recovered the left out shape and the transformation offset applied successfully (with mean TRE less than 1 mm) in 97.37% of the 1749 registrations performed. As the number of shape parameters increased, the performance of GD-IMLOP either stabilized or continued to improve gradually as convergence rate slowed down (Fig. 6.16). Although, the errors produced by deformable CPD are comparable to GD-IMLOP using more than 20 modes, CPD was slower than GD-IMLOP at its slowest. GD-IMLOP required 28.89s average time to converge using 50 modes, while CPD required 40.55s (Fig. 6.17). Finally, unlike CPD (Fig. 6.18), errors produced by GD-IMLOP show correlation with the TRE, allowing it to accept or reject the registrations produced (Fig. 6.21).

#### 6.5.6.2 Experiment 2: Right nasal airway

The right nasal airway models, also from the sinus dataset, were used to generate sample points for this experiment. When assuming the same anisotropic noise in

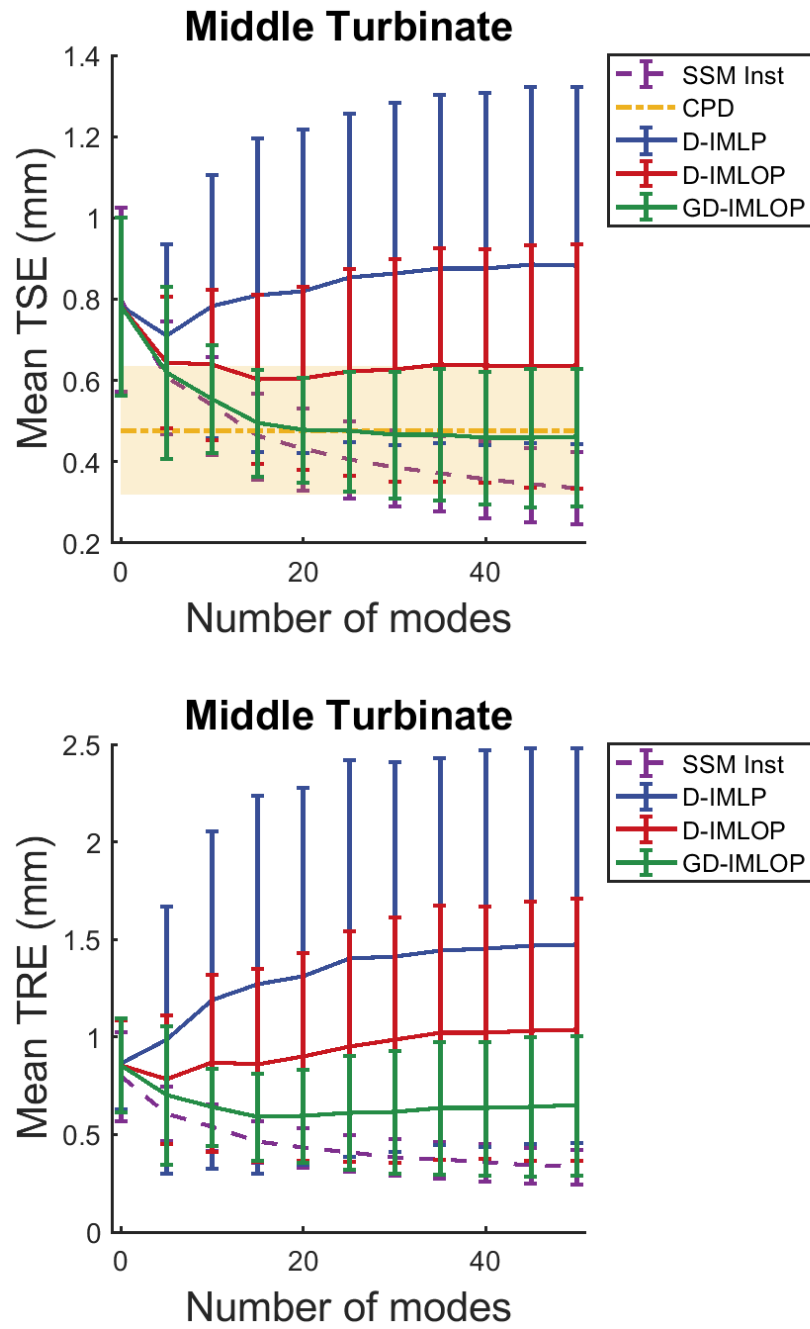


**Figure 6.16:** Leave-one-out experiment: TSE (top) and TRE (bottom) produced by GD-IMLOP compared against that produced by CPD and SSM using the middle turbinate meshes in the leave-one-out experiment.

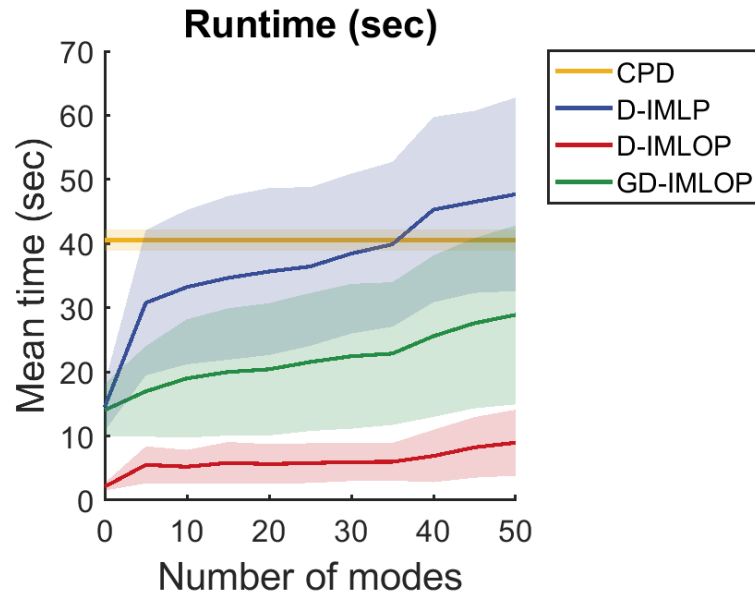


**Figure 6.17:** Leave-one-out experiment: runtime comparison between CPD, D-IMLP, D-IMLOP and GD-IMLOP.

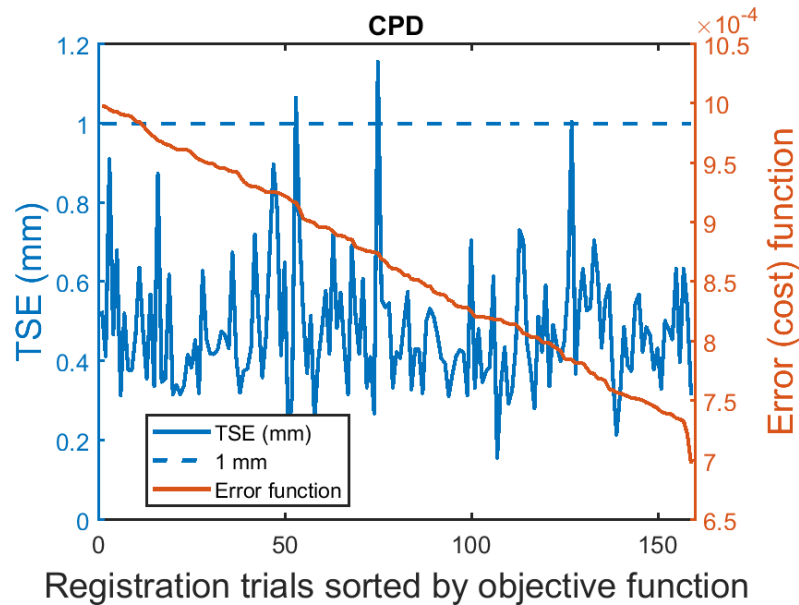


**Figure 6.18:** Leave-one-out experiment: errors produced by CPD compared against TSE using the middle turbinate meshes in the leave-one-out experiment. The two measures do not exhibit correlation and, therefore, errors produced by CPD cannot be used to assign success or failure to the registration.

both position and orientation components as was used to generate the data samples, the left-out right nasal cavity meshes recovered using GD-IMLOP were comparable to the estimates produced by the SSM. GD-IMLOP produced mean TSEs almost equal to those produced by the SSM up to about 30 modes (Fig. 6.19). This is an extremely strong result since the errors produced by the SSM serve as the upper limit for how well the left-out shapes can be estimated. GD-IMLOP performs almost as well as is possible. Of the 1749 runs, 99.60% of the GD-IMLOP runs recovered the left out mesh with mean TRE less than 1 mm. Further, errors produced by GD-IMLOP were also in correlation with the TRE (Fig. 6.22). If the noise assumption made by GD-IMLOP is modified so that the orientation noise assumed is isotropic, then GD-IMLOP is essentially identical to D-IMLOP. The performance of GD-IMLOP with  $e = 0$  reflects this with results identical to those produced by D-IMLOP (Fig. 6.20).

### 6.5.6.3 Experiment 3: Right nasal airway with outliers

As in Sections 4.5.6.3 and 5.5.6.3, GD-IMLOP is evaluated on more realistic data containing outliers. This experiment is set up similarly as the previous experiment (Sec. 6.5.6.2), but with 10% and 20% of the sample points perturbed to simulate outliers. The perturbation is similar to that in Sec. 6.5.4, and outliers are detected and rejected using the techniques described in Sec. 6.2. Results show that adding outliers caused some degradation in errors, but registrations performed comparably with 10% and 20% outliers in the sample points. Despite up to 20% outliers in the

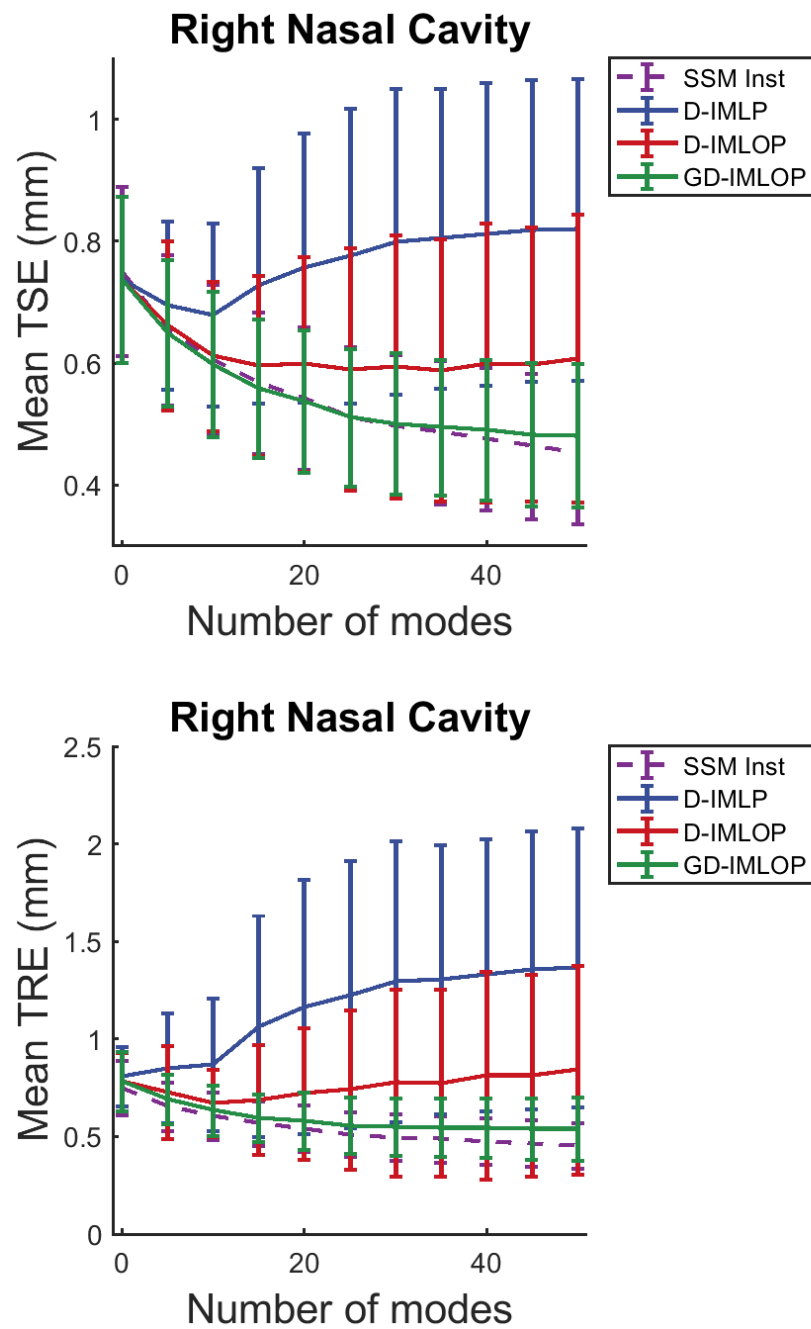


**Figure 6.19:** Leave-one-out experiment: TSE (top) and TRE (bottom) produced by GD-IMLOP compared against that produced by the SSM estimate using the right nasal cavity meshes.

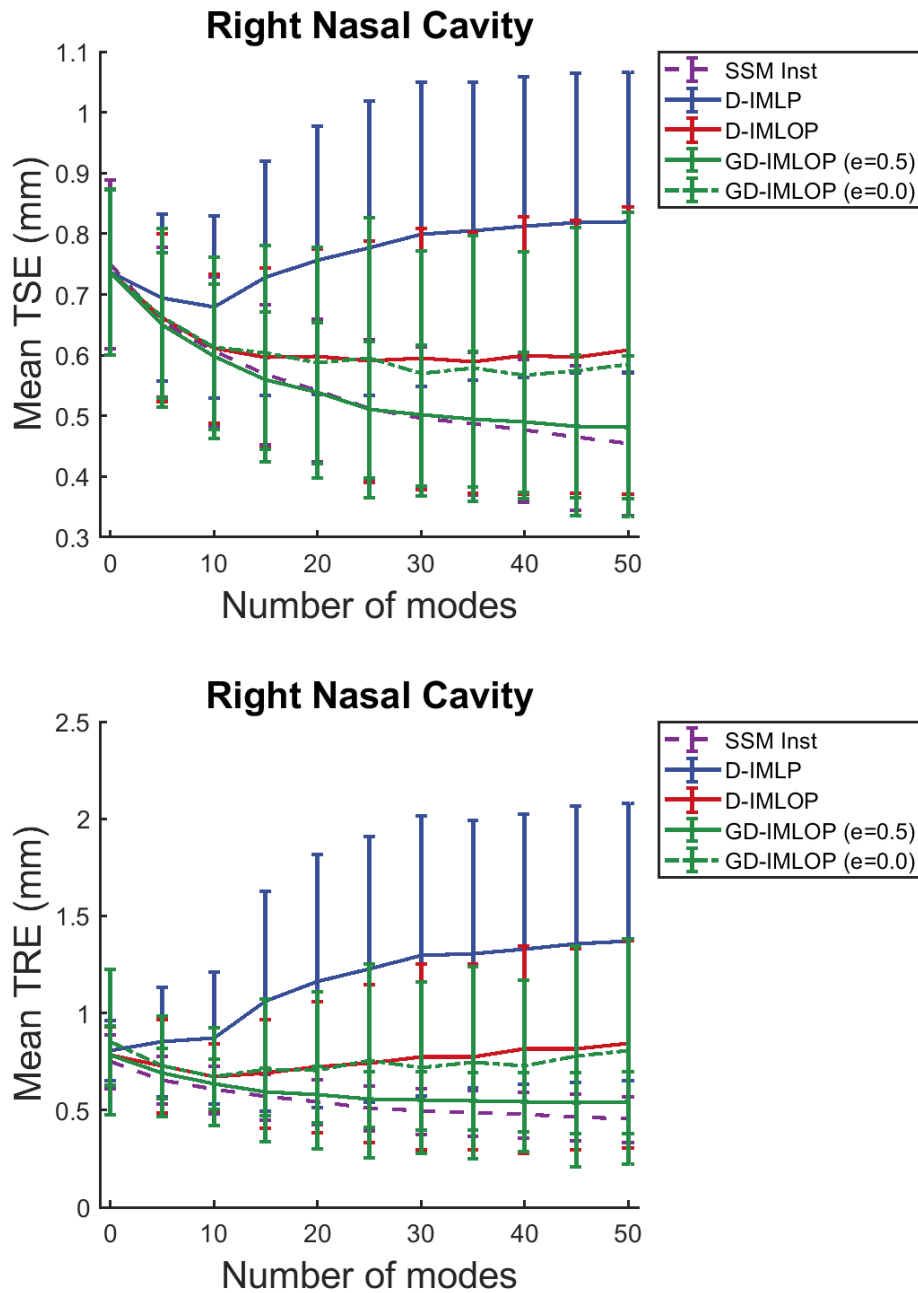


**Figure 6.20:** Leave-one-out experiment: TSE (top) and TRE (bottom) produced by GD-IMLOP with  $e = 0$  (dotted green curve) compared against that produced by D-IMLOP using the right nasal cavity meshes.

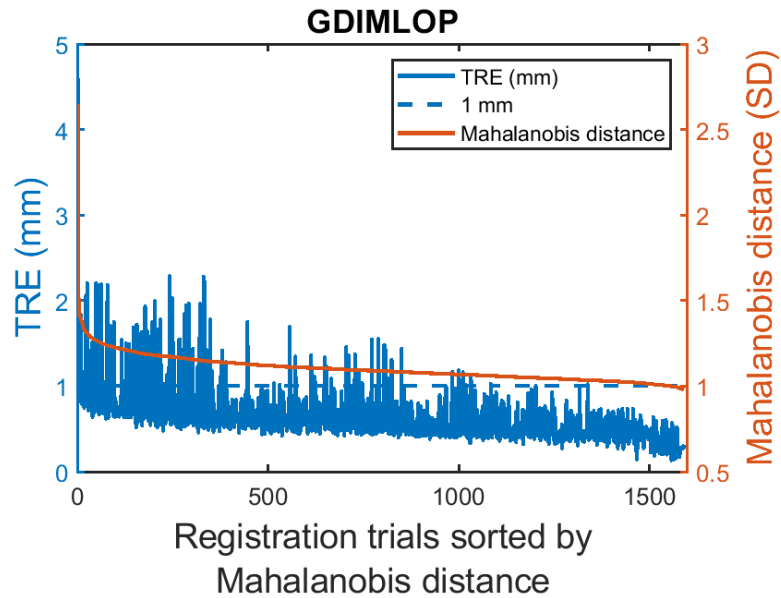


**Figure 6.21:** Leave-one-out experiment: residual errors compared against TRE using the middle turbinate meshes in the leave-one-out experiment. The two measures exhibit correlation with correlation coefficients of 0.61.

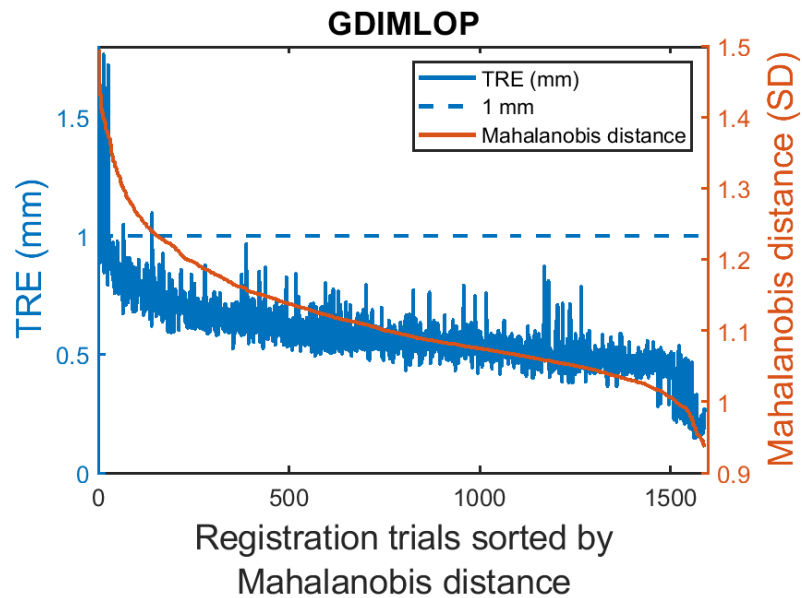


**Figure 6.22:** Leave-one-out experiment: residual errors compared against TRE using the right nasal cavity meshes in the leave-one-out experiment. The two measures exhibit correlation with correlation coefficients of 0.85.

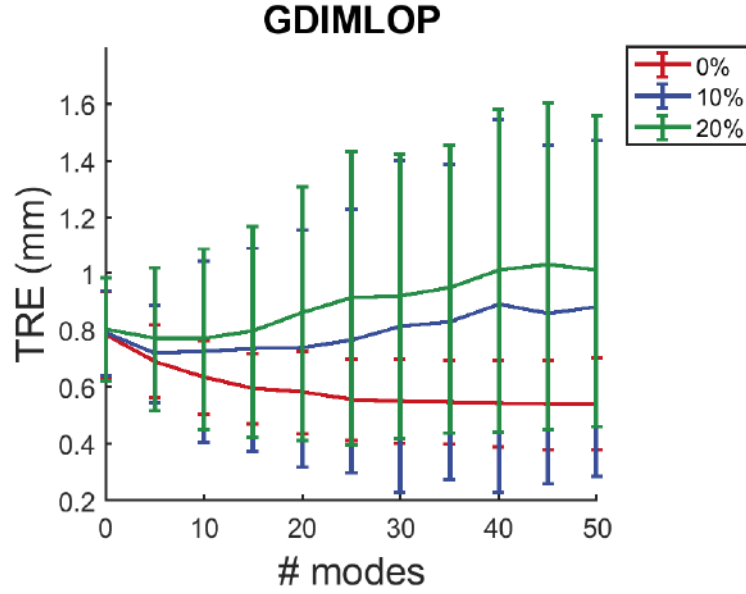


**Figure 6.23:** Leave-one-out experiment: TRE produced by D-IMLOP with 0%, 10% and 20% outliers in the data points sampled from the right nasal cavity meshes in the leave-one-out experiment.

data, mean TREs for almost all modes remained below 1 mm (Fig. 6.23).

## 6.5.7 Partial data experiment

### 6.5.7.1 Experiment 1: Pelvis

Anisotropic noise with SD  $1 \times 1 \times 2 \text{ mm}^3$  and  $10^\circ$  ( $e = 0.5$ ) was used to generate sampled position and orientation data, respectively, from a partial CT scan of the pelvis. An instance of the full pelvis is then estimated by GD-IMLOP using these



## CHAPTER 6. GD-IMLOP ALGORITHM

sampled points and a generous noise assumption with SD  $2 \times 2 \times 3 \text{ mm}^3$  and  $30^\circ$  ( $e = 0.5$ ) for position data and orientation data, respectively. The performance of GD-IMLOP almost exactly matches that of D-IMLOP with a large improvement in both transformation parameters and TSE from 0 to 10 modes followed by stabilization or gradual improvement as convergence rate decreased with increasing number of shape parameters. The trend followed by the TSE is similar to that followed by the error between the left out shape and the SSM instance of the left out shape (Fig. 6.24), with the mean TRE falling below 2mm with only 10 modes (Fig. 6.24), which is the desired accuracy for pelvis registrations. The improvement in these errors is also reflected in the residual errors produced by GD-IMLOP (Fig. 6.26).

### 6.5.7.2 Experiment 2: Right nasal airway

Anisotropic noise with SD  $0.5 \times 0.5 \times 1 \text{ mm}^3$  and  $10^\circ$  ( $e = 0.5$ ) was added to position data and orientation data, respectively, since this produced point clouds that resembled reconstructions obtained from in-vivo data using the method described in the chapter 7. Position noise in the generated samples has a larger standard deviation in the z-direction since it is more difficult to estimate depth from video data. The left out nasal cavity was then estimated using these sampled points and a noise model assumption with SD  $1 \times 1 \times 2 \text{ mm}^3$  and  $30^\circ$  ( $e = 0.5$ ) for position data and orientation data, respectively. Despite the increased complexity of the right nasal airway models, the TSE using GD-IMLOP shows steady improvement (Fig. 6.25).

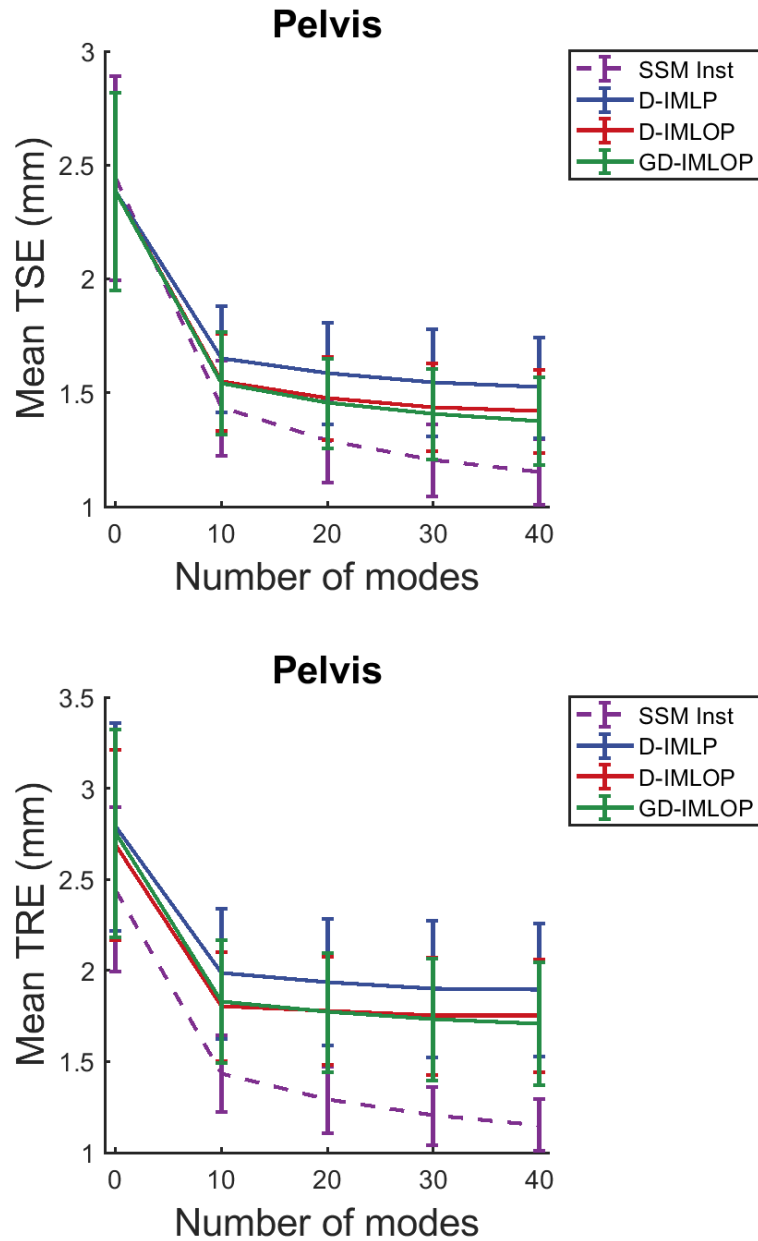


**Figure 6.24:** Partial data experiment: TSE (top) and TRE (bottom) produced by GD-IMLOP compared against that produced by the SSM estimate using the pelvis meshes.

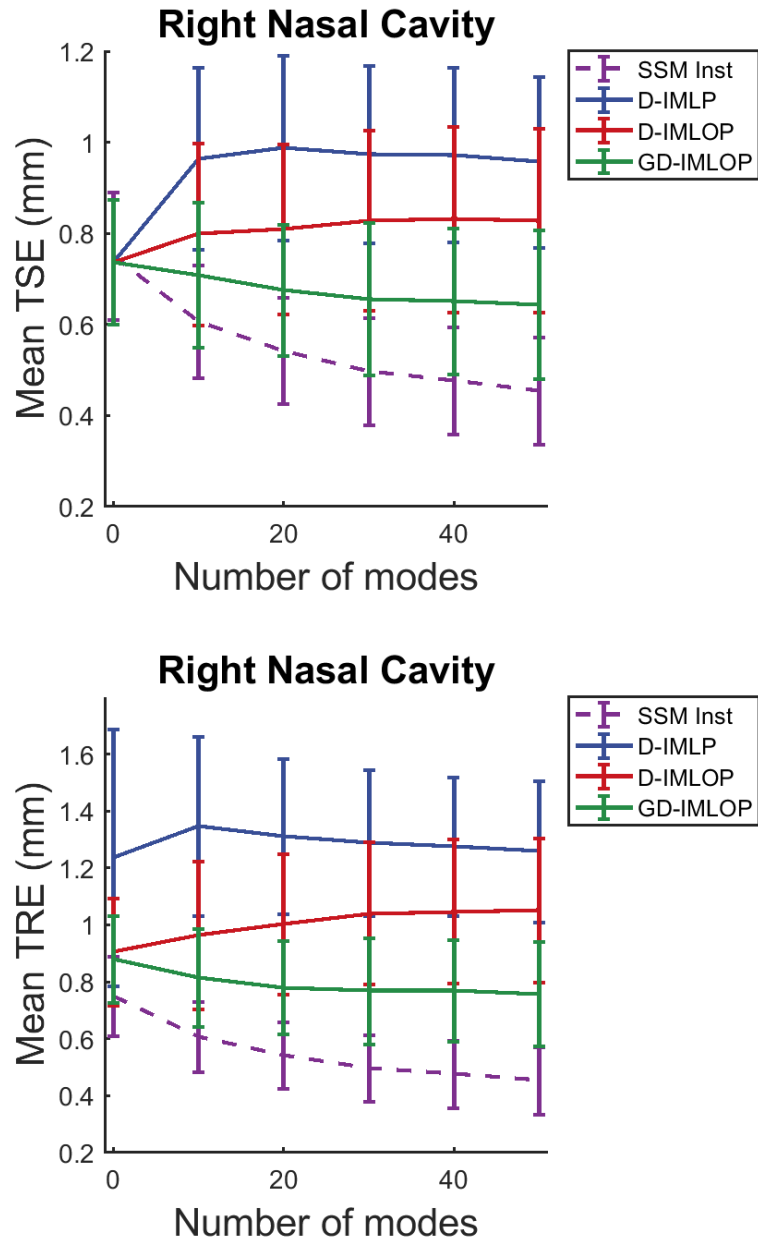


**Figure 6.25:** Partial data experiment: TSE (top) and TRE (bottom) produced by D-IMLOP compared against that produced by the SSM estimate using the right nasal airway meshes.

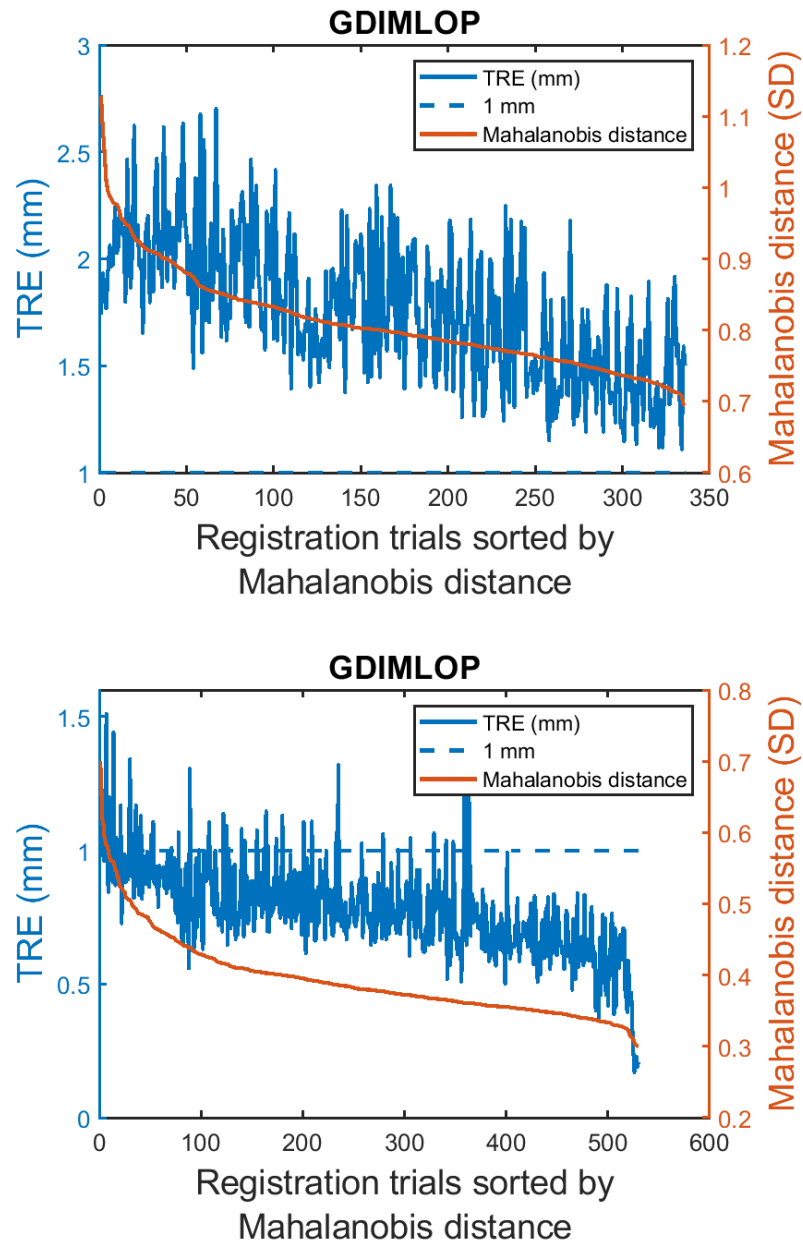


**Figure 6.26:** Partial data experiment: residual errors compared against TRE using the pelvis (top) and right nasal airway (bottom) meshes. The two measures exhibit correlation in both experiments 1 and 2 with correlation coefficients of 0.56 and 0.64, respectively.

The transformation parameters shows gradual improvement or stabilization, resulting in submillimeter mean TRE (Fig. 6.25). Again, the improvement in errors produced by GD-IMLOP is reflected in the residual errors produced by the algorithm (Fig. 6.26).

## 6.5.8 Failure detection experiment

### 6.5.8.1 Experiment 1: Known noise

This setup for this experiment is the same as the setup for the leave-one-out experiment with right nasal airway data (Sec. 6.5.6.2). As in Sec. 6.5.6.2, this experiment makes the same anisotropic noise assumptions as were used to generate the data samples. Results show that the chi-square test using  $E_p$  at  $p = 0.95$  is not only able to correctly detect almost all successful registrations, but is also able to successfully reject a majority of the unsuccessful registrations (Fig. 6.27, top). This also means that using the additional  $E_o$  test along with  $E_p$  only improves the percentage of incorrectly labeled failed registrations from 27% to about 25.5% (Fig. 6.27, bottom). However, using GD-IMLOP, these tests are able to retain more correctly labeled successful registrations than D-IMLOP. This result is reasonable since GD-IMLOP is able to model the noise in the data most accurately leading to better results than the previous two algorithms. Again, both  $E_p$  and  $E_o$  are strongly correlated with the TREs produced. Therefore, confidence can be assigned to the registrations based on the  $E_p$  and  $E_o$  scores (Fig. 6.28).

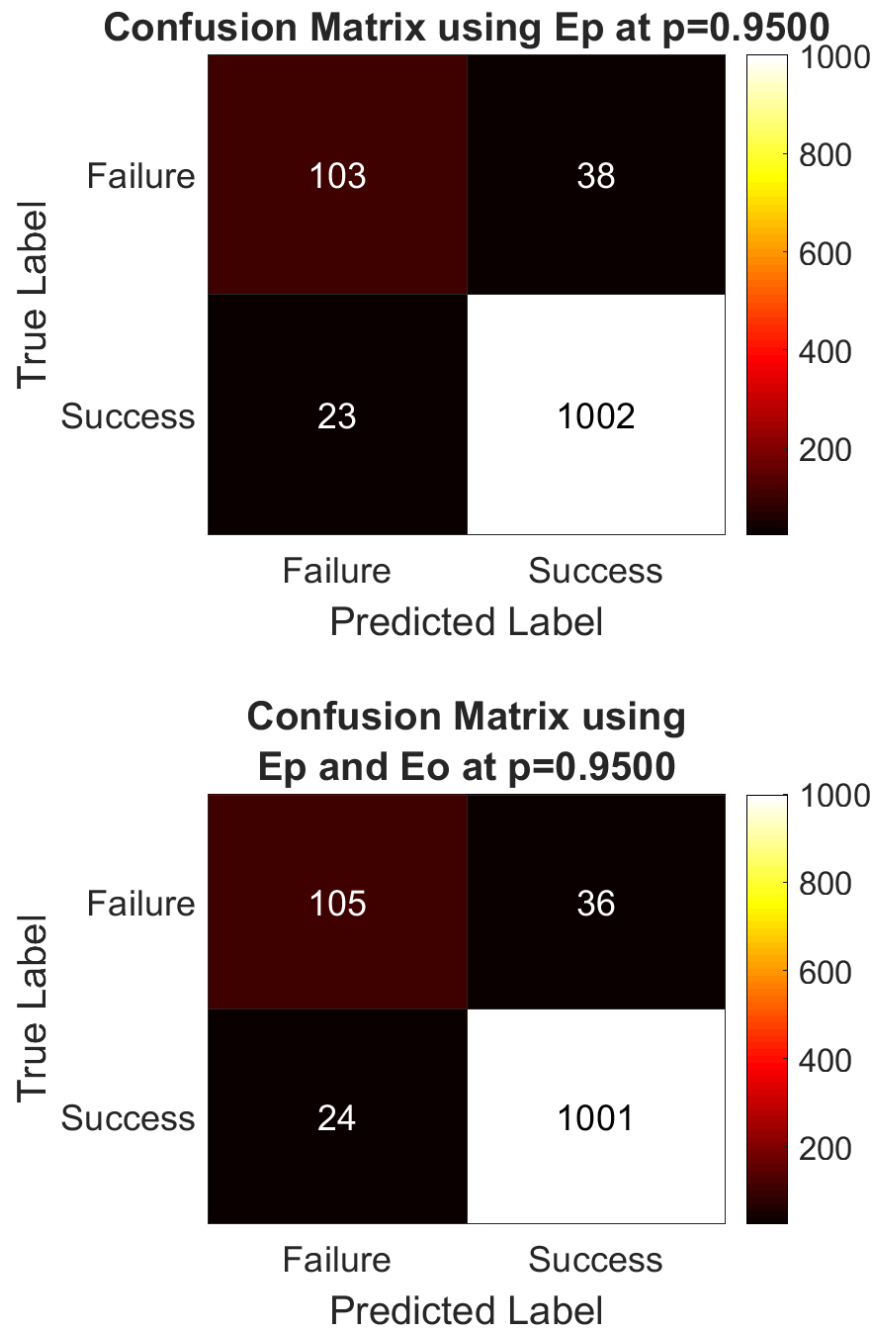


**Figure 6.27:** Failure detection experiment: Confusion matrix using  $E_p$  alone (top) and both  $E_p$  and  $E_o$  (bottom).

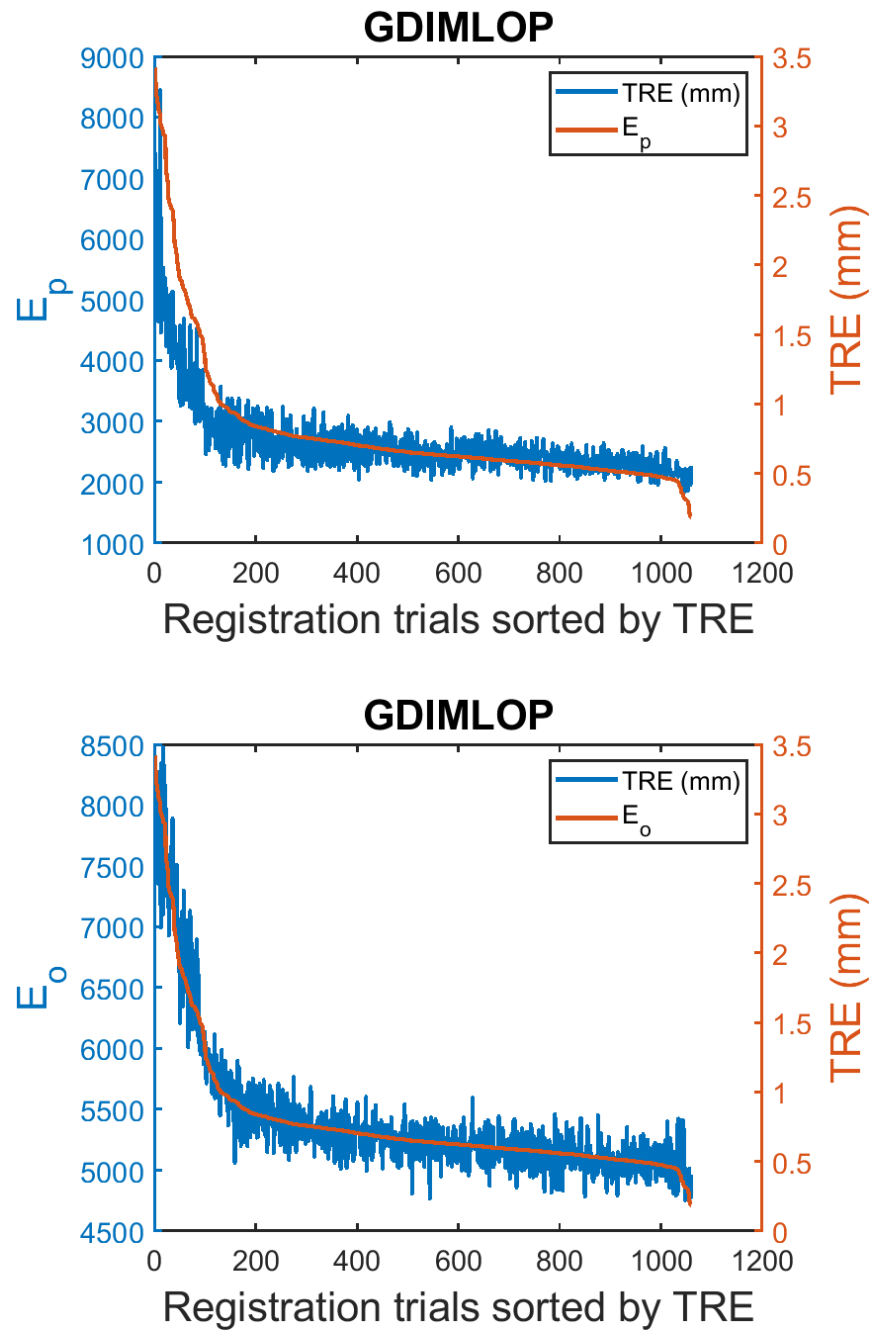


**Figure 6.28:** Failure detection experiment: Both  $E_p$  and  $E_o$  are correlated with the TRE (bottom) with correlation coefficients of 0.92 and 0.96, respectively, when the noise in the data is known.

### 6.5.8.2 Experiment 2: Unknown noise

The setup for this experiment is as described in Sections 4.5.8 and 5.5.8. The anisotropic noise in the sampled points has a SD of  $0.5 \times 0.5 \times 0.75 \text{ mm}^3$  and  $10^\circ$  ( $e = 0.5$ ) in the position and orientation components, respectively. GD-IMLOP makes more generous noise assumptions with SDs  $1 \times 1 \times 2 \text{ mm}^3$  and  $30^\circ$  ( $e = 0.5$ ) for position and orientation data, respectively. As with the previous two algorithms, the chi-square test using  $E_p$  at  $p = 0.95$  is able to successfully detect all successful registrations, but also incorrectly labels almost all unsuccessful registrations as successful (Fig. 6.30, top). On the other hand, using both  $E_p$  and  $E_o$ , all failed registrations are successfully rejected, but almost all successful registrations are also rejected as unsuccessful (Fig. 6.30, bottom). That is,  $E_p$  is too lenient, while  $E_o$  is too strict. By increasing  $p$  to 0.9975, the chi-square test using  $E_p$  produces the same results as with  $p = 0.95$  (Fig. 6.30, top), but adding  $E_o$  is able to correctly detect more successful registrations while still rejecting all unsuccessful registrations (Fig. 6.30, bottom). Further, both  $E_p$  and  $E_o$  are correlated with the TRE, enabling some assignment of confidence to the registration based on these scores (Fig. 6.31).

Registrations with  $E_p < \text{chi2inv}(0.95, 3n_{\text{data}})$  and  $E_o < \text{chi2inv}(0.95, 2n_{\text{data}})$  can be **very confidently** classified as successful. The average TRE produced by registrations in this category over all modes was  $0.34 (\pm 0.03) \text{ mm}$ . At  $p = 0.9975$ , all successful registrations were again correctly identified. These registrations can be **confidently** classified as successful with mean TRE increasing to  $0.62 (\pm 0.03) \text{ mm}$ .



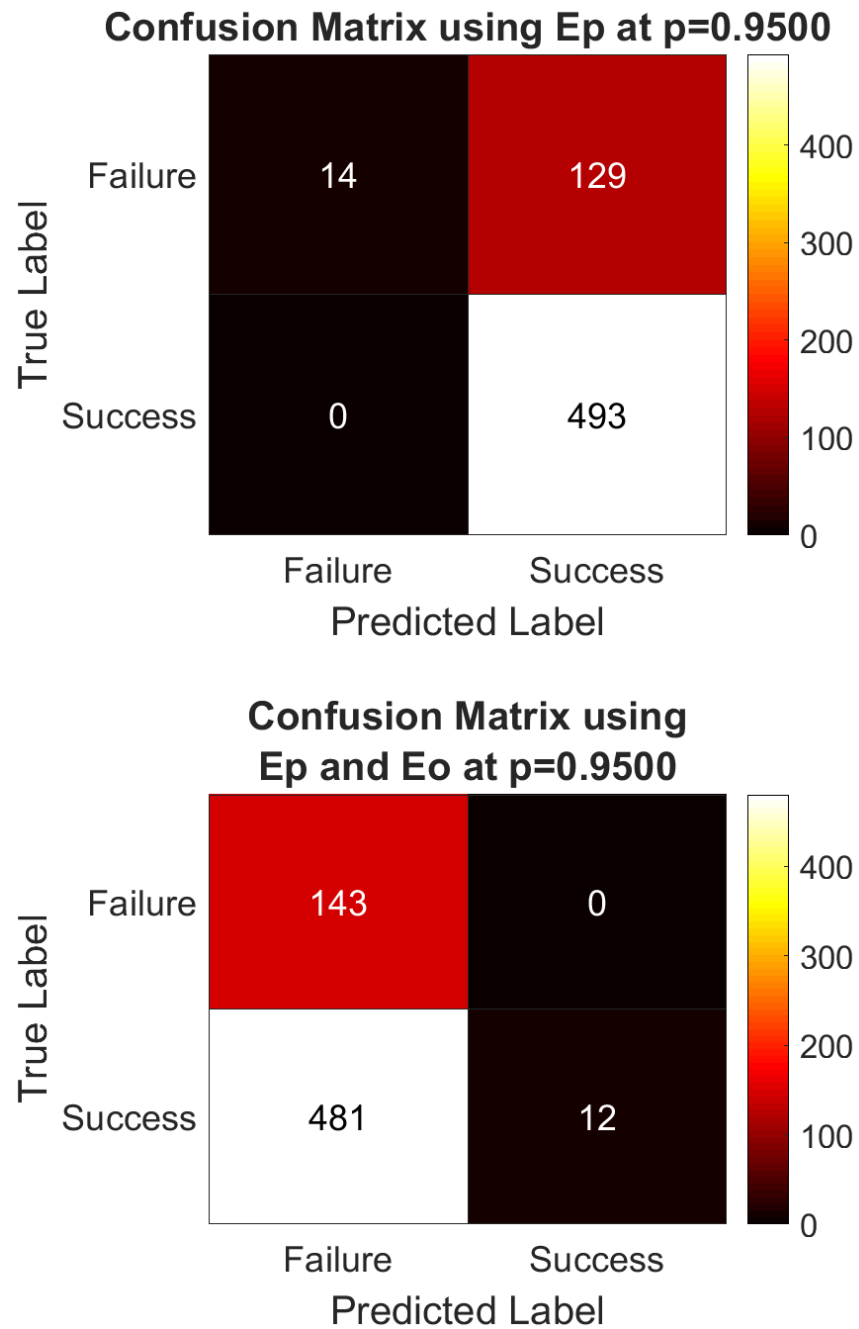


**Figure 6.29:** Failure detection experiment: Confusion matrix using  $E_p$  alone (top) and both  $E_p$  and  $E_o$  (bottom) at  $p = 0.95$ .

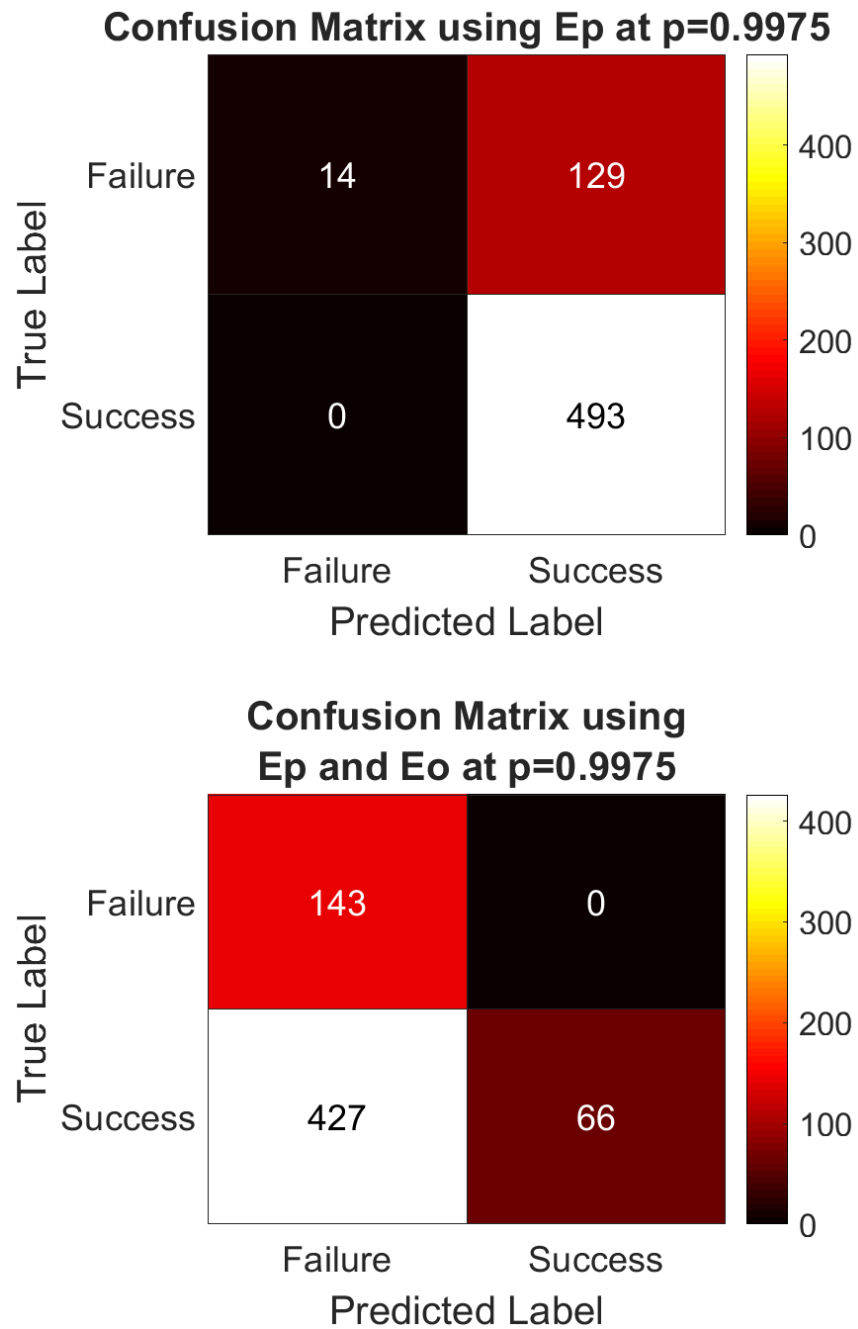


**Figure 6.30:** Failure detection experiment: Confusion matrix using  $E_p$  alone (top) and both  $E_p$  and  $E_o$  (bottom) at  $p = 0.9975$ .

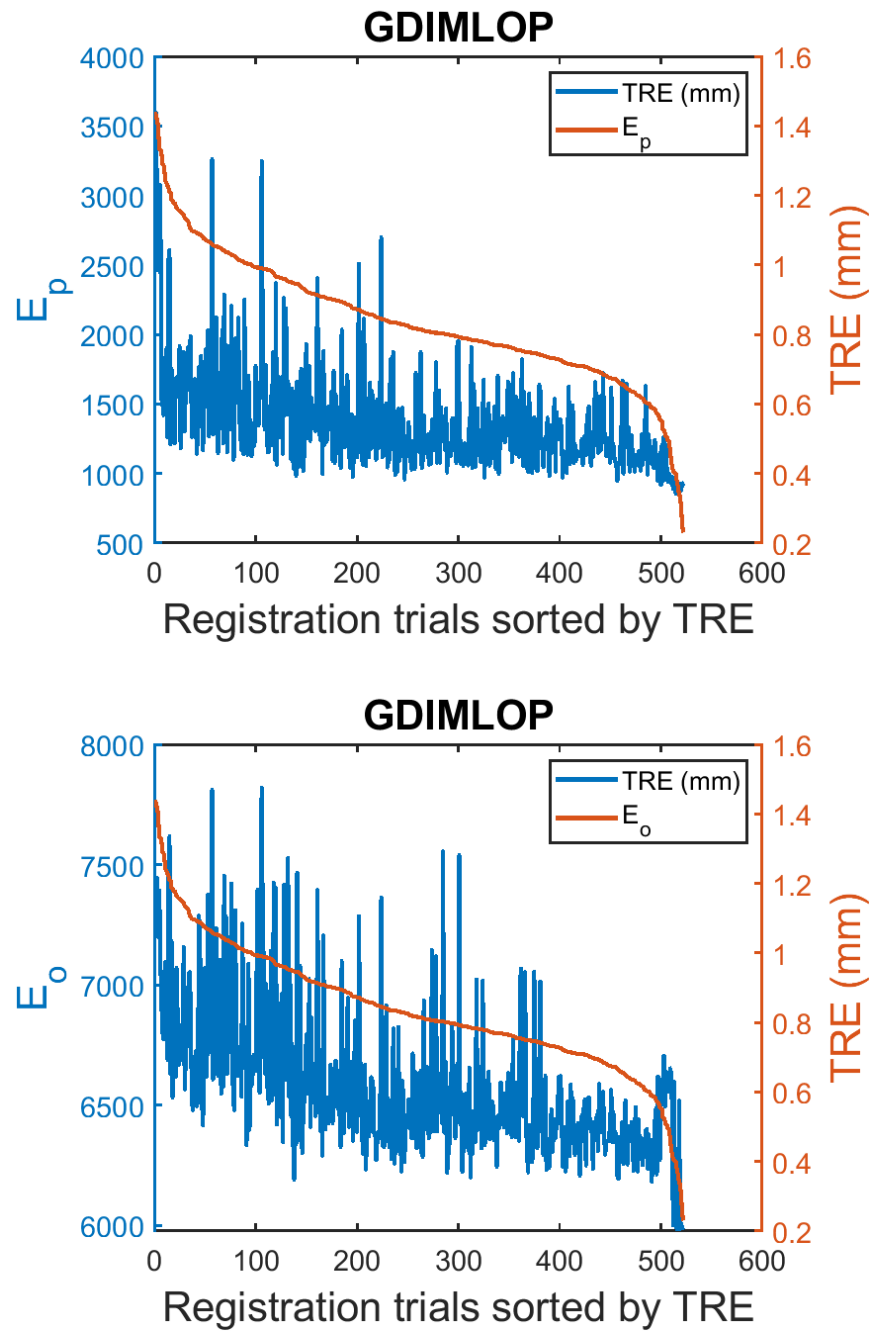


**Figure 6.31:** Failure detection experiment: both  $E_p$  (top) and  $E_o$  (bottom) are weakly correlated with the TRE with correlation coefficients of 0.56 and 0.58, respectively, when the noise in the data is unknown.

## CHAPTER 6. GD-IMLOP ALGORITHM

Errors in correct classification creep in with  $p = 0.9999$ , where 3 out of 124 registrations are incorrectly labeled successful. These registrations can be **somewhat confidently** classified as successful with mean TRE increasing slightly to  $0.78 (\pm 0.04)$  mm. Increasing  $p$  to 0.999999 further decreases classification accuracy. 10 out of 121 registrations in this category are incorrectly classified as successful with the mean TRE increasing to  $0.8 (\pm 0.05)$  mm. These registrations can, therefore, be classified as successful with **low confidence**. The mean TRE for the remaining registrations increases to over 1 mm at  $1.31 (\pm 0.85)$  mm, with no registration passing the  $E_p$  threshold except for registrations using 0 modes. Of these, however, 0 are correctly classified as successful. Therefore, although about half the registrations that fall in this category are successful, there can be **no confidence** in their correct classification. Fig. 6.32 (top) shows the distribution of TREs in these categories.

GD-IMLOP can, therefore, compute successful registrations between a statistically mean right nostril mesh and points sampled only from the nasal cavity region of the left-out shapes, and reliably assign confidence to these registrations. Further, GD-IMLOP can accurately estimate the shape of the nasal cavity since points are sampled from this region, while errors gradually deteriorate away from the cavity, e.g., towards the front of the septum since points are not sampled from this region (Fig. 6.32, bottom). Overall, mean shape estimation error was 0.77 mm.

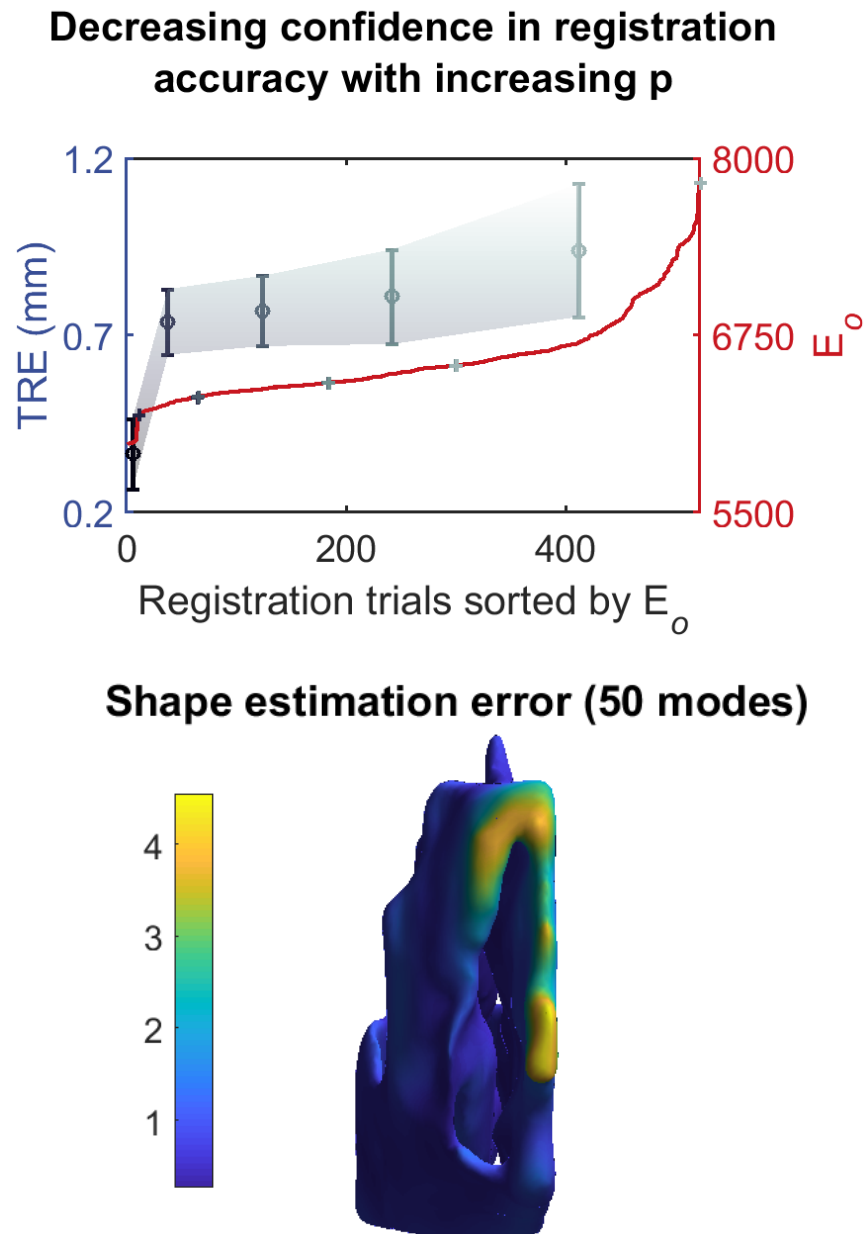


**Figure 6.32:** Failure detection experiment: mean TRE and standard deviation increase as  $E_o$  increases (top), and average error at each vertex computed over all left-out trials using 50 modes (bottom).

## 6.5.9 Non-medical data experiment

### 6.5.9.1 Experiment 1: Human expression

Points were sampled from meshes in the test set with anisotropic position noise and orientation noise with SD  $1 \times 1 \times 2 \text{ mm}^3$  and  $10^\circ$  ( $e = 0.5$ ), respectively. This simulates a realistic situation in which a scan of a head is obtained using a depth camera, where error is larger in the depth direction. GD-IMLOP was executed with a slightly more relaxed noise assumption, assuming that the position and orientation noise model has a SD of  $2 \times 2 \times 4 \text{ mm}^3$  and  $20^\circ$  ( $e = 0.5$ ), respectively. GD-IMLOP deformably registered the mean face mesh to points sampled from test faces to produce relatively low TREs and TSEs, as seen before using D-IMLP and D-IMLOP (Fig. 6.36). The residual errors produced by GD-IMLOP correlate with the TRE, indicating that it has the ability to handle such data (Fig. 6.36, top). Using more sample points also further drives down the errors (Fig. 6.33).

### 6.5.9.2 Experiment 2: Human pose

For this experiment, points were sampled with the same anisotropic position and orientation noise model as before. GD-IMLOP was, again, deployed with a more relaxed noise assumption where the SD of the position and orientation noise model was assumed to be  $2 \times 2 \times 4 \text{ mm}$  and  $30^\circ$  ( $e = 0.5$ ), respectively. The search space for shape parameters,  $\mathbf{s}$ , in this case was restricted to  $\pm 1$  SD.

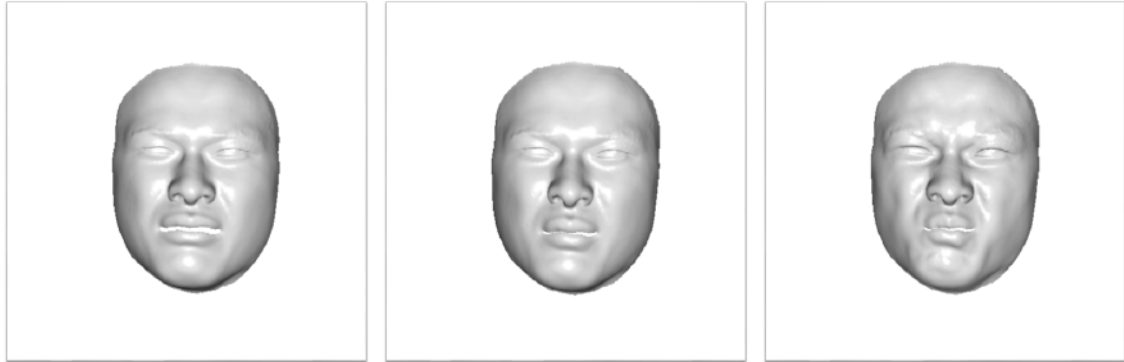


**Figure 6.33:** Non-medical data experiment: this particular target shape (right) has a large amount of detail which is necessary to convey the emotion in this face. 1000 sample points are too few to capture this detail resulting in an inaccurate reconstruction (left). However, with 2000 sample points, we are able to estimate this expression better (middle) since more sample points are better able to capture the detail in the target.

GD-IMLOP, like D-IMLP and D-IMLOP, failed to produce meaningful reconstructions and alignments with this dataset, as is clear from the high TREs and TSEs (Fig. 6.35). This was expected since the limited data available and the linearity assumptions made by PCA-based SSMs are possibly not sufficient to explain the complex variations observed in different poses. The slight improvement in errors for D-IMLOP over GD-IMLOP is, again, due to the relatively simpler objective function minimized by D-IMLOP leading to faster descent towards the minima, as explained in Sec. 6.5.3.4. The failure of GD-IMLOP to accommodate this dataset is clear from Fig. 6.36 (bottom).

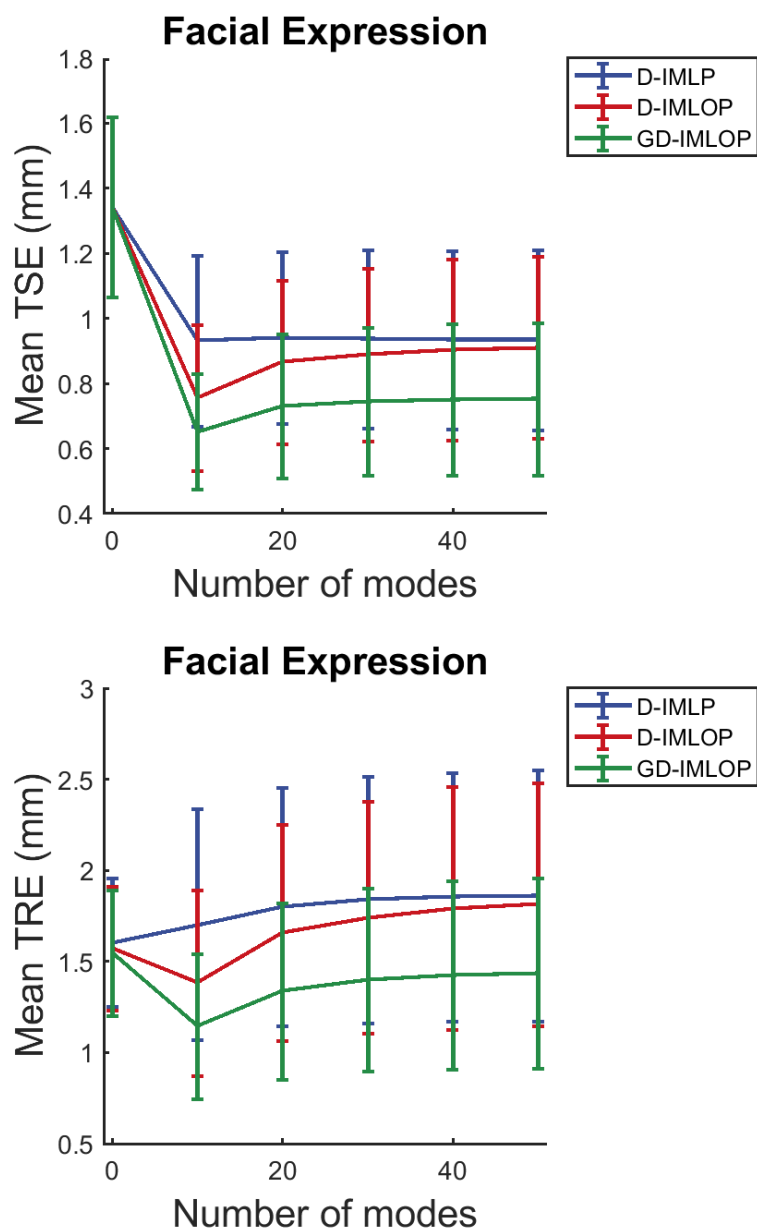


**Figure 6.34:** Leave- $n$ -out experiment: TSE (top) and TRE (bottom) produced by GD-IMLOP.



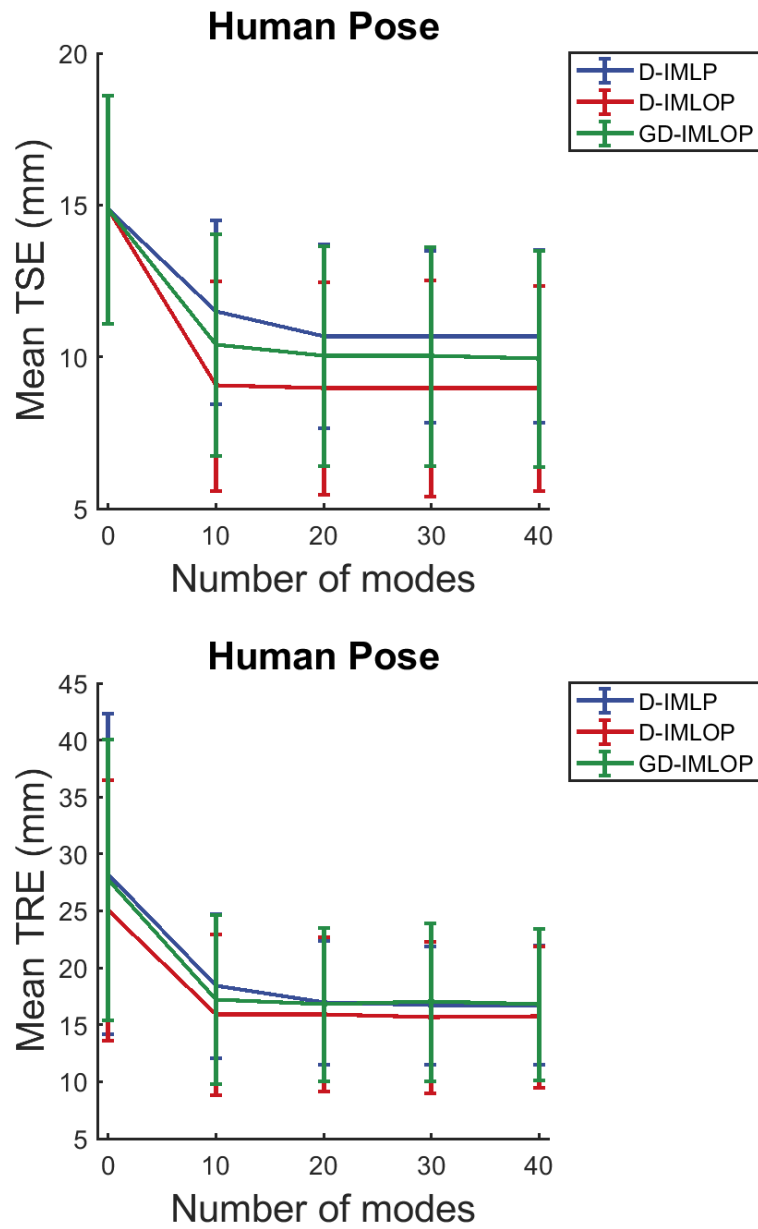


**Figure 6.35:** Leave- $n$ -out experiment: TSE (top) and TRE (bottom) produced by GD-IMLOP.

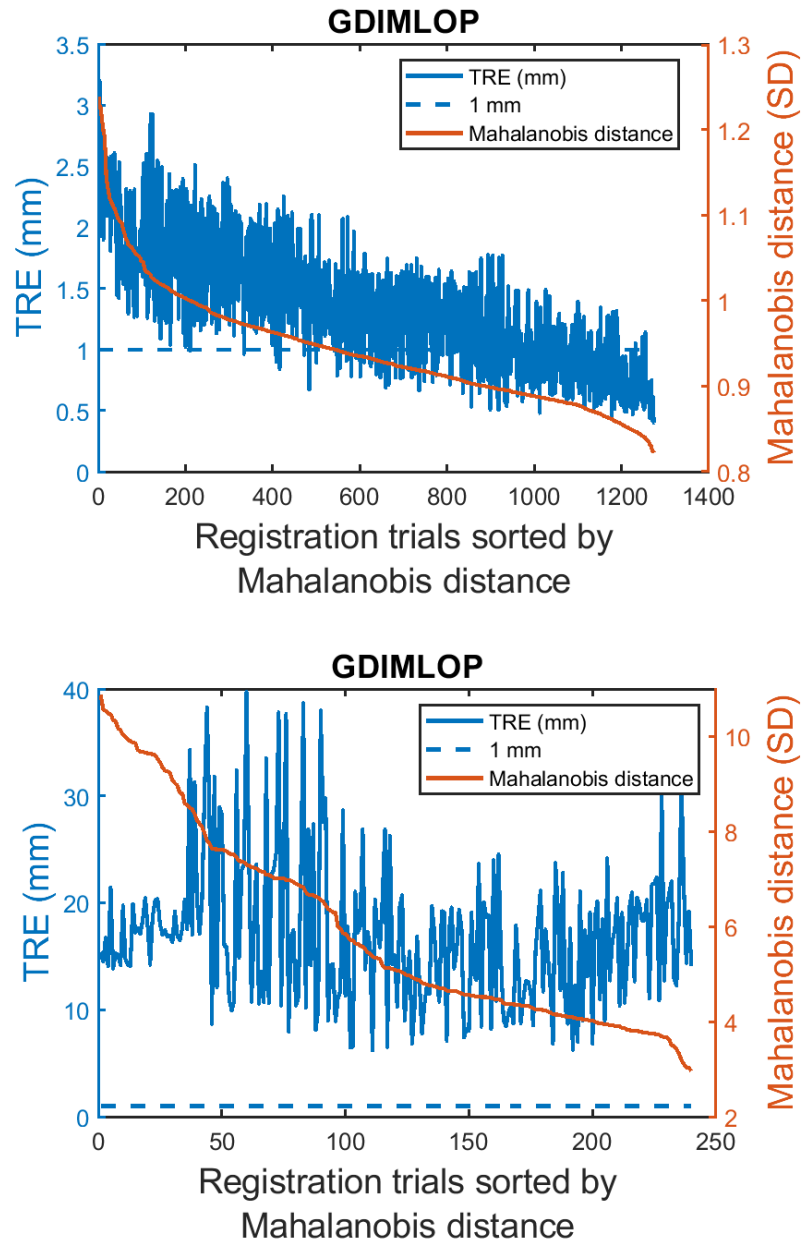


**Figure 6.36:** Leave- $n$ -out experiment: residual errors compared against TRE show that the two measures exhibit high correlation using the facial expression data with a correlation coefficient of 0.78 (top), and no correlation using the human pose data with a correlation coefficient of 0.18 (bottom).

## 6.6 Concluding remarks

A novel deformable variant of G-IMLOP, known as the generalized deformable iterative most likely oriented point (GD-IMLOP) algorithm, is presented in this chapter. This algorithm is able to compute the optimal alignment between a mean shape and data samples and simultaneously deform the mean shape to estimate the shape represented by the data samples. GD-IMLOP shows improvement in accuracy with increasing number of data samples, and is not significantly affected by increasing number of outliers. GD-IMLOP also shows improvement in performance as the noise model assumption becomes more pessimistic. These results make GD-IMLOP a favorable option for real world applications where data samples may be sparse, noisy, and contain outliers. Since GD-IMLOP produces improving results as the assumed noise model becomes larger than the true noise model, it allows GD-IMLOP to make extremely pessimistic assumptions when noise in data samples is unknown and hard to estimate and still perform well.

GD-IMLOP is able to match the performance of CPD in terms of errors using more than  $\sim 20$  modes, and is about  $1.5\text{--}2\times$  faster than CPD. GD-IMLOP also does not suffer from the high memory requirements of CPD. Finally, unlike CPD, GD-IMLOP produces errors that correlate with the true error allowing it to make confidence assignments for registrations based on these errors. Although GD-IMLOP produces highly accurate registrations, further improvements can be made using additional features such as contours.

## 6.7 Contributions

The contributions of this chapter include:

1. The development, implementation and evaluation of the generalized deformable iterative most likely oriented point (GD-IMLOP)<sup>77</sup> algorithm
  - (a) which incorporates deformable shape transformations using SSMs within a probabilistic registration algorithm that uses point and orientation features with associated unconstrained noise for both types of features
  - (b) performs an efficient implementation of PD-tree update to accommodate a deforming model shape
  - (c) computes a gradient-based solution to the optimization problem using an off-the-shelf nonlinear box-constrained BFGS quasi-Newton optimizer<sup>80</sup>
  - (d) incorporates a mechanism for autonomously evaluating a registration in order to assign confidence to the resulting alignment

## 6.8 Published work

Material from this Chapter appeared in the following publication:

1. A. Sinha, S. D. Billings, A. Reiter, X. Liu, M. Ishii, G. D. Hager, R. H. Taylor, “The deformable most-likely-point paradigm,” *submitted to Medical Image Analysis* (2018)

## CHAPTER 6. GD-IMLOP ALGORITHM

2. A. Sinha, X. Liu, A. Reiter, M. Ishii, G. D. Hager, R. H. Taylor, “Endoscopic navigation in the absence of CT imaging,” *submitted to MICCAI (2018)*

## Chapter 7

# Deformable video-CT registration

Minimally invasive procedures are increasingly becoming the preferred approach for all interventions where such a procedure is possible. These procedures are carried out through natural openings in the anatomy or small openings created by the surgeon, and often make use to endoscopes or laparoscopes to visualize the target anatomy. The advantages of such procedures are immense, resulting in faster patient recovery time, shorter hospital stays, reduced scarring as well as reduced surgical trauma.<sup>115</sup> However, minimally invasive surgery also brings along with it several challenges. These challenges include a higher learning curve for surgeons, increased cost due to the requirement of specialized equipment, and longer operating times. However, one of the biggest challenges to minimally invasive surgeries is presented by the limited field of view provided by endoscopes and laparoscopes.

In procedures such as functional endoscopic sinus surgery (FESS), the restricted

## CHAPTER 7. DEFORMABLE VIDEO-CT REGISTRATION

field of view of endoscopes is further complicated by the small size and thin boundaries of the nasal passage and sinus cavities. Further, the proximity of critical structures like the brain, eyes, optic nerves and carotid arteries make any breach of the sinus boundaries potentially fatal. For instance, the thickness of the fovea ethmoidalis or the roof of the sinuses that separates the sinuses from the brain can be as low as 0.5 mm, while the thickness of the lateral lamella, which separates the sinuses from the olfactory system, can be as small as 0.2 mm.<sup>100</sup> The sheath surrounding the optic nerves ranges between 0.45 mm and 0.91 mm closer to the eyeball.<sup>116</sup> Several of these measurements include the layers of mucosa covering the boundaries. For example, the bony parts of the uncinated process are about 0.16 mm thick, although the total thickness of the uncinated process, including the mucosa covering the bony structures, can be as large as 0.67 mm.<sup>117</sup> However, mucosa are extremely soft and provide little resistance to tools. This makes it extremely critical that tools be kept away from the skeletal boundaries of the nasal cavity and sinuses. Minimally invasive procedures can, therefore, benefit tremendously from accurate surgical navigation systems since they can provide context information, inform the clinicians about the safety margins, and warn them when these margins are about to be violated. Further, navigating complex anatomy like the ethmoidal cells of the sinuses can be extremely disorienting for clinicians, and context cues from the navigation system can help reorient the clinicians.

Several commercial navigation systems are available in operating rooms and are

## CHAPTER 7. DEFORMABLE VIDEO-CT REGISTRATION

used during several procedures. Some examples include optical navigation systems, which use markers attached to the endoscope that must be visible to some optical tracking device, and electromagnetic (EM) navigation systems, which do not require line-of-sight, but do require a sensor attached to the endoscope to remain within the magnetic field of the EM field generator.<sup>118</sup> These commercial tracker-based navigation systems generally report errors around or larger than 2 mm. Image-based navigation systems, which rely on extracting features from video frames or images and registering these features to features extracted from some preoperative image (e.g. CT, MRI), have also been presented in several experimental settings.<sup>119</sup> Most such systems developed more recently report errors around or below 1 mm. Registrations performed between features obtained from preoperative and intraoperative images can be rigid or deformable. Rigid registrations simply transform features from one space to another via a rotation and a translation. ICP is a standard rigid registration algorithm.<sup>35</sup> Its simplicity led to its popularization, but also contributes to its limitations. For instance, standard ICP is unable to robustly handle outliers and noise in the data. Further, in a clinical setting, often changes in the anatomy occur making a simple rigid transformation insufficient for accurate registration. On the other hand, deformable algorithms additionally modify features in some way.



## 7.1 Deformable registration

As mentioned earlier, in realistic clinical settings, rigid registration is often not sufficient to produce accurate registrations. For instance, due to the scale ambiguity in camera-based vision, most algorithms that extract features from video frames are only accurate up to scale. Therefore, additionally solving for scale is a desired property in image-based navigation systems.<sup>54</sup> Further, anatomy can change between preoperative and intraoperative imaging. These changes can be natural, for instance, stemming from heartbeat, breathing, or nasal cycle. Changes can also be artificially introduced, for instance, from insufflation, cutting, tearing or moving of tissues during surgical procedures. These require more complex local deformations to be accounted for in order to produce accurate registrations. Such deformations can be applied via displacement or deformation fields<sup>50</sup> or using statistics that explain how features derived from known anatomy can deform.<sup>77</sup> Several deformable registration algorithms have been introduced in order to counter these problems presented in real world surgical settings. A more thorough discussion of these is presented in Sec. 1. However, one main assumption that these methods make is the availability of preoperative images. This assumption is not accurate in all settings.

For instance, it cannot be assumed that a protocol requiring the acquisition of a preoperative image exists worldwide since often these image acquisitions are expensive, and those requiring medical intervention could possibly not afford such image acquisitions. Further, even if image acquisition is affordable, high doses of ionizing

radiation exposure from some image acquisition technologies is not desired. Often, a decision on whether surgical intervention is required or not, as in the case of FESS, is preceded by endoscopic exploration of the target anatomy for diagnosis and/or surgical planning. Although FESS is accompanied by a preoperative patient CT image, prior endoscopic exploration is not since radiation exposure is avoided unless necessary. This means that clinicians performing endoscopic exploration must rely entirely on the endoscopic camera for visualization and, therefore, must cope with its restricted field of view. Further, monocular lenses used in most endoscopic cameras make depth perception difficult. These in addition to the challenges presented by the complex anatomy of the nasal cavity and pseudostochastic growth pattern of some sinuses, like the ethmoidal cells, lead to clinicians becoming disoriented.

### 7.1.1 The deformable most-likely-point paradigm

In order to reduce the reliance of clinicians on experience or memory in such cases, the deformable registration paradigm and associated algorithms presented in the previous chapters (Chapters 3, 4, 5 and 6) can be used to estimate patient anatomy and enable navigation without the need for accompanying patient CT image. That is, the abundance of available CT scans from several different individuals can be used to build statistical shape models of relevant structures. Statistically derived shapes, for instance the mean shape, can then be deformably registered to features extracted from endoscopic video according to statistics explaining feasible deformations in these

structures. These registrations accomplish two tasks simultaneously. First, they align endoscopic video to the statistically derived shape. Second, they deform the statistically derived shape to fit the structure obtained from video and *estimate the patient shape*. These methods are also able to associate confidence measures to the navigation being provided allowing clinicians to know when and how much to rely on the navigation without introducing any additional devices, like trackers, etc., than those already used in clinical endoscopic exploration, that is, the endoscope. The confidence measures also allow the navigation system itself to attempt to improve itself if its current registration estimate has low confidence.

### 7.1.2 Dense reconstruction from video

Since the deformable registration algorithms presented in Chapters 4, 5 and 6 are additionally estimating the patient shape, they need to optimize over many more parameters than the 6 required to compute a rigid transformation. Therefore, they require more dense point clouds extracted from endoscopic video than algorithms like structure from motion (SfM) are able to extract due to the lack of texture in these videos.

Shape from shading based methods have been able to produce dense reconstructions from endoscopic videos by explicitly<sup>120</sup> or implicitly<sup>74</sup> modeling the relationship between appearance and depth using a bidirectional reflectance distribution function

(BRDF):

$$f_r(\omega_i, \omega_r) = \frac{dL_r(\omega_r)}{dE_i(\omega_i)} = \frac{dL_r(\omega_r)}{L_i(\omega_i) \cos \theta_i d\omega_i}, \quad (7.1)$$

where  $\omega_i$  and  $\omega_r$  represent the incoming and outgoing light directions, respectively, while the fraction on the right hand side of the equation is the ratio of reflected *radiance*,  $L$ , exiting along  $\omega_r$  to the *irradiance*,  $E$ , incident onto the surface along direction  $\omega_i$ .<sup>121</sup> Radiance is the luminous flux per unit area per unit solid angle, while irradiance is the incident luminous flux per unit area and depends on the incident radiance and the angle,  $\theta$ , between the incident direction,  $\omega_i$  and the surface normal,  $\mathbf{n}$ , where  $\omega_i$  intersects the surface. The purpose of BRDFs is to model how light incident from a particular direction and viewed from a particular direction interacts with surfaces of various geometries and material properties. If modeled accurately, a BRDF can explain how light forms pixel intensities on observed images and, therefore, can accurately describe the scene geometry from pixel values. However, it is difficult to know exactly how much light is incident on a surface, especially due to the presence of other light sources in the environment, as well as to know, for each incident angle, how much light is scattered in each outgoing direction.

One common way of simplifying this problem is by using the Lambertian reflectance model, which assumes that light is reflected equally in all directions. This assumption is more accurate for opaque objects, but not for surgical data. Different tissues have different reflectance properties, but can generally not be described as opaque, meaning that some light experiences absorption as well as subsurface scatter-

ing. Light that is reflected is not reflected equally in all directions. Further, presence of liquids and mucous in the nasal cavity can result in high specularities, which the Lambertian model cannot explain. Therefore, although previous methods have shown that dense point clouds can be reconstructed from endoscopic video, these methods are not accurately able to recover depth from images and fail in the presence of specularities. However, new deep learning based methods<sup>3</sup> have shown that these and other challenges, like occlusion and scale ambiguity, can be overcome to produce accurate and dense reconstructions from single frames of endoscopic video (Fig. 7.2). These reconstructions contain enough structure to allow deformable registration algorithms to accurately estimate the shape represented by the point clouds.

## 7.2 Experimental results and discussion

An anonymized in-vivo clinical dataset consisting of endoscopic videos of the nasal cavity and EM-tracking information was obtained from several consenting patients who were examined at the Johns Hopkins Outpatient Center. Permission to collect this dataset was approved by the Johns Hopkins internal review board (IRB) under application number NA\_00074677. Two experiments are performed on this clinical dataset using slightly different reconstructions from video that are manually initialized in the mean mesh of the appropriate nasal cavity. Since, ground truth for these datasets is not available, residual errors produced by the registration algorithms are

reported as registration error. Additionally, obvious registration failures can be detected by visualizing the final alignment produced.

### 7.2.1 Reconstruction from single frame

In this experiment, reconstructions from 2 individual frames were subsampled to obtain 2000 points which were manually initialized in the left nasal cavity mesh. Registrations were computed using D-IMLP, D-IMLOP and GD-IMLOP with 10 modes restricted within  $\pm 1$  SD. Scale estimation was also restricted to within  $[0.7, 1.3]$ , and anisotropic noise was assumed by the algorithms (where applicable) with SDs of  $1 \times 1 \times 2 \text{ mm}^3$  and  $40^\circ$  ( $e = 0.5$ ) for position and orientation, respectively. GD-IMLOP was able to produce submillimeter registrations for both sets of samples (Table 7.1), which also produced visually convincing alignments (Fig. 7.1). This is as expected since GD-IMLOP is best equipped to model the noise present in data extracted from real in-vivo endoscopy video. D-IMLP and D-IMLOP exhibit less reliable behavior. Using the first reconstruction (RcnStr01), D-IMLP appears to produce an extremely accurate alignment with very low mean residual error (Table 7.1). However, the TRE for this registration is larger than 1 mm, and the alignment, on visual inspection, appears to be wrong (Fig. 7.1). D-IMLOP, on the other hand, produces both high residual error and TRE (Table 7.1), and a visualization of the registration confirms the error in alignment (Fig. 7.1). For the second reconstruction (RcnStr02), both D-IMLP and D-IMLOP succeed in producing low residual errors and TRE (Table 7.1).

**Table 7.1:** Registration results using single frame reconstruction from in-vivo data.

	Algorithm	Residual error	TRE
RcnStr01	D-IMLP	0.25 ( $\pm 0.40$ )	1.26 ( $\pm 1.25$ )
	D-IMLOP	2.13 ( $\pm 3.28$ )	1.42 ( $\pm 1.39$ )
	GD-IMLOP	0.92 ( $\pm 1.44$ )	0.98 ( $\pm 0.81$ )
RcnStr02	D-IMLP	0.50 ( $\pm 0.82$ )	0.96 ( $\pm 0.83$ )
	D-IMLOP	0.61 ( $\pm 0.98$ )	0.95 ( $\pm 0.83$ )
	GD-IMLOP	0.77 ( $\pm 1.18$ )	0.95 ( $\pm 0.88$ )

Visualization (Fig. 7.1) shows improving alignment from D-IMLP to D-IMLOP to GD-IMLOP with fewer outliers (points outside the nasal cavity).

Two problems become clear from this experiment. First, although the dense reconstructions provide much needed structural information, reconstructions from single frames are unable to capture enough range of information to avoid falling into local minima in registration computation. This is what results in the low residual error produced by D-IMLP using RcnStr01, although the registration fails. This knowledge of failure will not be available during surgical navigation because of the absence of ground truth, and can cause serious damage to the patient if the surgeon is not able to catch the error in navigation. This creates an additional responsibility on the surgeon by having to divert attention from the patient to evaluating the navigation

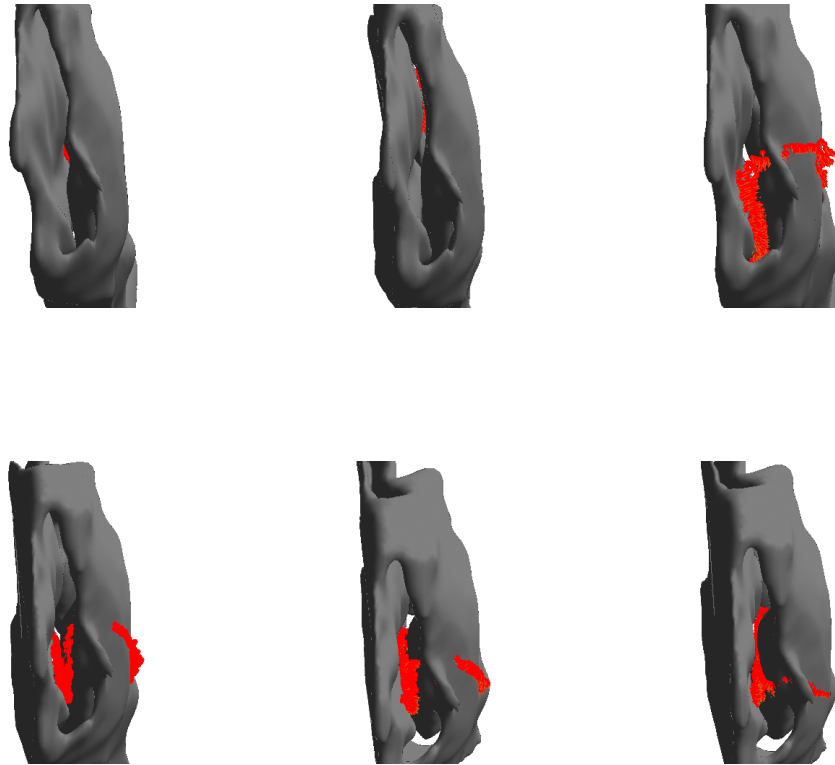


**Figure 7.1:** Using RcnStr01 (top), registration results using D-IMLP (left) and D-IMLOP (middle) show failed registrations, while that using GD-IMLOP (right) shows good alignment (along with some outliers). RcnStr02 (bottom) yields better results, with all three algorithms producing good alignments. However, we can see that the number of outliers or bad matches (red points matched to the outside of the nose) goes down as we go from D-IMLP (left) to D-IMLOP (middle) to GD-IMLOP (right).





**Figure 7.2:** A dense point cloud obtained from a single frame of endoscopic video using the method of Liu et al.<sup>3</sup>

being provided by technology meant to aid the surgeon. This brings up the second problem, which is that the residual error cannot always reliably be used as an indicator of registration success or failure, and that additional confidence measures are required to indicate the confidence of the system in the registration produced.

### 7.2.2 Reconstruction from multiple frames

In order to resolve the problems brought up by the first experiment, reconstructions used in this experiment were produced from individual *nearby* frames in en-

## CHAPTER 7. DEFORMABLE VIDEO-CT REGISTRATION

oscopic video sequences that were aligned using relative camera motion from SfM. Small misalignments due to errors in depth estimation were corrected using G-IMLOP with scale to produce reconstructions spanning larger areas of the nasal passage than those produced from single frames. Since it is clear from previous experiments that GD-IMLOP is best suited for registrations using this type of data with anisotropic noise in both position and orientation features, this experiment was only evaluated using GD-IMLOP. Registrations were computed using the GD-IMLOP with 3000 points sampled from these dense point clouds and assuming noise with SDs of  $1 \times 1 \times 2 \text{ mm}^3$  and  $30^\circ$  ( $e = 0.5$ ) for position and orientation data, respectively. Scale and shape parameter optimization was restricted to within  $[0.7, 1.3]$  and  $\pm 1$  SD, respectively. Registrations were computed using  $\mathbf{n}_m \in 0, 10, 20, 30, 40, 50$  modes. At 0 modes, GD-IMLOP is essentially G-IMLOP which was extended to additionally solve for scale. In addition to residual errors, confidence is assigned to the computed registrations based on the tests explained and validated in Chapter 6.

All registrations run with 0 modes terminated at the maximum iteration threshold of 100, while those run using modes converged at an average 10.36 iterations in 26.03 seconds. Fig. 7.3 shows registrations using increasing modes from left to right for each sequence plotted against  $E_p$  (middle) and  $E_o$  (right). All deformable registration results pass the  $E_p$  test as they fall below the  $p = 0.999999$  and  $p = 0.95$  thresholds (Fig. 7.3, top) using the chi-square inverse test. However, several of these fail the  $E_o$  test (Fig. 7.3, bottom). Deformable registrations on sequence 01 using 50 modes and

**Table 7.2:** Residual errors produced by registrations on clinical data.

	Residual errors (mm)		
	Mean	Max	Min
All	1.09 ( $\pm 1.03$ )	4.74	0.50
$E_p$	0.76 ( $\pm 0.14$ )	0.99	0.50
$E_p$ and $E_o$	0.78 ( $\pm 0.07$ )	0.94	0.74

on sequence 04 for all except 30 modes pass this test with **low confidence**. Using 30 modes, the registration passes **somewhat confidently**. The rigid registration on sequence 04 (the only rigid registration to pass both  $E_p$  and  $E_o$ ) and all deformable registrations on sequence 05 pass this test **very confidently**. Although, the rigid registration on sequence 05 passes this test very confidently,  $E_p$  already labels it a failed registration.

Successful registrations that passed both the  $E_p$  and  $E_o$  tests produced a mean residual error of 0.78 ( $\pm 0.07$ ) mm, with maximum residual error of 0.94 mm and a minimum residual error of 0.74 mm (Table. 7.2). The maximum residual error produced by successful registrations is smaller than the maximum residual error over all registrations and over all registrations that passed the  $E_p$  test, as is expected. The minimum residual error produced by successful registrations, however, is higher than the minimum over all registrations and over all registrations that pass the  $E_p$

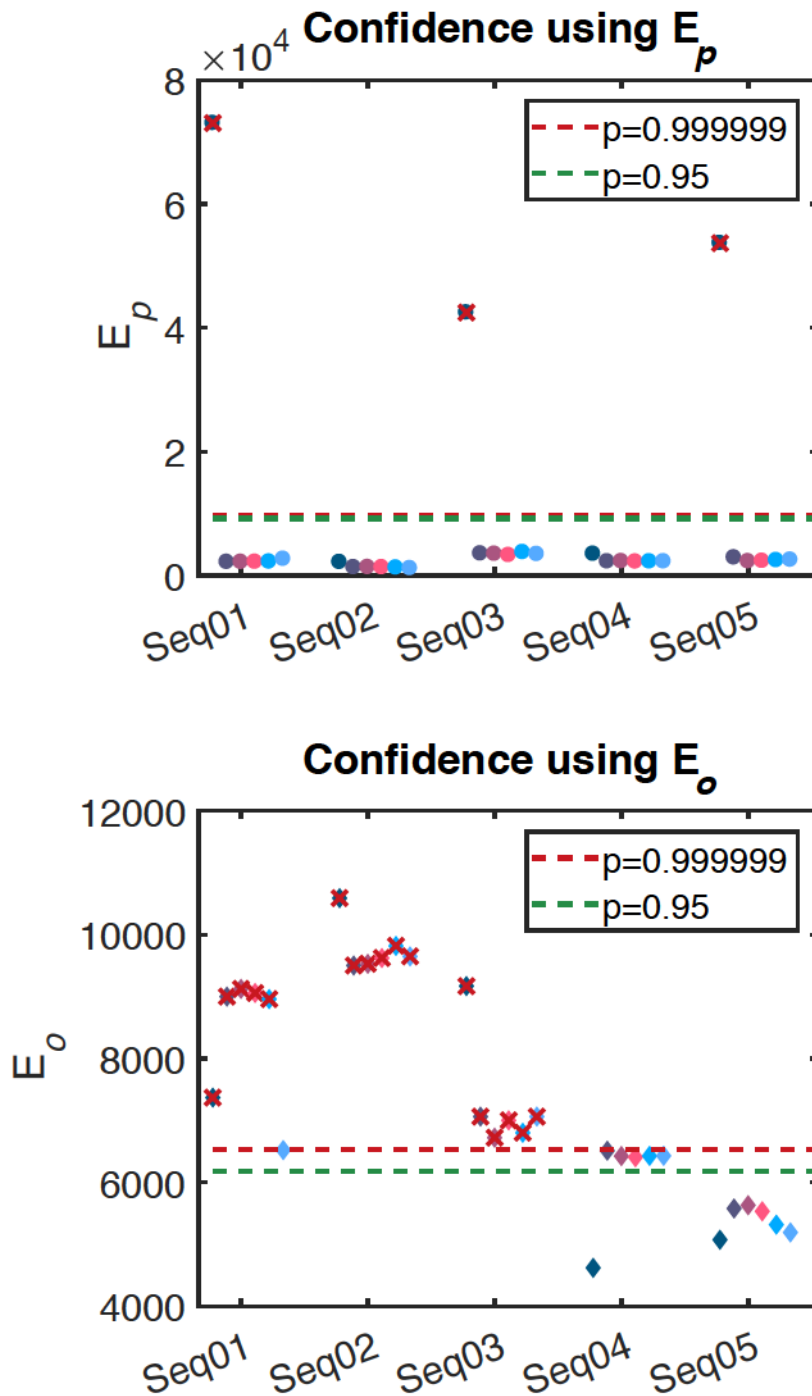


**Figure 7.3:**  $E_p$  (top) and  $E_o$  (bottom) for all registration computed using GD-IMLOP, plotted for each sequence. Within each sequence, from left to right, the plot points indicate scores achieved using 0 to 50 modes at increments of 10. Crossed out plot points indicate rejected registrations.

test. This is because registrations that converge to the wrong local minima will produce small positional errors and, therefore, pass the  $E_p$  test. However, this does not guarantee that orientations will also align well, causing these registrations to fail the  $E_o$  test. Visualizations of successful registrations also show accurate alignment (Fig 7.4).

### 7.3 Concluding remarks

Through experiments on in-vivo clinical data, it is shown that GD-IMLOP is able to produce submillimeter registrations in both simulation and in-vivo experiments and assign confidence to these registrations. Further, it can accurately predict the anatomy where video data is available. Using statistics built with thousands of CT scans to better cover the range of anatomical variations, these deformable algorithms could produce better estimations of patient anatomy. Additional features like contours can also be used, as in Billings et al.,<sup>55</sup> to further improve registration and to add an additional test to evaluate the success of the registration based on the quality of contour alignment. Using improved statistics and reconstructions from video along with confidence assignment, this approach can be extended to be used in place of CT images during endoscopic procedures.

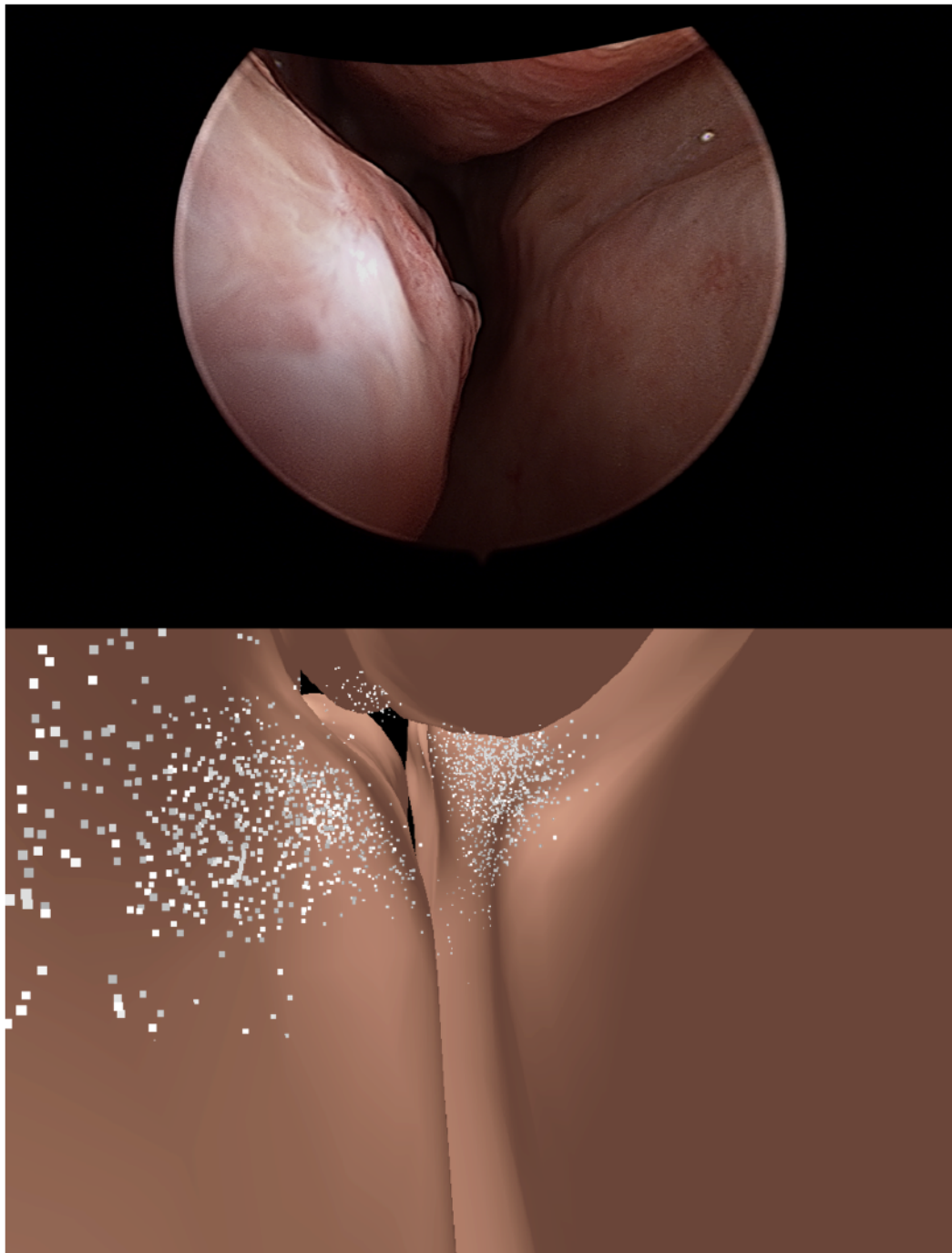


**Figure 7.4:** Top: One of the frames from the video sequence used to extract the dense structure. Bottom: Visualization of the final registration and reconstruction for Seq01 using 50 modes with dense structure points depicted in white.

## 7.4 Contributions

The work described in this chapter was done in collaboration with Xingtong Liu, whose work on dense reconstruction from single video frames was critical to producing the results presented in this chapter. The contributions of this chapter include:

1. An evaluation of the algorithms presented in Chapters 4–6 in a clinical setting through deformable registration between SSMs and dense reconstructions from in-vivo endoscopic video frames.<sup>77,79</sup>
2. Assignment of confidence to the computed registration in order to inform clinicians of the reliability of the computed registration.<sup>79</sup>

## 7.5 Published Work

Material from this chapter appeared in the following publications:

1. S. D. Billings, A. Sinha, A. Reiter, S. Leonard, M. Ishii, G. D. Hager, R. H. Taylor, “Anatomically Constrained Video-CT Registration via the V-IMLOP Algorithm,” In: Ourselin S., Joskowicz L., Sabuncu M., Unal G., Wells W. (eds) Medical Image Computing and Computer-Assisted Intervention – MICCAI 2016. MICCAI 2016. Lecture Notes in Computer Science, vol 9902. Springer, Cham (2016)

## CHAPTER 7. DEFORMABLE VIDEO-CT REGISTRATION

2. A. Sinha, S. D. Billings, A. Reiter, X. Liu, M. Ishii, G. D. Hager, R. H. Taylor, “The deformable most-likely-point paradigm,” *submitted to Medical Image Analysis* (2018)
3. A. Sinha, X. Liu, A. Reiter, M. Ishii, G. D. Hager, R. H. Taylor, “Endoscopic navigation in the absence of CT imaging,” *submitted to MICCAI* (2018)
4. X. Liu, A. Sinha, M. Ishii, G. D. Hager, R. H. Taylor, A. Reiter, “Depth Map Estimation from Endoscopic Video using Deep Network,” *submitted to MICCAI* (2018)



## Chapter 8

# Clinical applications of statistical shape models of sinuses and surrounding structures

Statistical shape models (SSMs) are extremely powerful tools and their advantages are not limited to interventional clinical applications. SSMs can be used for a variety of different applications in the study and understanding of anatomy prior to interventions to inform whether or what kind of interventions will prove useful, and also post interventions to understand what kinds of modifications best treat different symptoms. In order to diagnose an abnormality to inform what kind of intervention is required, there needs to be a strong understanding of what is normal. Such diagnoses can be performed subjectively by the surgeon. However, this can mean that diagnoses

## CHAPTER 8. CLINICAL APPLICATIONS

may differ between different clinicians. Further, in order to determine the distance of patient anatomy from normal anatomy by looking at endoscopic video data may require experience and expertise. Another way to perform diagnoses is quantitatively. Such diagnoses are objective and, therefore, if done accurately, can become a valuable tool for clinicians.

As mentioned earlier, in order to provide quantitative feedback on the deviation of patient anatomy from normal, the scope of normal anatomy must be studied. Few studies have explored how normal anatomy in population varies. Weiglein et al.<sup>122</sup> conducted a fairly large study of 134 dried human skulls, ranging from newborn to 12 years of age. The length, width, and height for each of the sinuses (maxillary, ethmoidal, frontal, and sphenoid) were measured directly from the skulls. Spaeth et al.<sup>7</sup> performed a very large scale study using 5641 low resolution CT scans of male and female subjects whose ages spanned from birth to 25 years. The ventrodiscal length and mediolateral width were measured for each of the sinuses using a compass. Barghouth et al.<sup>123</sup> also performed a fairly large scale study using 179 head MRI scans to evaluate the variation in the maxillary, sphenoid, and frontal sinuses. The population studied consisted of children under the age of 17 years. The statistics learned from Weiglein et al.<sup>122</sup> and Barghouth et al.<sup>123</sup> may not fully explain the variance in adults since the age of the sampled population in these two studies is below 17 years, while sinuses continue to develop until about age 20. Although the age of the population studied by Spaeth et al.<sup>7</sup> goes up to 25, the method of manually collecting

## CHAPTER 8. CLINICAL APPLICATIONS

statistics employed is hard to scale and can introduce significant errors between the first and last sets of CT scans measured. Further, only 2 or 3 discrete measurements are likely not be enough dimensionality to fully explain the variance in the sinuses. More recent studies, like Emirzeoglu et al.,<sup>124</sup> evaluate the volume of sinuses. This study uses CT scans from 77 adult patients. However, the procedure employed by this study to compute the volume of the sinuses is not scalable either since it involves printing CT image slices on films and superimposing point-counting grids to count the number of points making contact with the sinuses.

Similarly, few studies have extensively studied the nasal cavity or structure within the nasal airway. For instance, the nasal conchae or turbinates that reside within the nasal airway are known to undergo periodic alternating expansion and contraction. This phenomenon, called the nasal cycle, has been studied via rhinoresistometry, or the measurement of change in airflow resistance between the left and right sides of the nasal airway.<sup>6</sup> These findings have more recently been confirmed using endoscopy as well as acoustic rhinometry, where the geometry of the nasal cavity is estimated based on reflected sound waves.<sup>125</sup> Although these methods show that a difference in resistance occurs and changes sides at least once during a 7 hour period, it is not able to quantify the amount of expansion and contraction in the turbinates that cause the resistance. These and other methods have also been employed in the measurement of nasal patency.<sup>30</sup> Similar methods,<sup>31</sup> along with methods involving volumetric scans like those used in the measurement of sinuses,<sup>32</sup> have also been used to measure

## CHAPTER 8. CLINICAL APPLICATIONS

particular landmarks in the nasal airway, like the piriform aperture. These methods, however, either require patient interaction or manual measurements, and can be hard to scale.

The methods presented in Chapters 2, 4, 5, 6, and 7 can be used to automatically compute statistics explaining the variation in different structures over a large population as well as to estimate patient specific statistics. For initial proof of concept, a relatively small set of publicly available CT scans was used to conduct experiments. However, due to the automated nature of the methods used, these statistics can easily be recomputed using larger datasets.

### 8.1 Experimental results and discussion

The studies described below are performed on the publicly available dataset containing 53 patient head CT scans that is described in Chapter 2. The automatic segmentation of relevant structures in these CT images is also described in Chapter 2. The studies described in this chapter use these automatically segmented shapes in order to establish statistics on the variance present in a sample of *normal* population, that is, population without sinus disease or other nasal anomalies. Statistics are established using PCA on the segmented shapes as described in Chapter 2.

### 8.1.1 Variation in population

As mentioned before, a clear understanding of the nasal airway and sinuses in a normal population is critical in understanding deviations from normal. In order to achieve this understanding, SSMs of different structures were built and variations along different modes or principal axes were observed. These structures include the maxillary sinuses, relatively simple structures within the nasal passage like the nasal conchae or turbinates, as well as the full complex nasal passage along with the structures within.

Sinuses are formed due to the pneumatization of bones, or formation of cavities within bones, that occurs over several years until about the age of 20. The maxillary sinuses are perhaps the simplest sinuses to automatically and reliably segment because they are formed by the pneumatization of the maxilla or the upper jawbone and do not interact with the septum. This is a key difference between the maxillary sinuses and the remaining sinuses, frontal, ethmoidal, and sphenoid. This interaction with the septum in the frontal, ethmoidal, and sphenoid sinuses complicates the pneumatization since the septum often deviates from the middle of the nasal cavity. If the deviation is large, it may not be captured during deformable registration between CT images causing errors in automatic segmentation. The ethmoid sinuses are by far the most complicated sinuses because the pneumatization process is pseudostochastic leading to the formation of several chambers in the ethmoid bone compared to the two chambers on either side of the septum present in the other sinuses.

## CHAPTER 8. CLINICAL APPLICATIONS

The variation present in the right maxillary sinuses of the population studied is shown in Figures 8.1 and 8.2, while that in the left is shown in Figures 8.3 and 8.4. The primary mode for both right and left maxillary sinuses shows variation along the axial and coronal directions, while the second mode shows variation along the sagittal or lateral direction. The third and fourth modes show enlargement of the posterior section of the maxillary sinuses relative to the anterior section and the enlargement of the anterior section relative to the posterior, respectively. This fifth shows that there is an interdependent growing and shrinking between the medial and lateral sections of the maxillary sinuses.

Next, the variation present in the nasal conchae or the nasal turbinates are studied. There are three pairs of nasal turbinates, the inferior, middle, and superior turbinates, that are present in the nasal cavity. These structures are important for various reasons, but perhaps the most important reason comes from the fact that these structures contain erectile tissue which allows them to exhibit a periodic alternating shrinking and growing behavior known as the nasal cycle. Understanding the nasal cycle is important for surgical navigation because patients obtain head CT scans and undergo procedures at different times resulting in a change in the turbinate structure. Further, patients are generally administered decongestants before any tools are inserted into the nasal cavity. Therefore, the appearance of the turbinates in an endoscopic video is almost guaranteed to be different from that in a previously acquired CT scan. Knowledge of how turbinates change, the range of normal variation,

## CHAPTER 8. CLINICAL APPLICATIONS

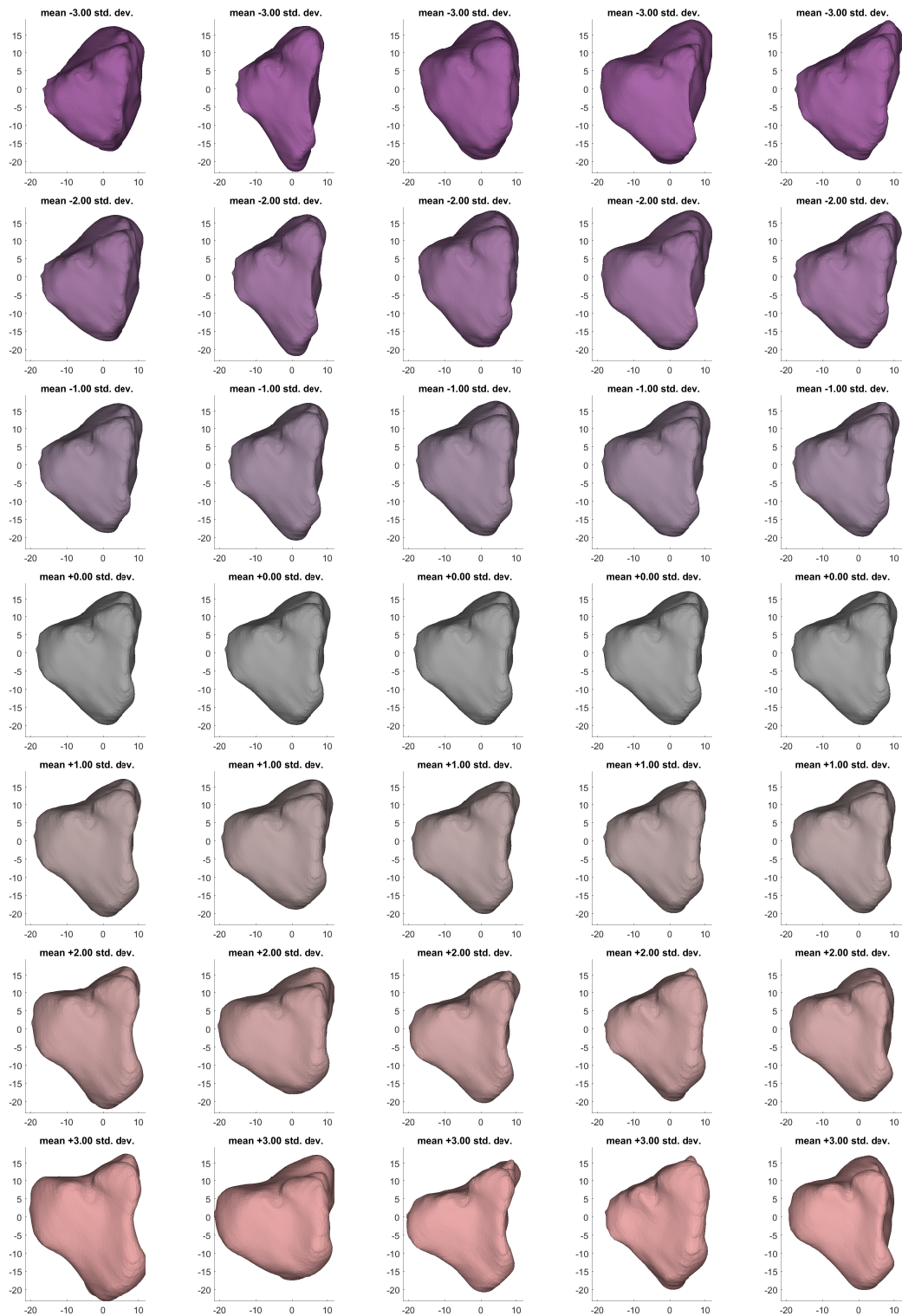


**Figure 8.1:** Front view of the right maxillary sinus: (L-R) Modes 1 to 5 with variance ranging from  $-3$  (top) to  $3$  (bottom) SDs.

## CHAPTER 8. CLINICAL APPLICATIONS

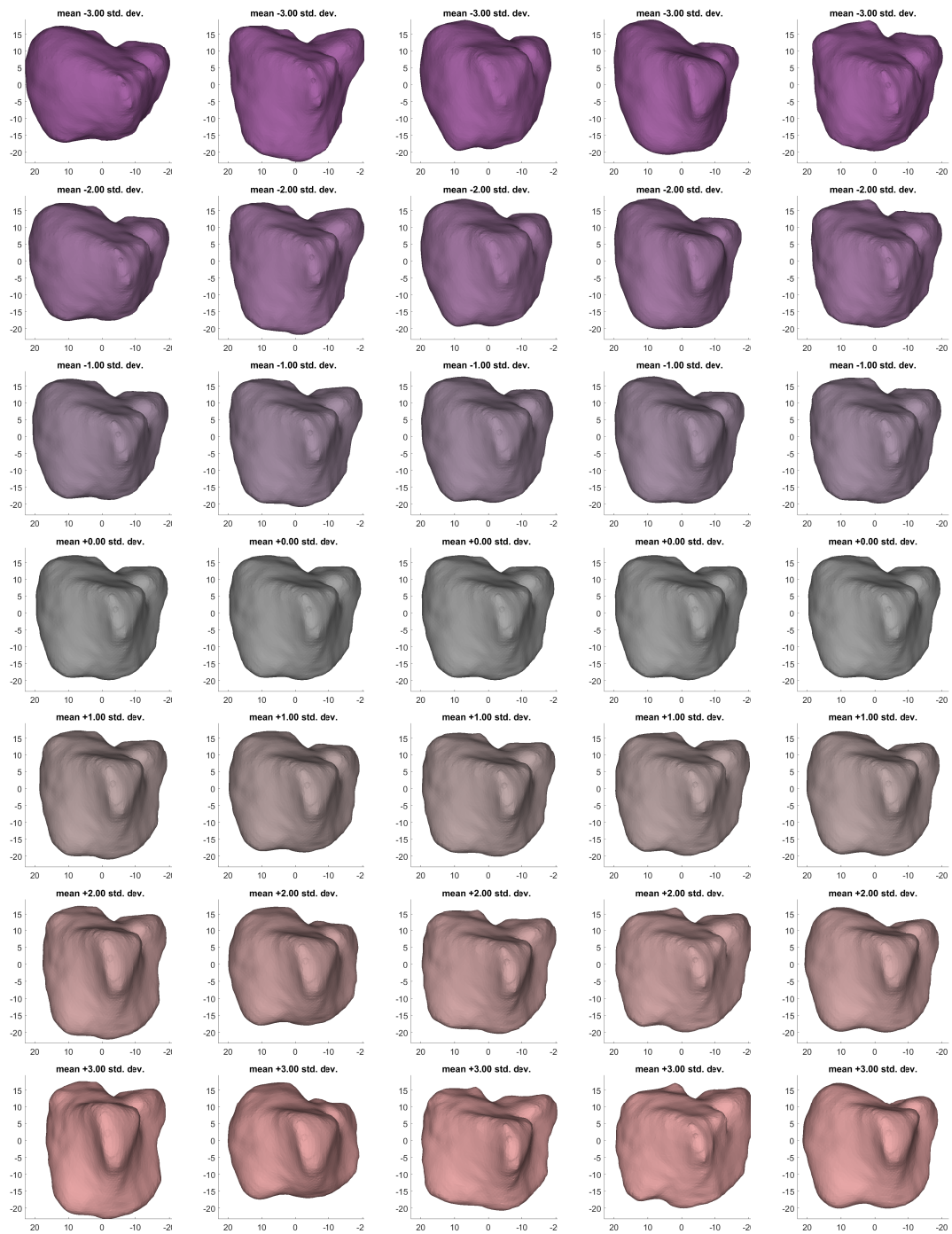


**Figure 8.2:** Right view of the right maxillary sinus: (L-R) Modes 1 to 5 with variance ranging from  $-3$  (top) to  $3$  (bottom) SDs.



## CHAPTER 8. CLINICAL APPLICATIONS



**Figure 8.3:** Front view of the left maxillary sinus: (L-R) Modes 1 to 5 with variance ranging from  $-3$  (top) to  $3$  (bottom) SDs.

## CHAPTER 8. CLINICAL APPLICATIONS

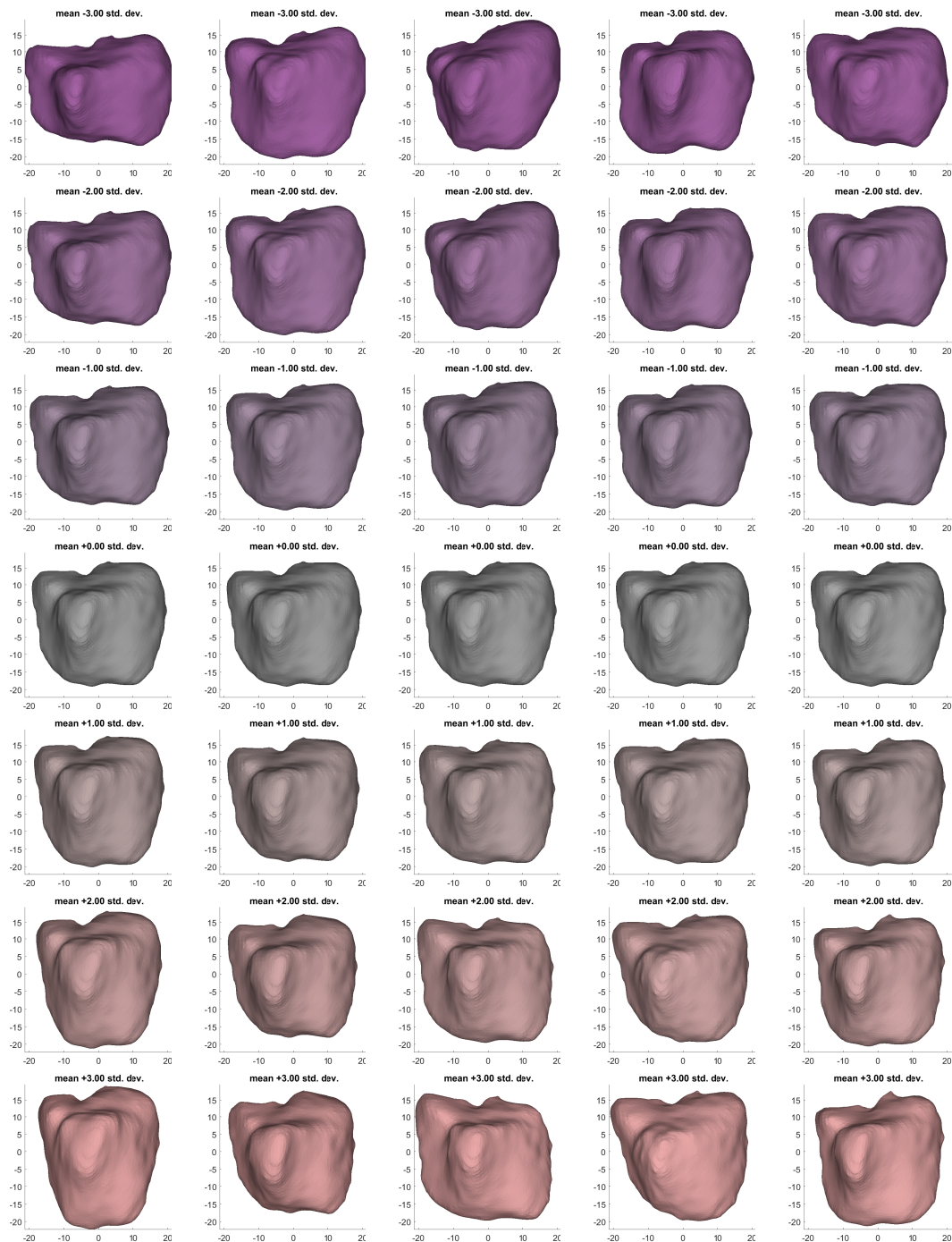


**Figure 8.4:** Left view of the left maxillary sinus: (L-R) Modes 1 to 5 with variance ranging from  $-3$  (top) to  $3$  (bottom) SDs.

## CHAPTER 8. CLINICAL APPLICATIONS

and the phase of the turbinates in the CT scan can enable navigation systems to make up for the change in the structure between CT image acquisition and medical intervention. Another reason to understand the normal amount of variation present in the nasal turbinates is because the size of the turbinates is considered to be related to the amount of nasal obstruction. An understanding of normal variation will allow clinicians to quantify the amount of deviation from normal in patients with nasal obstruction, and how much turbinate reduction could optimally improve airway resistance.

The variation observed in the inferior turbinates is shown in Figures 8.5 and 8.6, and that in the middle turbinates is shown in Figures 8.7 and 8.8. The primary mode for both the inferior and middle turbinates shows variation along the lateral direction with slight stretching along the coronal direction. The second mode shows variation along the axial direction, depicting a change in the height of the turbinates. Past the second mode, the variation observed in the inferior and middle turbinates changes slightly. For the inferior turbinates, the third mode shows an alternating variation between the left and right turbinates along the lateral direction. This variation appears to show the turbinates swelling and contracting, as in the nasal cycle. A more thorough study of the nasal cycle is described in the next section (Sec. 8.1.2). The fourth mode also shows swelling and contraction in the lateral direction, but these are more focused in the middle section of the turbinates and involve less lateral movement. The fifth mode shows slight variation in both the axial and coronal direction,

## CHAPTER 8. CLINICAL APPLICATIONS

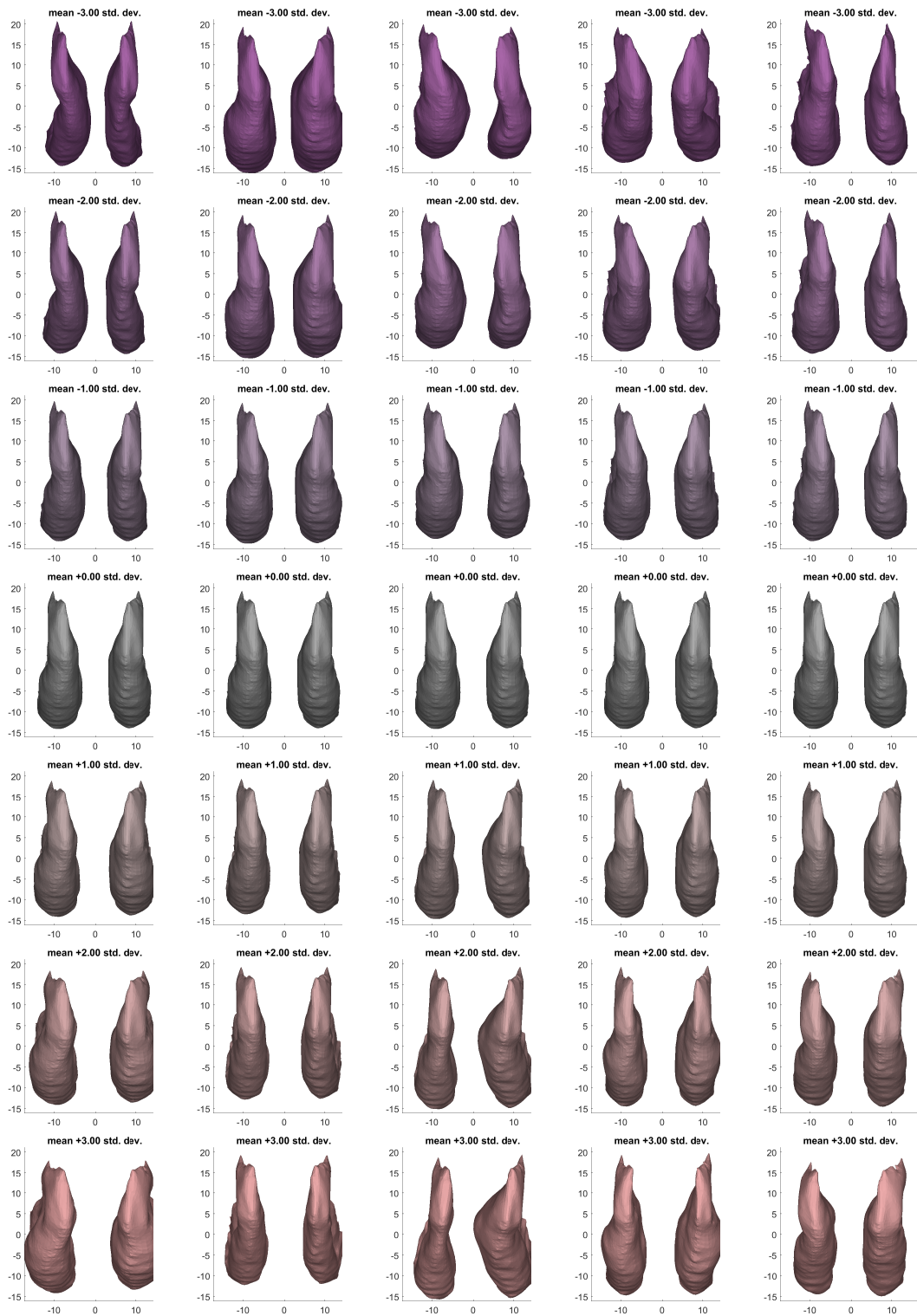


**Figure 8.5:** Front view of the inferior turbinates: (L-R) Modes 1 to 5 with variance ranging from  $-3$  (top) to  $3$  (bottom) SDs.

## CHAPTER 8. CLINICAL APPLICATIONS

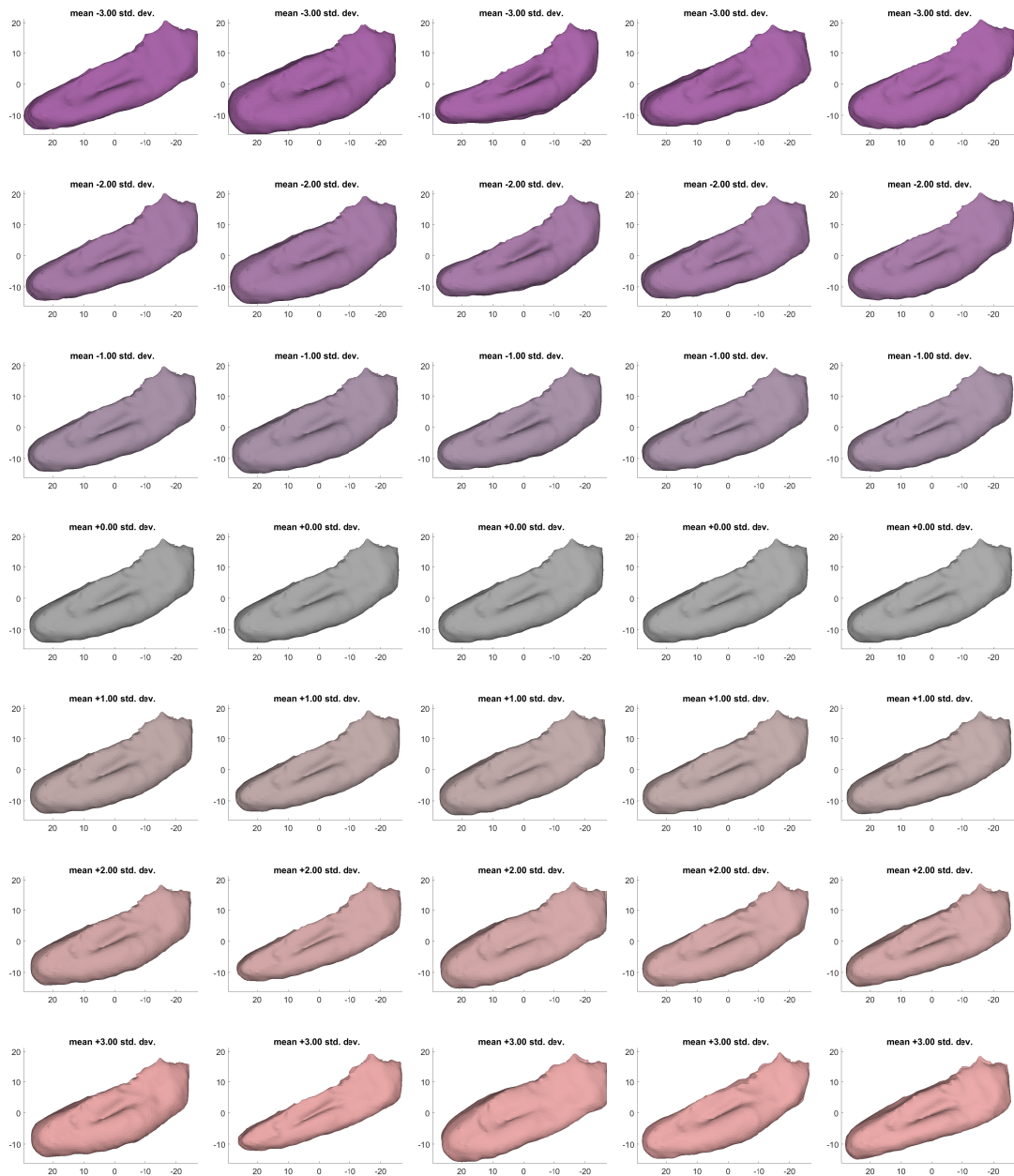


**Figure 8.6:** Right view of the inferior turbinates: (L-R) Modes 1 to 5 with variance ranging from  $-3$  (top) to  $3$  (bottom) SDs.

## CHAPTER 8. CLINICAL APPLICATIONS

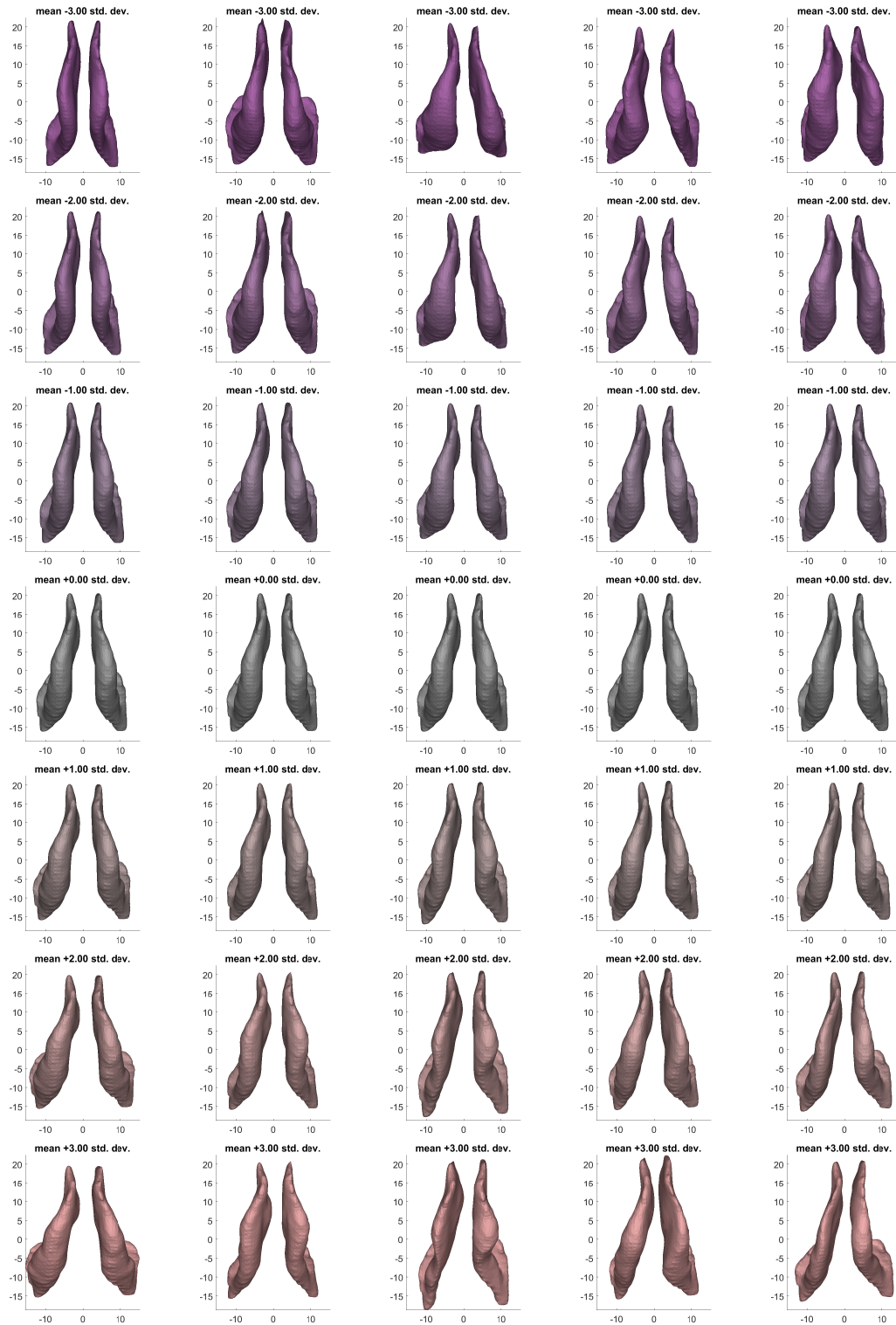


**Figure 8.7:** Front view of the middle turbinates: (L-R) Modes 1 to 5 with variance ranging from  $-3$  (top) to  $3$  (bottom) SDs.

## CHAPTER 8. CLINICAL APPLICATIONS



**Figure 8.8:** Right view of the middle turbinates: (L-R) Modes 1 to 5 with variance ranging from  $-3$  (top) to  $3$  (bottom) SDs.

## CHAPTER 8. CLINICAL APPLICATIONS

with some lateral variation in the rightside section of the turbinates, which perhaps depicts the variation in how the turbinates are connected to the lateral wall. For the middle turbinate, on the other hand, the third mode depicts swelling and contraction in the middle section with alternating lateral movement between the left and right turbinates, while the fourth mode shows alternating swelling and contraction between the left and right turbinates with the variation more focused toward the posterior section of the turbinates. The fifth mode shows swelling and contraction toward the anterior section of the turbinates with some amount of alternating lateral movement between the left and right turbinates.

The final structure studied are the nasal passages. This includes the boundaries surrounding the right and left nasal passages, such as the septum and floor and roof of the nasal cavity, as well as the structures contained within the nasal passages. Understanding the variation in the nasal cavity is important for some of the same reasons as the turbinates. Nasal airway patency is shown to be correlated to nasal obstruction.<sup>126</sup> Further, understanding the normal range of septal deviations can help clinicians quantify the amount of deviation from the normal range in patients with septal deviation related disorders. The variations observed in the right nasal passage are shown in Figures 8.9 and 8.10, while those in the left nasal passage are shown in Figures 8.11 and 8.12. The first mode for both the right and left nasal passages depicts variation in the form of stretching along the coronal direction. The second and third modes show variation resembling septal deviation, with the second mode



## CHAPTER 8. CLINICAL APPLICATIONS



**Figure 8.9:** Front view of the right nasal airway: (L-R) Modes 1 to 5 with variance ranging from  $-3$  (top) to  $3$  (bottom) SDs.

## CHAPTER 8. CLINICAL APPLICATIONS



**Figure 8.10:** Right view of the right nasal airway: (L-R) Modes 1 to 5 with variance ranging from  $-3$  (top) to  $3$  (bottom) SDs.

## CHAPTER 8. CLINICAL APPLICATIONS

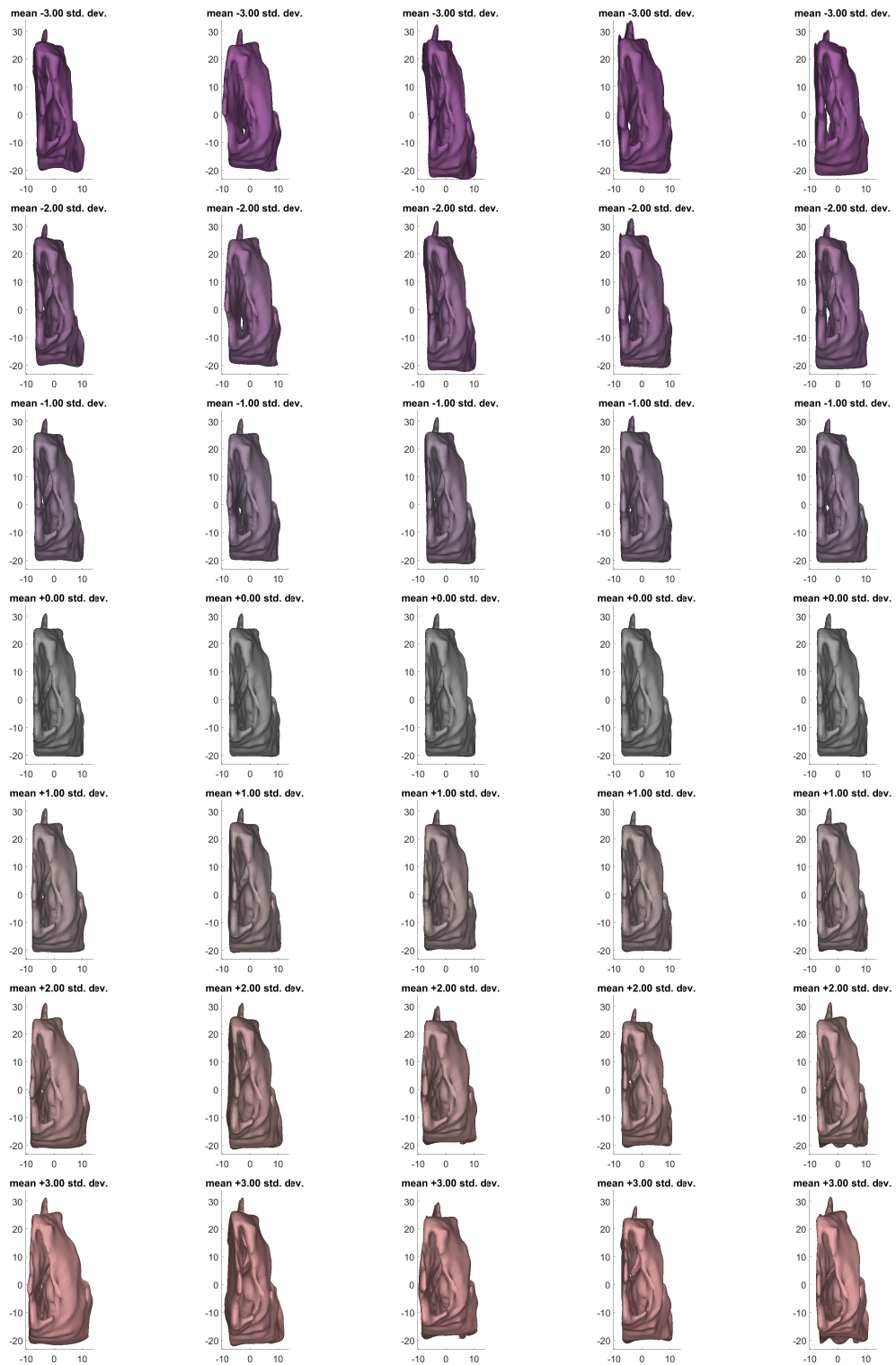


**Figure 8.11:** Front view of the left nasal airway: (L-R) Modes 1 to 5 with variance ranging from  $-3$  (top) to  $3$  (bottom) SDs.

## CHAPTER 8. CLINICAL APPLICATIONS

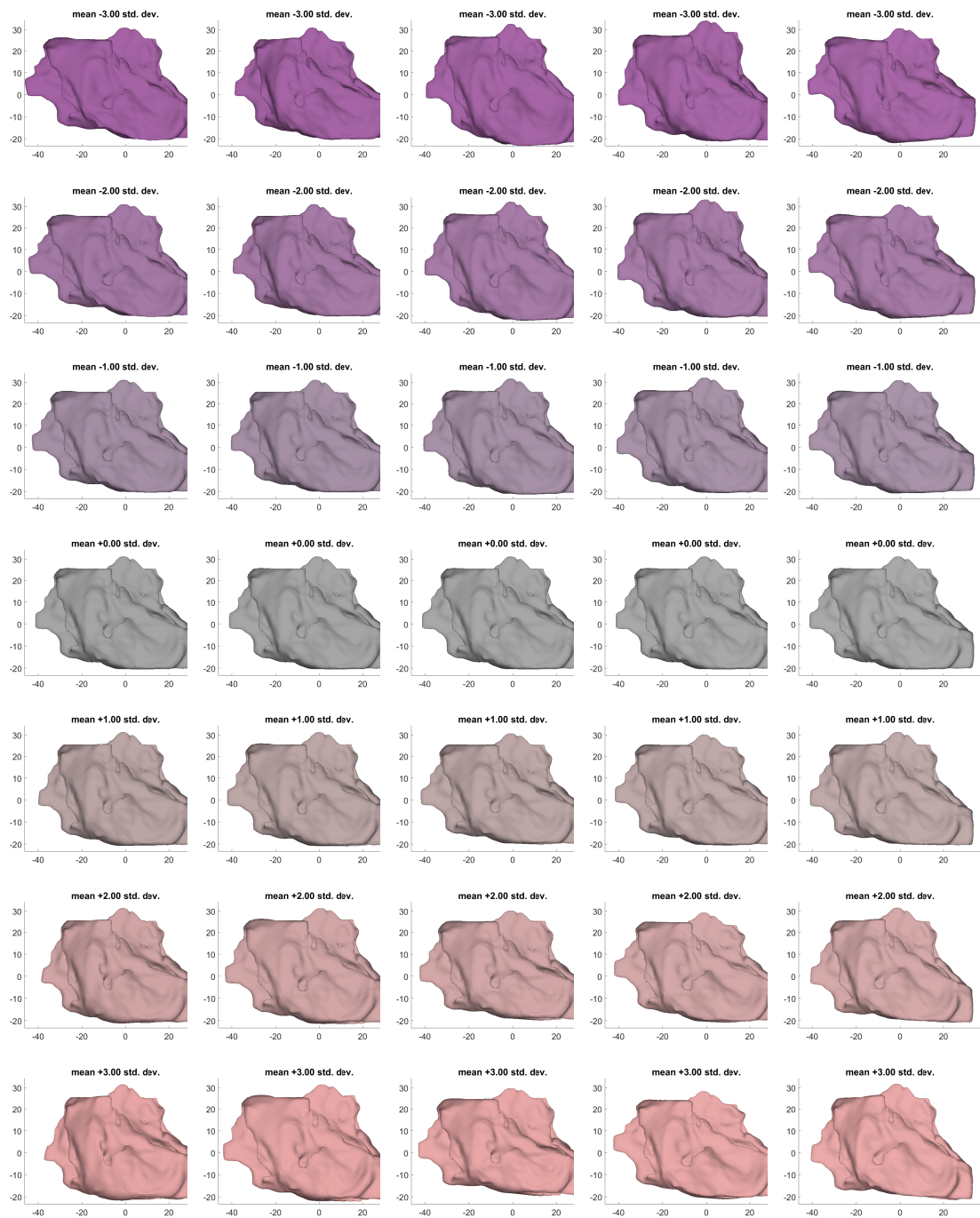


**Figure 8.12:** Left view of the left nasal airway: (L-R) Modes 1 to 5 with variance ranging from  $-3$  (top) to  $3$  (bottom) SDs.

## CHAPTER 8. CLINICAL APPLICATIONS

showing the septal wall deforming closer to the floor of the nasal cavity, while the third mode showing septal deviation in the middle of the septal wall. The fourth mode shows variation along the axial direction, while the fifth mode, again, shows variation in the septal wall towards the posterior part of the nasal cavity.

### 8.1.2 Nasal cycle

Having shown that SSMs provide valuable information about the range of variation present in anatomical structures, the next objective is to determine whether these SSMs built from population data are able to capture the nasal cycle in individuals without requiring a longitudinal study. Since the nasal cycle is a continuous process taking place in each individual, it can be assumed that each image in the public CT image dataset contains turbinates at different phases of the nasal cycle. Therefore, it can be hypothesized that while most of the variation captured by the SSM must reflect anatomical differences between individuals of different shapes and sizes as well as anatomical differences between different turbinates, at least some of the variation captured must reflect the nasal cycle. In order to evaluate this hypothesis, the skull and inferior turbinates of an adult patient are automatically segmented in 2 CT images, preoperative and postoperative, using the methods described in Chapter 2. Both shapes were projected onto the respective SSMs (Eq. 2.2) in order to observe the SSM estimate (Eq. 2.1) of the patient's skull and inferior turbinates.

The pre- and postoperative skulls produce similar mode weights and, consequently,

## CHAPTER 8. CLINICAL APPLICATIONS

similar shapes, which is the expected outcome for the two skull segmentations since the skull of an adult is not expected to change (Fig. 8.13). The minor differences in the mode weights likely resulted from small segmentation errors. However, the pre- and postoperative inferior turbinates exhibited a large difference in the mode weights produced and, therefore, also in the estimated shapes (Fig. 8.14). This result is also expected since it can be assumed that the inferior turbinates of the patient studied were at different phases of the nasal cycle in the 2 CT images. Therefore, it can be concluded that at least some of the variance captured by SSMs of the turbinates can be attributed to the nasal cycle. However, a more thorough study with a larger number of patients who have at least 2 head CT scans will be required to confirm exactly which mode or modes capture the nasal cycle.

### 8.1.3 Shape inference

Results from Chapter 2 as well as from Sec. 8.1.2 show that SSMs are able to accurately estimate shapes segmented from CT scans when these shapes are in correspondence with the shapes used to build the SSM. Further, results from Chapters 4, 5 and 6 show that SSMs are able to estimate shapes even in the absence of correspondences. Features sampled uniformly from shapes and deformably registered using the registration algorithms presented in these chapters result in accurate reconstructions of the shapes that points were sampled from. Finally, in Chapter 7, results show that SSMs are able to estimate shapes even in the absence of CT scans using

## CHAPTER 8. CLINICAL APPLICATIONS

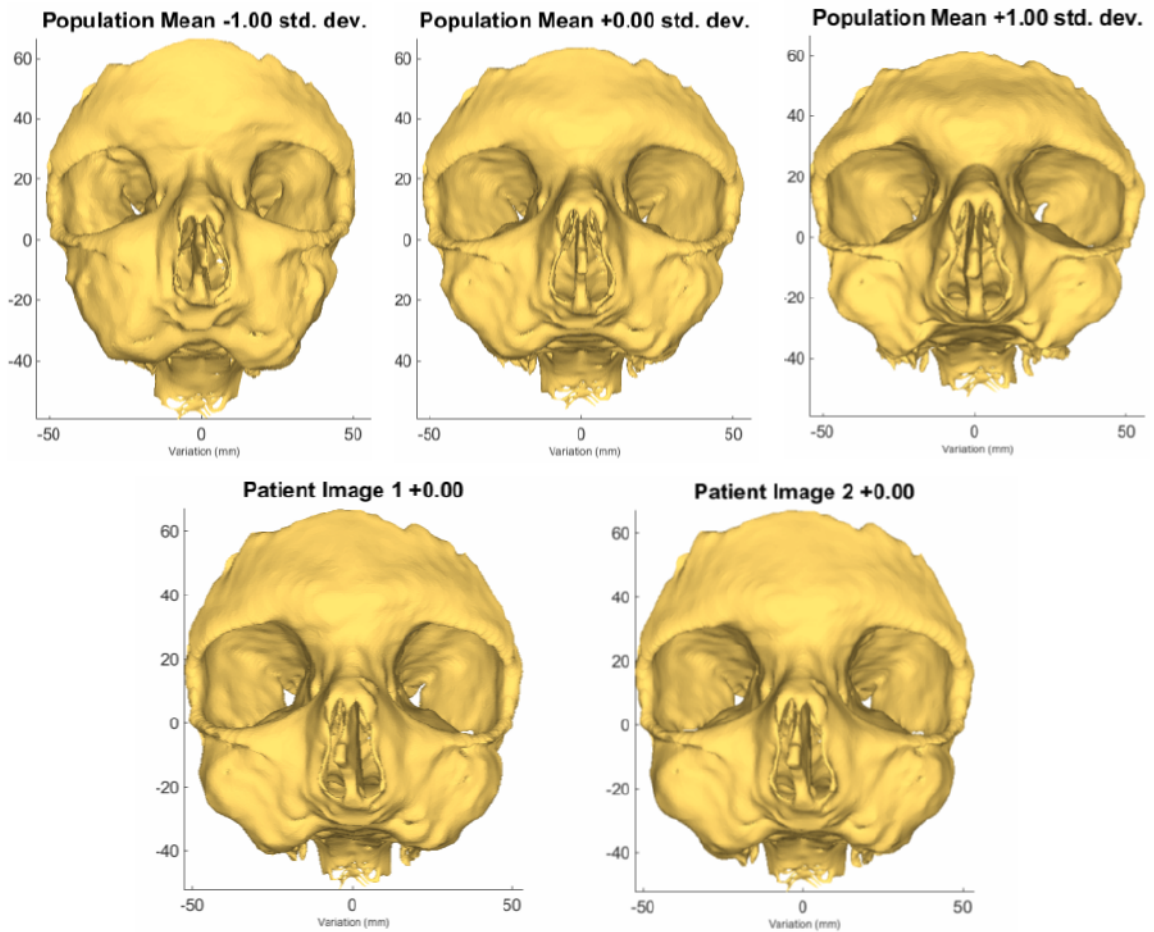


**Figure 8.13:** Top: Population variation in the skull model. The middle shape is the mean shape, the left shape shows mean shape with  $-1\sigma$ , where  $\sigma$  is the standard deviation, and the right shape is the mean shape with  $+1\sigma$ . Bottom: The left image shows the pre-op patient skull, and the right image shows the post-op patient skull. The two images show no, or negligible, difference, where minute difference can sometimes be observed due to errors in registration. However, we can see that the population variation is not reflected in the two patient images.

## CHAPTER 8. CLINICAL APPLICATIONS

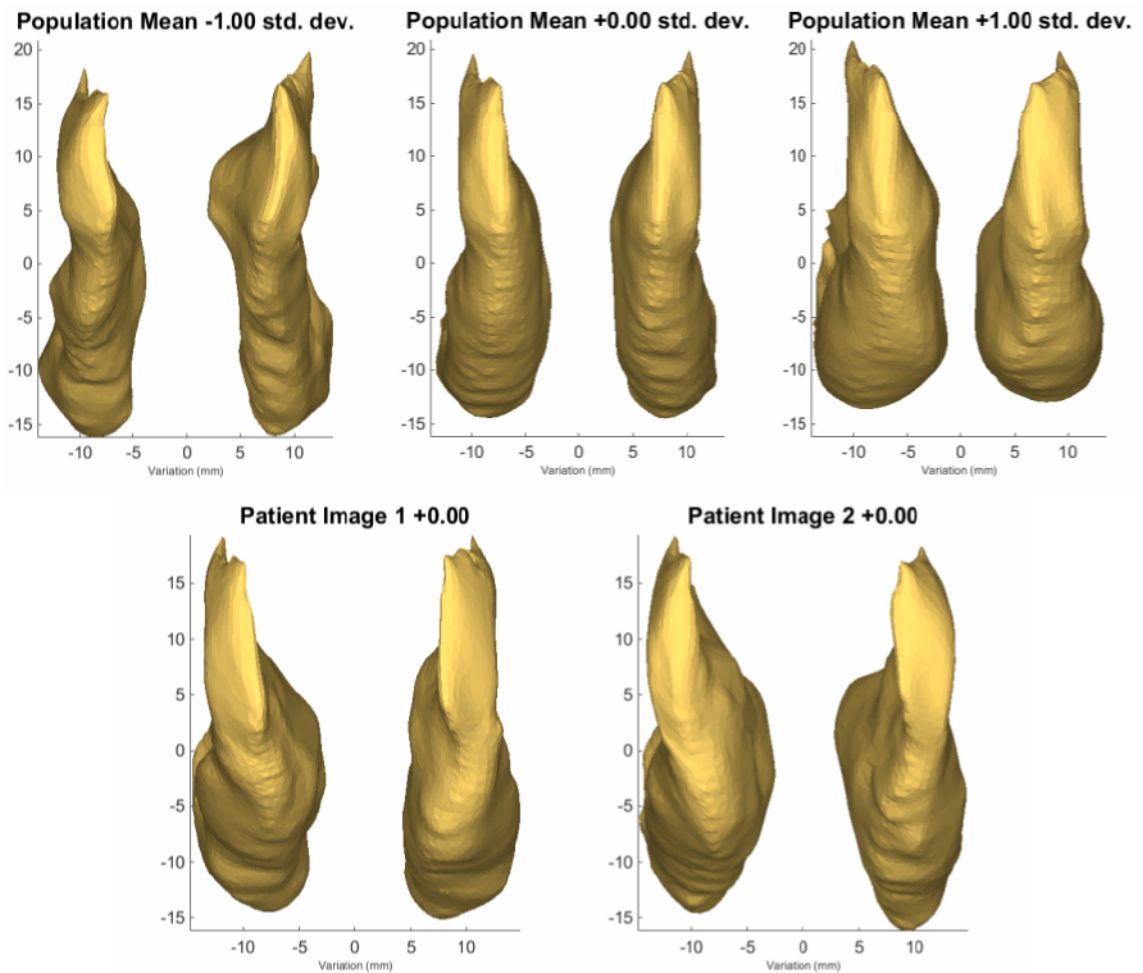


**Figure 8.14:** Top: Population variation in the inferior turbinate (IT) model. The middle shape is the mean shape, the left shape shows mean shape with  $-1\sigma$ , and the right shape is the mean shape with  $+1\sigma$ . Bottom: The left image shows the pre-op patient IT, and the right image shows the post-op patient IT. The two images show significant differences, allowing us to conclude that the population variation is reflected in the patient images.



## CHAPTER 8. CLINICAL APPLICATIONS

features extracted from different modalities, like video. This result is extremely valuable because it enables quantitative measurements in the nasal cavity directly from endoscopic video, without requiring CT scans.

As mentioned earlier in the chapter, little work has been done towards achieving accurate measurements of the nasal cavity. Prior work reported straight line estimates of distances between landmarks in order to compute approximate cross-sectional areas in CT images, or used acoustic rhinometry to estimate the volume of different parts of the nasal cavity when CT images were not available. However, these estimates are not accurate since straight lines are gross simplifications of the complex geometry of the nasal cavity and acoustic rhinometry measures are affected by the sinuses. The downsides of such estimations have caused considerable uncertainty in diagnosing and predicting successful surgical outcomes for problems like nasal obstruction. Accurate estimates can help mitigate these uncertainties. Directly estimating the shape of the nasal cavity from endoscopic video using deformable registration has several advantages. First, a CT scan of the patient is not required which prevents exposure to ionizing radiation. Second, patient segmentations produced are in correspondence with the statistically mean shape. Therefore, landmarks only need to be chosen once on the mean shape and are transferred to patient shapes via registration. This property can be used to define 3 non-collinear points or landmarks on the mean shape that define a roughly coronal plane in each region where the cross-sectional area must be computed (Fig. 8.15, top). These points should describe corresponding landmarks in

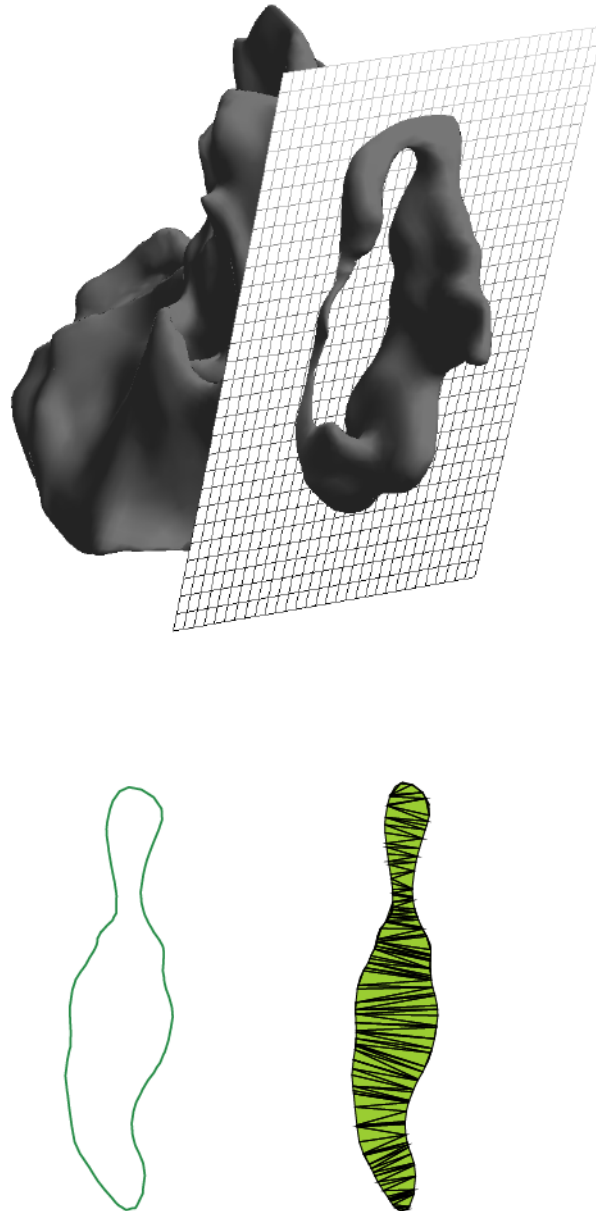


**Figure 8.15:** Intersection (top) between a plane and a mesh, shown here at the external nasal valve, produces contours which enable the computation of the cross-sectional area within the contours (bottom).

## CHAPTER 8. CLINICAL APPLICATIONS

the deformed patient shapes after registration. An intersection between the shape and the corresponding plane produces contours of the shape along that plane (Fig. 8.15, bottom). The contours for each shape can be triangulated and the area can be accurately computed (Fig. 8.15, bottom). These accurate measurements can enable better understanding of nasal patency and, perhaps, will allow better correlation between patency and disease or predicted outcome.

In order to evaluate how well information like cross-sectional area can be inferred from estimated shapes, results from Experiment 6.5.8.2 on simulated data were used. As a reminder, registration in these experiments are computed using the algorithms described in previous chapters in a leave-one-out setting, where the left-out shape is estimated based only on points sampled from the airway section of the left-out shape. Results from this experiment showed that shape estimation errors are lowest in the regions where sampled points were available, while errors increase away from these regions. It is important to understand how these errors affect shape inference both within and away from the regions where features were available. For all the left-out and estimated shapes, the cross-sectional area of the internal and external nasal valves is computed and compared to evaluate how well this area is estimated by the deformable algorithms. The nasal valve is the sight of the highest nasal resistance, and the internal and external nasal valves are the first few landmarks encountered when entering the nose.

### 8.1.3.1 Internal nasal valve

The internal nasal valve is evaluated first since it lies in the region where data points were sampled from in Exp. 6.5.8.2. Therefore, this evaluation is expected to produce reliable results. In order to evaluate the cross-sectional area at the internal nasal valve, three landmarks were selected on the mean right nostril mesh that define a plane intersecting through the mean mesh at the internal nasal valve. Since all left-out shapes and estimated left-out shapes are in correspondence with the mean shape, the same landmarks can be used to define planes intersecting through each of the left-out and estimated left-out shapes. This intersection produces contours where the plane intersects the mesh, and the area within the contours can be computed producing the cross-sectional area at the internal nasal valve for each left-out shape as well as for each of the estimated left-out shapes. Errors between the cross-sectional areas computed for the left-out shapes and those for the estimated shapes are compared to evaluate how accurately the internal nasal valve can be estimated by GD-IMLOP.

The mean cross-sectional area at the internal nasal valve over all left-out meshes was  $116.44 (\pm 24.22) \text{ mm}^2$ , which is comparable to the normal range of cross-sectional area near the internal nasal valve estimated via acoustic rhinometry.<sup>127</sup> The mean and median relative errors in cross-sectional area estimation are shown in Fig. 8.16 and Table 8.1. The errors show a clear trend downward as the number of modes used for shapes estimation increases, with shape estimation using 50 modes producing the lowest relative errors. However, even the lowest mean error is as high as 15.4%. One

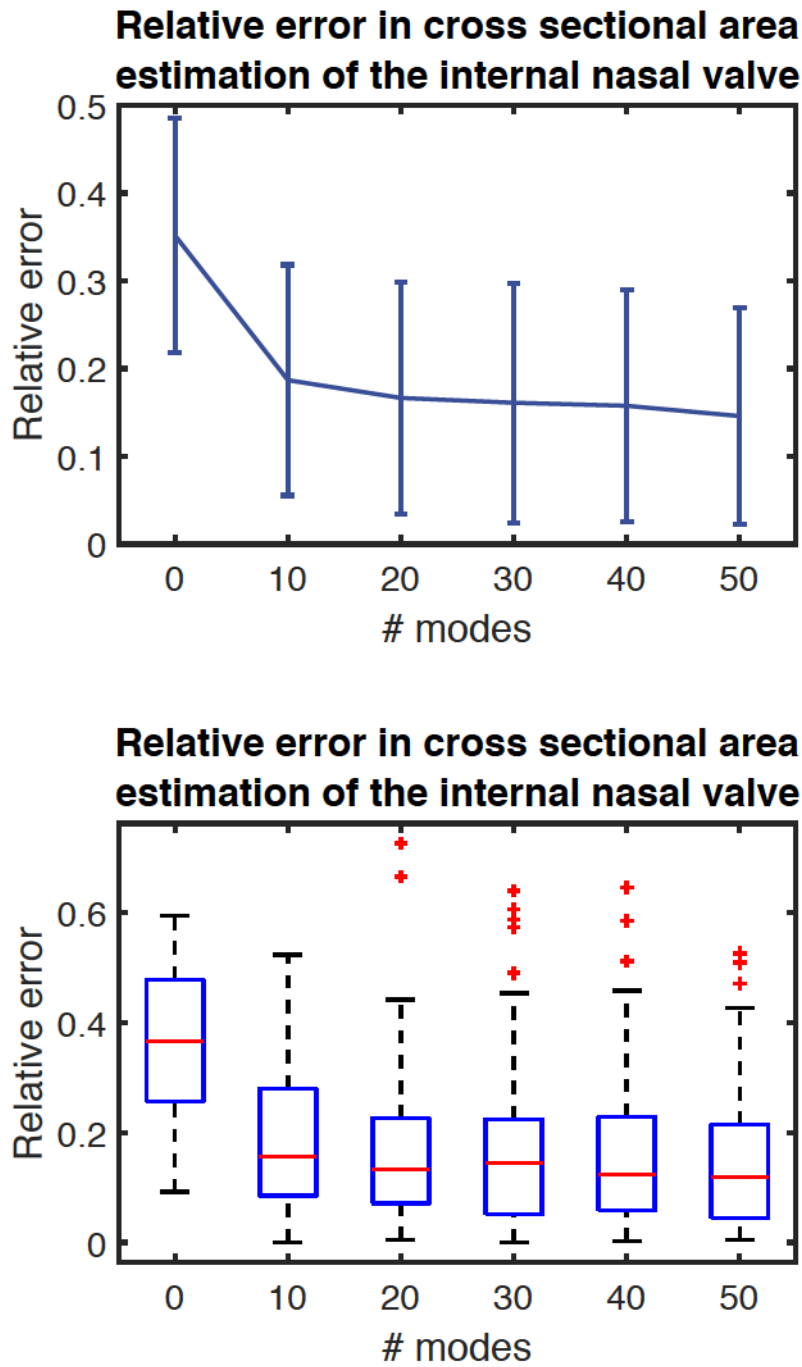


**Figure 8.16:** Top: Mean relative error and standard deviation in cross-sectional area estimation of the internal nasal valve. Bottom: Median relative error along with the 25th and 75th percentile errors (box) and min and max errors (bars) excluding outliers, which are marked with + signs.

## CHAPTER 8. CLINICAL APPLICATIONS

**Table 8.1:** Percent errors in cross-sectional area estimation of the internal nasal valve.

# modes	Mean relative error ( $\pm$ SD)	Median relative error
0	0.352 ( $\pm$ 0.134)	0.366
10	0.183 ( $\pm$ 0.140)	0.133
20	0.165 ( $\pm$ 0.138)	0.127
30	0.165 ( $\pm$ 0.138)	0.145
40	0.167 ( $\pm$ 0.142)	0.127
50	0.154 ( $\pm$ 0.134)	0.126

reason for this observation could be that the number of data points sampled from the target region were not sufficient. Experiments using a larger number of data samples can be used to evaluate whether the internal nasal valve can be better estimated.

### 8.1.3.2 External nasal valve

Unlike the internal nasal valve, the external nasal valve is situated at the periphery of the region where data points were sampled from for the registration experiment. This enables an evaluation of how well can information be inferred in areas that are not *seen*, in the context of endoscopy. The cross-sectional area at the external nasal valve for each mesh is computed using the same technique explained in Sec. 8.1.3.1. Errors between the cross-sectional areas of left-out shapes and of estimated shapes

## CHAPTER 8. CLINICAL APPLICATIONS

using increasing number of modes are computed to evaluate how well information at the external nasal valve can be inferred by GD-IMLOP.

The mean cross-sectional area at the external nasal valve over all the left out meshes was  $119.01 (\pm 20.92) \text{ mm}^2$ , which is comparable to the normal range of cross-sectional area near the external nasal valve estimated via acoustic rhinometry.<sup>127</sup> The mean and median relative errors in cross-sectional area estimation are shown in Fig. 8.17 and also in Table 8.2. Although errors in cross-sectional area estimation are lowest using 50 modes, the decrease in error from 0 modes to 50 modes is small. That is, errors when the left-out shape is not being estimated or errors between the mean and left-out shapes are lower than expected. Several factors can lead to such results. Only 52 CT scans are used to build the SSMs used in this study. It is possible that these 52 individuals do not represent the full extent of variation that could exist in the external nasal valve and, therefore, the the meshes extracted from these CTs are similar to the mean shape. Another explanation for the low errors between the mean and left out shapes could be that the automatic segmentation method was not able to capture the external nasal valve region accurately. This could result in low variance from the mean among the segmented meshes even if the CT scans do capture a fair extent of variation in the external nasal valve.

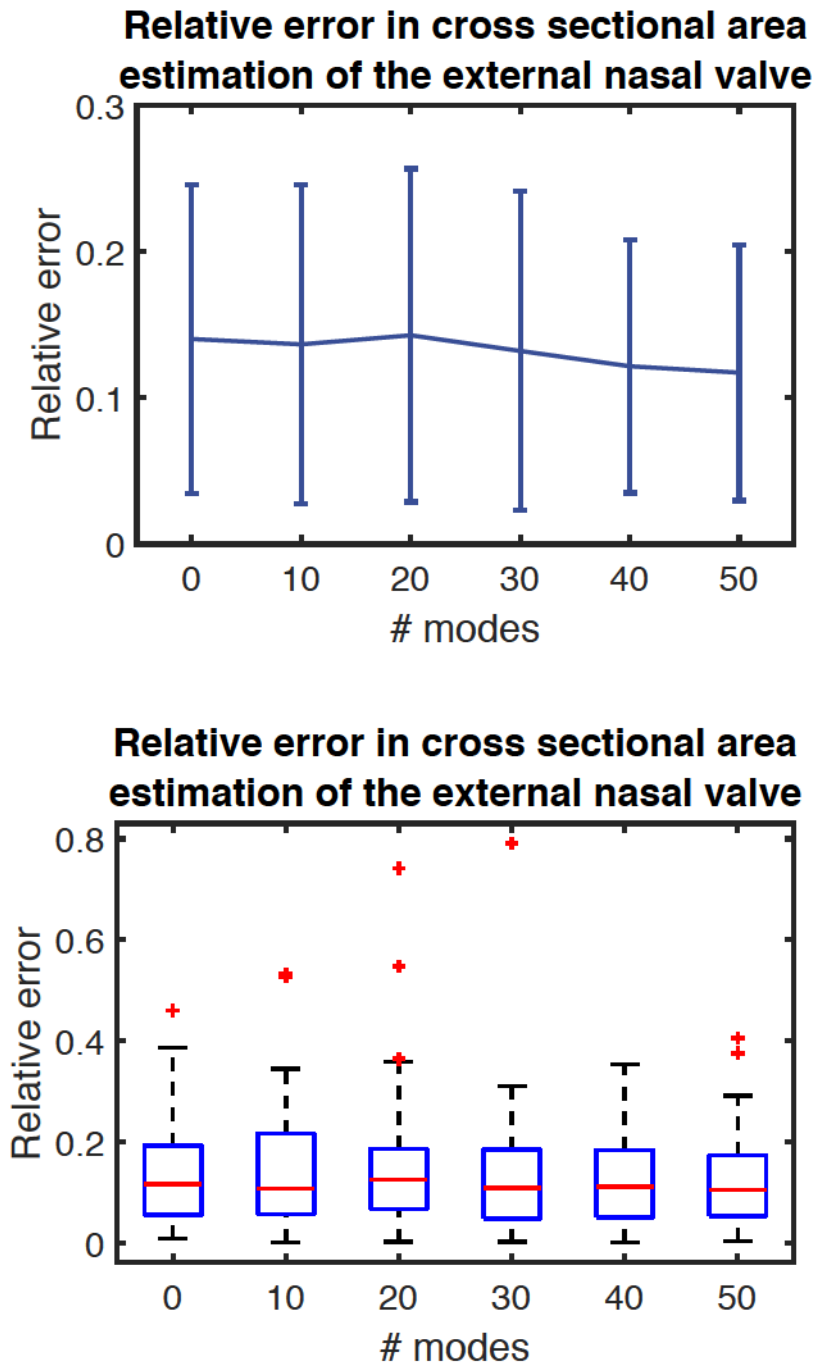


**Figure 8.17:** Top: Mean relative error and standard deviation in cross-sectional area estimation of the external nasal valve. Bottom: Median relative error along with the 25th and 75th percentile errors (box) and min and max errors (bars) excluding outliers, which are marked with + signs.



**Table 8.2:** Percent errors in cross-sectional area estimation of the external nasal valve.

# modes	Mean relative error ( $\pm$ SD)	Median relative error
0	0.155 ( $\pm$ 0.130)	0.132
10	0.143 ( $\pm$ 0.117)	0.112
20	0.193 ( $\pm$ 0.355)	0.119
30	0.157 ( $\pm$ 0.178)	0.122
40	0.149 ( $\pm$ 0.195)	0.107
50	0.121 ( $\pm$ 0.117)	0.095

## 8.2 Concluding Remarks

The application of the methods presented in this dissertation towards several clinical applications is demonstrated. SSMs of various anatomical structures enable an understanding of the types and extents of variation present in population. The variance present in the maxillary sinuses, middle and inferior turbinates, and the nasal cavity is shown. Population data can also be used show periodic variation in structures that occurs in every individual. For instance, the nasal cycle is responsible for the periodic expansion and contraction of the nasal turbinates. This periodic variation can be observed in population data. Further, the deformation registration methods presented in this dissertation use SSMs to drive the deformation and can

## CHAPTER 8. CLINICAL APPLICATIONS

be used estimate patient shape from video when CT images are not available. This enables the inference of information like cross-sectional area at different landmarks. Using more CT images to build SSMs and a larger set of data samples to estimate patient shapes can improve results further.

### 8.3 Contributions

The contributions of this chapter include:

1. Evaluation of anatomical variation in the maxillary sinuses, inferior and middle turbinates, right and left nasal cavities in a normal population<sup>75</sup>
2. Demonstration of the nasal cycle in one patient with preoperative and postoperative CT scans<sup>75</sup>
3. A method for automatic and exact measurement of the cross-sectional area at the internal and external nasal valves.

### 8.4 Published Work

Material from this chapter appeared in the following publications:

1. A. Sinha, S. Leonard, A. Reiter, M. Ishii, R. H. Taylor, G. D. Hager, “Automatic segmentation and statistical shape modeling of the paranasal sinuses to estimate

## CHAPTER 8. CLINICAL APPLICATIONS

natural variations,” Proc. SPIE 9784, Medical Imaging 2016: Image Processing, 97840D (2016)

2. A. Sinha, S. D. Billings, A. Reiter, X. Liu, M. Ishii, G. D. Hager, R. H. Taylor, “The deformable most-likely-point paradigm,” *submitted to Medical Image Analysis* (2018)

# Chapter 9

## Conclusions

The main contribution of this dissertation is the development of deformable registration algorithms that use statistical shape models (SSMs) to drive the registration in a probabilistic framework. In order to use SSMs to compute accurate registrations, the SSMs themselves must be accurate. Therefore, a novel method for simultaneous improvement of shape segmentation in images and correspondence improvement among a set of such shapes is introduced in Chapter 2. This method helps build SSMs that can estimate accurate segmentations of anatomical structures with low errors. These SSMs are incorporated into a probabilistic registration framework called the deformable most likely point paradigm, presented in Chapter 3. This framework enables registration between data samples and a statistically derived shape while simultaneously deforming the statistically derived shape using an SSM to fit the data samples. This registration framework is an iterative two phase framework, where the

## CHAPTER 9. CONCLUSIONS

first phase finds correspondences between the data samples and the current deformed shape and the second phase finds the transformation and shape parameters that transform the data samples and deform the shape to best align the correspondences. The transformation and shape parameters are computed using a gradient-based solution to the optimization problem, which is computed using an off-the-shelf nonlinear box-constrained BFGS quasi-Newton optimizer. Three algorithms were developed within this framework with different optimization problems. The first, deformable iterative most likely point (D-IMLP) algorithm, uses point position features with unconstrained or anisotropic noise and is presented in Chapter 4. The second, deformable iterative most likely oriented point (D-IMLOP) algorithm, uses orientation features with constrained or isotropic noise in addition to the position features with unconstrained noise and is presented in Chapter 5. The third, generalized deformable iterative most likely oriented point (GD-IMLOP) algorithm, uses both point position and orientation features with unconstrained noise and is presented in Chapter 6. An efficient PD-tree update routine is also implemented to accommodate the deforming model shapes in these algorithms.

These algorithms were evaluated on data simulated from several different datasets, including pelvis data, nasal cavity data, and human expression and pose data. In all experiments except those using human pose data, all three algorithms are able to accurately compute the optimal alignment between the deforming shape and data samples, with accuracy increasing from D-IMLP to D-IMLOP to GD-IMLOP. Im-

## CHAPTER 9. CONCLUSIONS

provement in results using D-IMLOP and GD-IMLOP over D-IMLP is as expected since D-IMLOP and GD-IMLOP use orientations in addition to position features and, therefore, make use of more information to compute the registration. D-IMLOP and GD-IMLOP produce comparable results when the noise in the orientation components is isotropic and both algorithms make isotropic noise assumptions. However, if the noise in the orientations is anisotropic, then GD-IMLOP outperforms D-IMLOP since GD-IMLOP is able to accurately model the anisotropic noise, whereas D-IMLOP is only able to model isotropic noise. All three algorithms show improvement with increasing number of data samples and do not show large deterioration in the presence of outliers since they all employ outlier rejection mechanisms. D-IMLP shows stability under changing noise assumptions, whereas D-IMLOP shows better performance when noise assumptions are more optimistic because the simplicity of its formulation leads to faster convergence. GD-IMLOP, on the other hand, shows improvement in performance as the noise assumptions become more pessimistic. Coherent point drift (CPD), a standard deformable registration algorithm, outperformed both D-IMLP and D-IMLOP in terms of errors, but GD-IMLOP was able to match the performance of CPD using  $\sim 20$  modes. However, in terms of runtime, D-IMLP was faster than CPD with fewer than  $\sim 35$  modes and comparable with more modes. Both D-IMLOP and GD-IMLOP were faster than CPD by about  $5\text{--}8\times$  and  $1.5\text{--}2\times$ , respectively. Further, none of the algorithms presented in this dissertation suffer from the prohibitively high memory requirements that CPD suffers from. Finally, unlike

## CHAPTER 9. CONCLUSIONS

CPD, the errors produced by the algorithms presented here are correlated with the ground truth errors, allowing these algorithms to assign success or failure labels or some amount of confidence to computed registrations based on these errors.

These algorithms are also evaluated on in-vivo clinical endoscopic video data in Chapter 7. Since ground truth is not available for this data, results were evaluated using residual errors produced and visually. On this dataset, GD-IMLOP outperformed D-IMLOP, which outperformed D-IMLP. This is expected since reconstructions from video data tend to have higher uncertainty or noise in the z-direction and, therefore, are best characterized by anisotropic noise in both position and orientation. Finally, in Chapter 8, other medical applications of SSMs and deformable registration are explored. Results show that SSMs can be used to observe how different anatomical structures vary in population as well as to understand the variation in structures that naturally deform in each individual. Further, results also show that deformable registration can be used to estimate the anatomical shape of an individual and make some inference about that shape, particularly in regions where data samples were matched because these regions are more accurately estimated.

### 9.1 Future work

The results presented in this dissertation used SSMs built from relatively small datasets, as described in Sec. 4.5. It is highly likely that these datasets do not

## CHAPTER 9. CONCLUSIONS

capture the full range of variation present in the anatomical structures and in human expression and pose. A recently acquired head CT image dataset containing roughly 5000 CT scans will be used in the future to build SSMs that are able to explain the full range of variation in different anatomical structures present in the head. Results for pose estimation reported in this dissertation show that the algorithms are not able to accurately reconstruct pose. With a larger pose dataset, the performance of these algorithms in pose estimation could show improvement. Human expression results could also be improved by using curvature based sampling techniques since most of the details are near high curvature areas like eyes and mouth. Further, principal component analysis (PCA), which assumes that samples are drawn from a multivariate Gaussian distribution, is used to build SSMs in this dissertation. It is possible that this is not an accurate assumption for some anatomical structures and, perhaps, also for human expression and pose.<sup>108</sup>

The algorithms presented in this dissertation can also be used to expand datasets of shapes with correspondences. Any new shape that is not in correspondence with the dataset can be estimated using the deformable registration algorithms to find correspondences. The estimated shape, which is in correspondence with the dataset, can then be added to the dataset and a new SSM can be built. Different methods for building SSMs can also be explored to improve results. Another experiment where the performance of the algorithms presented in this dissertation could be improved was the partial data experiment, where data points were sampled from a part of



## CHAPTER 9. CONCLUSIONS

the full mesh. This experiment simulates real in-vivo scenarios where the full nasal cavity is not visible in a video sequence or only a partial pelvic CT image is available. Although the deformable registration methods presented here are able to estimate the full shapes with lowest errors where data is available, these errors can be further reduced by stitching together the available data from the video or partial CT and the estimated mesh where data was not available using thin plate splines<sup>128</sup> as described by Grupp et al.<sup>104</sup>

The current deformable registration paradigm assumes that the mean shape is the most likely shape and, therefore, the shape parameters,  $s$ , are initialized to 0. However, during minimally invasive surgery through the nasal cavities, decongestants are administered to patients that lead to shrinking in several structures like the nasal conchae or turbinates. Therefore, in this scenario, the mean shape is no longer the most likely shape, but a decongested shape is. Therefore, for these shapes,  $s$  should be initialized according to the weights that represent a decongested shape. However, for the surrounding structures that are not affected by decongestants, the mean shape remains the most likely shape. Since different anatomical structures may vary differently, it may be a useful extension to the current method to incorporate multiple model shapes along with their respective SSMs. In this system, correspondences would be found on the combined set of model shapes, but each model shape would deform according to its own statistics. Additional measures would have to be taken in order to prevent the shapes from intersecting. Finally, additional algorithms can

## CHAPTER 9. CONCLUSIONS

be built within the deformable most likely point paradigm that can further improve registration results. For instance, the video iterative most likely oriented point (V-IMLOP) algorithm uses 3D point features (like IMLP) along with 2D oriented point features that represent occluding surface contours.<sup>55</sup> Although this method only computes a similarity transformation (rotation, translation and scale) between the data samples and model shape, it achieves submillimeter registrations by avoiding suboptimal local minima due to the additional constraints provided by the contours. These occluding contours can be incorporated into the deformable registration algorithms presented here in order to provide these algorithms with more information to guide the registration.

The implementation of the deformable most likely point paradigm opens up the opportunity to develop many types of deformable registration algorithms for varying applications that use different features, make different noise assumptions, or use different types of SSMs. Such developments can accelerate the process of solving the preoperative and intraoperative image alignment problem in computer assisted medical interventions and, therefore, improve the quality of care provided to patients. Outside the medical field, machines using video feeds to view the world could make better estimates of human emotion and action based on estimated human expression and pose, respectively. The possible set of contributions of the deformable most likely point paradigm and the algorithms built with it is large and will hopefully continue to be tapped.

# Bibliography

- [1] T. F. Cootes, C. J. Taylor, D. H. Cooper, and J. Graham, “Active shape models—their training and application,” *Comput. Vis. Image Underst.*, vol. 61, no. 1, pp. 38–59, Jan 1995. [Online]. Available: <http://dx.doi.org/10.1006/cviu.1995.1004> (Cited on pages xx, 17, 20, 36, and 39)
- [2] S. Seshamani, G. Chintalapani, and R. Taylor, “Iterative refinement of point correspondences for 3d statistical shape models,” in *Medical Image Computing and Computer-Assisted Intervention – MICCAI 2011: 14th International Conference, Toronto, Canada, September 18-22, 2011, Proceedings, Part II*, G. Fichtinger, A. Martel, and T. Peters, Eds. Berlin, Heidelberg: Springer Berlin Heidelberg, 2011, pp. 417–425. [Online]. Available: [https://doi.org/10.1007/978-3-642-23629-7\\_51](https://doi.org/10.1007/978-3-642-23629-7_51) (Cited on pages xx, 20, 38, 40, 42, and 43)
- [3] X. Liu, A. Sinha, M. Ishii, G. D. Hager, R. H. Taylor, and A. Reiter, “Depth map estimation from endoscopic video using deep network,” *MICCAI (in sub-*

## BIBLIOGRAPHY

- mission*), 2018. (Cited on pages xxx, 18, 21, 277, and 281)
- [4] W. J. Fokkens, V. J. Lund, J. Mullol, C. Bachert, I. Alobid, F. Baroody, N. Cohen, A. Cervin, R. Douglas, P. Gevaert, C. Georgalas, H. Goossens, R. Harvey, P. Hellings, C. Hopkins, N. Jones, G. Joos, L. Kalogjera, B. Kern, M. Kowalski, D. Price, H. Riechelmann, R. Schlosser, B. Senior, M. Thomas, E. Toskala, R. Voegels, d. e. Y. Wang, and P. J. Wormald, “EPOS 2012: European position paper on rhinosinusitis and nasal polyps 2012. A summary for otorhinolaryngologists,” *Rhinology*, vol. 50, no. 1, pp. 1–12, Mar 2012. [Online]. Available: <http://www.ep3os.org/EPOS2012.pdf> (Cited on pages 1, 2, 5, 6, and 7)
- [5] R. O’Rahilly, F. Mller, S. Carpenter, and R. Swenson, “Basic human anatomy: A regional study of human structure,” 2008. [Online]. Available: <https://www.dartmouth.edu/~humananatomy/index.html> (Cited on pages 2 and 4)
- [6] M. Hasegawa and E. B. Kern, “The human nasal cycle,” vol. 52, no. 1, May 1977, pp. 28–34, IR: 20131213; JID: 0405543; ppublish. [Online]. Available: <https://www.ncbi.nlm.nih.gov/pubmed/609283> (Cited on pages 4, 56, and 291)
- [7] J. Spaeth, U. Krügelstein, and G. Schlöndorff, “The paranasal sinuses in ct-imaging: Development from birth to age 25,” *International Journal of*

## BIBLIOGRAPHY

- Pediatric Otorhinolaryngology*, vol. 39, no. 1, pp. 25–40, Feb 1997. [Online]. Available: [http://dx.doi.org/10.1016/S0165-5876\(96\)01458-9](http://dx.doi.org/10.1016/S0165-5876(96)01458-9) (Cited on pages 4 and 290)
- [8] I.-H. Park, J. S. Song, H. Choi, T. H. Kim, S. Hoon, S. H. Lee, and H.-M. Lee, “Volumetric study in the development of paranasal sinuses by ct imaging in asian: A pilot study,” *International Journal of Pediatric Otorhinolaryngology*, vol. 74, no. 12, pp. 1347–1350, December 2010. [Online]. Available: <http://dx.doi.org/10.1016/j.ijporl.2010.08.018> (Cited on page 4)
- [9] N. Bhattacharyya, “Contemporary assessment of the disease burden of sinusitis,” *Allergy & Rhinology*, vol. 1, no. 1, pp. 8E–8E, 2010. [Online]. Available: <https://www.ingentaconnect.com/content/ocean/rhino/2010/00000001/00000001/art00006> (Cited on page 7)
- [10] M. A. Kaliner, J. D. Osguthorpe, P. Fireman, J. Anon, J. Georgitis, M. L. Davis, R. Naclerio, and D. Kennedy, “Sinusitis: Bench to bedside: Current findings, future directions,” *Journal of Allergy and Clinical Immunology*, vol. 99, no. 6, Part 3, pp. S829 – S847, 1997, sinusitis: Bench to Bedside Current Findings, Future Directions. [Online]. Available: <http://www.sciencedirect.com/science/article/pii/S0091674997800371> (Cited on page 7)
- [11] R. Shashy, E. Moore, and A. Weaver, “Prevalence of the chronic sinusitis

## BIBLIOGRAPHY

- diagnosis in Olmsted County, Minnesota,” *Archives of OtolaryngologyHead & Neck Surgery*, vol. 130, no. 3, pp. 320–323, 2004. [Online]. Available: [+http://dx.doi.org/10.1001/archotol.130.3.320](http://dx.doi.org/10.1001/archotol.130.3.320) (Cited on page 7)
- [12] Hughes and Jones, “The role of nasal endoscopy in outpatient management,” *Clinical Otolaryngology & Allied Sciences*, vol. 23, no. 3, pp. 224–226, 1998. [Online]. Available: <http://dx.doi.org/10.1046/j.1365-2273.1998.00131.x> (Cited on page 7)
- [13] N. Bhattacharyya, “Clinical and symptom criteria for the accurate diagnosis of chronic rhinosinusitis,” *The Laryngoscope*, vol. 116, no. S110, pp. 1–22, 2006. [Online]. Available: <http://dx.doi.org/10.1097/01.mlg.0000224508.59725.19> (Cited on page 7)
- [14] R. Goering, H. Dockrell, M. Zuckerman, I. Roitt, and P. L. Chiodini, *Mims’ Medical Microbiology*. Elsevier, 2012. [Online]. Available: <https://www.clinicalkey.com/#!/browse/book/3-s2.0-C20090597917> (Cited on page 7)
- [15] V. J. Lund, “Therapeutic targets in rhinosinusitis: Infection or inflammation?” *Medscape J Med*, vol. 10, no. 4, pp. 105–105, Apr 2008, 571207[PII]. [Online]. Available: <http://www.ncbi.nlm.nih.gov/pmc/articles/PMC2390689/> (Cited on page 7)
- [16] A. Masood, I. Moumoulidis, and J. Panesar, “Acute rhinosinusitis in adults: an update on current management,” *Postgrad Med J*, vol. 83,

## BIBLIOGRAPHY

- no. 980, pp. 402–408, Jun 2007, pj54767[PII]. [Online]. Available: <http://www.ncbi.nlm.nih.gov/pmc/articles/PMC2600057/> (Cited on page 7)
- [17] A. R. Gnoy, P. J. Gannon, E. Ganjian, L. Fliegelman, D. Farber, A. Silvers, and W. Lawson, “A potential role for nasal obstruction in development of acute sinusitis: An infection study in rabbits,” *American Journal of Rhinology*, vol. 12, no. 6, pp. 399–404, 1998. [Online]. Available: <https://www.ingentaconnect.com/content/ocean/ajr/1998/00000012/00000006/art00004> (Cited on page 7)
- [18] R. S. Leung and R. Katial, “The diagnosis and management of acute and chronic sinusitis,” *Primary Care: Clinics in Office Practice*, vol. 35, no. 1, pp. 11 – 24, 2008, allergy, Asthma, and Immune Deficiency. [Online]. Available: <http://www.sciencedirect.com/science/article/pii/S009545430700084X> (Cited on page 7)
- [19] D. P. Skoner, “Complications of allergic rhinitis,” *Journal of Allergy and Clinical Immunology*, vol. 105, no. 6, pp. S605–S609, June 2000. [Online]. Available: <http://dx.doi.org/10.1067/mai.2000.106150> (Cited on page 7)
- [20] J. M. Gwaltney, Jr., J. O. Hendley, C. D. Phillips, C. R. Bass, N. Mygind, and B. Winther, “Nose blowing propels nasal fluid into the paranasal sinuses,” *Clinical Infectious Diseases*, vol. 30, no. 2, pp. 387–391, 2000. [Online]. Available: [+http://dx.doi.org/10.1086/313661](http://dx.doi.org/10.1086/313661) (Cited on page 7)
- [21] J. Hickner, J. Bartlett, R. Besser, R. Gonzales, J. Hoff-

## BIBLIOGRAPHY

- man, and M. Sande, “Principles of appropriate antibiotic use for acute rhinosinusitis in adults: Background,” *Annals of Internal Medicine*, vol. 134, no. 6, pp. 498–505, 2001. [Online]. Available: [+http://dx.doi.org/10.7326/0003-4819-134-6-200103200-00017](http://dx.doi.org/10.7326/0003-4819-134-6-200103200-00017) (Cited on page 8)
- [22] F. L. van Buchem, J. A. Knottnerus, V. J. J. Schrijnemaekers, and M. F. Peeters, “Primary-care-based randomised placebo-controlled trial of antibiotic treatment in acute maxillary sinusitis,” *The Lancet*, vol. 349, no. 9053, pp. 683–687, March 1997. [Online]. Available: [http://dx.doi.org/10.1016/S0140-6736\(96\)07585-X](http://dx.doi.org/10.1016/S0140-6736(96)07585-X) (Cited on page 8)
- [23] J. Young, A. D. Sutter, D. Merenstein, G. A. van Essen, L. Kaiser, H. Varonen, I. Williamson, and H. C. Bucher, “Antibiotics for adults with clinically diagnosed acute rhinosinusitis: a meta-analysis of individual patient data,” *The Lancet*, vol. 371, no. 9616, pp. 908 – 914, 2008. [Online]. Available: <http://www.sciencedirect.com/science/article/pii/S014067360860416X> (Cited on page 8)
- [24] J. B. Anon, M. R. Jacobs, M. D. Poole, P. G. Ambrose, M. S. Benninger, J. A. Hadley, W. A. Craig, and S. . A. H. Partnership, “Antimicrobial treatment guidelines for acute bacterial rhinosinusitis,” *OtolaryngologyHead*



## BIBLIOGRAPHY

- and Neck Surgery*, vol. 130, no. 1\_suppl, pp. 1–45, 2004. [Online]. Available: <https://doi.org/10.1016/j.otohns.2003.12.003> (Cited on page 8)
- [25] J. G. Krings, D. Kallogjeri, A. Wineland, K. G. Nepple, J. F. Piccirillo, and A. E. Getz, “Complications of primary and revision functional endoscopic sinus surgery for chronic rhinosinusitis,” *The Laryngoscope*, vol. 124, no. 4, pp. 838–845, 2014. [Online]. Available: <http://dx.doi.org/10.1002/lary.24401> (Cited on page 9)
- [26] S. M. Ragab, V. J. Lund, and G. Scadding, “Evaluation of the medical and surgical treatment of chronic rhinosinusitis: A prospective, randomised, controlled trial,” *The Laryngoscope*, vol. 114, no. 5, pp. 923–930, 2004. [Online]. Available: <http://dx.doi.org/10.1097/00005537-200405000-00027> (Cited on page 9)
- [27] J. Myller, P. Dastidar, T. Torkkeli, M. Rautiainen, and S. Toppila-Salmi, “Computed tomography findings after endoscopic sinus surgery with preserving or enlarging maxillary sinus ostium surgery,” *Rhinology*, vol. 49, no. 4, pp. 438–444, Oct 2011. [Online]. Available: <http://www.rhinologyjournal.com/Abstract.php?id=1021> (Cited on page 9)
- [28] S. J. Atlas, P. M. Gallagher, Y. A. Wu, D. E. Singer, R. E. Gliklich, R. B. Metson, and F. J. Fowler, “Development and validation of a new health-related quality of life instrument for patients with sinusitis,” *Quality*

## BIBLIOGRAPHY

- of Life Research*, vol. 14, no. 5, pp. 1375–1386, 2005. [Online]. Available: <http://www.jstor.org/stable/4039940> (Cited on page 9)
- [29] M. L. Hytönen, M. Lilja, A. A. Mäkitie, H. Sintonen, and R. P. Roine, “Does septoplasty enhance the quality of life in patients?” *European Archives of Oto-Rhino-Laryngology*, vol. 269, no. 12, pp. 2497–2503, Dec 2012. [Online]. Available: <https://doi.org/10.1007/s00405-012-1931-9> (Cited on page 9)
- [30] O. Hilberg, “Objective measurement of nasal airway dimensions using acoustic rhinometry: methodological and clinical aspects,” *Allergy*, vol. 57, pp. 5–39, 2002. [Online]. Available: <http://dx.doi.org/10.1046/j.0908-665x.2001.all.doc.x> (Cited on pages 9 and 291)
- [31] G. Ottaviano and W. J. Fokkens, “Measurements of nasal airflow and patency: a critical review with emphasis on the use of peak nasal inspiratory flow in daily practice,” *Allergy*, vol. 71, no. 2, pp. 162–174, 2016. [Online]. Available: <http://dx.doi.org/10.1111/all.12778> (Cited on pages 9 and 291)
- [32] E. Moreddu, L. Puymerrail, J. Michel, M. Achache, P. Dessi, and P. Adalian, “Morphometric measurements and sexual dimorphism of the piriform aperture in adults,” *Surgical and Radiologic Anatomy*, vol. 35, no. 10, pp. 917–924, Dec 2013. [Online]. Available: <https://doi.org/10.1007/s00276-013-1116-2> (Cited on pages 9 and 291)
- [33] W. R. Crum, T. Hartkens, and D. L. G. Hill, “Non-rigid image

## BIBLIOGRAPHY

- registration: theory and practice,” *The British Journal of Radiology*, vol. 77, no. suppl.2, pp. S140–S153, 2004, pMID: 15677356. [Online]. Available: <https://doi.org/10.1259/bjr/25329214> (Cited on pages 10 and 54)
- [34] A. A. Goshtasby, *2-D and 3-D Image Registration: For Medical, Remote Sensing, and Industrial Applications*. John Wiley & Sons, Inc., 2005, pp. i–258. [Online]. Available: <http://dx.doi.org/10.1002/0471724270> (Cited on pages 10 and 11)
- [35] P. J. Besl and N. D. McKay, “A method for registration of 3-d shapes,” *IEEE Transactions on Pattern Analysis and Machine Intelligence*, vol. 14, no. 2, pp. 239–256, Feb 1992. [Online]. Available: <https://doi.org/10.1109/34.121791> (Cited on pages 11, 12, 55, and 272)
- [36] K. Pulli and M. Pietikäinen, “Range Image Segmentation Based on Decomposition of Surface Normals,” vol. 2, pp. 893–893, 1993. [Online]. Available: <http://people.csail.mit.edu/kapu/papers/SCIApap.pdf> (Cited on pages 11, 140, and 141)
- [37] G. C. Sharp, S. W. Lee, and D. K. Wehe, “Icp registration using invariant features,” *IEEE Transactions on Pattern Analysis and Machine Intelligence*, vol. 24, no. 1, pp. 90–102, Jan 2002. (Cited on pages 11, 13, and 80)
- [38] C. Schutz, T. Jost, and H. Hugli, “Multi-feature matching algorithm for free-form 3d surface registration,” in *Proceedings. Fourteenth International Confer-*

## BIBLIOGRAPHY

- ence on Pattern Recognition (Cat. No.98EX170)*, vol. 2, Aug 1998, pp. 982–984  
vol.2. (Cited on page 11)
- [39] J. Maintz and M. A. Viergever, “A survey of medical image registration,” *Medical Image Analysis*, vol. 2, no. 1, pp. 1 – 36, 1998. [Online]. Available: <http://www.sciencedirect.com/science/article/pii/S1361841501800268> (Cited on pages 11 and 17)
- [40] G. K. L. Tam, Z. Q. Cheng, Y. K. Lai, F. C. Langbein, Y. Liu, D. Marshall, R. R. Martin, X. F. Sun, and P. L. Rosin, “Registration of 3d point clouds and meshes: A survey from rigid to nonrigid,” *IEEE Transactions on Visualization and Computer Graphics*, vol. 19, no. 7, pp. 1199–1217, July 2013. (Cited on pages 11 and 14)
- [41] C. A. Pelizzari, G. T. Y. Chen, D. R. Spelbring, R. R. Weichselbaum, and C.-T. Chen, “Accurate three-dimensional registration of ct, pet, and/or mr images of the brain,” *Journal of Computer Assisted Tomography*, vol. 13, no. 1, 1989. [Online]. Available: [https://journals.lww.com/jcat/Fulltext/1989/01000/Accurate\\_Three\\_Dimensional\\_Registration\\_of\\_CT,.4.aspx](https://journals.lww.com/jcat/Fulltext/1989/01000/Accurate_Three_Dimensional_Registration_of_CT,.4.aspx) (Cited on page 12)
- [42] G. Champleboux, S. Lavalée, R. Szeliski, and L. Brunie, “From accurate range imaging sensor calibration to accurate model-based 3d object localization,” in *Proceedings 1992 IEEE Computer Society Conference on Computer Vision and Pattern Recognition*, Jun 1992, pp. 83–89. (Cited on page 12)

## BIBLIOGRAPHY

- [43] Z. Zhang, “Iterative point matching for registration of free-form curves and surfaces,” *International Journal of Computer Vision*, vol. 13, no. 2, pp. 119–152, Oct 1994. [Online]. Available: <https://doi.org/10.1007/BF01427149> (Cited on page 13)
- [44] C. R. Maurer, G. B. Aboutanos, B. M. Dawant, R. J. Maciunas, and J. M. Fitzpatrick, “Registration of 3-d images using weighted geometrical features,” *IEEE Transactions on Medical Imaging*, vol. 15, no. 6, pp. 836–849, Dec 1996. (Cited on page 13)
- [45] Y. Chen and G. Medioni, “Object modelling by registration of multiple range images,” *Image Vision Comput.*, vol. 10, no. 3, pp. 145–155, Apr. 1992. [Online]. Available: [http://dx.doi.org/10.1016/0262-8856\(92\)90066-C](http://dx.doi.org/10.1016/0262-8856(92)90066-C) (Cited on page 13)
- [46] J. Minguéz, L. Montesano, and F. Lamiroux, “Metric-based iterative closest point scan matching for sensor displacement estimation,” *IEEE Transactions on Robotics*, vol. 22, no. 5, pp. 1047–1054, Oct 2006. (Cited on page 13)
- [47] L. Armesto, J. Minguéz, and L. Montesano, “A generalization of the metric-based iterative closest point technique for 3d scan matching,” in *2010 IEEE International Conference on Robotics and Automation*, May 2010, pp. 1367–1372. (Cited on page 13)
- [48] S. Gold, A. Rangarajan, C. ping Lu, and E. Mjolsness, “New

## BIBLIOGRAPHY

- algorithms for 2d and 3d point matching: Pose estimation and correspondence,” *Pattern Recognition*, vol. 31, pp. 957–964, 1997. [Online]. Available: <https://papers.nips.cc/paper/977-new-algorithms-for-2d-and-3d-point-matching-pose-estimation-and-correspondence.pdf> (Cited on page 13)
- [49] S. Granger and X. Pennec, *Multi-scale EM-ICP: A Fast and Robust Approach for Surface Registration*. Berlin, Heidelberg: Springer Berlin Heidelberg, 2002, pp. 418–432. [Online]. Available: [http://dx.doi.org/10.1007/3-540-47979-1\\_28](http://dx.doi.org/10.1007/3-540-47979-1_28) (Cited on pages 13 and 14)
- [50] A. Myronenko and X. Song, “Point set registration: Coherent point drift,” *IEEE Transactions on Pattern Analysis and Machine Intelligence*, vol. 32, no. 12, pp. 2262–2275, Dec 2010. [Online]. Available: <https://doi.org/10.1109/TPAMI.2010.46> (Cited on pages 13, 14, 55, 113, and 273)
- [51] S. D. Billings, E. M. Boctor, and R. H. Taylor, “Iterative most-likely point registration (impl): A robust algorithm for computing optimal shape alignment,” *PLOS ONE*, vol. 10, no. 3, pp. 1–45, 03 2015. [Online]. Available: <https://doi.org/10.1371/journal.pone.0117688> (Cited on pages 13, 54, 65, 71, 72, 73, 74, 75, 77, 78, 79, 80, 81, 82, 83, 84, 85, 87, 154, 174, 218, and 237)
- [52] S. Billings and R. Taylor, *Iterative Most Likely Oriented Point Registration*. Cham: Springer International Publishing, 2014, pp. 178–185. [Online].

## BIBLIOGRAPHY

- Available: [https://doi.org/10.1007/978-3-319-10404-1\\_23](https://doi.org/10.1007/978-3-319-10404-1_23) (Cited on pages 13, 139, 142, 144, 149, 150, and 153)
- [53] S. D. Billings and R. H. Taylor, “Generalized iterative most likely oriented-point (g-imlop) registration,” *International Journal of Computer Assisted Radiology and Surgery*, vol. 10, no. 8, pp. 1213–1226, 2015. [Online]. Available: <http://dx.doi.org/10.1007/s11548-015-1221-2> (Cited on pages 13, 174, 203, 204, 205, 207, 208, 216, 217, and 237)
- [54] S. Leonard, A. Reiter, A. Sinha, M. Ishii, R. H. Taylor, and G. D. Hager, “Image-based navigation for functional endoscopic sinus surgery using structure from motion,” pp. 97 840V–97 840V–7, 2016. [Online]. Available: <http://dx.doi.org/10.1117/12.2217279> (Cited on pages 14, 18, and 273)
- [55] S. D. Billings, A. Sinha, A. Reiter, S. Leonard, M. Ishii, G. D. Hager, and R. H. Taylor, *Anatomically Constrained Video-CT Registration via the V-IMLOP Algorithm*. Cham: Springer International Publishing, 2016, pp. 133–141. [Online]. Available: [http://dx.doi.org/10.1007/978-3-319-46726-9\\_16](http://dx.doi.org/10.1007/978-3-319-46726-9_16) (Cited on pages 14, 285, and 330)
- [56] S. Leonard, A. Sinha, A. Reiter, M. Ishii, G. L. Gallia, R. H. Taylor, and G. D. Hager, “Evaluation and stability analysis of video-based navigation system for functional endoscopic sinus surgery on in-vivo clinical data,” *IEEE Transactions in Medical Imaging (in submission)*, 2018. (Cited on page 14)

## BIBLIOGRAPHY

- [57] D. Burschka, M. Li, M. Ishii, R. H. Taylor, and G. D. Hager, “Scale-invariant registration of monocular endoscopic images to ct-scans for sinus surgery,” *Medical Image Analysis*, vol. 9, no. 5, pp. 413–426, Oct 2005. [Online]. Available: <http://dx.doi.org/10.1016/j.media.2005.05.005> (Cited on page 14)
- [58] H. Chui and A. Rangarajan, “A feature registration framework using mixture models,” in *Proceedings IEEE Workshop on Mathematical Methods in Biomedical Image Analysis. MMBIA-2000 (Cat. No.PR00737)*, June 2000, pp. 190–197. (Cited on page 14)
- [59] B. Combès and S. Prima, “An efficient em-icp algorithm for symmetric consistent non-linear registration of point sets,” *Med Image Comput Comput Assist Interv*, vol. 13, no. Pt 2, pp. 594–601, 2010, 20879364[pmid]. [Online]. Available: <http://www.ncbi.nlm.nih.gov/pmc/articles/PMC3077756/> (Cited on page 14)
- [60] Y. Tsin and T. Kanade, “A correlation-based approach to robust point set registration,” in *Computer Vision - ECCV 2004*, T. Pajdla and J. Matas, Eds. Berlin, Heidelberg: Springer Berlin Heidelberg, 2004, pp. 558–569. (Cited on page 15)
- [61] B. Jian and B. C. Vemuri, “Robust point set registration using gaussian mixture models,” *IEEE Transactions on Pattern Analysis and Machine Intelligence*, vol. 33, no. 8, pp. 1633–1645, Aug 2011. (Cited on page 15)



## BIBLIOGRAPHY

- [62] D. L. Pham, C. Xu, and J. L. Prince, “Current methods in medical image segmentation,” *Annual Review of Biomedical Engineering*, vol. 2, no. 1, pp. 315–337, 2000, pMID: 11701515. [Online]. Available: <https://doi.org/10.1146/annurev.bioeng.2.1.315> (Cited on page 16)
- [63] P. Sahoo, S. Soltani, and A. Wong, “A survey of thresholding techniques,” *Computer Vision, Graphics, and Image Processing*, vol. 41, no. 2, pp. 233 – 260, 1988. [Online]. Available: <http://www.sciencedirect.com/science/article/pii/0734189X88900229> (Cited on page 16)
- [64] R. M. Haralick and L. G. Shapiro, “Image segmentation techniques,” *Computer Vision, Graphics, and Image Processing*, vol. 29, no. 1, pp. 100 – 132, 1985. [Online]. Available: <http://www.sciencedirect.com/science/article/pii/S0734189X85901537> (Cited on page 16)
- [65] A. K. Jain and R. C. Dubes, *Algorithms for Clustering Data*. Upper Saddle River, NJ, USA: Prentice-Hall, Inc., 1988. [Online]. Available: <https://dl.acm.org/citation.cfm?id=46712> (Cited on page 16)
- [66] C. Xu and J. L. Prince, “Gradient vector flow: a new external force for snakes,” in *Proceedings of IEEE Computer Society Conference on Computer Vision and Pattern Recognition*, Jun 1997, pp. 66–71. [Online]. Available: <https://doi.org/10.1109/CVPR.1997.609299> (Cited on pages 17, 20, 28, and 32)

## BIBLIOGRAPHY

- [67] —, “Snakes, shapes, and gradient vector flow,” *IEEE Transactions on Image Processing*, vol. 7, no. 3, pp. 359–369, Mar 1998. [Online]. Available: <https://doi.org/10.1109/83.661186> (Cited on pages 17, 20, 32, and 33)
- [68] S. Sandor and R. Leahy, “Surface-based labeling of cortical anatomy using a deformable atlas,” *IEEE Transactions on Medical Imaging*, vol. 16, no. 1, pp. 41–54, Feb 1997. [Online]. Available: <http://ieeexplore.ieee.org/document/552054/> (Cited on page 17)
- [69] D. L. Collins, C. J. Holmes, T. M. Peters, and A. C. Evans, “Automatic 3d modelbased neuroanatomical segmentation,” *Human Brain Mapping*, vol. 3, no. 3, pp. 190–208, 1995. [Online]. Available: <https://onlinelibrary.wiley.com/doi/abs/10.1002/hbm.460030304> (Cited on page 17)
- [70] C. Davatzikos, “Spatial normalization of 3d brain images using deformable models,” *Journal of Computer Assisted Tomography*, vol. 20, no. 4, pp. 656–665, 7 1996. (Cited on page 17)
- [71] G. E. Christensen, S. C. Joshi, and M. I. Miller, “Volumetric transformation of brain anatomy,” *IEEE Transactions on Medical Imaging*, vol. 16, no. 6, pp. 864–877, Dec 1997. (Cited on page 17)
- [72] M. Spetsakis and J. Y. Aloimonos, “A multi-frame approach to visual motion perception,” *International Journal of Computer Vision*, vol. 6, no. 3, pp.

## BIBLIOGRAPHY

- 245–255, Aug 1991. [Online]. Available: <https://doi.org/10.1007/BF00115698>  
(Cited on page 18)
- [73] B. Triggs, P. F. McLauchlan, R. I. Hartley, and A. W. Fitzgibbon, “Bundle adjustment — a modern synthesis,” in *Vision Algorithms: Theory and Practice*, B. Triggs, A. Zisserman, and R. Szeliski, Eds. Berlin, Heidelberg: Springer Berlin Heidelberg, 2000, pp. 298–372. (Cited on page 18)
- [74] A. Reiter, S. Leonard, A. Sinha, M. Ishii, R. H. Taylor, and G. D. Hager, “Endoscopic-ct: learning-based photometric reconstruction for endoscopic sinus surgery,” pp. 978 418–978 418–6, 2016. [Online]. Available: <http://dx.doi.org/10.1117/12.2216296> (Cited on pages 18, 21, and 275)
- [75] A. Sinha, S. Leonard, A. Reiter, M. Ishii, R. H. Taylor, and G. D. Hager, “Automatic segmentation and statistical shape modeling of the paranasal sinuses to estimate natural variations,” *Proc. SPIE*, vol. 9784, pp. 97 840D–97 840D–8, 2016. [Online]. Available: <http://dx.doi.org/10.1117/12.2217337> (Cited on pages 19, 21, 25, and 322)
- [76] A. Sinha, A. Reiter, S. Leonard, M. Ishii, G. D. Hager, and R. H. Taylor, “Simultaneous segmentation and correspondence improvement using statistical modes,” pp. 101 331B–101 331B–8, 2017. [Online]. Available: <http://dx.doi.org/10.1117/12.2253533> (Cited on pages 20, 22, 41, and 52)
- [77] A. Sinha, S. D. Billings, A. Reiter, X. Liu, M. Ishii, G. D. Hager, and R. H.

## BIBLIOGRAPHY

- Taylor, “The deformable most-likely-point paradigm,” *Medical Image Analysis (in submission)*, 2018. (Cited on pages 20, 21, 23, 24, 25, 61, 68, 69, 137, 201, 268, 273, and 287)
- [78] S. D. Billings, “Probabilistic feature-based registration for interventional medicine,” Ph.D. dissertation, The Johns Hopkins University, Baltimore, Maryland, 8 2015. (Cited on pages 20, 23, 57, 59, 60, 61, 63, 64, 66, 68, 69, 137, 138, 141, 152, and 216)
- [79] A. Sinha, X. Liu, A. Reiter, M. Ishii, G. D. Hager, and R. H. Taylor, “Endoscopic navigation in the absence of ct imaging,” *MICCAI (in submission)*, 2018. (Cited on pages 21, 25, and 287)
- [80] D. E. King, “Dlib-ml: A machine learning toolkit,” *J. Mach. Learn. Res.*, vol. 10, pp. 1755–1758, Dec. 2009. [Online]. Available: <http://dl.acm.org/citation.cfm?id=1577069.1755843> (Cited on pages 23, 24, 25, 87, 137, 201, and 268)
- [81] T. Heimann, B. van Ginneken, M. A. Styner, Y. Arzhaeva, V. Aurich, C. Bauer, A. Beck, C. Becker, R. Beichel, G. Bekes, F. Bello, G. Binnig, H. Bischof, A. Bornik, P. M. M. Cashman, Y. Chi, A. Cordova, B. M. Dawant, M. Fidrich, J. D. Furst, D. Furukawa, L. Grenacher, J. Hornegger, D. Kainmller, R. I. Kitney, H. Kobatake, H. Lamecker, T. Lange, J. Lee, B. Lennon, R. Li, S. Li, H. P. Meinzer, G. Nemeth, D. S. Raicu, A. M. Rau, E. M. van Rikxoort, M. Rousson,

## BIBLIOGRAPHY

- L. Rusko, K. A. Saddi, G. Schmidt, D. Seghers, A. Shimizu, P. Slagmolen, E. Sorantin, G. Soza, R. Susomboon, J. M. Waite, A. Wimmer, and I. Wolf, “Comparison and evaluation of methods for liver segmentation from ct datasets,” *IEEE Transactions on Medical Imaging*, vol. 28, no. 8, pp. 1251–1265, Aug 2009. (Cited on page 28)
- [82] R. Adams and L. Bischof, “Seeded region growing,” *IEEE Transactions on Pattern Analysis and Machine Intelligence*, vol. 16, no. 6, pp. 641–647, Jun 1994. (Cited on page 28)
- [83] A. Beck and V. Aurich, “Hepatux a semiautomatic liver segmentation system,” 01 2007. (Cited on page 28)
- [84] K. D. T. Regina Pohle, “Segmentation of medical images using adaptive region growing,” pp. 4322 – 4322 – 10, 2001. [Online]. Available: <https://doi.org/10.1117/12.431013> (Cited on page 28)
- [85] A. Sotiras, C. Davatzikos, and N. Paragios, “Deformable medical image registration: A survey,” *IEEE Transactions on Medical Imaging*, vol. 32, no. 7, pp. 1153–1190, July 2013. (Cited on page 29)
- [86] B. B. Avants, P. Yushkevich, J. Pluta, D. Minkoff, M. Korczykowski, J. Detre, and J. C. Gee, “The optimal template effect in hippocampus studies of diseased populations,” *NeuroImage*, vol. 49, no. 3, pp. 2457 – 2466,

## BIBLIOGRAPHY

2010. [Online]. Available: <http://www.sciencedirect.com/science/article/pii/S1053811909010611> (Cited on page 29)
- [87] B. B. Avants, N. J. Tustison, G. Song, P. A. Cook, A. Klein, and J. C. Gee, “A reproducible evaluation of {ANTs} similarity metric performance in brain image registration,” *NeuroImage*, vol. 54, no. 3, pp. 2033 – 2044, 2011. [Online]. Available: <http://www.sciencedirect.com/science/article/pii/S1053811910012061> (Cited on page 30)
- [88] W. E. Lorensen and H. E. Cline, “Marching cubes: A high resolution 3d surface construction algorithm,” in *Proceedings of the 14th Annual Conference on Computer Graphics and Interactive Techniques*, ser. SIGGRAPH '87. New York, NY, USA: ACM, 1987, pp. 163–169. [Online]. Available: <http://doi.acm.org/10.1145/37401.37422> (Cited on page 30)
- [89] R. Delgado-Gonzalo, N. Chenouard, and M. Unser, “Spline-based deforming ellipsoids for interactive 3d bioimage segmentation,” *IEEE Transactions on Image Processing*, vol. 22, no. 10, pp. 3926–3940, Oct 2013. [Online]. Available: <https://doi.org/10.1109/TIP.2013.2264680> (Cited on page 32)
- [90] K. Weiler, “Edge-based data structures for solid modeling in curved-surface environments,” *IEEE Comput. Graph. Appl.*, vol. 5, no. 1, pp. 21–40, Jan 1985. [Online]. Available: <http://dx.doi.org/10.1109/MCG.1985.276271> (Cited on page 33)

## BIBLIOGRAPHY

- [91] R. R. Beichel, E. J. Ulrich, C. Bauer, A. Wahle, B. Brown, T. Chang, K. A. Plichta, B. J. Smith, J. J. Sunderland, T. Braun, A. Fedorov, D. Clunie, M. Onken, J. Riesmeier, S. Pieper, R. Kikinis, M. M. Graham, T. L. Casavant, M. Sonka, and J. M. Buatti, “Data from qin-headneck. the cancer imaging archive.” 2015. [Online]. Available: <http://doi.org/10.7937/K9/TCIA.2015.K0F5CGLI> (Cited on pages 44 and 91)
- [92] W. R. Bosch, W. L. Straube, J. W. Matthews, and J. A. Purdy, “Data from head-neck\_cetuximab,” The Cancer Imaging Archive., 2015. [Online]. Available: <http://doi.org/10.7937/K9/TCIA.2015.7AKGJUPZ> (Cited on pages 44 and 91)
- [93] K. Clark, B. Vendt, K. Smith, J. Freymann, J. Kirby, P. Koppel, S. Moore, S. Phillips, D. Maffitt, M. Pringle, L. Tarbox, and F. Prior, “The cancer imaging archive (tcia): Maintaining and operating a public information repository,” *Journal of Digital Imaging*, vol. 26, no. 6, pp. 1045–1057, Dec 2013. [Online]. Available: <https://doi.org/10.1007/s10278-013-9622-7> (Cited on pages 44 and 91)
- [94] A. Fedorov, D. Clunie, E. Ulrich, C. Bauer, A. Wahle, B. Brown, M. Onken, J. Riesmeier, S. Pieper, R. Kikinis, J. Buatti, and R. R. Beichel, “Dicom for quantitative imaging biomarker development: a standards based approach to sharing clinical data and structured pet/ct analysis results in head and

## BIBLIOGRAPHY

- neck cancer research,” *PeerJ*, vol. 4, p. e2057, Feb 2016. [Online]. Available: <https://doi.org/10.7717/peerj.2057> (Cited on pages 44 and 91)
- [95] H. Alt, P. Braß, M. Godau, C. Knauer, and C. Wenk, *Computing the Hausdorff Distance of Geometric Patterns and Shapes*. Berlin, Heidelberg: Springer Berlin Heidelberg, 2003, pp. 65–76. [Online]. Available: [https://doi.org/10.1007/978-3-642-55566-4\\_4](https://doi.org/10.1007/978-3-642-55566-4_4) (Cited on pages 44, 46, and 47)
- [96] O. Van Kaick, H. Zhang, G. Hamarneh, and D. Cohen-Or, “A survey on shape correspondence,” in *Computer Graphics Forum*, vol. 30, no. 6. Wiley Online Library, 2011, pp. 1681–1707. (Cited on page 54)
- [97] D. Hahnel, S. Thrun, and W. Burgard, “An extension of the icp algorithm for modeling nonrigid objects with mobile robots,” in *Proceedings of the 18th International Joint Conference on Artificial Intelligence*, ser. IJCAI’03. San Francisco, CA, USA: Morgan Kaufmann Publishers Inc., 2003, pp. 915–920. [Online]. Available: <http://dl.acm.org/citation.cfm?id=1630659.1630791> (Cited on page 55)
- [98] H. Chui and A. Rangarajan, “A new point matching algorithm for non-rigid registration,” *Computer Vision and Image Understanding*, vol. 89, no. 2, pp. 114 – 141, 2003, nonrigid Image Registration. [Online]. Available: <http://www.sciencedirect.com/science/article/pii/S1077314203000092> (Cited on page 55)



## BIBLIOGRAPHY

- [99] T. Reichl, X. Luo, M. Menzel, H. Hautmann, K. Mori, and N. Navab, *Deformable Registration of Bronchoscopic Video Sequences to CT Volumes with Guaranteed Smooth Output*. Berlin, Heidelberg: Springer Berlin Heidelberg, 2011, pp. 17–24. [Online]. Available: [https://doi.org/10.1007/978-3-642-23623-5\\_3](https://doi.org/10.1007/978-3-642-23623-5_3) (Cited on page 55)
- [100] J. Kainz and H. Stammberger, “The roof of the anterior ethmoid: A place of least resistance in the skull base,” *American Journal of Rhinology*, vol. 3, no. 4, pp. 191–199, 1989. [Online]. Available: <http://www.ingentaconnect.com/content/ocean/ajr/1989/00000003/00000004/art00002> (Cited on pages 55 and 271)
- [101] A. L. Ogilvy-Stuart and S. M. Shalet, “Effect of radiation on the human reproductive system.” *Environ Health Perspect*, vol. 101, no. Suppl 2, pp. 109–116, Jul 1993, 8243379[pmid]. [Online]. Available: <http://www.ncbi.nlm.nih.gov/pmc/articles/PMC1519954/> (Cited on page 56)
- [102] A. Segal, D. Haehnel, and S. Thrun, “Generalized-icp,” in *Proceedings of Robotics: Science and Systems*, Seattle, USA, June 2009. [Online]. Available: <http://www.roboticsproceedings.org/rss05/p21.pdf> (Cited on page 78)
- [103] L. Maier-Hein, A. M. Franz, T. R. dos Santos, M. Schmidt, M. Fangerau, H. P. Meinzer, and J. M. Fitzpatrick, “Convergent iterative closest-point algorithm to accomodate anisotropic and inhomogenous localization error,” *IEEE Trans-*

## BIBLIOGRAPHY

- actions on Pattern Analysis and Machine Intelligence*, vol. 34, no. 8, pp. 1520–1532, Aug 2012. (Cited on page 78)
- [104] R. Grupp, Y. Otake, R. Murphy, J. Parvizi, M. Armand, and R. Taylor, “Pelvis surface estimation from partial ct for computer-aided pelvic osteotomies,” *Bone Joint J*, vol. 98, no. SUPP 5, pp. 55–55, 2016. (Cited on pages 91 and 329)
- [105] L. Zhang, N. Snavely, B. Curless, and S. M. Seitz, “Spacetime faces: High resolution capture for modeling and animation,” *ACM Trans. Graph.*, vol. 23, no. 3, pp. 548–558, Aug 2004. [Online]. Available: <http://doi.acm.org/10.1145/1015706.1015759> (Cited on page 91)
- [106] F. Bogo, J. Romero, M. Loper, and M. J. Black, “FAUST: Dataset and evaluation for 3D mesh registration,” in *Proceedings IEEE Conf. on Computer Vision and Pattern Recognition (CVPR)*. Piscataway, NJ, USA: IEEE, June 2014, pp. 3794–3801. (Cited on page 91)
- [107] A. Danilchenko and J. M. Fitzpatrick, “General approach to first-order error prediction in rigid point registration,” *IEEE Transactions on Medical Imaging*, vol. 30, no. 3, pp. 679–693, March 2011. [Online]. Available: <https://doi.org/10.1109/TMI.2010.2091513> (Cited on pages 107, 174, and 238)
- [108] I. Buciu, C. Kotropoulos, and I. Pitas, “Comparison of ica approaches for facial expression recognition,” *Signal, Image and Video Processing*, vol. 3, no. 4, p.

## BIBLIOGRAPHY

- 345, Sep 2008. [Online]. Available: <https://doi.org/10.1007/s11760-008-0074-3>  
(Cited on pages 131 and 328)
- [109] R. I. Hartley and A. Zisserman, *Multiple View Geometry in Computer Vision*, 2nd ed. Cambridge University Press, ISBN: 0521540518, 2004. (Cited on page 140)
- [110] H. Hoppe, T. DeRose, T. Duchamp, J. McDonald, and W. Stuetzle, “Surface reconstruction from unorganized points,” in *Proceedings of the 19th Annual Conference on Computer Graphics and Interactive Techniques*, ser. SIGGRAPH '92. New York, NY, USA: ACM, 1992, pp. 71–78. [Online]. Available: <http://doi.acm.org/10.1145/133994.134011> (Cited on page 140)
- [111] T. Tsujimura and T. Yabuta, “A tactile sensing method for employing force/torque information through insensitive probes,” in *Proceedings 1992 IEEE International Conference on Robotics and Automation*, May 1992, pp. 1315–1320 vol.2. (Cited on page 140)
- [112] M. Charlebois, K. Gupta, and S. Payandeh, “Shape description of general, curved surfaces using tactile sensing and surface normal information,” in *Proceedings of International Conference on Robotics and Automation*, vol. 4, Apr 1997, pp. 2819–2824 vol.4. (Cited on page 140)
- [113] M. Levoy, K. Pulli, B. Curless, S. Rusinkiewicz, D. Koller, L. Pereira, M. Ginzton, S. Anderson, J. Davis, J. Ginsberg, J. Shade, and D. Fulk,

## BIBLIOGRAPHY

- “The digital michelangelo project: 3d scanning of large statues,” in *Proceedings of the 27th Annual Conference on Computer Graphics and Interactive Techniques*, ser. SIGGRAPH '00. New York, NY, USA: ACM Press/Addison-Wesley Publishing Co., 2000, pp. 131–144. [Online]. Available: <http://dx.doi.org/10.1145/344779.344849> (Cited on page 140)
- [114] K. V. Mardia and P. E. Jupp, *Directional Statistics*. John Wiley & Sons, Inc., 2008. [Online]. Available: <http://dx.doi.org/10.1002/9780470316979> (Cited on pages 141, 174, 205, and 238)
- [115] K. H. Fuchs, “Minimally invasive surgery,” *Endoscopy*, vol. 34, no. 02, pp. 154–159, 2002, 154. [Online]. Available: <https://www.thieme-connect.com/products/ejournals/html/10.1055/s-2002-19857> (Cited on page 270)
- [116] H. Tao, Z. Ma, P. Dai, and L. Jiang, “Computer-aided three-dimensional reconstruction and measurement of the optic canal and intracanalicular structures,” *The Laryngoscope*, vol. 109, no. 9, pp. 1499–1502, 1999. [Online]. Available: <http://dx.doi.org/10.1097/00005537-199909000-00026> (Cited on page 271)
- [117] G. Berger, E. Eviatar, T. Kogan, and R. Landsberg, “The normal uncinate process: histology and clinical relevance,” *European Archives of Oto-Rhino-Laryngology*, vol. 270, no. 3, pp. 959–964, 2013. [Online]. Available: <http://dx.doi.org/10.1007/s00405-012-2169-2> (Cited on page 271)

## BIBLIOGRAPHY

- [118] K. Cleary and T. M. Peters, “Image-guided interventions: Technology review and clinical applications,” *Annual Review of Biomedical Engineering*, vol. 12, no. 1, pp. 119–142, 2010, pMID: 20415592. [Online]. Available: <https://doi.org/10.1146/annurev-bioeng-070909-105249> (Cited on page 272)
- [119] D. J. Mirota, M. Ishii, and G. D. Hager, “Vision-based navigation in image-guided interventions,” *Annual Review of Biomedical Engineering*, vol. 13, no. 1, pp. 297–319, 2011, pMID: 21568713. [Online]. Available: <https://doi.org/10.1146/annurev-bioeng-071910-124757> (Cited on page 272)
- [120] K. Tatematsu, Y. Iwahori, T. Nakamura, S. Fukui, R. J. Woodham, and K. Kasugai, “Shape from endoscope image based on photometric and geometric constraints,” *Procedia Computer Science*, vol. 22, pp. 1285 – 1293, 2013, 17th International Conference in Knowledge Based and Intelligent Information and Engineering Systems - KES2013. [Online]. Available: <http://www.sciencedirect.com/science/article/pii/S1877050913010090> (Cited on page 275)
- [121] F. E. Nicodemus, “Directional reflectance and emissivity of an opaque surface,” *Appl. Opt.*, vol. 4, no. 7, pp. 767–775, Jul 1965. [Online]. Available: <http://ao.osa.org/abstract.cfm?URI=ao-4-7-767> (Cited on page 276)
- [122] A. Weiglein, W. Anderhuber, and G. Wolf, “Radiologic anatomy of the paranasal sinuses in the child,” *Surgical and Radiologic Anatomy*,

## BIBLIOGRAPHY

- vol. 14, no. 4, pp. 335–339, Dec 1992. [Online]. Available: <https://doi.org/10.1007/BF01794761> (Cited on page 290)
- [123] G. Barghouth, J. Prior, D. Lepori, B. Duvoisin, P. Schnyder, and F. Gudinchet, “Paranasal sinuses in children: size evaluation of maxillary, sphenoid, and frontal sinuses by magnetic resonance imaging and proposal of volume index percentile curves,” *European Radiology*, vol. 12, no. 6, pp. 1451–1458, Jun 2002. [Online]. Available: <https://doi.org/10.1007/s00330-001-1218-9> (Cited on page 290)
- [124] M. Emirzeoglu, B. Sahin, S. Bilgic, M. Celebi, and A. Uzun, “Volumetric evaluation of the paranasal sinuses in normal subjects using computer tomography images: A stereological study,” *Auris Nasus Larynx*, vol. 34, no. 2, pp. 191–195, June 2007. [Online]. Available: <http://dx.doi.org/10.1016/j.anl.2006.09.003> (Cited on page 291)
- [125] C. Lang, S. Grtzenmacher, B. Mlynski, S. Plontke, and G. Mlynski, “Investigating the nasal cycle using endoscopy, rhinoresistometry, and acoustic rhinometry,” *The Laryngoscope*, vol. 113, no. 2, pp. 284–289, 2003. [Online]. Available: <http://dx.doi.org/10.1097/00005537-200302000-00016> (Cited on page 291)
- [126] C. S. Kim, B. K. Moon, D. H. Jung, and Y.-G. Min, “Correlation between nasal obstruction symptoms and objective parameters of acoustic rhinometry

## BIBLIOGRAPHY

- and rhinomanometry,” *Auris Nasus Larynx*, vol. 25, no. 1, pp. 45–48, Jan 1998. [Online]. Available: [http://dx.doi.org/10.1016/S0385-8146\(97\)10011-6](http://dx.doi.org/10.1016/S0385-8146(97)10011-6) (Cited on page 304)
- [127] O. Hilberg, A. C. Jackson, D. L. Swift, and O. F. Pedersen, “Acoustic rhinometry: evaluation of nasal cavity geometry by acoustic reflection,” *Journal of Applied Physiology*, vol. 66, no. 1, pp. 295–303, 1989, pMID: 2917933. [Online]. Available: <https://doi.org/10.1152/jappl.1989.66.1.295> (Cited on pages 316 and 319)
- [128] F. L. Bookstein, “Principal warps: Thin-plate splines and the decomposition of deformations,” *IEEE Transactions on Pattern Analysis and Machine Intelligence*, vol. 11, no. 6, pp. 567–585, 1989. (Cited on page 329)

# Vita



Ayushi Sinha received her Bachelor of Science degree in Computer Science and Bachelor of Arts degree in Mathematics from Providence College in 2011, and enrolled in the Computer Science Ph.D. program at the Johns Hopkins University that same year. She was inducted into the Pi Mu Epsilon honor society in 2009, Chi Alpha Sigma honor society and the American Mathematical society in 2010, and Upsilon Pi Epsilon honor society in 2017. She also received the Jun Wu and Yan Zhang endowed graduate student fellowship in 2011. Her research focuses on deformable registration techniques for information inference. She has submitted papers to several prestigious conferences and journals, and her paper on segmentation and correspondence improvement was a finalist for best student paper award at the SPIE medical imaging conference in 2017.



## VITA

Starting the summer of 2018, Ayushi will continue at the Johns Hopkins University as a Provost Postdoctoral Fellow, where she will continue to develop her ideas on segmentation, modeling and deformable registration. She hopes to help better understand the variations that exist in various anatomical structures, and leverage this knowledge to provide better medical care to patients.